

Book of Proceedings

Edited by:

Francisco Pimenta

Sérgio Pereira

João Pacheco

Mário Sobrinho

Filipe Magalhães

DECEMBER 2020

University of Porto

16th EAWE PhD Seminar on Wind Energy



*Artistic paint by Joana Vasconcelos

Photography by TAKEMEDIA – Digital Motion



Index

Aerodynamics	1
Control	29
Farm / Wind Turbine Modelling	32
Foundation & Geotechnics	59
New Concepts	67
O & M	81
Offshore Wind	104
Reliability	131
Social Acceptance & Techno-Economics	150
Structural Analysis	160
Wind Resource, Turbulence & Wake	191

AERODYNAMICS

CFD solver and meshing techniques verification using the DANAERO database

T. Potentier^{a,b}, E. Guilmineau^a, and C. Braud^a

^aLHEEA (Centrale Nantes / CNRS), 1 rue de la Noë 44321 Nantes Cedex 3 - FRANCE

^bENGIE Green, 15 rue Nina Simone 44000 Nantes - FRANCE

14-16/12/2020

E-mail: thomas.potentier@ec-nantes.fr

Keywords: aerofoils, aerodynamics, CFD, FINETM/Marine, DANAERO

Abstract

A CFD (Computational Fluid Dynamics) software is tested against the DANAERO database, which consists of field experiments, wind tunnel tests and CFD simulations. The aim of the paper is to verify FINETM/Marine in the context of wind turbines so as to use it in more advanced modelling, e.g.: 2D CFD for aerofoil with aerodynamic add-ons, 2D dynamic stall effects. Several aerofoil thicknesses will be benchmarked. The results will be presented in the form of lift and drag coefficients curves for the different sections. Simulations on a structured mesh showed a good agreement with DANAERO's CFD results. The next stage, after the verification of FINETM/Marine, will be to take the simulation one step further and model the full wind turbine in 3D CFD.

Keywords: aerofoils, aerodynamics, CFD, FINETM/Marine, DANAERO, Design of Experiments

1 Introduction

In order to verify FINETM/Marine in the context of wind turbine aerodynamics, a Design of Experiment (DoE) approach will be employed to help define the CFD domain boundaries. FINETM/Marine has already been extensively validated in 2D and 3D marine hydrodynamics applications [1, 2, 3, 4]. However, it has not been used for 2D aerofoil aerodynamics. By applying a DoE approach, the authors will build a robust test matrix which will provide the means to study the effects and interactions between the selected factors. Then, once the domain is chosen, aerodynamic polars will be calculated using an unsteady 2D CFD solver and compared against the reference C_L and C_D . The DANAERO database [5, 6] will be used as the reference in this paper. The database is available since 2010 and comprises of field data, wind tunnel data and simulation data. Troldborg et al.[7] have already compared the wind tunnel results with EllipSys[8]. To verify FINETM/Marine, a goal of 2% difference with the wind tunnel results for the C_L in the linear region is set. This threshold has been chosen following a previous codes comparison where seven CFD software were benchmarked against each other[9]. Four of the the software tested were within a 2% accuracy, it seems to the authors an appropriate target to achieve with FINETM/Marine.

2 Simulation set-up

2.1 FINETM/Marine - ISIS-CFD

ISIS-CFD, developed by Centrale Nantes and CNRS and available as a part of the FINETM/Marine computing suite, is an incompressible Unsteady Reynolds-Averaged Navier-Stokes (URANS) method. The solver is based on the finite volume method to build the spatial discretization of the transport

equations. The unstructured discretization is face-based, which means that cells with an arbitrary number of arbitrarily shaped faces are accepted. A second order backward difference scheme is used to discretize time. The solver can simulate both steady and unsteady flows. The velocity field is obtained from the momentum conservation equations and the pressure field is extracted from the mass equation constraint, or continuity equation, transformed into a pressure equation. In the case of turbulent flows, transport equations for the variables in the turbulence model are added to the discretization.

The sections analysed in this paper were the aerofoils used to design the LM38.8 blade installed on the DANAERO test turbine [10]. The sections name are listed in the Table 1 and plotted in Figure 1. The Reynolds number in this benchmark is set at $Re = 5E6$ as it is the average Reynolds calculated along the blade radius for an inflow of approximately 6.5m/s. The turbulence model used is SST $k-\omega$ [11], the flow characteristics are representing the air at sea level at a temperature of $15^\circ C$, i.e.: $\nu = 1.81e^{-5}$ (dynamic viscosity [$kg.m^{-1}.s^{-1}$]) and $\rho = 1.225$ (air density [$kg.m^{-3}$]). Regarding the simulation boundary conditions, the aerofoil related surfaces were described as “no slip wall”. The free stream velocity condition was imposed on the Inlet, Outlet and Top/Bottom and the Outlet was using the condition Prescribed pressure. Finally, $y+ = 0.15$ was imposed on the aerofoil surfaces.

Table 1: Aerofoil analysed

Section ID	Aerofoil thickness
Section05	24%
Section08	19.6%
Section10	18.6%

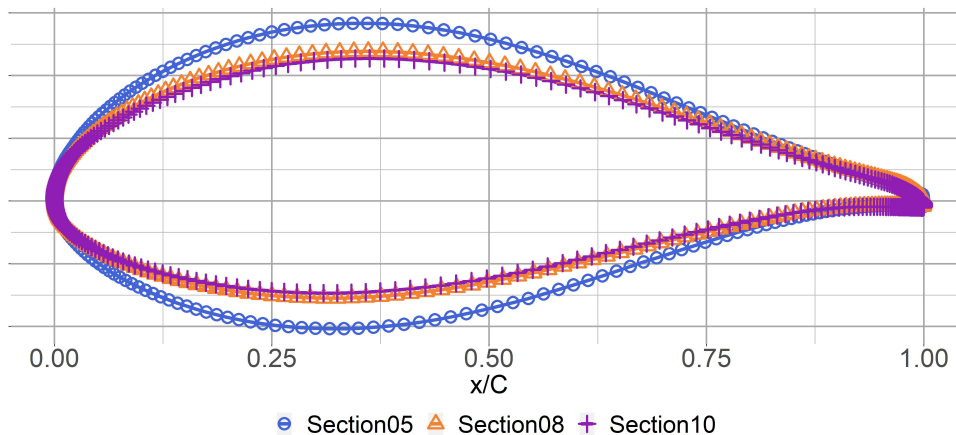


Figure 1: All three DANAERO sections analysed. The marker (\circ) represents the Section05, the marker (\triangle) represents the Section08 and the marker ($+$) represents the Section10.

2.2 Six Sigma - Design of Experiments

The Six Sigma purpose is to understand the relationship between factors and their possible interactions in order to reduce variation in the outcome. The DoE is a standardised way of ordering possible combinations of several factors (parameters) and levels (values they can take) to compare the outcome with a validation criteria. The validation criteria will be the calculated lift coefficient (C_L). Extrapolating on the DoE results will allow the authors to decide on the appropriate calculation domain size.

In our case, several factors related to the flow model and turbulence model were already fixed and will not be taken into account here. However, the domain boundaries for an infinite simulation remain unknown and the test matrix will help us decide which domain size is the most appropriate. The term “infinite simulation” here, means free from any interaction with external boundaries, e.g. the wind tunnel walls are not simulated, therefore the aerofoil is considered at rest in the moving fluid.

The factors chosen in this experiment are the Inlet position, the Outlet position (both together defining the domain length) and the Top/Bottom position (constituting the domain vertical dimension). All factors are expressed in aerofoil chord length, defined between 0 and 1. The aerofoil leading edge is positioned at the domain origin (0,0) with the trailing edge pointing towards the Outlet. Consequently the Inlet is positioned in front of the leading edge and the Outlet behind the trailing edge while the aerofoil chord is parallel to the Top/Bottom boundaries. The vertical dimension is symmetrical around the aerofoil chord (See Figure 2). Since all aerofoils are all relatively thin, it is assumed that using the outcome of the DoE will be valid for all studied sections. The section ran through the DoE is the Section05.

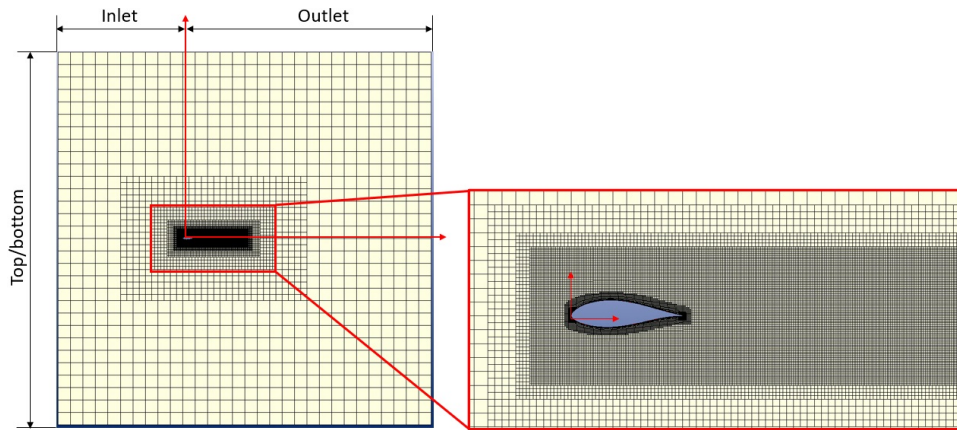


Figure 2: Factors definition applied to an arbitrary domain.

By using three factors with two levels each, the total number of possible combinations is $2^3 = 8$. The total number of cases possible are proportional to the power of the number of levels, i.e. if three levels are utilised for the same three factors, the DoE will yield more detailed results but the numbers of cases will increase drastically ($3^3 = 27$). To avoid running many unnecessary test cases, a centre point will be added to the 8 cases. It will assess the non-linearity in the results for a lower cost. The Table 2a, shows how the parameters must be set to run the DoE. The values 1 and -1 represent the low (Level 1) and high (Level 2) levels for each parameters while the 0 represents the centre point case between the chosen levels (see Table 2b). In order to assess the independence of the domain with the angle of attack, a DoE for three angles of attack ($\alpha_1 = 0^\circ$, $\alpha_2 = 7^\circ$, $\alpha_3 = 12^\circ$) will be calculated. The test matrix will be run once for each angle of attack. The results presented in section 3.1 will only show the outcome for $\alpha_1 = 0^\circ$.

Table 2: Design of Experiments

(a) Test matrix				(b) Factors levels			
Test ID	Inlet position	Outlet position	Top/Bottom position	Factor	Level 1	Level 2	Center point
1	-1	-1	-1	Inlet position	-20	-40	-30
2	1	-1	-1	Outlet position	20	40	30
3	-1	1	-1	Top/bottom position	-20/20	-40/40	-30/30
4	1	1	-1				
5	-1	-1	1				
6	1	-1	1				
7	-1	1	1				
8	1	1	1				
9	0	0	0				

3 Results

3.1 DoE results analysis

The Figure 3 shows the main effects for each factor. The x-axis shows the different levels (centre point included) for each parameter, while the y-axis shows the averaged C_L response. The dotted line is the average C_L for all 9 cases. Each data point on any subplot is calculated by taking the average C_L corresponding to this factor level. For instance, the data point when the Outlet is at Level 2 is calculated by averaging all the C_L values for the test ID: 3, 4, 7 and 8. The Figure 3 is read as follow: for the first subplot, the further from the origin the inlet position is the more the average C_L tends to increase. For the second subplot the line is almost flat, which means that the position of the Outlet doesn't influence the average C_L . Lastly, the third subplot shows that the vertical dimension tends to reduce slightly the C_L with increasing size. The maximum effect from a factor upon the C_L is seen for the Inlet position: $\Delta C_L = 0.360 - 0.338 = 0.021$, which is equivalent to a variation of 6%. Analysing those plots alone is not enough, since we are averaging the test cases based on the factor, it may be possible that interactions between factors play a more significant role than a factor alone. Moreover, the centre point (*) is far from the linear model, which indicates that some non-linearity exists. Again the analysis of interaction between factors will help us define the non-linearity.

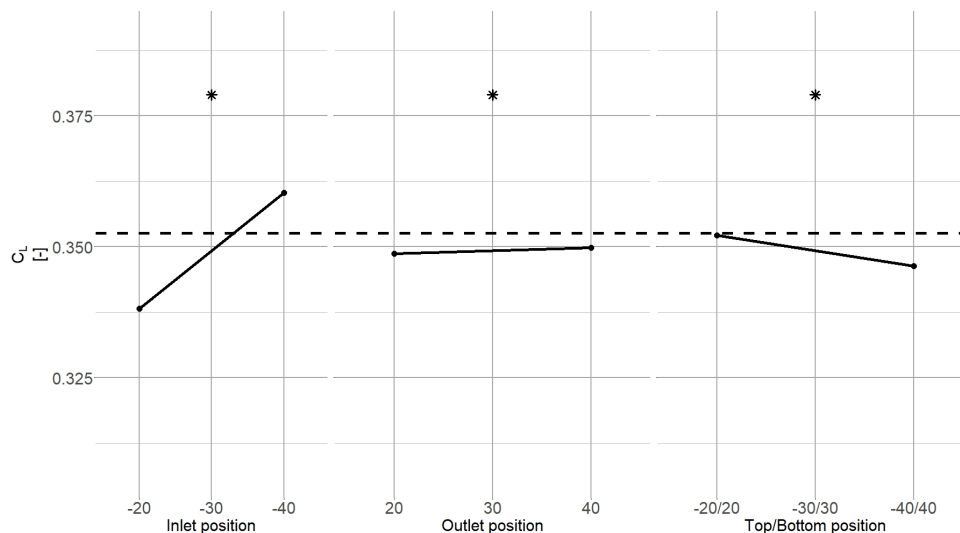


Figure 3: Main effects plot for all factors for $\alpha = 0^\circ$. The dashed line represents the average C_L across the test matrix. The (*) represents the centre point case.

The Figure 4 shows the interactions between the factors. The x-axis shows the different levels (centre point included) for each parameter. The y-axis shows the averaged C_L response for this factor when only a single other factor is considered. Looking at the first subplot, the interaction between the Inlet (marker shapes \bullet and \triangle) and Outlet position (line types and colours) is assessed. The lines are intersecting, it indicates a strong interaction between the two factors, as it should be expected since they both define the domain length where the wake is calculated. However, the two lines for the second subplot are parallel, meaning there is no interaction between the Inlet position and the Top/Bottom position. The third subplot shows also an intersection but not at the centre, closer to the Level 1 results; indicating that there is also an interaction between the Outlet position and the Top/Bottom position.

Analysing those plots is not trivial: while looking more carefully at the results the authors found out that the interaction between factors and the non-linearity seen in the main effect is explained by the non-symmetrical chordwise dimension of the domain. Indeed, the test cases 2, 3, 6 and 7 are responsible for the behaviour seen in Figure 4. This is an important conclusion: the unstructured mesh from FINETM/Marine can behave unexpectedly if the domain is not symmetric. In particular, the automatic refinement process may not refine properly small surfaces e.g.: trailing edge. The first cell is skewed and too small for a

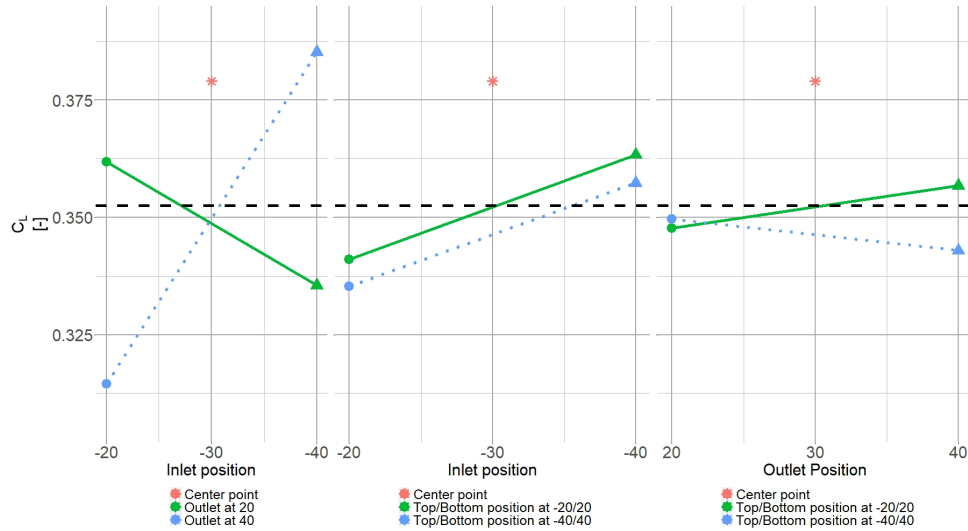


Figure 4: Interaction diagram for $\alpha = 0^\circ$. The dashed line represents the average C_L across the test matrix. The (*) represents the centre point case. The (●) represent the considered factor at Level 1. The (△) represents the analysed factor at Level 2. The solid and dotted line represent the Level 1 and Level 2 of the other factor analysed.

proper viscous cells insertion. Therefore, acknowledging this new information and analysing the rest of the plots, the domain dimensions chosen are:

- Inlet position: -40
- Outlet position: 40
- Top/bottom position: -40/40

Following the decided boundaries, the refinement strategies and the number of data point making the aerofoil (384 coordinates points), the total number of cells in the Section05 calculation domain is 133516.

3.2 CFD calculated polars

The FINETM/Marine results were obtained using the same domain size for different aerofoil thicknesses. The Figure 5, Figure 6 and Figure 7 show the comparison between the aerodynamic coefficients (C_L and C_D) calculated using FINETM/Marine, the wind tunnel reference and EllipSys.

The Figure 5 shows a perfect agreement between FINETM/Marine and the wind tunnel data in the linear region ($-10^\circ < \alpha < 9^\circ$) for the C_L curve. The stall and post-stall ($\alpha > 9^\circ$ and $\alpha < -10^\circ$) characteristics however, are poorly captured. The simulation results overshoot the wind tunnel measurements. Both CFD software tend to overpredict the overall C_D value compared to the wind tunnel reference, the stall points are also not well captured.

The Figure 6 exhibits a different behaviour from the Figure 5. The slope of the FINETM/Marine results is not perfectly aligned with the wind tunnel results. Moreover, the C_L value in the linear region is slightly underpredicted. Looking carefully at the plot, it appears that the EllipSys simulations yields similar results. The stall and post-stall characteristics are again poorly captured. Similarly to the Section05 results, the drag coefficient is overpredicted.

Similar to the Figure 5, the Figure 7 shows a good agreement between FINETM/Marine and the wind tunnel data in the linear region ($-10^\circ < \alpha < 9^\circ$) for the C_L curve. The stall and post-stall ($\alpha > 9^\circ$) characteristics however, are poorly captured but it remains lower than the value simulated by EllipSys. Again, the CFD software tend to overpredict the C_D value compared to the wind tunnel reference missing also the stall point prediction.

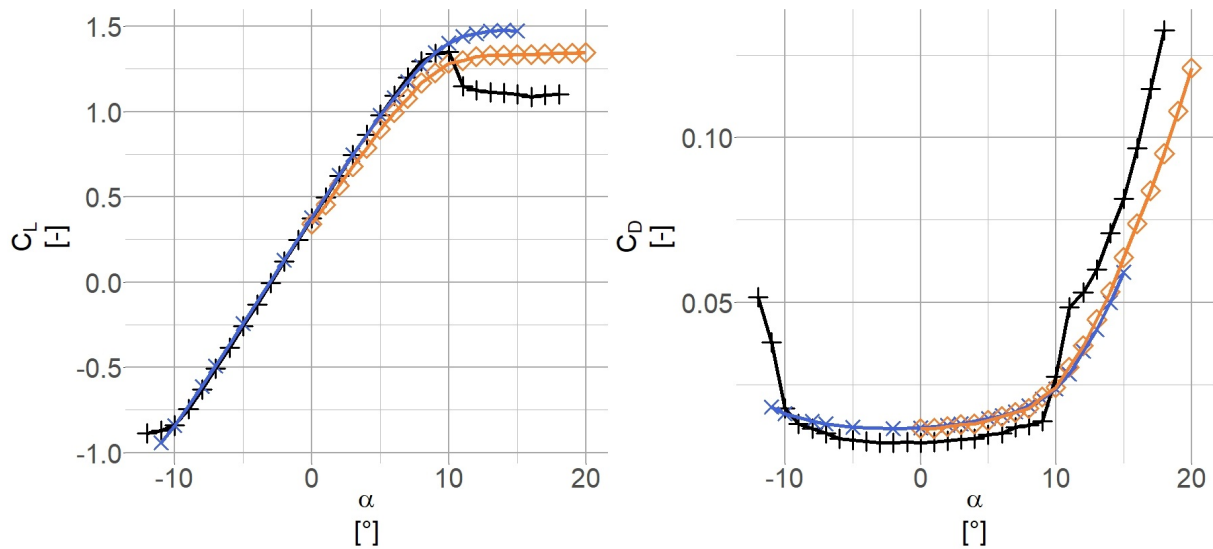


Figure 5: DANAERO Section05: the blue (×) represent the FINETM/Marine results, the orange (◇) the DANAERO CFD reference and the black (+) are the DANAERO wind tunnel data results. Left: C_L , right: C_D curve.

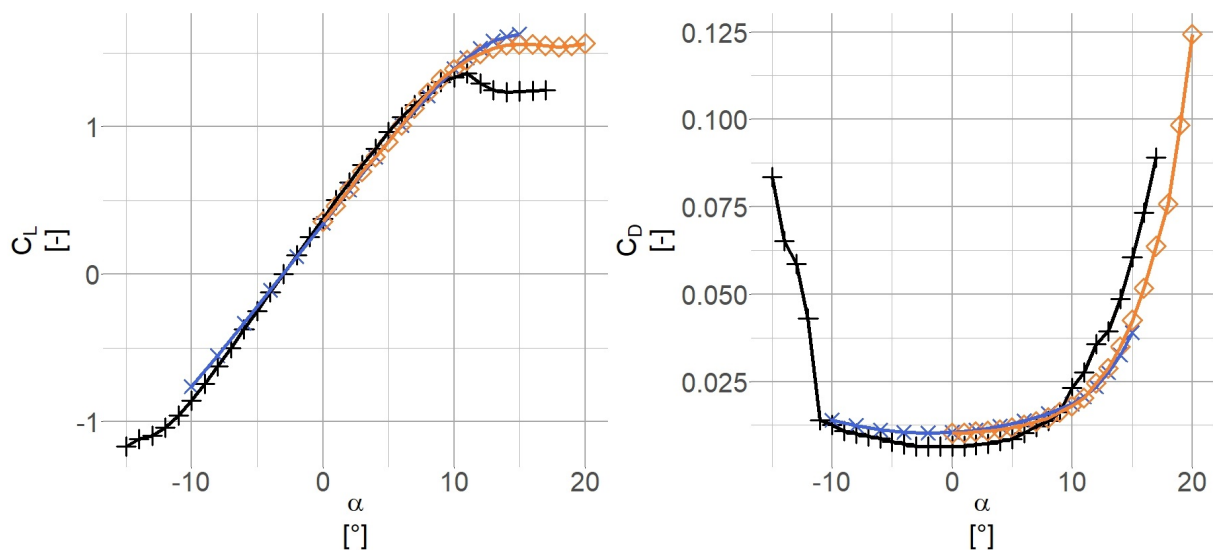


Figure 6: DANAERO Section08: the blue (×) represent the FINETM/Marine results, the orange (◇) the DANAERO CFD reference and the black (+) are the DANAERO wind tunnel data results. Left: C_L , right: C_D curve.

The Table 3 shows the average deviation between the different sections analysed and the wind tunnel in the linear region ($-10^\circ < \alpha < 9^\circ$). The Section05, which was used in the DoE, shows the best agreement. However, the results from the Section08 are outside the set tolerance of 5% defined. It is to be noted that the differences calculated for FINETM/Marine are of the same order of magnitude than the ones calculated for EllipSys.

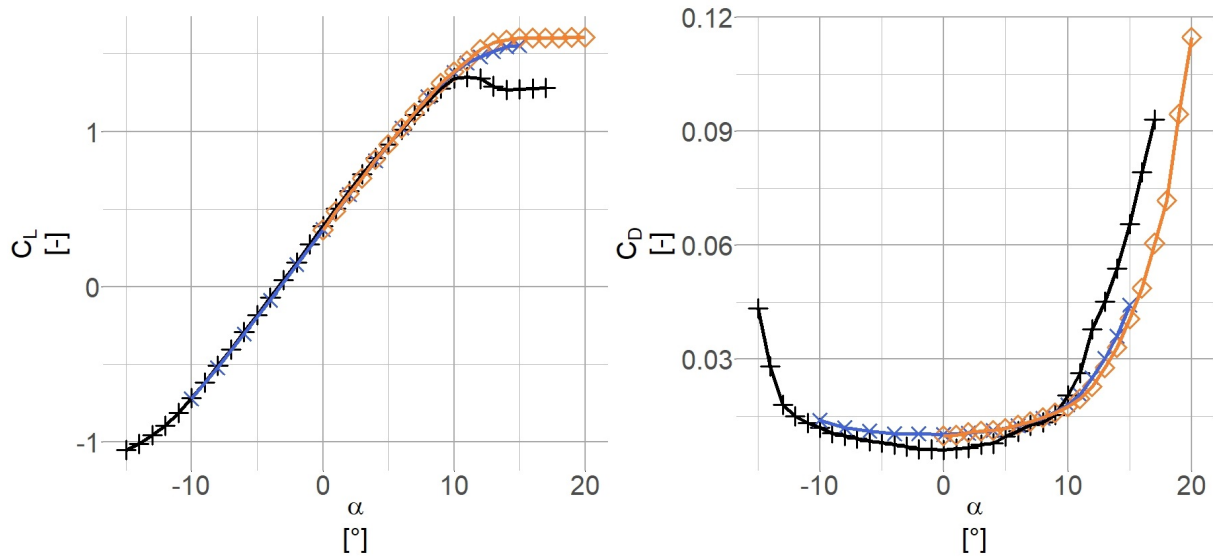


Figure 7: DANAERO Section10: the blue (×) represent the FINE™/Marine results, the orange (◇) the DANAERO CFD reference and the black (+) are the DANAERO wind tunnel data results. Left: C_L , right: C_D curve.

Table 3: Average C_L deviation with wind tunnel reference in the linear region

Sections	FINE™/Marine difference with WT		EllipSys difference with WT
	$-10^\circ < \alpha < 9^\circ$	$0^\circ < \alpha < 9^\circ$	$0^\circ < \alpha < 9^\circ$
Section05	-0.6%	-0.3%	-9%
Section08	-8%	-6%	-5%
Section10	-0.8%	-0.7%	-1%

4 Conclusion

A CFD software has been verified against a validated database. Despite not fully meeting the goal set in the introduction, FINE™/Marine can be considered validated. The results show satisfactory results for the Section05 and the Section10. In particular, the lift coefficient (C_L) is slightly better predicted than EllipSys. The poorer results for the Section08 are to be put into perspective since the results are aligned with the EllipSys reference. A dedicated calculation domain would have probably improved the calculated coefficients. The stall overprediction of CFD simulations compared to wind tunnel experiments when using URANS [12, 13] is well known. Using IDDES (Improved Detached Eddies Simulation) simulations could be a solution for more accurate stall prediction. However, due to high computational costs inherent to it, it would be an expensive solution[14].

References

- [1] Deng G B, Guilmineau E, Queutey P and Visonneau M 2005 Ship Flow Simulations with the ISIS CFD Code *CFD Workshop Tokyo 2005 (CFDWS2005)* pp 474–482
- [2] Deng G B, Queutey P and Visonneau M 2006 A code verification exercise for the unstructured finite-volume cfd solver isis-cfd *European Conference on Computational Fluid Dynamics ECCOMAS CFD 2006* p 18
- [3] Guilmineau E, Deng G B, Leroyer A, Queutey P, Visonneau M and Wackers J 2018 *Journal of Fluids Engineering* **140** 021111 ISSN 0098-2202, 1528-901X URL <https://asmedigitalcollection.asme.org/fluidsengineering/article/doi/10.1115/1.4037984/374183/Numerical-Simulations-for-the-Wake-Prediction-of-a>
- [4] Guilmineau E, Deng G, Leroyer A, Queutey P, Visonneau M and Wackers J 2017 *Computers & Fluids* **176** 302–319 ISSN 00457930 URL <https://linkinghub.elsevier.com/retrieve/pii/S0045793017300051>
- [5] Madsen H A, Bak C, Paulsen U S, Gaunaa M, Fuglsang P, Romblad J, Olesen N A, Enevoldsen P, Laursen J and Jensen L 2010 *The DAN-AERO MW Experiments: Final report* (DTU Wind Energy) ISBN 978-87-550-3809-7 URL <https://orbit.dtu.dk/en/publications/the-dan-aero-mw-experiments-final-report>
- [6] Trodborg N, Bak C, Madsen H and Skrzypinski W 2013 *DANAERO MW II Final Report (DTU Wind Energy E no 0027(EN))* (DTU Wind Energy) URL <https://orbit.dtu.dk/en/publications/danaero-mw-final-report>
- [7] Troldborg N, Bak C, Sørensen N N, Madsen H A, Réthoré P E, Zahle F and Guntur S 2013 Experimental and numerical investigation of 3D aerofoil characteristics on a MW wind turbine *Proceedings - European Wind Energy Conference & Exhibition 2013* (European Wind Energy Association (EWEA)) tex.ids: troldborgExperimentalNumericalInvestigation2013 URL <https://orbit.dtu.dk/en/publications/experimental-and-numerical-investigation-of-3d-aerofoil-character>
- [8] Sørensen N N 1995 *General purpose flow solver applied to flow over hills* Ph.D. thesis DTU publisher: Risø National Laboratory URL <https://orbit.dtu.dk/en/publications/general-purpose-flow-solver-applied-to-flow-over-hills>
- [9] Sorensen N N, Mendez B, Munoz A, Sieros G, Jost E, Lutz T, Papadakis G, Voutsinas S, Barakos G, Colonia S, Baldacchino D, Baptista C and Ferreira C 2016 *Journal of Physics: Conference Series* **753** 082019 ISSN 1742-6588, 1742-6596 URL <https://iopscience.iop.org/article/10.1088/1742-6596/753/8/082019>
- [10] Bak C, Madsen H A, Troldborg N, Sørensen N and Madsen J 2013 DANAERO MW: Data for the NM80 turbine at Tjæreborg Enge for aerodynamic evaluation Tech. rep. DTU Wind Energy Report
- [11] Menter F 1993 Zonal Two Equation k-w Turbulence Models For Aerodynamic Flows *23rd Fluid Dynamics, Plasmadynamics, and Lasers Conference* Fluid Dynamics and Co-located Conferences (American Institute of Aeronautics and Astronautics) URL <https://arc.aiaa.org/doi/10.2514/6.1993-2906>
- [12] Shelton A, Abras J, Jurenko R and Smith M 2005 *Improving the CFD Predictions of Airfoils in Stall* (American Institute of Aeronautics and Astronautics)
- [13] Wolfe W, Ochs S, Wolfe W and Ochs S 1997 CFD calculations of S809 aerodynamic characteristics *35th Aerospace Sciences Meeting and Exhibit* (Reno,NV,U.S.A.: American Institute of Aeronautics and Astronautics) URL <http://arc.aiaa.org/doi/10.2514/6.1997-973>
- [14] Sørensen N N and Timmer W A 2017 CFD prediction of airfoil deep stall performance using Improved Delayed Detached Eddy Simulations *Wind Energy Science Conference* (Lyngby, Sweden) p 17 URL https://orbit.dtu.dk/files/141969070/280617_14.20_S08.pdf

Dynamic Stall Modelling for Wind Turbines: URANS simulations on 2D wind turbine airfoils

D V G Santos^{a,b}, B Stoevesandt^{b,c}, J Peinke^{a,b}

^a Carl von Ossietzky Universität Oldenburg – Germany

^b TWiSt – Germany

^c Fraunhofer IWES – Ammerländer Heerstraße 136, 26129 Oldenburg, Germany

E-mail: daniel.von.glehn.dos.santos@uni-oldenburg.de

Abstract. This work is part of my PhD thesis, which focuses on computational fluid dynamics (CFD) methods to investigate the characteristics of the flow around an airfoil under dynamic stall. Since the results strongly depend on the turbulence characteristics, the approach to turbulence modeling is of large importance. Currently, URANS simulations have been run for a S809 airfoil and compared to modeled and measured data from the literature. Then, the same setup was applied to a DU 91-W2-250 airfoil. These cases were set with Re of 10^6 and the airfoil pitches around $0.25C$ with reduced frequency of 0.079 , main angle of attack of 8° and amplitude of $\pm 10^\circ$. Both k -OmegaSST and Spalart-Allmaras turbulence models were tested and the first one gave the best results, when compared to the literature data.

Keywords: Dynamic Stall, Wind Turbines, Aerodynamics, CFD

1 Introduction

Due to the turbulent nature of the flow, stall onset and therefore dynamic stall are hard to predict. However, wind energy relies on good models for dynamic stall and the existing ones have not been made specially for thick airfoils. Stall onset, separation and impingement points are difficult to predict due to the dependency on wall turbulence. A wrong prediction of these points leads to a large deviation in the aerodynamics of airfoils. And this large deviation can be harmful to the blade structure by increasing fatigue loads [1] or by violent flutter led by the stall inception [2].

There have been some experimental investigations on dynamic stall lately. However, the information of these experiments are usually limited, since only forces are measured. The physics of the flow, which is important for the generation of a generalizable model, is however not taken into account.

Visbal [6] investigated the unsteady boundary layer on the leading edge of an airfoil while changing the rotation of the blades using LES (Large Eddy Simulation). The simulations show that the local effects of transition, separation of the boundary layer and compression are important in the development of the dynamic stall vortices. In the studied profile, the occurrence of vortices was closely associated with the detachment of laminar separation bubbles. For quantitative simulations with Unsteady Reynolds Average Navier-Stokes Equations (URANS), the challenge is therefore to map the laminar separation, which makes the use of a transition model indispensable.

In a comparison between simulations with URANS and measurements of Particle Image Velocimetry (PIV), Buchner *et al.* [4] showed that many aspects of dynamic stall can be reasonably well described with URANS. Also, Wang *et al.* [7] showed that URANS, especially with the k -Omega Shear Stress Transport (STT) – as an improvement over the standard k -Omega turbulence model – is useful for the fast design or research intensification, when simulating dynamic stall.

The NREL's S809 airfoil was selected for the first URANS simulations because it is a very common profile for wind turbines, it has a moderate thickness (21% relative thickness) and there are some works in the literature that investigate its behavior under dynamic stall, both numerically – by Bangga [3] – and experimentally – by Ramsay *et al.* [5]. Another profile used in this work is the DU 91-W2-250, to which the same setup was applied.

In this work, URANS was used in order to provide some insights on the setup for further LES and DDES simulations and also to evaluate how well it can represent the dynamic stall phenomena despite its limitations.

2 Simulation Setup

The software OpenFOAM was used to conduct the simulations. First a steady case was run with potentialFOAM solver and then it was used to initialize another 2-steps steady-state simulations with simpleFOAM solver. The results from the 2-step steady-state simulation were then used as input for an unsteady case with fixed angle of attack (AoA) through the solver pimpleFOAM. At last, this result was used as initialization for the pitching airfoil case, also with pimpleFOAM solver.

This setup was approached with 2 different turbulence models: Spalart-Allmaras (SA) and k-OmegaSST (SST).

The two-dimensional mesh (Figure 1a) has an O-grid shape with 256 points over the airfoil surface, 128 points in the normal direction, diameter of 50 times the chord length (C) and y^+ equal to 1. The total number of cells is 32512. The Reynolds number is 1 million and timestep is 0.002s.

For pitching the airfoil, the SolidBodyMotion function from OpenFOAM was used. In this case, an oscillating rotating motion was imposed to the whole mesh with center of rotation at a quarter chord position. It started from the mean AoA of 8° , pitching with amplitude of $\pm 10^\circ$ and reduced frequency of 0.079.

The exact same setup was applied to the DU 91-W2-250 airfoil. The mesh used for the DU 91-W2-250 airfoil is shown in Figure 1b.

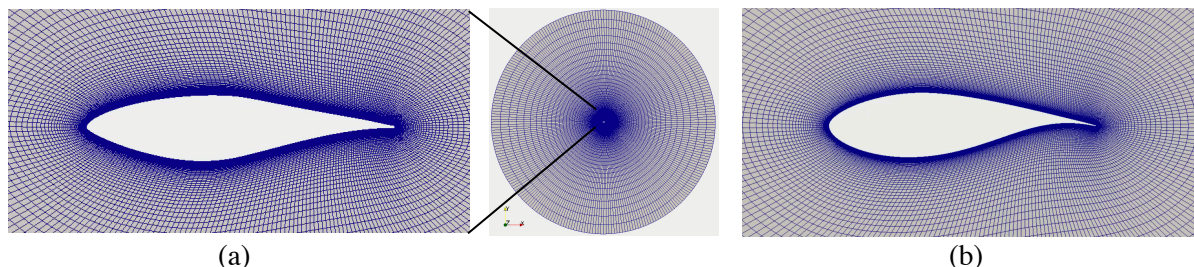


Figure 1 2D O-grid over the (a) NREL's S809 airfoil and (b) DU 91-W2-250 airfoil used in this study.

The total duration of the simulation is 20 seconds, which corresponds to 5 complete cycles of 4 seconds. Only the last cycle i.e., from 16s to 20s, was used to compare the results.

3 Results

The results of the CFD simulations are presented in this section as plots of aerodynamic lift coefficients (C_L) over AoA. The results for the S809 airfoil from all sources i.e., the present work, Bangga's simulations and the experimental data, are plotted in Figure 2. The black and blue lines represent the present work's results for SA and SST, currently, the green and red lines represent the results from Bangga and the black dots are the experimental data.

From the plot, one can see that the simulations were able to capture the hysteretic behaviour of the lift coefficient and also the sudden drop of C_L after around AoA 15° during stall. It is noticeable that the SST simulation provided the closest results to the experimental data. The SA simulation shows a

damped shape, clear and without any oscillation, with a good agreement before stall point and overestimation at the post-stall region.

When compared to the results from Bangga, the present work's SST also shows better agreement with the experiments than the SA-Bangga results, which were his best results.

The experimental data seems to have an offset of approximately 0.2 in the C_L axis, but no explanation about it was found in the paper.

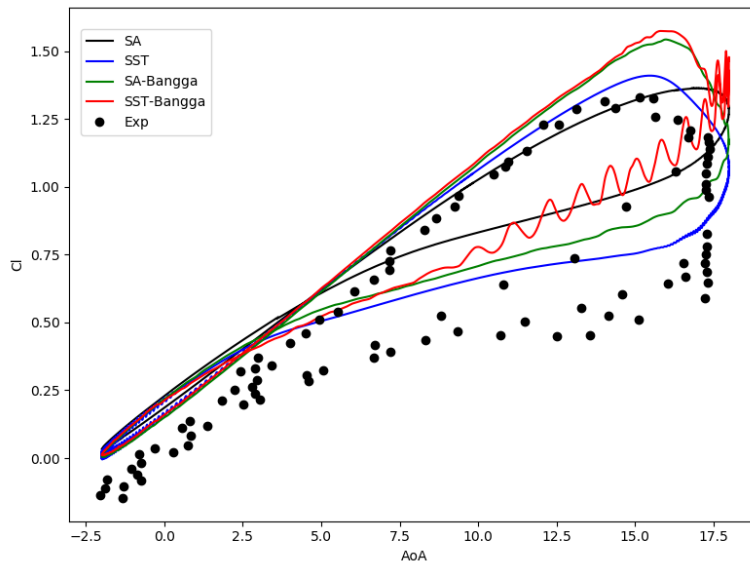


Figure 2 Comparison of the dynamic lift coefficient C_L over the angle of attack AoA for the S809 airfoil.

Figure 3 shows the results from the simulations generated with the setup applied to the DU 91-W2-250 airfoil. The black and blue lines represent SA and SST simulations, currently. Here, it is also noticeable that the SA simulation has the same damped-like behaviour and overestimation in the post-stall region. There is currently no experimental data available to validate these simulations, it will be probably done with future LES studies.

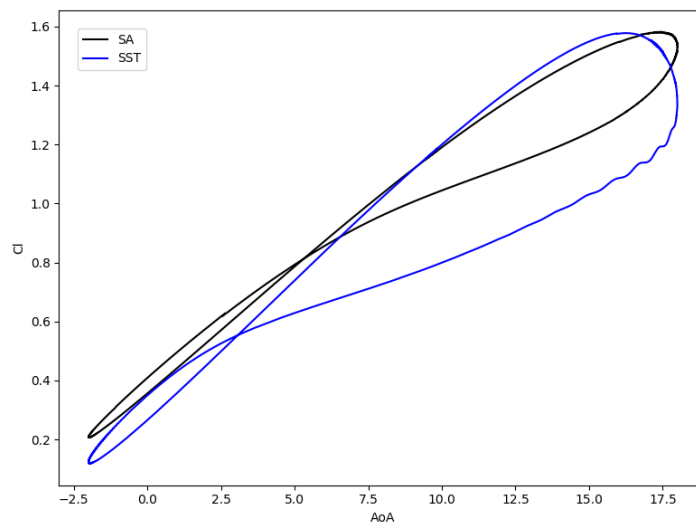


Figure 3 Dynamic lift coefficient C_L over the angle of attack AoA for the DU 91-W2-250 airfoil.

4 Conclusion and further considerations

The aim of this paper was to develop a proper URANS setup for a 2D flow over a pitching NREL's S809 airfoil under dynamic stall conditions and validate it against numerical and experimental results from the literature. Two different turbulence were tested: Spalart-Allmaras (SA) and kOmegaSST (SST). The results were validated against experimental data from the literature [5] and then compared to numerical simulations from Bangga [3]. The validated setup was later applied to a DU 91-W2-250 airfoil.

The S809 results revealed that the SST model better represents the phenomena when compared to the SA model, which shows a somehow damped behavior and overestimation of the aerodynamic lift after the stall region. The setup with SST model showed results closer to the experiments than the numerical results from Bangga, especially in the post-stall region.

After validation, the setup was to the DU 91-W2-250 and the same damped-like behavior of the SA was observed.

The next step, which is in progress, is the development of a very fine and well structured mesh to run LES simulations.

Acknowledgements

Acknowledgments to the University of Oldenburg and in particular to the TWiSt group and the CFD colleagues. Special thanks to Dr. Galih Bangga for kindly and promptly providing his data.

This work was carried out with support from CNPq (National Council for Scientific and Technological Development) – Brazil.

Bibliography

- [1] Bangga G, Kim Y, Lutz T, Weihing P, Krämer E 2016 *Journal of Physics: Conference Series* **753** 22026
- [2] Bangga G, Hutomo G, Wiranegara R, Sasongko H 2017 *Journal of Mechanical Science and Technology* **31** 261 – 267
- [3] Bangga G 2019 *Journal of Mechanical Science and Technology* **33** 1257 – 1262
- [4] Buchner A J, Lohry M W, Martinelli L, Soria J, Smits A J 2015 *Journal of Wind Engineering and Industrial Aerodynamics* **146** 163 – 171
- [5] Ramsay R F, Hoffman M J, Gregorek G M 1995 *Effects of grit roughness and pitch oscillations on the S809 airfoil* Technical Report Number NREL/TP-442-7817
- [6] Visbal M R 2014 *52nd Aerospace Sciences Meeting, AIAA SciTech Forum*, AIAA 2014 – 0591
- [7] Wang S, Ingham D B, Ma L, Pourkashanian M, Tao Z 2010 *Computers and Fluids* **39** 1529 – 1541

Design and evaluation of a blade for experiments on fluid structure interaction

A Langidis^a, S Nietiedt^b, L Kröger^a, T Wester^a, F Berger^a, and M Kühn^a

^aForWind - University of Oldenburg, K upkersweg 70, 26129, Oldenburg, Germany

^bJade University of Applied Sciences, Ofener Str. 16/19, 26121, Oldenburg, Germany

E-mail: apostolos.langidis@uol.de

Keywords: wind tunnel, model wind turbine, scaling

1 Introduction

Wind tunnel experiments with scaled wind turbine models at various sizes have been used in the past to get valuable insights into wind turbine aerodynamics and the wake behaviour. They were further used to test and validate algorithms for turbine and wind farm control. Most of these models feature rather stiff blades, such as the carbon fiber made blades of the model wind turbine Oldenburg with 1.8 m diameter (MoWiTO 1.8) [1]. These blades have a much smaller tip deflection, normalized with their length, than contemporary multi MW wind turbines. Due to this reduced deflection of the blades, fluid structure interaction on the blade cannot sufficiently be studied. The present contribution's objective is to present the design procedure for a set of aeroelastically scaled blades for MoWiTO and evaluating their behaviour under wind tunnel conditions.

2 Design and manufacture

The scaling approach for the blades is formulated on the preservation of the tip speed ratio, the Lock number and the non-dimensional eigenfrequencies. The aerodynamic shape of the MoWiTO stiff blades', which have been designed with the target of maintaining the tip speed ratio of the 5MW NREL turbine and the lift distribution of the reference rotor, is preserved.

For the chosen geometrical scaling ratio of 1/70 and for the time ratio of 50, a first flapwise eigenfrequency of 33 Hz and a total mass of approximately 50 g is desired. This is rather challenging to be achieved. A new flexible and lightweight structural layout is adopted. The structure consists of a foam core, two carbon spars and skin from carbon fiber layers. The final design was a compromise between the scaling and strength requirements, dependent on manufacturing constraints. The weight of the externally produced blades is approximately 82 g.

3 Simulation model and experiment

Next, the blades were deployed in an experimental campaign (Fig. 1a), which included PIV measurements on the rotating blades and digital image correlation techniques to obtain the deflection of the rotor blade during operation of the MoWiTO 1.8 with the new blade set [2]. Experiments were performed in tailored turbulent wind conditions (Fig. 1b), which were generated with an active grid in the WindLab wind tunnel of the University of Oldenburg [3]. Quantities such as the turbine's rotor speed, the blade root bending moments and the rotor thrust were measured using MoWiTO's onboard instrumentation.

In order to evaluate the blades in comparison with the ideally scaled ones, a simulation model was built in openFAST. The input for the aerodynamic model was the blade geometry and the airfoil polars, while the structural model input was defined from scaling down the reference blades' properties.

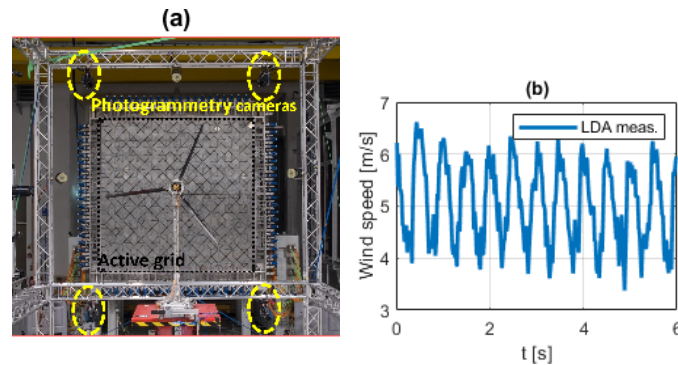


Figure 1: (a) MoWiTO setup in the wind tunnel. (b) 2 Hz sinusoidal wind generated by the active grid.

4 Results and outlook

The first measurements are compared with the simulation results for the perfectly scaled model turbine and previous measurements with the stiff blades (Fig. 2). The tip deflection under different wind regimes is to be presented. The blade's behaviour is to be evaluated in regard to the aeroelastic scaling requirements and therefore, whether it allows the study of fluid structure interaction phenomena.

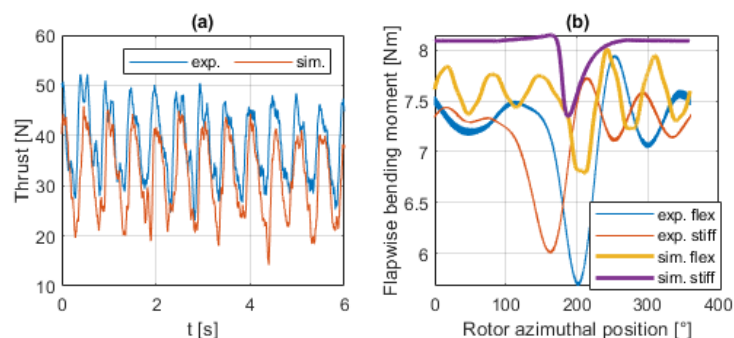


Figure 2: (a) Rotor thrust under the 2 Hz sinusoidal wind. (b) Blade root bending moments under constant 6.1 m/s wind.

Acknowledgements

This work is partially funded by the European Regional Development Fund (project TurbuMetric).

References

- [1] Berger F, Kröger L, Onnen D, Petrovic V and Kühn M 2018 *IOP Conf. Series: Journal of Physics: Conf. Series* **1104** 012026
- [2] Nietiedt S, Goering M, Willemsen T, Wester T T B, Kröger L, Guelker G, Luhmann T 2019 *The International Archives of the Photogrammetry, Remote Sensing and Spatial Information Sciences*, **XLII-2/W18** 143 – 149
- [3] Kröger L, Frederik J, van Wingerden J W, Peinke J and Hölling M 2018 *IOP Conf. Series: Journal of Physics: Conf. Series* **1037** 052002

Validation and development of Active Trailing Edge Flap models on commercial scale wind turbine, PhD project and first results

A Gamberini^{a,b}, A Gomez Gonzalez^a, and T Barlas^b

^aSiemens Gamesa Renewable Energy A/S, Brande, Denmark

^bDTU, Dept. of Wind Energy, Roskilde, Denmark

E-mail: andrea-gamberini@hotmail.it

Keywords: Trailing Edge Flap, Field test, Validation

Abstract

Since the 90s, smart rotor concepts have been investigated in order to control and reduce loads on Wind Turbines (WT). Active Trailing Edge Flap (ATEF) has shown to be one of the most promising concepts. ATEF unsteady aerodynamics and ATEF applications on load reduction have been extensively investigated but until today no commercial WT is equipped with ATEF and furthermore only limited field validations of ATEF models and applications have been performed.

The purpose of this industrial PhD project is firstly to validate and further develop the ATEF models currently available in HAWC2 and BHawC aeroelastic codes. Secondly, to develop and validate control strategies aiming the reduction of asymmetrical rotor loads and blade deflection. The validation is based on the data obtained from the field tests of the full-scale ATEF prototype installed on a modern multi-megawatt Siemens Gamesa WT. The knowledge developed in the PhD project will be extremely valuable to the design of commercial WT equipped with ATEF.

Background

Active smart rotor concepts have been investigated since the 90's as a mean to control and reduce loads on Wind Turbines (WT) and thus reduce the cost of wind energy. Despite all the effort and more than 260 scientific papers published on the subject, until today no feasible applications have been developed and installed on commercial WTs.

Among the several active smart rotor concepts investigated, Trailing Edge Flaps (ATEF) has showed to be one of the most promising technologies. Several aerodynamic model approaches have been proposed to describe the ATEF unsteady aerodynamics. Furthermore, a wide spectrum of load reduction strategies based on ATEF have been studied, showing in most recent studies [1], [2], [3] and [4] a load reduction of approx. 3-10% for main horizontal axis wind turbine components, allowing an approx. 5% increase of the rotor diameter and 2-3% increase in AEP.

Validation of the fidelity level, accuracy and performance of the ATEF models has been conducted mainly via numerical simulations, wind tunnel experiments and on outdoor rotating rig. As for field tests on a full scale WT, only three are known: Sandia field test on a Micon 65/13 turbine (115kW) [5]; DTU and Vestas test on a V27 (225kW) turbine [6], SGRE and DTU tests on a SWT-4.0-130 (4.0 MW) [7] as part of the INDUFLAP2 project. The field tests confirmed the potential of ATEF in controlling the aerodynamic loads but also showed the need of a further development and validation of the numerical ATEF models.

PhD Project Description

This industrial PhD project is a collaboration between DTU Wind Energy and Siemens Gamesa Renewable Energy (SGRE). SGRE and DTU Wind Energy have been collaborating for the development and test of a prototype flap system for wind turbines since the project INDUFLAP2.

Firstly, the PhD project aims to validate and further develop the ATEF models of both the DTU aeroelastic code HAWC2 and the SGRE's BHawC. The validation is based on the field data obtained from the full-scale test of a modern multi-megawatt SGRE WT equipped with ATEF. The validation covers both normal production conditions and off-design conditions like high yaw angle or high angle of attack.

The second objective of the PhD project is to carry out the development and field validation of load reduction strategies based on the developed ATEF models and aiming to reduce asymmetrical rotor loads and blade deflections.

The overall objective is to validate ATEF aeroelastic models and load reduction strategies that will allow to bring the ATEF technology into use in the next generation of commercial WT, contributing to reduce the levelized cost of energy (LCOE) of wind power.

Acknowledgements

This industrial PhD is funded by Danmarks Innovationsfond, Case no. 9065-00243B, PhD Title: "Advanced model development and validation of Wind Turbine Active Flap system".

INDUFLAP2 is a research and development project carried out by SGRE and DTU Wind Energy in the period from 2015 to 2019 and founded by EUDP (journal nr. 64015-0069).

References

- [1] Barlas A, Pettas V, Gertz D P and Madsen H A 2016 *Journal of Physics, conference series* **753**
- [2] Pettas V, Barlas A, Gertz D P and Madsen H A 2016 *Journal of Physics, conference series* **749**
- [3] Gonzalez A G, Enevoldsen P B, Akay B, Barlas A, Fische A and Madsen H A 2018 *Journal of Physics, conference series* **1037**
- [4] McWilliam M K, Barlas A, Madsen H A and Zahle F 2018 *Wind Energy Science* **3** 231–241
- [5] Berg J C, Barone M F and Resor B R 2013 *51st AIAA Aerospace Sciences Meeting including the New Horizons Forum and Aerospace Exposition January* 1–10
- [6] Castagnet D, Barlas T, Buhl T and Poulsen N K 2014 *Wind Energy* **17** 549–564
- [7] Gonzalez A G, Enevoldsen P B, Barlas A and Madsen H A 2019 *Wind Energy Science Conference 2019 Cork, Ireland, 17-20 June 2019*

A framework for quick identification of inflow conditions inducing destructive aeroelastic instabilities in wind turbines

Chandramouli Santhanam^a, Riccardo Riva^b, and Torben Knudsen^a

^aDepartment of Electronic Systems, Aalborg University, Aalborg, Denmark

^bDepartment of Wind Energy, Technical University of Denmark, Roskilde, Denmark

E-mail: chsa@es.aau.dk, ricriv@dtu.dk, tk@es.aau.dk

Keywords: Wind Turbine, Aeroelastic stability, Stall Induced Vibrations, Artificial Neural Network, Optimization

1 Introduction

Stall-Induced Vibrations (SIV) are an aeroelastic instability that happen when large portions of a wind turbine blade experience an angle of attack such that the slope of the lift coefficient is negative ($\partial C_L / \partial \alpha < 0$) [1]. With a rising necessity to design larger and more flexible wind turbine blades, SIV are an important design consideration as the loads generated during the occurrence might severely damage the blades. The severity of SIV depends on the blade design and inflow conditions.

Exploration of the design and inflow space that cause SIV has a high computational cost, since it involves high fidelity aeroelastic simulations. The aim of this work is to formulate a framework based on an aeroelastic simulator, a surrogate model and an optimizer that can automatically identify the conditions that maximize SIV in a wind turbine with the minimal number of simulations. The framework is based on a type of an optimization algorithm called Surrogate-Based Optimization (SBO), which makes use of surrogate models to approximate to expensive objective functions in the design space and guide the selection of new sample points towards the optimum [2].

2 Methodology, setup and SIV characterisation

In this work, the IEA 10 MW [3] turbine is chosen for investigation. The occurrence and characteristics of SIV in this turbine are studied for a parked rotor with a 90 deg pitch angle, 0 deg azimuth angle (blade 1 pointing upwards) and constant wind conditions. The inflow conditions and simulation setup are similar to the considerations in the AVATAR project [4], where the characteristics of SIV was studied on a large wind turbine rotor. In this work, we have focused on the effects of wind speed and yaw angle on SIV, therefore we have defined a first regular grid of inflow conditions. The aeroservoelastic tool HAWC2 [5] is used to simulate the motion of the wind turbine.

The edgewise bending moment at the root of blade 1 is chosen as the response to characterise SIV. For certain inflow conditions, the system is asymptotically stable. For some others the system is unstable, and the response grows exponentially, until it stabilizes on a nonlinear limit cycle oscillation. The initial part of the simulation is discarded to remove the effect of the initial condition. Then, the length of the signal is truncated to limit the response to the linear range. The severity of SIV is estimated by band pass filtering the response around the frequency of the first blade edgewise mode, and identifying the damping ratio.

Different methods were attempted to identify the damping ratio. The classical logarithmic decrement method and a variant, based on computing the slope of the straight line passing through the logarithm of the signal peaks, the half power bandwidth, and fitting an Auto Regressive model. The results from the different methods were found to be in good agreement with each other. The variation of the log decrement method has been eventually chosen for its robustness. The key difference with respect to the classical

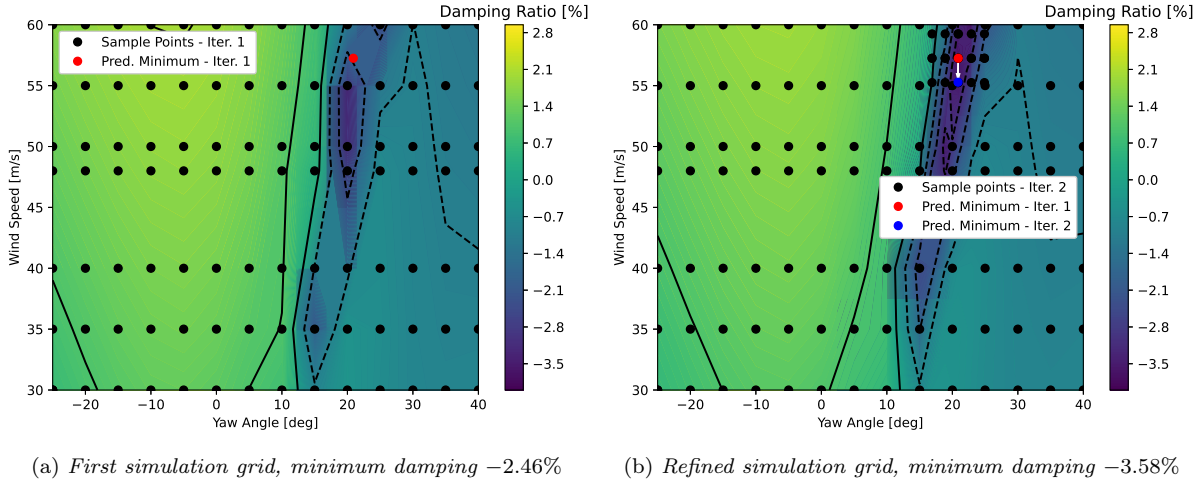


Figure 1: Simulation grid and contour of damping ratio over iterations.

version is that it uses all peaks, as opposed to the classical one which uses only two. By indicating with (t_i, y_i) the time and value of the i -th signal peak, ω the mode frequency and ζ the mode damping ratio, we can write

$$\log(y_i) = -\zeta\omega t_i + c \quad (1)$$

where c is the line intercept. The mode damping ratio is finally computed with the least-squares method.

3 Optimization

We have identified the damping ratio for all points of the initial inflow grid, and then trained an Artificial Neural Network (ANN) on it, so as to convert it into a continuous variable. The ANN is trained using the TensorFlow library [6], with 2 hidden layers containing 8 neurons each. The ANN function is then minimized to obtain the inflow conditions that leads to the minimum damping ratio (i.e. maximum SIV). After the first optimization, new inflow conditions are defined around the one of the minimum damping ratio, and the procedure is repeated. The grid and minimum damping ratio for the first two iterations is shown in Fig. 1.

The improvement in the estimated minimum damping ratio due to the inclusion of the additional simulations is nearly 1.12% measured in absolute value. It can be seen that the framework drastically limits the number of simulations needed to find the most critical inflow condition.

4 Conclusion

In this work we have studied Stall-Induced Vibrations on the IEA 10 MW wind turbine. We have developed a framework based on an Artificial Neural Network, that allows to find the most critical inflow conditions with the minimum number of high fidelity simulations. Future works will regard the conversion of the framework to OpenMDAO [7], and the application to Vortex-Induced Vibrations.

Acknowledgements

This work has been partially supported by ‘‘Predicting wind turbine stability in general inflow’’ (PRES-TIGE) project, which received funding from Innovation Fund Denmark.

References

- [1] M. H. Hansen. “Aeroelastic instability problems for wind turbines.” In: *Wind Energy* 10 (2007), pp. 551–557.
- [2] Zhong-Hua Han. “Surroopt: a generic surrogate-based Optimization code for aerodynamic and Multidisciplinary design.” In: *Proc. 30th Congress of International Council of the Aeronautical Sciences (ICAS)*. 2016.
- [3] Pietro Bortolotti et al. *IEA Wind Task 37 on Systems Engineering in Wind Energy WP2.1 Reference Wind Turbines*. Tech. rep. International Energy Agency, 2019.
- [4] Joachim Heinz et al. *Aerodynamics of Large Rotors WP4 Deliverable 4.5. AdVanced Aerodynamic Tools for lArge Rotors (AVATAR)*, 2016.
- [5] T J Larsen et al. *How 2 HAWC2, the user’s manual*. Risø National Laboratory, Denmark, 2007.
- [6] Martin Abadi et al. *TensorFlow: Large-Scale Machine Learning on Heterogeneous Systems*. 2015.
- [7] Justin S. Gray et al. “OpenMDAO: An open-source framework for multidisciplinary design, analysis, and optimization.” In: *Structural and Multidisciplinary Optimization* 59.4 (2019), pp. 1075–1104.

Modelling Horizontal Axis Wind Turbine Aerodynamics in Terms of Cascade Elements

N Golmirzaee and D H Wood

Department of Mechanical and Manufacturing Engineering, University of Calgary

E-mail: narges.golmirzaee@ucalgary.ca

Abstract

The simplest aerodynamic model of wind turbines is the blade element momentum theory, which divides the blades into small elements. By the so-called “aerofoil assumption”, blade elements behave as aerofoils in an unbounded flow. All horizontal axis wind turbine blades, however, have neighbours. Hence, a more accurate two-dimensional representation for a horizontal axis wind turbine section is an infinite cascade of identical, equispaced lifting bodies. In the present study, cascades comprised of aerofoils at spacings typical of wind turbine applications are analyzed, and the force equations used in the blade element momentum theory through their cascade counterparts are investigated. Using the impulse form of the force equations, two exact equations for the components of the force acting on a stationary cascade element in a two-dimensional, steady, incompressible flow are derived as well. OpenFOAM software is used to simulate the flow through cascades of NACA 0012 aerofoils at Reynolds number of 6×10^6 . The derived equations agree well with the body forces determined directly from the OpenFOAM simulations for four spacing ratios. Examining the terms of these equations reveals the importance of the circulation, the viscous drag, and the displacement effect of the body’s wake due to its finite width. It seems that the viscous effects must influence the circulation. Also, for a very low tip speed ratio, the accuracy of the aerofoil assumption is assessed, and it is observed that the lift and the drag forces are in good agreement with the experimental data for the lift and the drag of a NACA 0012 aerofoil.

Keywords: Horizontal Axis Wind Turbine, Cascade, Impulse Equation, Steady Flow, Incompressible Flow, Lift, Drag

1 Introduction

A cascade consists of an infinite number of identical bodies that are equally distant from each other [1]. There are periodic boundary conditions between cascade bodies as well as blade elements of an axisymmetric horizontal axis wind turbine (HAWT). Therefore, there is an equivalence between an axial section of a HAWT and a cascade, as shown in figure 1. In this figure, an airfoil-shaped blade element is indicated by red. Similar to the blade element momentum (BEM) theory, the cascade analysis gives the force equations from the change in axial and angular momentums of the airflow. In the BEM theory, an additional assumption is made that those forces are equivalent to the lift and the drag on a blade element as an aerofoil at the same Reynolds number, Re , and the same angle of attack, α . This assumption is called the “aerofoil assumption”. It has not been independently tested, and it is difficult to see how this could be done experimentally for typical wind turbine blades spacings.

In a cascade of lifting bodies, the imposition of periodic boundary conditions causes a component of the induced velocity (which is generated by the singularity) to lie on the y -axis. The sum of this velocity in the y -direction and the wind velocity, \mathbf{U}_∞ , is the velocity at the body, \mathbf{W} . \mathbf{U}_∞ is at a “geometric” angle of attack, α_g , to the chord line. The angle between \mathbf{U}_∞ and \mathbf{W} is called the induced angle of attack, α_i . Also, α is the (effective) angle of attack between \mathbf{W} and the chord line (figure 2). Therefore, we have:

$$\alpha = \alpha_g - \alpha_i. \quad (1)$$

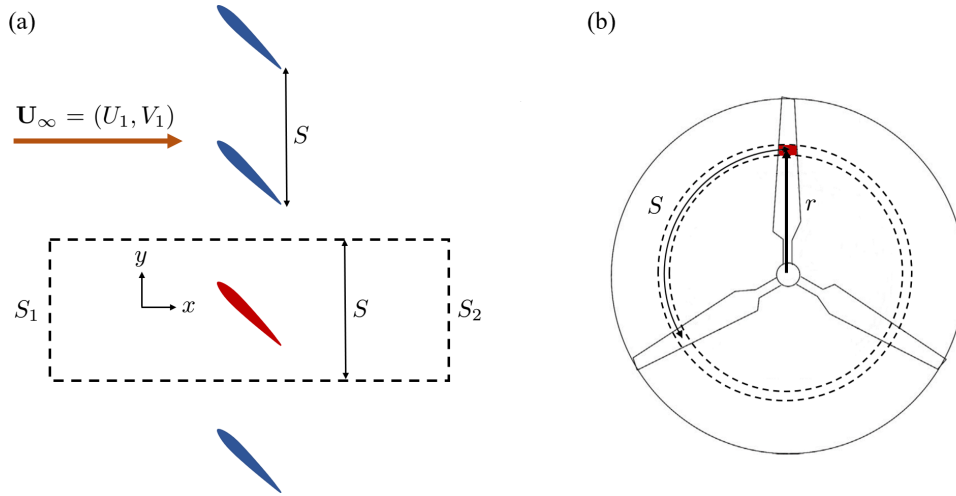


Figure 1: (a) Two-dimensional cascade of infinite bodies. (b) An annular section of a three-bladed HAWT at an arbitrary radius, r . The figure in part (b) is adopted from [2].

For isolated aerofoils, $\alpha_g = \alpha$. Using cascade analysis and the aerofoil assumption, the lift, \mathbf{L} , and the drag, \mathbf{D} , exerted on a wind turbine blade element with the geometric angle of attack of α_g and the wind velocity of \mathbf{U}_∞ is equal to \mathbf{L} and \mathbf{D} on an aerofoil with the same shape but with α and \mathbf{W} [1]. Figure 2 indicates that the angle between the force vector in the x -direction, \mathbf{F}_x , and \mathbf{D} (or the force vector in the y -direction, \mathbf{F}_y , and \mathbf{L}), θ , is given by:

$$\theta = 90 - \beta - \alpha. \quad (2)$$

D and L are the drag and the lift per unit span, respectively. The drag coefficient, C_d , and the lift coefficient, C_l , are defined as:

$$C_d = \frac{2D}{\rho W^2 c} \quad \text{and} \quad C_l = \frac{2L}{\rho W^2 c}, \quad (3)$$

where c is the chord. The definitions of C_d and C_l here apply to cascade elements as well as aerofoils. Once we know θ (or α), L , and D , we have:

$$F_x = L \sin \theta + D \cos \theta, \quad (4)$$

$$F_y = L \cos \theta - D \sin \theta, \quad (5)$$

where F_x and F_y are the x and y -components of the force on a blade element per unit span, respectively.

The spacing to the chord ratio for a B -bladed HAWT at radius r is $S/c = 2\pi r/Bc$, where B is the number of blades, [3]. For a conventional HAWT with $B = 3$, S/c lies between 1.5 and 40 (table 3.3 of [4]) and usually increases towards the tip. Since a large wind tunnel to test models of infinite cascades of bodies with values of S/c typical of wind turbines does not exist, it is not possible to undertake realistic experiments on cascades.

One of the basic force equations in aerodynamics is the Kutta-Joukowski equation for a steady flow around an aerofoil [2]:

$$L = \rho U_\infty \Gamma, \quad (6)$$

where ρ is the density, and Γ is the circulation. Γ around a closed curve, \mathcal{C} , is equal to:

$$\Gamma = \oint_{\mathcal{C}} \mathbf{U} \cdot d\mathbf{l} = \iint_{\mathcal{S}} \boldsymbol{\Omega} \cdot \hat{\mathbf{n}} \, dA, \quad (7)$$

where \mathbf{U} is the fluid velocity vector, \mathcal{S} is the surface whose boundary is \mathcal{C} , $d\mathbf{l}$ is the infinitesimal displacement vector along the curve \mathcal{C} , $\hat{\mathbf{n}}$ is the outward-facing unit normal to \mathcal{S} , dA is the magnitude of the

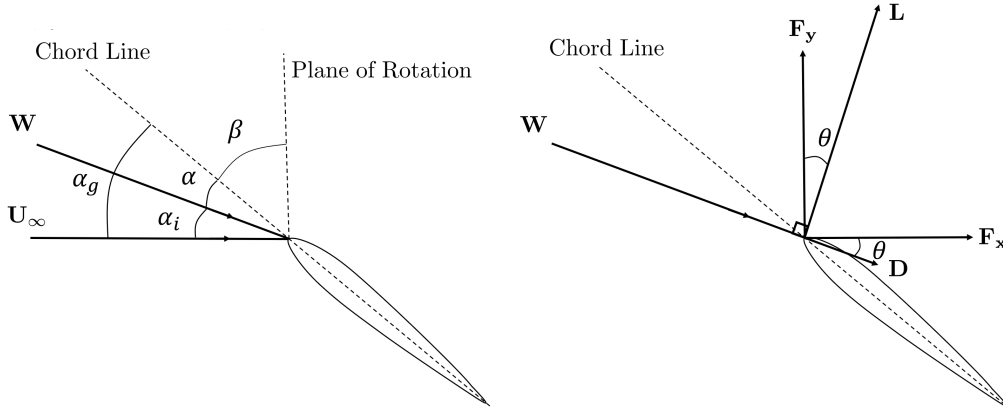


Figure 2: Representation of velocities, angles, and forces on a cascade element.

infinitesimal area vector normal to \mathcal{S} , and $\boldsymbol{\Omega}$ is the vorticity. The vorticity consists of the bound vorticity and the wake vorticity, but only the bound vorticity contributes to the circulation. The Kutta-Joukowski theorem relates the force to the vorticity. For a two-dimensional, steady, unbounded, inviscid flow, the drag is zero. Therefore, the Kutta-Joukowski theorem for an aerofoil indicates that the circulation does not contribute to the drag, or conversely, the drag does not affect the circulation. Also, blade element analyses usually ignore the contribution of the vorticity in the wake to the thrust (or F_x). Limacher and Wood [5] also ignored the effect of the vorticity in the wake when they proved the equivalence of the thrust and the Kutta-Joukowski theorem for wind turbines and gave the conditions for its validity. The present work uses cascade analysis to assess the importance of the ignored vorticity term in the BEM theory. Further, we consider the influence of the circulation, the viscous drag, and the displacement effect of the body's wake (the increase in the velocity outside the wake due to the finite width of the wake) to the force components, which has not been done before.

2 Impulse Equation of the Fluid Force on a Body

Using the conservation of momentum and the Reynolds transport theorem, the equation of the force on a stationary body submerged in a two-dimensional, steady, incompressible fluid flow can be written as ([6], equation (2.15)):

$$\frac{\mathbf{F}}{\rho} = \oint\oint_{\mathcal{S}} \hat{\mathbf{n}} \cdot \left(-\frac{p}{\rho} \mathbf{I} - \mathbf{U}\mathbf{U} \right) dA, \quad (8)$$

where $\mathbf{U} = (U, V)$ is the velocity vector, p is the pressure, \mathcal{S} is the closed external surface of the control volume, CV, and \mathbf{I} is the $m \times m$ unit tensor, where m is the dimension of the space. In this study, $m = 2$. Using linear algebra techniques and employing the Navier-Stokes equation, Noca removed p from the force equation to derive an impulse equation (equations (3.55) and (3.56) of [6]). For a stationary body in a two-dimensional, steady, incompressible flow, this equation becomes:

$$\frac{\mathbf{F}}{\rho} = \oint\oint_{\mathcal{S}} \hat{\mathbf{n}} \cdot \left[\frac{1}{2} \mathbf{U}^2 \mathbf{I} - \mathbf{U}\mathbf{U} - \mathbf{U}(\mathbf{x} \times \boldsymbol{\Omega}) \right] dA, \quad (9)$$

where $\mathbf{x} = (x, y)$ is the position vector. This equation excludes the pressure and includes the vorticity. These changes make the force equation more tractable because measuring or calculating the pressure is difficult and costly, but calculating the vorticity just needs the velocity field. Moreover, equation (9) reveals the importance of the vorticity in the force equation.

3 Equations of the Force on Cascade Elements

To derive the x and y -components of the force on cascade elements, we use the rectangular CV in figure 1 (a). We assume that there exists only one lifting body in the CV, and it is placed at $y = 0$. S_1 is the inlet boundary, and S_2 is a face anywhere downstream. The top and the bottom boundaries are periodic, so any contribution of the top boundary cancels the bottom boundary's contribution in all derivations.

For such a CV, equation (8) becomes:

$$\frac{F_x}{\rho} = \int_{S_1} \left(\frac{p}{\rho} + U^2 \right) dy - \int_{S_2} \left(\frac{p}{\rho} + U^2 \right) dy \quad (10)$$

and

$$\frac{F_y}{\rho} = \int_{S_1} UV dy - \int_{S_2} UV dy. \quad (11)$$

These two equations are the conventional force equations in the x and y -directions for a cascade element.

At the inlet, the z -component of the vorticity vector, Ω_z , is zero, so if the inlet velocity is $\mathbf{U}_\infty = (U_1, V_1)$, the x and y -components of the force in equation (9) become:

$$\frac{F_x}{\rho} = \frac{1}{2}(U_1^2 - V_1^2)S - \int_{S_2} \left(\frac{1}{2}U^2 - \frac{1}{2}V^2 + yU\Omega_z \right) dy \quad (12)$$

and

$$\frac{F_y}{\rho} = U_1V_1S - \int_{S_2} (UV - xU\Omega_z) dy. \quad (13)$$

From now on, we denote the x and y -components of the velocity vector at S_2 by U_2 and V_2 , respectively. By moving S_2 far enough downstream, we can use the slender flow approximation, $\Omega_z \approx \partial U_2 / \partial y$. Without loss of generality, we can assume that $y = 0$ is at the centre of the wake. Using the conservation of mass, the approximate form of equation (12) is:

$$\frac{F_x}{\rho} \approx \frac{1}{2}(U_1^2 - \bar{U}_2^2)S + \int_{-\delta/2}^{\delta/2} (\bar{U}_2^2 - U_2^2) dy - \tilde{V}_b \Gamma + \frac{1}{2} \int_{S_2} v_2^2 dy, \quad (14)$$

where \bar{U}_2 is the value of U_2 outside the wake, and δ is the thickness of the wake at S_2 . $\tilde{V}_b = (V_1 + \tilde{V}_2)/2$ is the average vertical velocity at the body, where \tilde{V}_2 is the average of V_2 . Γ is the circulation of the body, and $v_2 = V_2 - \tilde{V}_2$. Each of the four terms on the right-hand side of equation (14) has an interesting interpretation. The first two terms show the displacement effect of the wake and the increase in the velocity outside the wake due to the finite δ . The third term can be related to the x -component of the lift on the body. It is one component of the Kutta-Joukowski theorem and represents the contribution of the bound circulation to the thrust. It is also similar to the induced drag in the lifting line theory of wings. The fourth ‘‘quadratic’’ term arises from any non-uniformity of V_2 over the outlet and the non-linearity of the thrust equation. Limacher and Wood [5] ignored the effect of the first two terms and the last term, so if their analysis is applied to a cascade, only the third term remains. One of the important reasons for doing the present analyses is to see the importance of the terms that were ignored.

Equations (1.5) and (1.6) of [7] give:

$$\int_{S_2} (U\Omega_z) dy = 0 \quad \text{and} \quad \int_{S_2} \Omega_z dy = 0, \quad (15)$$

which means that there is no flux of the vorticity from the outlet, so equation (13) becomes:

$$\frac{F_y}{\rho} = U_1\Gamma - \int_{S_2} u_2v_2 dy, \quad (16)$$

where $u_2 = U_2 - \tilde{U}_2$, and \tilde{U}_2 is the average of U_2 . From equations (4) and (5), D should contribute to F_y , and equation (16) shows that F_y has a term that includes the circulation and a quadratic term, which is shown later to be very small. Therefore, we come to the conclusion that the viscous effects must influence the circulation.

If we ignore the vorticity in the wake and spatial variations in the velocities, equations (14) and (16) and the velocity at the body can be approximated as:

$$\frac{F_x}{\rho} \approx -\tilde{V}_b \Gamma, \quad \frac{F_y}{\rho} \approx U_1 \Gamma \quad \text{and} \quad \mathbf{W} \approx (U_1, \tilde{V}_b). \quad (17)$$

From equations (4), (5) and (17), we have:

$$L = F_y \cos \theta + F_x \sin \theta \approx \rho U_1 \Gamma \frac{U_1}{W} + \rho \tilde{V}_b \Gamma \frac{\tilde{V}_b}{W} \approx \frac{\rho W^2 \Gamma}{W} = \rho W \Gamma \xrightarrow{S/c \rightarrow \infty} \rho U_\infty \Gamma, \quad (18)$$

which is the Kutta-Joukowski equation for an aerofoil.

4 OpenFOAM Simulation

Since it is not possible to experimentally measure cascade behaviours for the range of S/c for a typical HAWT, the flow was simulated using the OpenFOAM [8], which is a well-known open-source CFD software. OpenFOAM calculates the values of F_x and F_y directly from the pressure and the shear stress on the surface of the body. For the present simulations, $Re = U_1 c / \nu$ was set to 6×10^6 to have a turbulent flow over the whole body. The density and the kinematic viscosity were 1.225 kg/m^3 and $8.58 \times 10^{-6} \text{ m}^2/\text{s}$, respectively. With $c = 1 \text{ m}$, $U_1 = 51.48 \text{ m/s}$.

In this work, all simulations were done using the Spalart-Allmaras model, one of the most common RANS turbulence models [9]. The Spalart-Allmaras model is a one-equation model that is accurate for simulations of flows around aerofoils in terms of the computed lift and drag and mean velocity distribution in the wake [10]. The simpleFoam algorithm, which is used for simulating incompressible, steady, turbulent flows, was chosen. A NACA 0012 aerofoil with $\alpha = 5^\circ$ and $\alpha = 10^\circ$ was simulated, followed by the cascade simulations using the same aerofoil. To reduce the effect of boundary conditions – zero gradient velocity and zero pressure at the outlet and zero gradient pressure and the defined velocity at the inlet – the inlet and the outlet boundaries were set to $30c$ from the body. These boundaries were parallel to the y axis. For the sake of brevity, we omit the details of the checks on the size of the domain, the number of cells, and the requirement to have small values of y^+ on the body surfaces.

β in cascade simulations can be related to the tip speed ratio, λ , of wind turbines, and it decreases as λ increases. Therefore, large β corresponds to small λ .

5 Cascade Simulation with $\alpha_g = 0^\circ$ and $\beta = 90^\circ$

This section describes the simulation of the flow through a cascade of aerofoils with $\alpha_g = 0^\circ$, $\beta = 90^\circ$, and $S/c = 20$. In this simple case, since there is no circulation, we can concentrate on investigating the viscous effects on the thrust. The NACA 0012 is a symmetrical aerofoil, so it has no lift when $\alpha = 0$. Therefore, in the cascade simulation with $\alpha_g = 0^\circ$, $\tilde{V}_2 = 0$, and equation (14) reduces to:

$$\frac{F_x}{\rho} \approx \int_{-\delta/2}^{\delta/2} \left(U_2 + \frac{\bar{U}_2 - U_1}{2} \right) (\bar{U}_2 - U_2) dy. \quad (19)$$

From the OpenFOAM simulation, $-\tilde{V}_b \Gamma$ and $\int_{S_2} v_2^2 dy / 2$ normalized by $U_1^2 c / 2$ are 7.21×10^{-17} and 7.34×10^{-11} , respectively, so they are ignorable. We also normalize F_x / ρ and F_y / ρ by $U_1^2 c / 2$ and denote them by C_x and C_y , respectively. The computed C_x from the simulation is 0.00821. Also, C_x from equations (10), (12) and (19) is 0.00827, 0.00813 and 0.00817, respectively. According to McCroskey [11], a good fit for the tripped data of C_d for an aerofoil with $\alpha = 0^\circ$ and $Re = 6 \times 10^6$ is $C_{d0} = 0.00823 \pm 0.0002$, and our result lies within this range. C_y is -2.62×10^{-6} and very small.

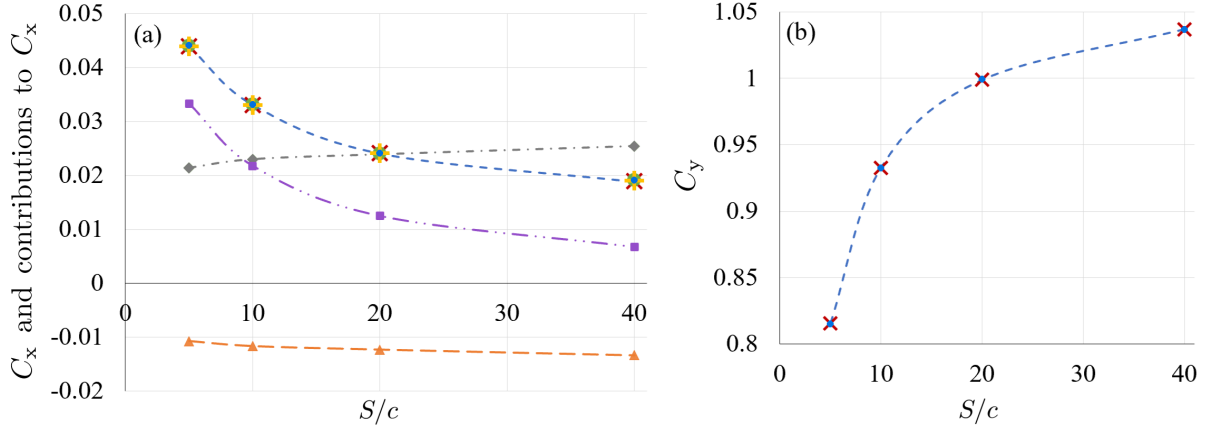


Figure 3: (a) Comparison of C_x computed by the OpenFOAM (red crosses) and equations (10) (green circles), (12) (yellow pluses) and (14) (blue circles), and the normalized terms of equation (14): $(U_1^2 - \bar{U}_2^2)S/U_1^2c$ (orange triangles), $2 \int_{-\delta/2}^{\delta/2} (\bar{U}_2^2 - U_2^2) dy / U_1^2 c$ (grey diamonds) and $-2\tilde{V}_b \Gamma / U_1^2 c$ (purple squares), (b) Comparison of C_y computed by the OpenFOAM (red crosses) and equation (16) (blue circles); evaluated at the outlet of the cases with $\alpha_g = 10^\circ$, $\beta = 80^\circ$ and varying S/c .

For a single, non-lifting body, $\bar{U}_2 \xrightarrow[S/c \rightarrow \infty]{} U_1$. Therefore:

$$\frac{F_x}{\rho} \xrightarrow[S/c \rightarrow \infty]{} \int_{-\delta/2}^{\delta/2} U_2(U_1 - U_2) dy, \quad (20)$$

which is the conventional drag equation for an isolated, non-lifting body. This equation is derived in most fundamental fluid mechanics books using the continuity and the momentum equations, e.g., equation (2.84) of [12]. C_x from equation (20) is 0.00799 and very close to the simulation result.

6 Cascade Simulations with $\alpha_g = 10^\circ$, $\beta = 80^\circ$ and Varying S/c

In this section, simulations of the airflow through a cascade of NACA 0012 aerofoils with $\alpha_g = 10^\circ$ and $\beta = 80^\circ$ for varying S/c (5, 10, 20, 40) are discussed. The domain used for the simulation of the case with $S/c = 5$ has parallel inlet and outlet boundaries and same-shaped top and bottom boundaries, which are inclined in the direction of V so that the whole wake exits from the outlet boundary only. C_x from equations (10), (12) and (14) for different values of S/c are compared in figure 3 (a). These three equations agree with the direct determination of the body forces. This figure also shows that as S/c increases, F_x and the circulation term in F_x decrease. Alternatively, with the decrease of S/c , the lift vector turns to make F_x larger and F_y smaller, which is compatible with figure 3 (b). As S/c increases, the circulation contribution to F_x (the purple squares) tends to zero and the sum of grey and orange curves asymptotes to C_d for $\alpha = 10^\circ$. For example, for $S/c = 40$, the sum of these two terms is 0.01207, which is close to $C_d = 0.01320$ for the single aerofoil with $\alpha = 10^\circ$. The order of magnitude of the normalized non-linear term in equation (14) for all values of S/c is 10^{-6} or less, so this term is negligible compared to the other terms and its values are not shown in figure 3 (a).

Figure 3 (b) shows that the values of C_y from equation (16) for the four values of S/c agree with the direct determinations of C_y as well. This figure also shows the monotonic increase in F_y with increasing S/c , which agrees with the theoretical results of [13]. For $S/c = 40$, the value of C_y is 1.03686, and it seems that if S/c increases, this value tends to C_l of the aerofoil with $\alpha = 10^\circ$, which is 1.07399. Table 1 presents the normalized values of \bar{U}_2 and \tilde{V}_b for the case with $S/c = 20$, as an example, in different downstream distances ($x = 1c, 2c, 5c, 10c, 20c$, and the outlet). As we can see, the values of \tilde{V}_b are approximately constant, which indicates that only the vorticity bound to the blade contributes to Γ .

	$x = 1c$	$x = 2c$	$x = 5c$	$x = 10c$	$x = 20c$	$x = 31c$ (outlet)
\bar{U}_2/U_1	0.98228	0.99497	0.99957	1.00018	1.00030	1.00031
$2\tilde{V}_b/U_1$	-0.02498	-0.02498	-0.02497	-0.02497	-0.02497	-0.02497
$(U_1^2 - \bar{U}_2^2)S/U_1^2c$	0.70250	0.20087	0.01724	-0.00720	-0.01195	-0.01231
$2 \int_{-\delta/2}^{\delta/2} (\bar{U}_2^2 - U_2^2) dy / U_1^2c$	0.05345	0.02651	0.02425	0.02342	0.02357	0.02388
$-2\tilde{V}_b\Gamma/U_1^2c$	0.01247	0.01248	0.01247	0.01247	0.01247	0.01247
$\int_{S_2} v_2^2 dy / U_1^2c$	0.01287	0.00318	0.00033	1.34×10^{-5}	9.69×10^{-8}	7.24×10^{-8}
C_x (equation (14))	0.78129	0.24303	0.05429	0.02870	0.02409	0.02404

Table 1: \bar{U}_2/U_1 , $2\tilde{V}_b/U_1$, and normalized terms of equation (14) for different sections in the downstream of the case with $\alpha_g = 10^\circ$, $\beta = 80^\circ$ and $S/c = 20$. The computed C_x from the simulation is 0.02414.

This is also a consequence of equation (15). Table 1 also shows the normalized terms of equation (14) in different sections at the downstream of the case with $S/c = 20$. It is observed that the farther from the body, the smaller the non-linear term and the more accurate the value of equation (14).

For $S/c = 5, 10, 20$ and 40 , using equations (3) and the equation of the velocity at the body, we calculate C_d and C_l and compare these values to the experimental data available for the NACA 0012 aerofoil from [14] in figure 4. From this figure, it is observed that the aerofoil assumption works well in our simulations. Note that the increase in the y -component of the velocity at the blade due to the increase in α does not significantly affect the Reynolds number and C_d .

7 Conclusion

In this study, we investigate several aspects of the blade element momentum theory by simulating the flow through two-dimensional cascades of bodies. From the impulse equation, equations of the force components and their approximate forms, using the slender flow simplification, are calculated for a cascade element. Then, these equations are compared with the direct determination of the body forces from the OpenFOAM simulations. The agreement was excellent. From these equations, the role of the vorticity components in determining the force is revealed. The approximate form of the impulse equation shows the contribution of the viscous drag to the thrust and its influence on the circulation. Figure 3 indicates that none of the terms in equation (14) are negligible at any realistic S/c . However, the Kutta-Joukowski theorem, [5], as used in blade element momentum calculations of the wind turbine performance, ignores the displacement and the viscous drag effects. Also, we show that the forces on a cascade body at high pitch angles are accurately determined by assuming that the body is an aerofoil. As the future work, we will study the accuracy of the aerofoil assumption for a cascade modelling higher tip speed ratios (lower pitch angles). Moreover, unsteady cascade simulations will be undertaken to model a change in the blade pitch of a horizontal axis wind turbine.

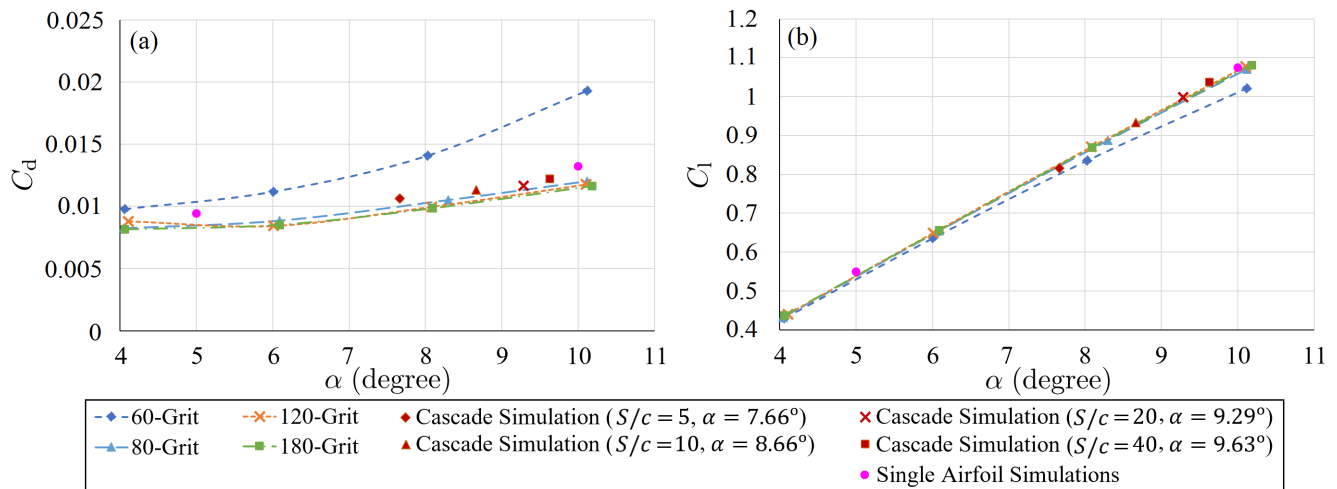


Figure 4: Assessing the aerofoil assumption using a comparison between the simulation results for different values of S/c , given in the legend, and experimental results from [14]. (a) C_d vs α . (b) C_l vs α . “Grit” refers to the roughness used on the aerofoil model to induce transition.

Acknowledgements

This work is supported by an NSERC Discovery Grant and the Schulich endowment to the University of Calgary.

References

- [1] Wood D 2011 *Small Wind Turbines: Analysis, Design, and Application* (Springer London)
- [2] Hansen M O L 2015 *Aerodynamics of wind turbines* 3rd ed (Routledge)
- [3] Burton T, Jenkins N, Sharpe D and Bossanyi E 2011 *Wind Energy Handbook* 2nd ed (John Wiley & Sons)
- [4] Manwell J F, McGowan J G and Rogers A L 2010 *Wind energy explained: theory, design and application* 2nd ed (John Wiley & Sons)
- [5] Limacher E and Wood D H 2019 *Wind Energy Science Discussions* **in review** 1 – 15
- [6] Noca F 1997 *On the evaluation of time-dependent fluid-dynamic forces on bluff bodies* Ph.D. thesis Caltech
- [7] Liu L Q, Zhu J Y and Wu J Z 2015 *Journal of Fluid Mechanics* **784** 304 – 341
- [8] Greenshields C J 2017 *OpenFOAM Foundation* **230**
- [9] Spalart P and Allmaras S 1992 A one-equation turbulence model for aerodynamic flows *30th aerospace sciences meeting and exhibit* p 439
- [10] Thomas F O and Liu X 2004 *Physics of Fluids* **16** 1725 – 1745
- [11] McCroskey W J 1987 A critical assessment of wind tunnel results for the naca 0012 airfoil Tech. rep. NASA TM 100019
- [12] Anderson J D 2017 *Fundamentals of aerodynamics* 6th ed (McGraw-Hill Education)
- [13] Baddoo P and Ayton L 2018 *Proceedings of the Royal Society A: Mathematical, Physical and Engineering Science* **474** 20180065
- [14] Ladson C L 1988 Effects of independent variation of mach and reynolds numbers on the low-speed aerodynamic characteristics of the naca 0012 airfoil section Tech. rep. NASA TM 4074

CONTROL

Envelope protection control for wind turbines

Suryans Chamoli, Vlaho Petrović, Martin Kühn

ForWind, Institute of Physics, University of Oldenburg, K pkersweg 70, Oldenburg, Germany

E-mail: suryans.chamoli@uol.de

Keywords: envelope protection, control, real-time optimization, blade deflection, tower clearance

1 Introduction

Recent trend shows a significant shift towards larger wind turbines due to their better capacity utilization. This inevitably leads to larger and more flexible structures. Thus, the safe operation of a wind turbine becomes very important. Inspired from the idea of envelope protection control implemented for helicopters (see e.g. [1]), a novel approach has been developed in the recent years [2] in order to guarantee safe operation of a wind turbine in all conditions. These conditions are characterised by extreme values of global loads, rotor speed, tower and blade oscillations.

Wind turbines are nonlinear and the operating points change with the wind speed. Moreover, quantities such as tower clearance and hence, permissible blade deflections depend on the position of the blade, i.e. blade azimuth angle. As the goal here is to avoid blade-tower collision, the use of an envelope based on an adaptive estimator for an extended wind turbine model derived in the Section 3 is considered. The envelope protection algorithm is briefly described in Section 2 and Section 4 gives a brief outlook on the future work.

2 Envelope protection algorithm

The safe operating envelope is defined by the maximum permitted value of a protected criterion, e.g. load, deflection etc. The approaching wind trajectory that will cause the criterion to reach the boundary value without exceeding it is called the envelope wind speed. This envelope wind speed acts as the worst case scenario and is determined by minimizing the area between the estimated value of the protected criterion and its maximum value in a forward looking prediction window. This optimization problem as formulated in [2] is

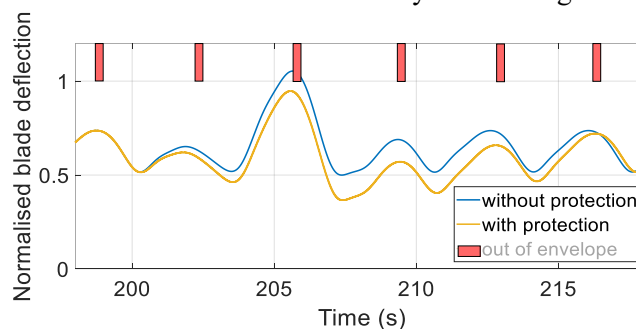


Fig. 1: The envelope protection control concept: The algorithm adjusts the blade pitch signal when the blade gets too close to the tower.

where y is the protected criterion, y_{max} is its maximum permissible value and T_w is the prediction horizon. v_w is the effective wind speed f and h represent the turbine dynamics described in next section, where x are the states, u are the inputs and η is the reference value for the protection control action. The actual wind speed is then compared with the worst case envelope wind speed and suitable control actions are taken if the former exceeds the latter. For this work, tower clearance is the protected criterion and blade pitch actuation is the control action. If the actual wind speed exceeds the envelope wind, the blade is pitched to feather in order to reduce the flapwise blade deflection and to prevent an impending blade-tower collision. *Fig. 1* shows how the envelope protection system would react in case of an extreme operating gust.

$$\begin{aligned} \min_{v_w(t)} \int_{T_w} |(y_{max} - y(t))| dt \\ \text{s.t. : } \dot{x} = f(x, u, \eta), \\ y = h(x, u, \eta) \leq y_{max}, \end{aligned}$$

3 Wind turbine model

A simplified model is developed that considers a two-mass system for the rotational dynamics given by

$$J_r \dot{\omega}_r = -C_d(\omega_r - \omega_g) - K_d(\vartheta_r - \vartheta_g) + T_a, \text{ and}$$

$$J_g \dot{\omega}_g = C_d(\omega_r - \omega_g) + K_d(\vartheta_r - \vartheta_g) - T_g.$$

Here, J , ω , ϑ , T , C and K are mass moments of inertia, rotation speed, rotation angle, torque, damping and stiffness coefficients, respectively. Subscripts r , g , a and d represent rotor, generator, aerodynamic and drivetrain, respectively. ω_g and ϑ_g are normalised using n_{gb} , the gear ratio. The flapwise blade dynamics and the fore-aft tower dynamics are described by second-order systems:

$$A_i \ddot{x}_{b_i} + B_i \dot{x}_{b_i} + C_i x_{b_i} = M_{flap_i}, \text{ and } P \ddot{x}_{nod} + Q \dot{x}_{nod} + R x_{nod} = F_t.$$

x_{b_i} , M_{flap_i} , A_i , B_i and C_i are the flapwise tip deflection, bending moment, modal mass, damping and stiffness coefficient for the i^{th} ($i=1,2,3$) blade, respectively. x_{nod} , F_t , P , Q and R are fore-aft displacement, aerodynamic thrust force, modal mass, damping and stiffness coefficients of the tower, respectively. Flapwise blade moment, flapwise force and edgewise blade moment variations for each blade δM_{flap_i} , δF_{flap_i} and δM_{edge_i} are mapped to flapwise relative wind speed v_{flap_i} and pitch angle variations β_i using linearized BEM theory neglecting wake and unsteady aerodynamics as in [3]. v_{flap_i} depends on translational and angular tower motion as well as blade effective wind speed u_i by relation:

$$v_{flap_i} = u_i - \dot{x}_{nod} + \frac{3R_b}{4} \dot{\theta}_{nod}, \text{ with } \dot{\theta}_{nod} = \sin \varphi_i \frac{3}{2H} \dot{x}_{nod}.$$

θ_{nod} is the blade azimuth (φ) dependant angular speed of the tower top. H and R_b are hub height and blade length, respectively. Consequently, aerodynamic torque and thrust variations are calculated as

$$\delta T_a = \sum_{i=1}^3 \delta M_{edge_i}(v_{flap_i}, \beta_i), \text{ and } \delta F_t = \sum_{i=1}^3 \delta F_{flap_i}(v_{flap_i}, \beta_i).$$

The above wind turbine model is linearized about the desired operating points and represented as a discrete state-space system; $x_{k+1} = A(\varphi)x_k + B(\varphi)u_k$, where $A(\varphi)$ and $B(\varphi)$ are system matrices, $x_k = [\omega_r \ \omega_g \ \Delta\vartheta \ \dot{x}_{b_1} \ x_{b_1} \ \dot{x}_{b_2} \ x_{b_2} \ \dot{x}_{b_3} \ x_{b_3} \ \dot{x}_{nod} \ x_{nod}]^T$ and $u_k = [\Delta u_1 \ \Delta u_2 \ \Delta u_3 \ \Delta \beta_1 \ \Delta \beta_2 \ \Delta \beta_3 \ \Delta T_g]^T$ are state and input vectors, respectively. Value at discrete time-step kT_s , where T_s is the sampling time, is denoted by the index k . The monitored criterion, tower clearance, can be estimated using the state variables x_{b_i} and x_{nod} .

4 Outlook

The estimator and envelope protection control will be tested in aeroelastic simulations using different inflow conditions and disturbances such as turbine faults. Furthermore, wind tunnel experiments with a scaled wind turbine model and field experiments are planned. For this, special attention will be given to the real-time implementation of the protection algorithm, especially because of the strongly reduced sampling time imposed by the fast dynamics of a wind turbine.

Acknowledgements

This work is partly funded by the Federal Ministry for Economic Affairs and Energy according to a resolution by the German Federal Parliament (project »ConUp« 03EE2012A).

Bibliography

- [1] Horn, J., Calise, A.J. and Prasad, J.V.R. 2002 Flight envelope limit detection and avoidance for rotorcraft. *Journal of the American Helicopter Society* 47(4) 253-262.
- [2] Petrović, V. and Bottasso, C.L. 2017 Wind turbine envelope protection control over the full wind speed range *Renewable energy* 111 836-848.
- [3] Markou, H., Buhl, T., Marrant, B. and Van Engelen, T.G. 2006 Morphological study of aeroelastic control concepts for wind turbines *ECN Report*.

FARM / WIND TURBINE MODELLING

Multi-row extension to laterally confined actuator disk model using a hybrid inviscid-viscous approach

Marcus C. R. Juniper and Takafumi Nishino

Department of Engineering Science, University of Oxford, OX1 3PJ, UK

E-mail: marcus.juniper@eng.ox.ac.uk

Abstract

The effects of blockage and wake mixing are fundamental but still unresolved problems in the aero/hydrodynamics of wind/tidal-stream turbine arrays. This paper aims to extend the linear momentum actuator disc theory (LMADT) to incorporate a large number of aligned or staggered turbine rows with inter-turbine wake mixing. The extension is performed by utilising alternating inviscid and viscous zones to calculate the flow around a turbine and to calculate mixing in the wake, respectively. Using the extended model this study explores the power extraction of a multi-row turbine array for a varying resistance coefficient. This exploration is performed for both aligned and staggered turbine arrangements for a range of blockage ratios and wake mixing rates. Results highlight the importance of the combined effects of blockage and wake mixing, particularly for staggered turbine arrays. The impact of the number of turbine rows and inter-turbine mixing rates on the maximum array performance is also investigated.

Keywords: Actuator Disk Theory, Blockage Effect, Wake Losses, Optimal Turbine Arrangement

1 Introduction

The effect of different turbine arrangements for both wind and tidal farms has been the focus of many studies, and is important in both current and future turbine array design and operation. The optimisation of any one of these layouts will not necessarily be the same for another case. This is due to the range of parameters that impact turbine dynamics, for example, environmental conditions, array size and inter-turbine distances. Thus, we have to consider many designs across the parameter space which can become computationally extensive to perform.

To model all fluid dynamical features of a turbine array would require vast computational resources. Therefore, in order to conduct optimisation of turbine array design across a large parameter space it is useful to make simplifications to the system. One common simplification is to replace the turbine with an actuator disk, which exerts a uniform streamwise resistance to the flow. The actuator disk model has been extended in both tidal and wind turbine contexts. This paper particularly focuses on the additions made by Garret and Cummins [1] (GC07) to model turbines in confined flows.

The foundation of the work in this paper comes from the expansions of GC07 made by Draper, Nishino and Adcock [2] along with the study by Draper and Nishino [3] which compared the efficiency of single row and two aligned or staggered rows of turbines. Their study [3] has shown that staggered arrangements extract more power from the flow when compared to aligned arrangements, although they do not perform as well as a single row with the same number of turbines. This study, however, did not account for streamwise inter-turbine mixing as the upstream conditions for the second row of turbines were determined directly from the downstream conditions of the first row. This paper aims to further develop the aforementioned actuator disk model by introducing an extended analytical quasi-1D model for a multi-row turbine farm with a perfectly staggered and aligned turbine arrangement.

To extend this model a series of alternating inviscid and viscous zones are introduced, with inviscid zones surrounding a turbine row and viscous zones placed in between turbine rows, as seen in figure 1. In practice the formulation for the inviscid region is similar to the formulation by Draper, Nishino and

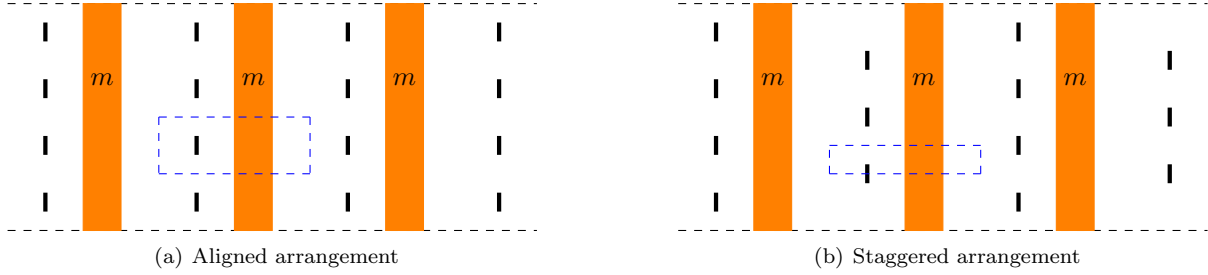


Figure 1: Diagram of four rows of (a) aligned and (b) staggered turbines. The dashed blue square represents the local flow domain depicted in detail in figure 2.

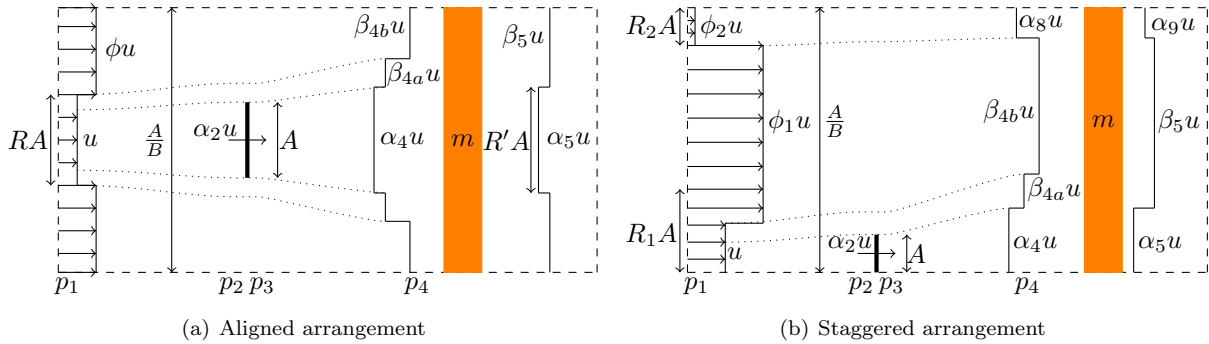


Figure 2: Diagram of the local flow domain for the (a) aligned and (b) staggered geometries.

Adcock [2] but the newly added viscous region acts to mix the wake and the bypass flows downstream of a turbine. A full description of these regions is given in Section 2. This hybrid inviscid-viscous approach was recently proposed by Nishino and Draper [4] for fully periodic arrays. In support of the hybrid inviscid-viscous modelling approach the large-eddy simulations by West and Lele [5] showed the inviscid process is dominant around the disk whereas the viscous process is dominant in the wake.

When examining the power extraction capabilities of a wind farm we often refer back to the seminal studies by Lanchester, Betz and Joukowsky [6] who place the theoretical maximum power coefficient of a wind turbine at 0.593. This limit however can be exceeded within an array of turbines when considering certain array set-ups, like those considered in Nishino and Wilden [7] who placed a higher limiting C_p value at 0.798 for a tidal array and a similar limit can be expected for wind [8]. This increase can be attributed to the effect of local blockage. Even though many of the studies on turbine performance in a channel are primarily targeted at tidal turbines, there is work to suggest that the confined flow model would be applicable to wind as well. This is as, for particularly offshore wind farms, a strong inversion layer in the atmospheric boundary layer (ABL) can act as a rigid lid confining the flow below the inversion layer [9]. Even in cases where the stratification is not large enough to imply a rigid lid we may still calculate an effective blockage ratio [2].

The paper is structured such that in Section 2 the theory is presented along with discussion and validation of the assumptions made in the model. In Section 3 the results of the aligned and staggered cases are discussed. A discussion on the implications of the theoretical predictions made in the model is presented in Section 4, followed by conclusions in Section 5.

2 Theory

We consider many rows of equally spaced turbines, as depicted in figure 1. The rows are considered to be infinitely wide; therefore we consider a local flow domain with symmetric boundary conditions for a single turbine, as shown in figure 2. We consider a uniform inflow for the first row of turbines. The turbines are positioned such that they are perfectly aligned or perfectly staggered. For the aligned case each turbine sits directly behind its upstream turbine, as depicted in figure 1a. For the staggered case

each turbine sits in the bypass flow of the upstream turbine, as depicted in figure 1b.

The velocity at a given streamtube cross-section is defined as a scalar times a reference velocity u (e.g. for $(0 \leq \alpha_4 \leq 1)$ we have that $\alpha_4 u$ is the velocity at the end of near wake). Here the near wake is defined to end at the end of the inviscid zone, at which the pressure has equalised across the local flow domain [3], and far wake starts in the viscous mixing zone. Here the reference velocity u is taken as the velocity upstream of the turbine. The value of u does not need to be specified as the outcome of our analysis, such as power coefficient, will depend only on the velocity ratios between streamtubes.

We define the cross sectional areas as a scalar times the disk area A (e.g. $\beta_{4b} u$ has cross sectional area $A_{\beta_{4b}} = R_{\beta_{4b}} A$). The disk is placed in a local flow domain of cross sectional area A/B where B is the local (cross-sectional) blockage ratio. If the inflow is uniform (i.e. for aligned $R = 1/B$ or $\phi = 1$) we get the classical problem from GC07.

The extension made in this model over previous similar models, such as [3][4], is the introduction of a viscous mixing zone between each turbine row to account for wake mixing, as mentioned in Section 1. We define this wake mixing rate by a constant parameter m ($0 \leq m \leq 1$), which determines the 'completeness' of mixing within each viscous zone. We also assume that the narrow bypass flow immediately outside the core flow is fully mixed with the main bypass flow. This is so that the flow will consistently recover to the same number of streamtubes no matter how many turbine rows it passes through. This allows the problem to be solved, even for a large number of rows, without extending the algebra for a high number of streamtubes. The validity of this assumption will be explored in Section 2.2.

2.1 Formulation for the Staggered Case

Only the full formulation for the staggered case will be presented here to conserve space and as the aligned case is simpler.

Application of the Bernoulli equation along the streamlines of the bypass flow immediately outside the core flow and the main bypass flow, respectively, lead to:

$$p_1 - p_4 = \frac{1}{2} \rho u^2 (\beta_{4a}^2 - 1) \quad (1)$$

$$p_1 - p_4 = \frac{1}{2} \rho u^2 (\beta_{4b}^2 - \phi_1^2) \quad (2)$$

Applying the Bernoulli equation to the bypass flow furthest from the core flow we obtain:

$$p_1 - p_4 = \frac{1}{2} \rho u^2 (\alpha_8^2 - \phi_2^2) \quad (3)$$

Equating both (1) and (2) gives us:

$$\beta_{4b}^2 = (\beta_{4a}^2 + \phi_1^2 - 1) \quad (4)$$

Equating both (1) and (3) gives us:

$$\alpha_8^2 = (\beta_{4a}^2 + \phi_2^2 - 1) \quad (5)$$

Conservation of mass across each streamtube gives us the following cross sectional area relationships:

$$R_{\alpha_8} = \frac{R_2 \phi_2}{\alpha_8}; \quad R_{\alpha_4} = \frac{\alpha_2}{\alpha_4}; \quad R_{\beta_{4b}} = \frac{\phi_1 (\frac{1}{B} - (R_1 + R_2))}{\beta_{4b}}; \quad R_{\beta_{4a}} = (\frac{1}{B} - (R_{\alpha_4} + R_{\alpha_8} + R_{\beta_{4b}}))$$

Conservation of mass across the entire flow gives us:

$$\alpha_4 = \frac{-\beta_{4a} \alpha_2}{R_1 - \alpha_2 - \beta_{4a} (\frac{1}{B} - \frac{R_2 \phi_2}{\alpha_8} - \frac{\phi_1}{\beta_{4b}} (\frac{1}{B} - (R_1 + R_2)))} \quad (6)$$

Again using the Bernoulli equation on the streamlines going through the turbine gives us:

$$p_2 - p_3 = p_1 - p_4 + \frac{1}{2} \rho u^2 (1 - \alpha_4^2)$$

which in combination with (1) gives the following:

$$T = \frac{1}{2} \rho A u^2 (\beta_{4a}^2 - \alpha_4^2) \quad (7)$$

where static equilibrium across the disk has been used to write the disk thrust, $T = A(p_2 - p_3)$. Finally, conservation of momentum across the entire flow gives us:

$$T = \frac{A(p_1 - p_4)}{B} - \rho u^2 A \left[(R_1 - \alpha_2)(\beta_{4a} - 1) + \alpha_2(\alpha_4 - 1) + \phi_1 \left(\frac{1}{B} - (R_1 + R_2) \right) (\beta_{4b} - \phi_1) + R_2 \phi_2 (\alpha_8 - \phi_2) \right] \quad (8)$$

This can be written as:

$$0 = (1 - B)\beta_{4a}^2 - 1 - 2B \left\{ \alpha_2(\alpha_4 - 1) + (\beta_{4a} - 1)(R_1 - \alpha_2) - \frac{\alpha_4^2}{2} + R_2 \phi_2 (\alpha_8 - \phi_2) + \phi_1 \left(\frac{1}{B} - (R_1 + R_2) \right) (\beta_{4b} - \phi_1) \right\} \quad (9)$$

These can then be solved numerically, using inputs $B, R_1, R_2, \phi_1, \phi_2$ and α_2 , to recover the post-turbine velocity profile. The power extracted by the turbine is then

$$P = T \alpha_2 u = \alpha_2 (\beta_{4a}^2 - \alpha_4^2) \frac{1}{2} \rho A u^3$$

We now define the local power coefficient, C_p^* , as the following:

$$C_p^* = \frac{P}{\frac{1}{2} \rho u_{av}^3 A} = \frac{\alpha_2 (\beta_{4a}^2 - \alpha_4^2) u^3}{u_{av}^3} \quad (10)$$

where u_{av} is the average velocity over the cross sectional area. We will adopt the convention of replacing our parameter α_2 with a resistance coefficient for the turbine, $k = (\beta_{4a}^2 - \alpha_4^2) / \alpha_2^2$. We also define the farm averaged C_p^* value, $\langle C_p^* \rangle$, which is the sum of C_p^* at each turbine divided by the number of turbines.

We then calculate $\beta_5, \alpha_5, \alpha_9$ values using mixing between the streamtubes. We define the mixing rate, m , such that at each cross-sectional region $u_{out} = m u_{av} + (1 - m) u_{in}$ where u_{in} is the velocity at the start of the viscous zone, and u_{out} is the velocity at the end of the viscous zone. Due to the assumption that the bypass flow immediately outside the core flow is fully mixed with the main bypass flow we get the following:

$$\beta_5 = m \left(\frac{u_{av}}{u} \right) + (1 - m) \frac{\beta_{4a} R_{4a} + \beta_{4b} R_{4b}}{R_{4a} + R_{4b}}$$

Essentially this is a 3-input-parameter model consisting of B, k and m . It is also worth noting that ϕ_1, ϕ_2, R_1 and R_2 are calculated within the model for each row.

2.2 Instant Mixing Assumption

There is an assumption in this model that the main bypass flow and the bypass flow immediately outside the core flow is fully mixed before it reaches the next downstream turbine. To test this assumption a comparison was made between an aligned case with a single core flow and bypass flow, as depicted in figure 2, and an aligned case in which an additional bypass streamtube is preserved. For clarity, in figure 2, the main bypass flow is the streamtube with velocity $\beta_{4b} u$ and the bypass flow immediately outside the core flow is the streamtube with velocity $\beta_{4a} u$. The formulation of the aligned case with an additional bypass flow (double streamtube case) is similar to the staggered case. To showcase the difference between the single and double bypass cases a comparison of $\langle C_p^* \rangle$ values for fixed k values for 4 turbine rows was constructed. The comparison as plotted in figure 4 shows the relative difference between the two cases, calculated by $(\langle C_p^{*d} \rangle - \langle C_p^{*s} \rangle) / \langle C_p^{*d} \rangle$ at each k value (where the d index indicates double and the s indicates single). The significance of the difference between the double and single streamtube cases varies with both blockage ratio and mixing rate. In figure 4 we observe differences up to 12%, with lesser differences as blockage ratio increases. One consistency across all blockage values is that the

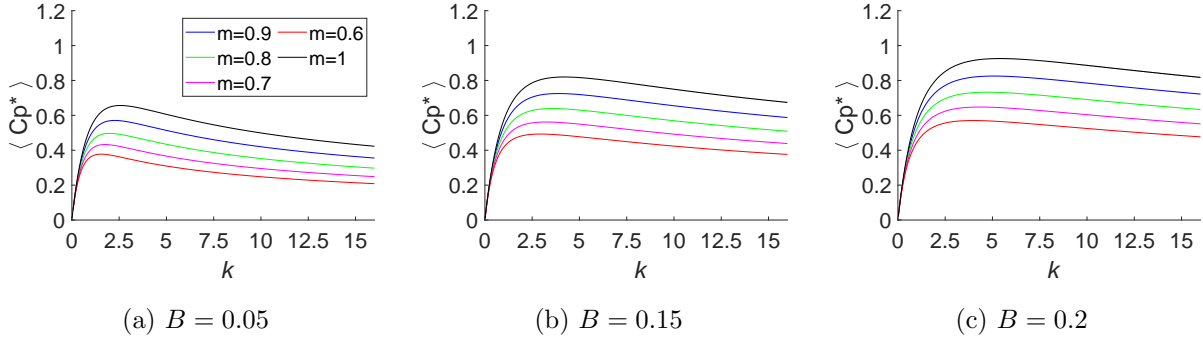


Figure 3: Average local power coefficient $\langle C_p^* \rangle$ for four aligned rows of turbines at three different blockage ratios: (a) $B = 0.05$, (b) $B = 0.15$, and (c) $B = 0.2$. The different colours correspond to different mixing rates.

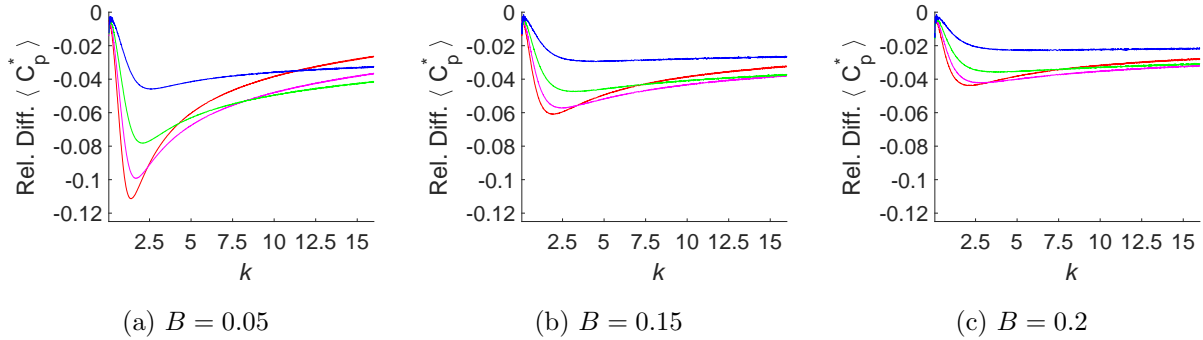


Figure 4: Relative difference in $\langle C_p^* \rangle$, calculated as in section 2.2, between the single bypass case and the double bypass streamtube case for four rows of aligned turbines.

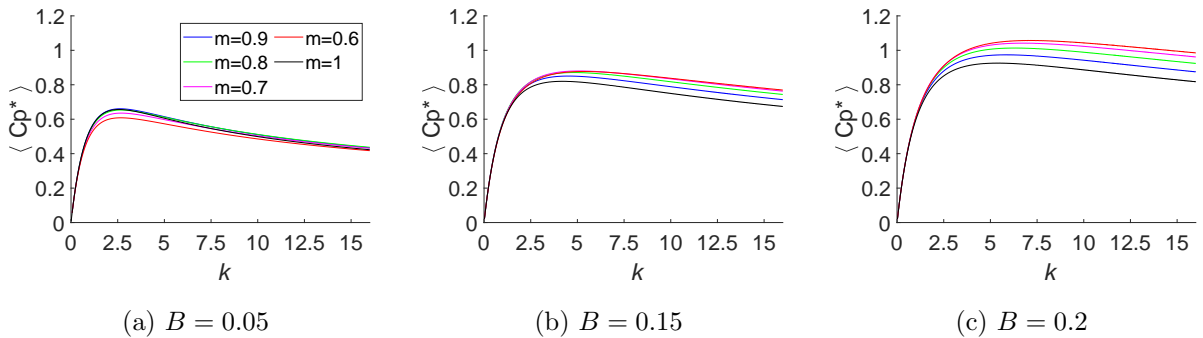


Figure 5: Average local power coefficient $\langle C_p^* \rangle$ for four staggered rows of turbines at three different blockage ratios: (a) $B = 0.05$, (b) $B = 0.15$, and (c) $B = 0.2$.

magnitude of $\langle C_p^* \rangle$ for the double streamtube case is always less than that of the single streamtube case (i.e. $\langle C_p^{*d}(k) \rangle \leq \langle C_p^{*s}(k) \rangle \forall k \in [0, 16]$). This means that the instant mixing assumption tends to overpredict $\langle C_p^* \rangle$.

The k value at which the relative difference is maximised corresponds closely to the point at which the $\langle C_p^* \rangle$ value is maximised. This is more prominent at lower blockage ratios and lower mixing values.

For the aligned case presented in the rest of the paper the double streamtube model is used. It is reasonable to consider that the difference between single and double streamtube is greater than the difference between double streamtube and more complex models with a larger number of streamtubes (i.e. less instant mixing). In support of this a comparison has been made between β_{4a} and β_{4b} for the single

and double streamtube cases. It was found that for the single streamtube case the difference between β_{4a} and β_{4b} was greater than that of the double streamtube cases. If $\frac{\beta_{4b}}{\beta_{4a}} \rightarrow 1$ instant mixing will have a negligible impact on the flow profile. To confirm this it would be useful to construct a model with an additional streamtube (i.e. a triple bypass streamtube case).

The impact of instant mixing for the staggered case is assumed here to be similar to that of the single streamtube for the aligned case. However, due to the staggered configuration the wake of a turbine passes through two mixing zones before it encounters another turbine. For this reason it is likely that, for low blockage ratios, the impact of instant mixing is reduced in the staggered case compared to the aligned.

3 Results

3.1 Aligned case

3.1.1 Combined effects of blockage and mixing on $\langle C_p^* \rangle$

For the aligned case, as expected and can be seen from figure 3, there is an observed increase in $\langle C_p^* \rangle$ values as the inter-turbine mixing increases. This is intuitive as each downstream turbine directly interacts with a faster flow and thus be able to extract more kinetic energy. The effect of mixing rate on $\langle C_p^* \rangle$ appears to have no great qualitative difference between each blockage ratio. For increasing blockage ratio there is also an observed increase in $\langle C_p^* \rangle$ for a given mixing rate. This echoes the work of Garrett and Cummins [1] who gave the analytical formulation for the maximum power coefficient for a given blockage ratio for a single disk ($m = 1$ in this study) as $C_{Pmax} = \frac{16}{27} \left(\frac{1}{1-B} \right)^2$. It is worth noting as well that as $B \rightarrow 0$ the system approaches the unconfined case in which $C_{Pmax} = \frac{16}{27}$, the Lanchester-Betz-Joukowski limit.

Another feature that can be observed as blockage ratio varies is that the shape of the $\langle C_p^* \rangle$ curve, in figure 3, alters. For lower blockage ratios there is a more pronounced peak $\langle C_p^* \rangle$, compared to high blockage ratio cases. It can be concluded from this that the operational range of k for optimal or near-optimal $\langle C_p^* \rangle$ is much narrower for the low blockage ratio case, most notably with low mixing rate, when compared to the high blockage ratio case. The optimal k value is also observed to reduce as mixing rate decreases. In essence the change in optimal k value as mixing rate changes is down to the relationship between u^3/u_{av}^3 and the other terms in (10).

3.1.2 Effect of the number of rows on $\langle C_p^* \rangle$

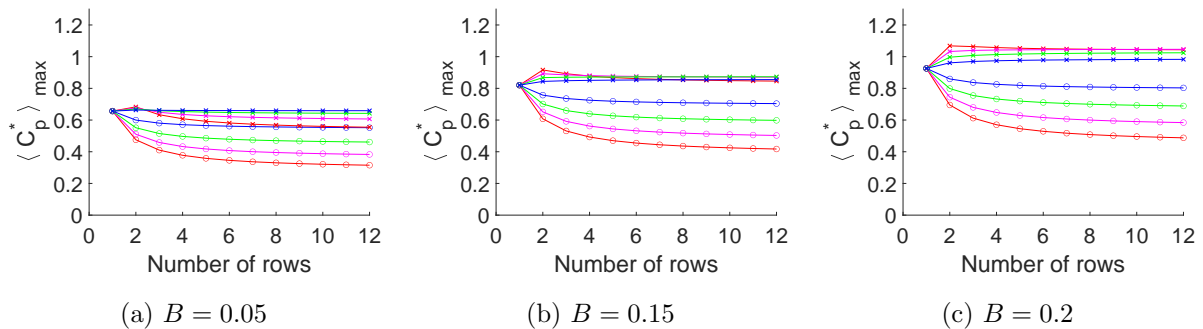


Figure 6: The maximum $\langle C_p^* \rangle$ value achieved by a given number of rows with a fixed k value for the whole array. The curves with crosses (x) and circles (o) are for the staggered and aligned cases, respectively.

Figure 6 shows how the maximum of the farm-average power coefficient, $\langle C_p^* \rangle_{max}$, approaches an equilibrium value (for a given set of B and m) as we increase the number of rows from 1 to 12. It is worth noting that systems with higher mixing rates are observed to converge earlier than those with low mixing rates. There is, however, no significant impact of the blockage ratio on this convergence. This is not to say there is no difference between the pre-converged $\langle C_p^* \rangle$ values at different blockage ratios. Note, the plot for $m = 1$ has been omitted here as for both staggered and aligned arrangements it is in the converged state immediately as they return to the GC07 case of a turbine in a channel of uniform inflow. The maximum $\langle C_p^* \rangle$ value for the $m = 1$ case is exactly the first point in each of figures 6a, 6b and 6c.

3.2 Staggered case

3.2.1 Combined effects of blockage and mixing on $\langle C_p^* \rangle$

In contrast to the aligned case, the staggered case does not, for all three blockage ratios, attain a maximum C_p^* value when $m = 1$, as seen in figure 5. It is worth noting, however, that in figure 5a the difference in maximum $\langle C_p^* \rangle$ between $m = 1$ and $m = 0.9$ is negligible. The optimal m can be seen as dependent on the blockage ratio B . Higher blockage ratio cases tend to show lower mixing values as optimal. In contrast, low blockage ratios tend towards the ordering observed for the aligned case in figure 3, with $\langle C_p^*(m_1) \rangle < \langle C_p^*(m_2) \rangle$ for $m_1 < m_2$. This can be understood intuitively as the upstream turbine diverts flow into the bypass flow and, unless the blockage ratio is negligibly small, the bypass flow speeds up, allowing the downstream turbine to extract more energy. Therefore, in cases with lower mixing values the higher velocity bypass flow approaching a downstream turbine is preserved, whereas a mixing value of $m = 1$ leads us back to the GC07 case. Another contrast to the aligned case is that the optimal k value required to maximise $\langle C_p^* \rangle$ increases as mixing rate decreases.

3.2.2 Effect of the number of rows on $\langle C_p^* \rangle$

The effects of this enhanced bypass flow can further be seen in figure 6. There is a peak in maximum $\langle C_p^* \rangle$ at two rows of turbines, and this peak is clearly more prominent in certain cases. As can be expected intuitively, a greater peak is observed for lower mixing values as it preserves the higher velocity bypass flow. As for the effect of blockage ratio it is expected that a higher blockage ratio will cause a greater peak. This is as, by conservation of mass and momentum, the flow diverted into the bypass will have a greater effect on the acceleration of the bypass flow.

4 Discussion

4.1 Implications of the Study

The theoretical analysis presented above is to model the 'internal' sub-problem of a wider turbine array modelling problem. Focusing on wind energy research, due to the complex multi-scale interaction between wind farms and the atmospheric boundary layer (ABL) it is often necessary to split the problem into two coupled sub-problems, the 'external' problem and the 'internal' problem [10]. The external problem is primarily composed of meso-macroscale geophysical flows and wind-farm scale flow patterns. The internal problem is primarily composed of turbine design, operating conditions and turbine arrangement. The value of u_{av} in this study, which is used to define the 'local' (or internal) power coefficient C_p^* , depends on the external problem. The full effects of the external problem on the model presented here are outside the scope of this paper. However, it is worth noting that the optimal k values to maximise the 'global' power coefficient is expected to be lower than the values obtained in this paper as some decrease in u_{av} due to the global blockage effect is inevitable [10].

This study has primarily concerned itself with the differences in performance for an array consisting of four turbine rows. Although the maximum $\langle C_p^* \rangle$, and the corresponding optimal fixed k for the entire farm, have been explored for varying number of rows, there is yet to be an assessment of varying k operating conditions across the farm.

As mentioned in Section 2.2, it is assumed that the staggered case will be impacted by instant mixing to a similar extent as the aligned single bypass case. For the staggered case, this assumption is expected to hold best for low blockage ratios where the system behaves similar to that of the aligned case with additional inter-turbine mixing. It is still unclear how the impact of instant mixing will be for the staggered case at higher blockage ratios.

The use of actuator disc models for quantitative insight should be considered as, most likely, an upper bound for the performance. This is as actuator discs are an approximation of ideal turbines and do not include losses associated with, for example, tip and hub vortices generated by real turbine rotors.

4.2 Limitations and Future Work

One assumption made in this model that can be improved upon in future studies is that of the constant mixing value m . Currently the value of m is not linked to the flow physics and the whole flow is mixed at

the same rate. In reality different streamtubes would mix at different rates and this depends on factors such as turbulent intensity and the velocity ratio between the flows.

5 Conclusions

In conclusion a study into the performance of an array of turbines with varying blockage ratios, local resistance coefficients and inter-turbine mixing rates was performed using an extended inviscid-viscous actuator disk model. The study is relevant to the design of both wind and tidal-stream turbine arrays.

It was shown that the performance of an aligned and staggered array is highly dependent on inter-turbine mixing rate, m , and blockage ratio, B . The greatest array performance was achieved at the highest blockage ratio. The performance of an aligned array was also maximised for higher mixing rates, with the GC07 case as the theoretical maximum. Although the low blockage ratio staggered case (C_p^{**}) is maximised for high mixing rates, when blockage ratio is increased the lower mixing rates start to outperform higher mixing rates. This is due to the effect of an accelerated bypass flow which is best preserved for low mixing values. The second row of staggered turbines outperform all other turbine rows as they benefit from the local inflow with highest velocity.

The validity of the instant mixing assumption utilised in the new model was also investigated for the aligned case. It was found that the impact of the instant mixing assumption increases for low blockage ratios and lower mixing rates. The impact decreases as more bypass streamtubes are explicitly calculated in the model. The effect of instant mixing on the staggered arrangement is likely similar at low blockage ratios to the effect in the aligned case. However, effect at high blockage ratios, at which lower mixing rates are expected to be beneficial, is still unclear and will require further study.

Acknowledgement

The authors would like to acknowledge the use of the University of Oxford Advanced Research Computing (ARC) facility in carrying out this work. The authors would also like to thank Prof. Richard Willden and Dr Scott Draper for helpful discussions.

References

- [1] Garrett C and Cummins P 2007 *Journal of Fluid Mechanics* **588** 243–251
- [2] Draper S, Nishino T and Adcock T 2014 *Proceedings of the 19th Australasian Fluid Mechanics Conference*
- [3] Draper S and Nishino T 2014 *Journal of Fluid Mechanics* **739** 72–93
- [4] Nishino T and Draper S 2019 *Proceedings of the 7th Oxford Tidal Energy Workshop* 31–32
- [5] West J R and Lele S K 2020 *Energies* **13** 1078
- [6] Van Kuik G A 2007 *Wind Energy* **10** 289–291
- [7] Nishino T and Willden R H 2012 *Journal of Fluid Mechanics* **708** 596–606
- [8] Nishino T and Draper S 2015 *Journal of Physics: Conference Series* **625** 012010
- [9] Smith R B 2010 *Wind Energy* **13** 449–458
- [10] Nishino T and Dunstan T D 2020 *Journal of Fluid Mechanics* **894** A2

Implementation of MrGARK schemes for multirate time stepping of actuator-line methods in LES of wind farms

K Ntrelia^a and J Meyers^a

^aDepartment of Mechanical Engineering, KU Leuven, Celestijnenlaan 300A, 3001 Leuven

E-mail: konstantina.ntrelia@kuleuven.be

Keywords: optimal control, large-eddy simulation, wind turbine modeling, numerical time integration

1 Introduction

In modern wind farms, turbines are typically placed together. Wake formulation downstream an individual wind turbine results in the aggregated interaction of wakes within the farm, leading to reduced power production and increased structural loading in downstream rows. Towards the alleviation of these detrimental phenomena, optimal control methods have been thoroughly investigated through various researches.

Optimal control strategies present a great interest, as they have widely demonstrated an increase to the overall farm efficiency when applied. Within this scope, Goit & Meyers [1] first introduced a dynamic induction control approach, using a Large-Eddy Simulation (LES) framework, integrated with an adjoint optimization method. In this work, wind turbines are represented as actuators that enact forces on the flow field, influencing it in a way that results in the maximization of the total power produced. For this reason, various models for representing wind turbines have been implemented. Initially, the LES tool was forged with the actuator disk model, later to be extended to an actuator line model by Yilmaz & Meyers [2]. Both models were employed for conducting optimal control studies and provided different control strategies as results. While studies by Munters & Meyers [3] provided very satisfactory primal insights for wind farm control, the latter model then revealed more realistic and interesting control techniques, based on new wake mixing mechanisms. However, it is commonly acknowledged that the actuator line model, although highly accurate, is also extremely computationally inefficient. The current study investigates the advantage of employing a multi-rate integration scheme inside the LES framework, aiming to reduce the computational cost of the method, while maintaining the accuracy.

2 Methodology

Multirate Generalized Additive Runge Kutta Methods (MrGARK) [4] are specific instants of generic Runge Kutta methods. These methods are based on the ability of different components often evolving at different time scales in dynamical systems. However, the former differentiates by dividing the Right Hand Side (RHS) of a differential equation in two parts: one part representing the slow evolving component and one part representing the fast evolving component. As a result, the former is integrated with a large time step H , while the latter is integrated with a small time step h . The concept of MrGARK methods resides on the fact that the partitions of the RHS are discretized with different time step sizes, but are concisely coupled so as to properly advance in time.

In advance to employing the MrGARK methods for integrating the Navier-Stokes equations, a resembling case study is first examined. Numerous high order schemes have been formulated by Sarshar, Roberts & Sandu [4], from which an explicit second order scheme (Ex2-Ex2 2[S]) and an explicit third order scheme (Ex3-Ex3 3[S]) have been selected, both with telescopic properties.

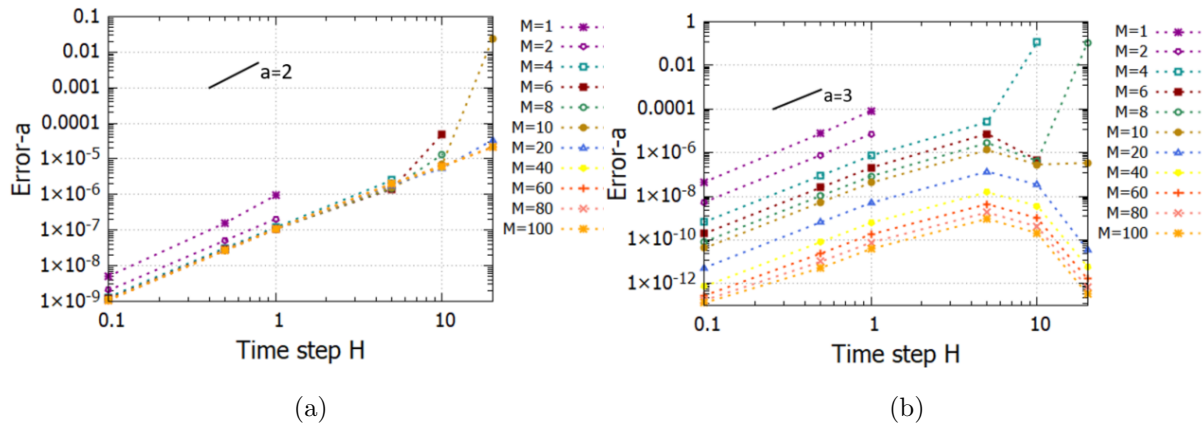


Figure 1: Error plots of study case variable a over a range of time steps $H = [0.1, 20]$. A fixed macrostep time integration is carried out with varying multirate step ratios M using MrGARK Ex2-Ex2 2[S](a) and Ex3-Ex3 3[S](b) methods.

The case study consists of a system of two first order ordinary differential equations (ODE). The first ODE represents the fast motion of the blades and the fast forcing term that is included in the Navier-Stokes RHS, therefore it entails solely a fast evolving component, denoted with C_T . The second ODE substitutes the momentum Navier-Stokes equations, by exploiting two RHS, accounting for the slow evolving flow terms, defined as a , and for the fast evolving forcing terms C_T .

3 Results and discussion

The performance of the schemes is tested through an error analysis. The error is computed using the L_1 norm and the reference case consists of a typical fourth order Runge Kutta. The obtained results are presented in Fig.1.

For both studies, a wide range of time steps H and multirate step ratios M have been used. From the figures above it is evident that the numerical solution is calculated with high accuracy and that the applied schemes follow a similar behaviour. The numerical order for both schemes matches their theoretical orders for the tested multirate step ratios. However, the numerical order appears to deflect from the theoretical pattern, at different combinations of H, M for each scheme. Finally, in contrast to a single rate method, where $M = 1$, it is suggested that the feasible range of time step sizes that can be used for the integration can be expanded, by applying the MRGARK methods.

4 Future Work

Having validated the performance of MrGARK methods through a case study, the next challenge involves the implementation of these high order schemes for the integration of the Navier-Stokes equations and a thorough stability analysis. An investigation on the separation of the blade motion and flow time scales, as well as the computational gains that can be achieved are interesting subjects to be further studied.

References

- [1] Goit J P and Meyers J 2015 *J. Fluid Mechanics* **768** 5-50
- [2] Yilmaz A E and Meyers J 2018 *Physics of Fluids* **30(8)** 085106
- [3] Munters W and Meyers J 2017 *Phil. Trans. R. Soc.* **375**:20160100
- [4] Sarshar A, Roberts S and Sandu A 2019 *SIAM J. Sci. Comput.* **41(2)** 816-847

A Gaussian Wake Model and OpenFAST Based Wind Farm Simulation

A. Cioffi^a, Z. Zhang^a, and C. Muscari^a

^aPolitecnico di Milano

E-mail: zhaoyu.zhang@polimi.it

Abstract

Wake interaction is a key issue in wind farms as it is the main cause of power loss and dynamically varying loads for the downstream turbines. To develop optimal control, It is necessary to properly model the rotor wake and to understand the effects and the interaction of wakes based on models tuned against experiments and numerical data. In this paper, a Gaussian Wake Model (GWM) is proposed and coupled with OpenFAST, improving the accuracy compared with other models. A GWM based platform, Floris, is used to simulate the wake and partial wake conditions and is coupled with OpenFAST. The OpenFAST aerodynamic module is adopted to calculate the rotor aerodynamics on the actual rotor flow field, in which the action of wake is revealed. With the designed layout, wake interaction changes with wind direction. The simulations show how the wake causes a significant decrease on torque and power generation. The relationship between these losses and the particular configuration provides fundamental information on how to use yaw control for a wake redirection strategy which maximizes the power.

Keywords: Wind Farm Control, Wind Turbine, Wake Model, Floris, OpenFAST, Gaussian Wake Model

1 Introduction

Wind energy is a relatively new research field. For many years it has had a marginal place in the global energy production scenario and because of the limited resources invested it slowly advanced by taking ideas from the aerospace world. The fossil fuels crisis and the growing awareness of climate and sustainability issues drastically changed the situation. Now wind energy is an exciting, flowery multidisciplinary field employing experts in aerodynamics, materials, monitoring and diagnostics, electric and control systems.

One of the main issues when dealing with wind turbines is their positioning. There is a lot of things to take into account such as the vicinity to human settlements, the nature of the ground, the wind uniformity and intensity, the feasibility of efficient energy storage and transmission. It turns out that there is actually a very limited amount of onshore sites meeting all of these requirements and this constraint is actively dictating the new research trends in the field. If we want to exploit favourable sites we can think of building bigger turbines and or clustering them. We can also think of going offshore. Each one of this ideas introduces new, big challenges. Bigger rotors means longer, more flexible blades with structural and fatigue issues, clustering means having to deal with optimizing the layout, to begin with, going offshore means to consider new loads and new sources of instability.

If all of this challenges have been extensively tackled in the last couple decades what could really be a game changer and break down the LCOE for this technology is control. At the turbine level the control system guarantees a smooth power output and may optimize it at lower wind speeds. At the wind farm level though, the power production can be increased of the order of 10 % (taking greedy control as a baseline) even with the simplest static techniques.

The key instrument for developing and testing such techniques is the modeling of wake interaction. Currently, a lot of study is dedicated to the development of wind plant models having different levels of complexity and fidelity, based on the purposes for which they are used. Wind plant models have very

different levels of complexity and fidelity and may have different purposes. Among these models, there are on one side high fidelity wake models which are particularly suited for model validation since they are able to grasp the physics behind the phenomenon represented and on the other side engineering and analytical models, that give a more rough estimation of the flow field or turbine performance, but are still valuable for the evaluation of turbine performances. Control oriented models are necessarily low fidelity since they have to be very quick to run in real-time if needed and dynamically optimize power extraction and loads.

An example of open-source control-oriented software is Floris, developed by NREL. It relies on the Bastankhah and Porté-Agel [1, 2] GWM and is able to fully characterize the flow field developed in a wind farm, considering steady-state environmental conditions. To work, this tool requires only four parameters determined experimentally and some inputs from the user related mainly to the farm geometry and the free stream wind. What we tried to do with this work was to position ourselves a bit further from the basic Floris on the spectrum that goes from very low fidelity models to CFD.

We will present a low-fidelity model based on the GWM and Floris. What makes it more advanced is that the GWM will be embedded and working in the OpenFAST framework coupled to the BEMT aerodynamic model of the turbine. The main difference with Floris is the capability of this new tool to model the wake generated by the machines keeping into account for the C_T and AIF developed on the whole plane of the rotor and calculated at runtime from the aero-elastic solver OpenFAST, and not only in a single point (at hub-height by means of pre-tabulated values like the $C_P - TSR$ or the $C_T - TSR$ table (like Floris does). This allows for a more accurate description of the wake. The proposed tool allows also for a characterization of the loads acting on the machines when they work in complete or partial wake condition under the assumption of steady-state environmental conditions. In addition to this, the model can be used to develop and test new control logics at wind farm level in order to maximize the power extraction under the hypothesis of steady-state flow condition but retaining the dynamics of the turbines (thanks to OpenFAST). It is also possible to investigate both the loads and the power extraction when the turbines are working in a yawed condition. Indeed, this new tool is particularly suited for research on wind farm control logics using wake steering methods, like the one proposed by van Dijk et al. [3] and Martinez et al. [4], Axial-Induction based methods, like the one presented by van Wingerden et al. [5], or a combination between them like in the work of Bossanyi et al. [6].

The paper is organized as follows. At first, there is an overview on the GWM and the analytical changes that have been made to it. Then there's a chapter dedicated to the implementation of the new GWM in the OpenFAST framework. Lastly, there is a presentation of a simulation carried out with the new developed tool and a discussion about the results and the future work.

2 Gaussian Wake Model

2.1 GWM Overview

One of the analytical models that can be used to characterize the wakes developing in a wind farm is the Gaussian Wake Model (or GWM) firstly proposed by Bastankhah and Porté-Agel [1, 2] and successfully implemented in the NREL's software FLORIS. The authors derived the wake model by performing a budgeting analysis on Reynolds Averaged Navier-Stokes equations (RANS). In this way, they were able to identify and to retain in the RANS equations the terms having the biggest impact on the wake's behaviour and to discard the other negligible terms. At the end of this process, the authors obtained two conditions that are used to obtain an expression for two fundamental terms of the model that are the wake deficit and the wake deflection as function of downstream position (with respect to the hub center point of the considered turbine).

For the wake deficit profile in wind speed (with respect to undisturbed wind), as it can be easily inferred from the title of the model, Bastankhah and Porté-Agel chose a gaussian shape; this choice was validated by further studies carried out by the authors, with the only limitation of having a relative angle between the free wind direction and the rotor plane of the turbines comprised in the range of [-30, +30] degrees. Out of this range, the gaussian shape is no more representing adequately the phenomenon. Another fundamental point described by the GWM is the wake deflection generated when the turbines are operating misaligned with respect to the undisturbed wind direction.

An important feature of the model is the separation of the wake in two main zones depending on the downstream distance from the turbine's rotor hub. The former is the near-wake region, while the latter is

the far-wake region. It is in this region that the authors assumed valid the hypothesis of gaussian shape for both the wake deficit in wind speed and the wake deflection. Their expression is reported in Eqn. (1) and Eqn. (2).

$$\frac{\bar{u}(x, y, z)}{u_\infty} = 1 - C(x) e^{-\frac{(y-\delta)^2}{2\sigma_y^2}} e^{-\frac{(z-z_h)^2}{2\sigma_z^2}} \quad (1)$$

$$\frac{\theta(x, y, z)}{\theta_m} = e^{-\frac{(y-\delta+\sigma_y)^2}{2\sigma_y^2}} e^{-\frac{(z-z_h)^2}{2\sigma_z^2}} \quad \text{and} \quad \theta_m = \frac{\theta_c}{e^{-0.5}} \quad (2)$$

where \bar{u} represents a time averaged velocity in a downstream location with respect to the considered turbine, $C(x)$ represents the normalized velocity deficit at the wake center in various downstream positions, δ represents the wake center deflection, z_h represents the hub height of the considered wind turbine, σ_y and σ_z represent the wake width in y and z direction, u_∞ represents the undisturbed fluid velocity and θ_c represents the wake skew angle of the wake center as function of the downstream distance.

For what regards the wake width, σ_y and σ_z , a linear formulation dependent on the downstream distance is proposed:

$$\frac{\sigma_z}{d} = k_z \frac{x - x_0}{d} + \frac{\sigma_{z0}}{d} \quad (3)$$

$$\frac{\sigma_y}{d} = k_y \frac{x - x_0}{d} + \frac{\sigma_{y0}}{d} \quad \text{and} \quad \frac{\sigma_{y0}}{d} = \frac{\sigma_{z0}}{d} \cos \gamma \quad (4)$$

$$k_y = k_z = k_a I + k_b \quad \text{and} \quad k_a = 0.38371, k_b = 0.003678 \quad (5)$$

where d represents the turbine's diameter, x_0 the downstream distance at which there is the onset of the far wake zone, σ_{y0} and σ_{z0} represent the wake width at the onset of the far wake zone, k_z and k_y are two constants hypothesized as linearly dependent from the wind turbulence intensity I , k_z and k_y are two constants determined experimentally and γ is the yaw angle of the turbine relative to the free-stream wind direction.

It is at this stage that the authors used the two conditions coming from the budgeted RANS equations (both in stream-wise and span-wise direction) to retrieve an expression for the wake center deflection δ and for the normalized velocity deficit at the wake center $C(x)$ as function of downstream position. The analytical expression for this functions can be found in Basthankhah and Porté-Agel's papers [1, 2].

To close the model, since all the functions obtained are strongly dependent on the onset of the far wake region, it is necessary to characterize it.

2.2 Determining the parameters in the far wake region

A relationship between the C_T and the a (AIF) of the turbine is needed; Basthankhah and Porté-Agel proposed a simplified, analytical formulation:

$$C_T \simeq 4a(1 - a \cos \gamma) \quad \text{and} \quad a \simeq \frac{1}{2 \cos \gamma} (1 - \sqrt{1 - C_T \cos \gamma}) \quad (6)$$

This analytical formulation, as will be seen in Sect. 2.4, is fundamental in the formulation of the GWM since all the principal model parameters are depending on it. In the Floris software, to run the model, a $C_T - TSR$ and a $C_P - TSR$ table are required as input parameters. Thanks to them, the AIFs of the simulated turbines are derived by means of Eqn. (6), using the input Wind Speed to define the TSRs at which the machines are operating ($TSR \rightarrow C_T \rightarrow AIF$).

Continuing with the GWM, by applying the definition of AIF and by applying the Bernoulli equation between an upstream (undisturbed wind) section and the rotor section of the turbine and between the rotor section and a downstream section, it is obtained:

$$\frac{u_R}{u_\infty} = \frac{C_T \cos \gamma}{2(1 - \sqrt{1 - C_T \cos \gamma})} \quad \text{and} \quad \frac{u_0}{u_\infty} = \sqrt{1 - C_T} \quad (7)$$

where u_R is the wind speed at the turbine's rotor plane.

From this considerations, the theoretical value of the deficit at the rotor plane section C_0 , a parameter on which $C(x)$ is relying (please make reference to Basthankhah and Porté-Agel [1, 2] for the complete dissertation), can be expressed as:

$$C_0 = 1 - \frac{u_0}{u_\infty} = 1 - \sqrt{1 - C_T} \quad (8)$$

Furthermore, assuming a constant velocity equal to u_0 in the the near wake zone, or "potential core" of the wake, and applying the budgeted RANS conditions at section $x = x_0$ and using Eqns. (7) it is possible to conclude that:

$$\frac{\sigma_{z0}}{d} = \sqrt{\frac{1 + \sqrt{1 - C_T \cos \gamma}}{8(1 + \sqrt{1 - C_T})}} \simeq \sqrt{\frac{1}{8}} \quad (9)$$

Passing to the wake deflection and using the Burton's approximation [7] to describe the flow skew angle with respect to the rotor's axis χ and by substituting the AIF with Eqn. (6) it is obtained that the θ angle (useful for estimating the flow angle at rotor disk) is:

$$\theta \simeq \frac{0.3\gamma}{\cos \gamma} (1 - \sqrt{1 - C_T \cos \gamma}) \quad (10)$$

Eqn. (10) is used to define the parameter θ_{c0} (the flow skew angle at the onset of the far wake region, where $x = x_0$). From this consideration, it is easy to see how the wake deflection δ_0 at $x = x_0$ can be expressed as:

$$\delta_0 = x_0 \tan \theta_{c0} \simeq x_0 \theta_{c0} \quad (11)$$

The last expression to be determined is x_0 , the downstream distance at which there is the onset of the far wake region. To determine this unknown, the authors adopt a model from Lee & Chu [8] suggesting a proportionality between the change in width of the shear layer σ_{y0} to the velocity difference between the potential core of the wake and the unperturbed surroundings. They also recognized a proportionality of σ_{y0} with the incoming turbulence I that enhances flow entrainment and the growth of the shear layer. So, by carrying out further analysis and manipulation on the model's equations, they were able to define x_0 as:

$$\frac{x_0}{d} = \frac{\cos \gamma (1 + \sqrt{1 - C_T})}{\sqrt{2} [4\alpha I + 2\beta (1 - \sqrt{1 - C_T})]} \quad (12)$$

2.3 Additional Considerations

The GWM model described above is used to reproduce the wake generated by a single turbine. In general, when considering wind farms, interaction between wakes may happen and we must able to correctly reproduce them in the model. Just think of the case where more turbine are aligned to the wind direction; it is clear that, if the rotors are not extremely far one from the other, the waked flow field acting on a generic downstream rotor is the result of a composition of the wakes generated by some of the upstream turbines as it is possible to see in Fig. 1 obtained using NREL's Floris [9].

In this subsection, the methods used to keep into account for this phenomenon are exactly the ones proposed in the open-source NREL's Floris software. The correction used for the wind velocity was developed by Katic et al. [10] and proposes a superimposition of the local wakes to estimate the wake deficit on the $n + 1$ downstream turbine while Crespo et al. [11] propose a correction for the added turbulence due to the wake generation and mixing with the free-stream velocity:

$$\Delta u_{n+1} = \sqrt{\sum_{i=1}^n \Delta u_i^2} \quad \text{and} \quad I_+ = C_I A_{ol,\%} a_i^{e_1} I_0^{e_2} \left(\frac{x}{D_i}\right)^{e_3} \quad (13)$$

where I_0 is the ambient turbulence intensity referred to the free stream condition, C_I , e_1 , e_2 and e_3 are parameters to be determined experimentally, $A_{ol,\%}$ represents the ratio of overlapping area between the rotor diameter of a turbine and the wake area generated by upstream machines, D_i , a_i and I_0 represent respectively the rotor diameter, the Axial Induction Factor AIF and the incoming turbulence intensity

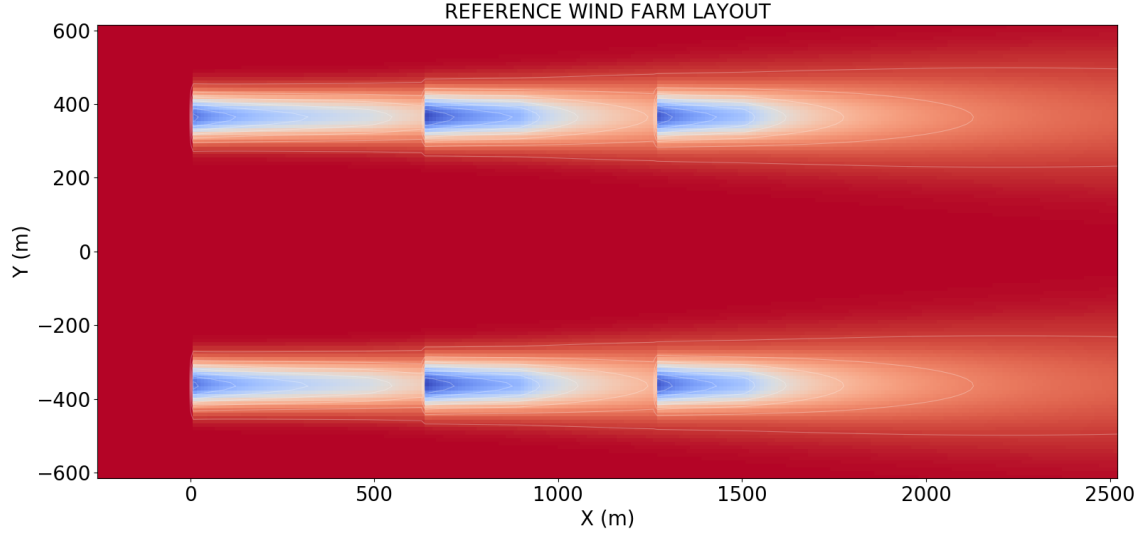


Figure 1: Wakes' superimposition in the layout used for this study, considering wind blowing from west direction (Image taken from NREL's Floris)

on the i -th considered machine. Also for the turbulence intensity I , due to the wake's superposition, a correction by Niayifar et al. [12] was implemented:

$$I = \sqrt{\sum_{i=1}^n I_{+,i}^2 + I_0^2} \quad (14)$$

2.4 Changes to the GWM and OpenFAST implementation

The GWM as presented makes reference to the original formulation of Basthankhah and Porté-Agel [1, 2]. Instead, the GWM used in this study has been changed to be implemented in OpenFAST (actually it is the C++ API of OpenFAST since it allows to run more turbine instances at the same time) [13] as an user-defined wind module written in Fortran in the file `IfW_UserWind.f90`.

The major change in this version is that both the C_T and AIF can be retrieved directly from OpenFAST as outputs of the AeroDyn module (performing the BEMT calculations on the aerodynamics of the turbine) of each simulated turbine composing the farm. We can treat OpenFAST as a black box that, given certain inputs is capable of output certain quantities like C_T and AIF, that are needed to run the GWM model. So, the analytical formulation in Eqn. (6) and all the mathematical steps deriving from it should be discarded when using OpenFAST; this means that Eqn. (7) has to be changed into:

$$\frac{u_R}{u_\infty} = 1 - a \quad \text{and} \quad \frac{\sigma_{z0}}{d} = \frac{1}{2} \sqrt{\frac{1 - a}{1 + \sqrt{1 - C_T}}} \quad (15)$$

while Eqn. (10) is changed into:

$$\theta = 0.6a\gamma \quad (16)$$

and finally Eqn. (12) is written as:

$$\frac{x_0}{d} = \frac{\cos \gamma \sqrt{(1 - a)(1 + \sqrt{1 - C_T})}}{4\alpha I + 2\beta(1 - \sqrt{1 - C_T})} \quad (17)$$

After applying these corrections to the GWM, the model is finally ready to be embedded in the OpenFAST framework.

The implemented function in `IfW_UserWind.f90` basically executes this task: given as input an array of positions near the rotor of each turbine (needed to solve the aerodynamics (BEMT) of the machine), the routine returns as output a matrix of values containing the wind speed in the three directions x , y and z for the selected positions.

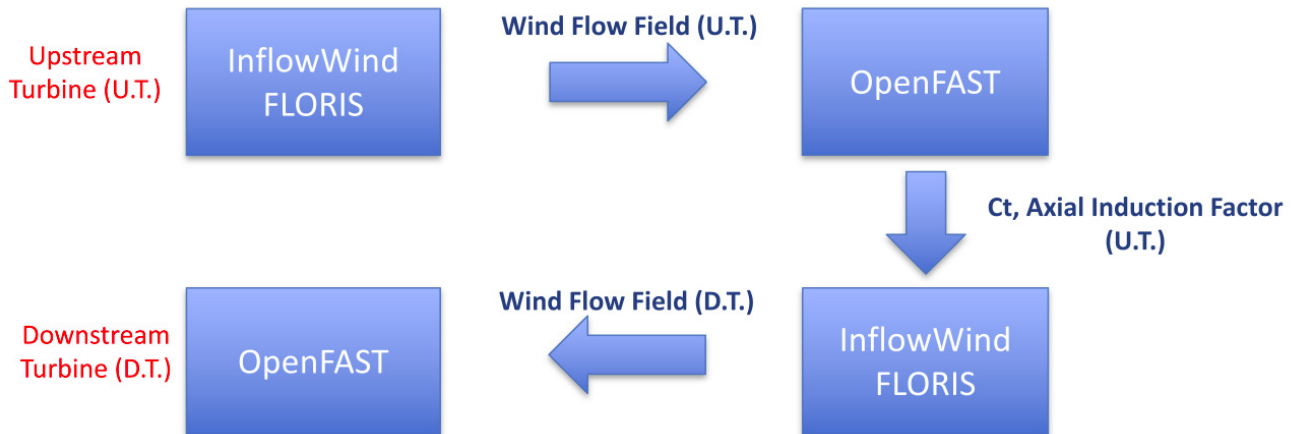


Figure 2: A schematic representation of how the GWM model is intended to work in the OpenFAST framework

In the main function, in addition to the GWM implementation, it was necessary to describe the free-stream wind acting on the first upstream turbine; to do so, the model chosen was the logarithmic profile of wind described in the EUROCODE [14].

In Fig. 2 a schematic representation of how the main routine is intended to work, when coupled with the OpenFAST framework, is presented.

For a generic time step, starting from the most upstream turbine, the wind routine evaluates the free-stream wind speed acting on it; then, the wind velocities are passed to the AeroDyn Module to solve the aerodynamics of the machine (using the BEMT model). After this passage, AeroDyn produces as output the $C_{T,i}$ value for the current turbine together with the AIF values at specific blades' section $a_{local,i}(r)$.

Then, once all the remaining calculations for the current OpenFAST instance (the current turbine) are over, the next instance of OpenFAST, simulating the first downstream turbine (or another upstream turbine depending on wind farm layout and wind direction) is called to perform all its tasks. Once again, the user-specified InflowWind routine evaluates the wind speed acting on the positions required by OpenFAST that, this time, are affected by a certain wake deficit defined accordingly to the model. To perform such task, the $C_{T,i-1}$ and AIF a_{i-1} averaged on the rotor plane of the upstream turbines are needed. As before, the obtained values will be passed to the AeroDyn Module of the current OpenFAST instance to obtain the $C_{T,i}$ and $a_{local,i}(r)$.

This procedure is carried out for every turbine in the farm at every time step of the simulation. The routine as written gives also the possibility to linearly interpolate the wind input parameters of the simulated wind farm (like the wind speed, direction, surface roughness, etc.).

3 Numerical Setup of GWM and OpenFAST

OpenFAST is a widely used open-source software for wind turbine simulation which was developed by the National Renewable Energy Laboratory (NREL). There are many modules that can be combined depending on what kind of simulation we want to perform. We can include the effects of aerodynamics, servo-dynamics, and elasto-dynamics. In this paper, the proposed Gaussian Wake Model is applied as inflow wind to improve the wind turbine control. Thus, two primary modules are utilised: inflow wind and wind farm layout.

For this study, the reference turbine model is the NREL 5MW. It is not an actual turbine but its characteristics make it suitable to support concept studies and model assessments. It has a diameter of $D = 126.0 \text{ m}$ and a hub height $z_h = 90.0 \text{ m}$.

3.1 Inflow Wind

In the inflow wind module, the user-defined input file is coded in Fortran language. The main reason for using this language is its quickness. Floris is another NREL developed open-source platform. It is applied to realise the GWM and pass the result to the OpenFAST.

Given a certain height z , the turbulence intensity and the wind speed are calculated with the following equations:

$$u_\infty(z) = V_b k_r \ln\left(\frac{z}{z_0}\right), \quad z_{min} \leq z \leq 200\text{m}/300\text{m} \quad (18)$$

$$u_\infty(z) = u_\infty(z_{min}), \quad z < z_{min} \quad (19)$$

$$k_r = 0.19 \left(\frac{z_0}{0.05}\right)^{0.07} \quad (20)$$

$$I_0 = \frac{1}{\ln\left(\frac{z}{z_0}\right)} \quad (21)$$

where z_0 is the surface roughness, V_b is the basic wind velocity, $z_{min} \in [1 - 10] \text{ m}$ is the minimum height at which the hypothesis of logarithmic profile is verified and k_r is the terrain factor.

Firstly, the free-stream wind is combined with GWM at the upstream wind turbine. There is an appropriate model for free-stream wind provided by the the EUROCODE [14]. The input parameters of the free-stream logarithmic profile are shown in Tab. 1:

Wind Magnitude Parameters		
V_b	[m/s]	5.85
z_0	[m]	0.005
z_{min}	[m]	10.0
k_r	-	0.1617
$u_\infty(z = z_h)$	[m/s]	9.2694
$u_\infty(z = z_{min})$	[m/s]	7.1900
$I_0(z = z_h)$	-	0.1020

Table 1: Wind Magnitude Input for the OpenFAST simulation

With the inflow kept constant we set the different wind directions to analyze the performance of the waked turbines. The initial parameters are shown in Tab. 2:

Wind Direction Parameters		
t_{end} [s]	$\theta_{w,start}$ [deg]	$\theta_{w,end}$ [deg]
50.0	270.0	270.0
100.0	300.0	300.0

Table 2: Wind Direction Input for the OpenFAST simulation

Finally, as previously explained, the Bastankhah and Porté-Agel [1, 2] GWM takes the parameters shown in Tab. 3:

3.2 Wind Farm Layout

The considered wind farm as a 3x2 layout. The initial wind direction is 270 degree, i.e. the wind comes from west. The positions of the 6 NREL 5MW turbines are shown in the Tab. 4, where the diameter of blades is $D = 126.0 \text{ m}$, and the hub height is $z_h = 90.0 \text{ m}$, as previously specified.

In this layout, when the wind direction is blowing from west, turbines in the second row are affected by the wake generated by the first row ones and the ones on the third row by a superposition of the wakes coming from first and second.

BPA-GWM Parameters	
k_a	0.200
k_b	0.003
α	0.48
β	0.077
C_I	0.8
e_1	0.73
e_2	0.1
e_3	-0.275

Table 3: Bastankhah and Porté-Agel [1, 2] GWM Parameters for the OpenFAST simulation

Wind Farm Layout			
	x [m]	y [m]	z [m]
T1	0	363.51	90
T2	630	363.51	90
T3	1260	363.51	90
T4	0	-363.51	90
T5	630	-363.51	90
T6	1260	-363.51	90

Table 4: Reference 3x2 Wind Farm geometric configuration

3.3 General Modules Setup

After setting the inflow and the layout we should set the modules accounting for the turbines dynamic response. The input file ElastoDyn contains the model for the structural behaviour of the machine. The rated angular speed of the turbine is set to $\dot{\theta}_r = 12.1 \text{ rpm}$. The wind speed considered in the simulations is lower than the rated one, $u_{\infty, \text{rated}} = 11.4 \text{ m/s}$. It takes a certain time, about 50.0 s, for a steady state model to get the equilibrium point.

ElastoDyn is also used to simulate the aerodynamics nearby the turbine. If we turn on the Yaw DOF, the wake steering can improve the performance of power generation. We have to take into account the fact that changing the yaw angle causes different the wind magnitude on the $x - axis$ direction.

The input file AeroDyn v15 is responsible for controlling the simulation. A classical BEMT model and the relative parameters are applied in this module. The maximum number iterations, $n_{it} = 10000$, activates convergence of the AIF and TIF in the simulation. In this input file, Glauert tip loss and hub loss correction are implemented. The unsteady Beddoes-Leishman model with the Minnema-Pierce variant is also used for blade aerodynamics.

4 Simulation and Result

4.1 Simulation With 270 Degree Wind Direction

Fig.3 shows the wind velocity at different rows. First, second and third row of turbines are represented by red line, yellow line, and blue line respectively. The first row sees the uniform free-stream wind at 9.4 m/s . On the second row, the yellow line, we see a sharp decrease (about 17%) as effect of the wake from the upstream row. A slight additional decrease (about 7%) is experienced by the third row, as shown by the blue line.

Torque and power of the turbines are shown in Fig.4 and Fig.5. Between the first row and last two rows, there is a obvious decrease on torque and power, consequence of the less energetic flow investing them. Specifically, torque and power generator have about 30% and 31% reduction respectively. Analogously to what happened for the wind speed in Fig.3, machines at second and third rows have closer outputs, about 5% decrease for both torque and power generation. This means that the wake from the closest upstream turbine takes primary effect in this wind farm layout.

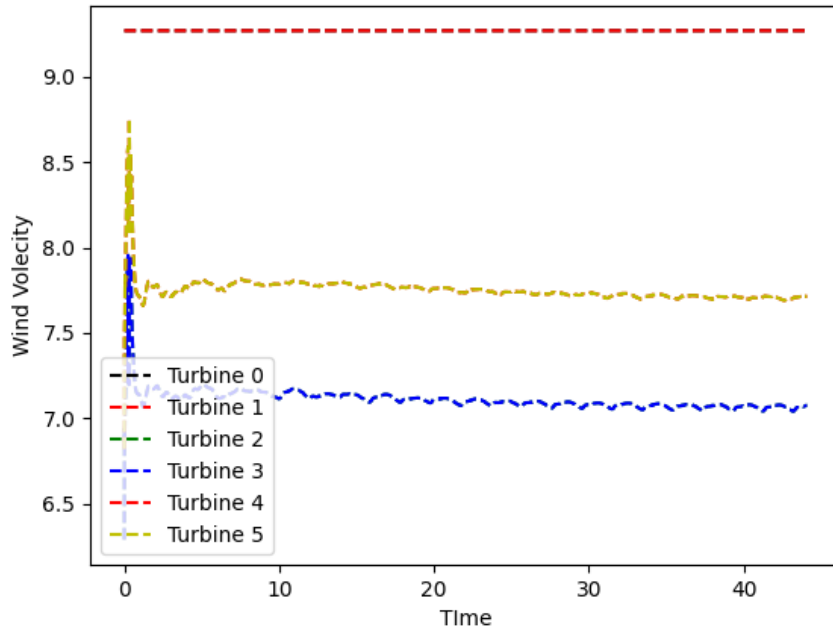


Figure 3: Wind velocity at different turbines against 270 degree wind direction

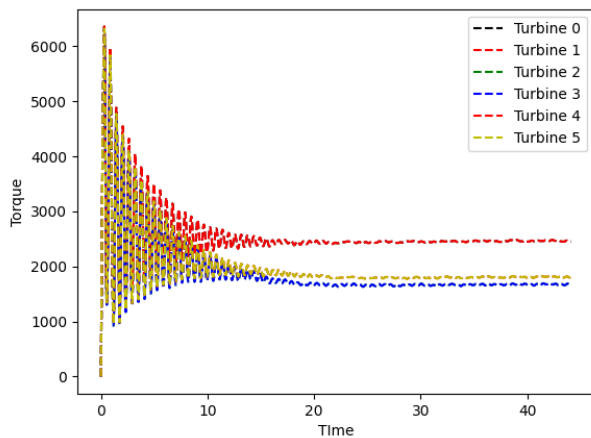


Figure 4: Torque of different turbines against 270 degree wind direction

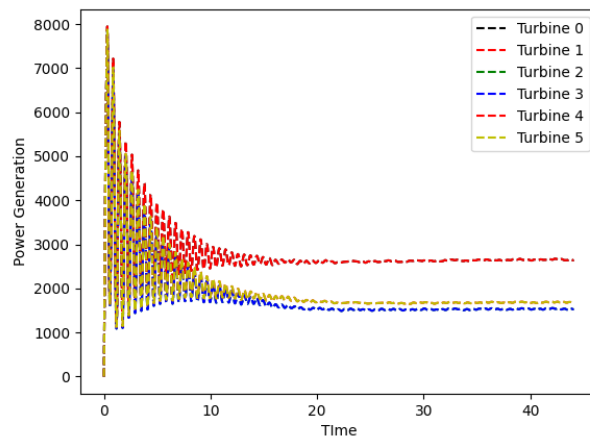


Figure 5: Power generation of different turbines against 270 degree wind direction

4.2 Simulation With 300 Degree Wind Direction

In this second simulation, the wind direction changes from 270 degrees to 300 degrees, i.e. there is a 30 degrees shift for each wind turbine. In this case, turbine 1 and turbine 6 align. With the proposed GWM, the diameter of the wake is too small to act on downstream turbines that do not align on the wind direction. Thus, only turbine 6 is affected by the wake from the turbine 1, other turbines are impacted by free-stream wind and their performances are not affected by waked conditions.

The incoming wind velocity on the different turbines is shown in Fig.6. Turbines 1 to 5 have same constant wind speed with the first row in Fig.3. Turbine 6 sees a lower velocity because of the influence of the wake. Because the high distance between the upstream turbine (1) and the downstream one (6),

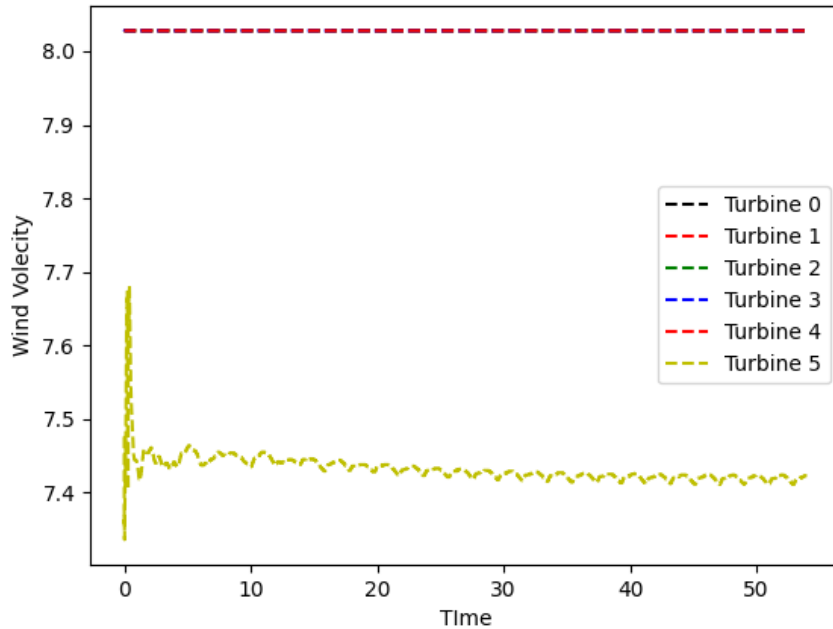


Figure 6: Wind velocity at different turbines against 300 degree wind direction

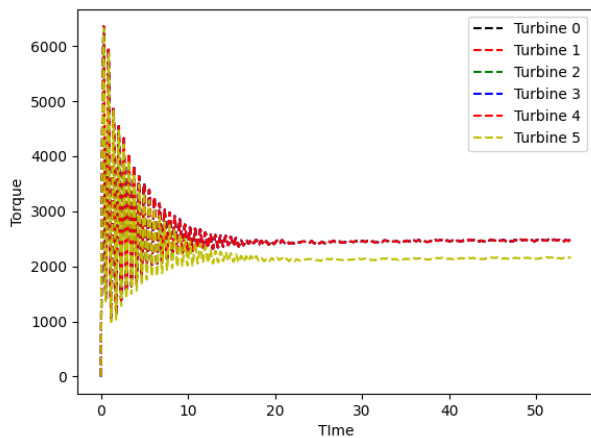


Figure 7: Torque of different turbines against 300 degree wind direction

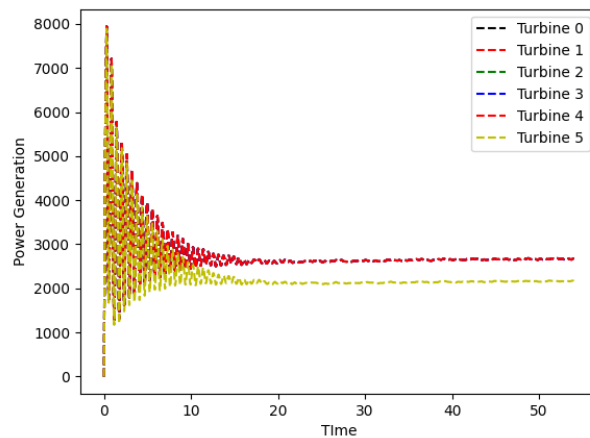


Figure 8: Power generation of different turbines against 300 degree wind direction

the influence of wake becomes smaller with respect to the previous simulation and wind speed decreases of 7% only.

Fig.7 and Fig.8 show the torque and power generation for this case. As expected, the outputs of downstream turbine are larger than those of the last two rows in the previous simulation. Turbine 6 has a 16% reduction on torque and a 17% reduction on power generation. Comparing the result in these two simulation, again, the distance between upstream turbine and downstream turbine appears to play a critical role.

5 Conclusion and Future Work

In this paper, the GWM originally proposed by Bastankhah and Porté-Agel [1, 2] has been changed in order to be coupled to OpenFAST. To accomplish this task, a user defined InflowWind routine has been written in Fortran language. To test the new wind model, a simulation was performed using a 3x2 layout in two different wind configurations. The first, with the wind blowing from 270° and the second with the wind blowing from 300°. From these simulations, it is possible to see that the model is working as expected (lower wind speed on downstream turbines and, when the wind is rotated of 30° from the west direction, the wake generated by the Turbine 1 is covering the rotor of Turbine 6).

The newly proposed tool (OpenFAST coupled to the GWM) is a refinement of NREL's FLORIS, since now the AIF and C_T of the various turbines are obtained from an aero-elastic code (able to evaluate AIF and C_T on the whole rotor) and no more from a $C_T - TSR$ table. However, further improvements can be made to this software; among them, the most important are a wake transport model (that could be implemented to have a more realistic simulation) and a more detailed turbulence model. Adding these two model to the tool, would lead to the creation of a more complete software that could be used for real-time control (or for estimation purposes) of wind farms.

For what regards future work, the coupling between the GWM and OpenFAST offers many new research opportunities.

Of course, since the tool is new, much more simulations with different wind farm layouts and wind input parameters can and will be performed. Moreover, it could be possible to use the tool to investigate different layout configurations for new wind farm sites in order to reduce the rental cost for the owner while maximizing the power extraction from the machines. Another possibility, instead, could be to use it on already existing wind farms to perform studies on power maximization (i.e.: finding the optimal yaw angle set-points of the farm using the wake steering method), load minimization or multi-objective optimization in general (i.e.: combining load minimization and power maximization).

Acknowledgements

Thanks to NREL for all the open-source softwares employed in this work.

Fundings

This project has received funding from the European Union's Horizon 2020 research and innovation programme under the Marie Skłodowska-Curie grant agreement No. 858358 (LIKE – Lidar Knowledge Europe).

References

- [1] Bastankhah M and Porté-Agel F 2016 *Journal of Fluid Mechanics* **806** 506–541
- [2] Bastankhah M and Porté-Agel F 2014 *Renewable Energy* **70** 116 – 123 ISSN 0960-1481 URL <http://www.sciencedirect.com/science/article/pii/S0960148114000317>
- [3] van Dijk M T, van Wingerden J W, Ashuri T and Li Y 2017 *Energy* **121** 561 – 569 ISSN 0360-5442 URL <http://www.sciencedirect.com/science/article/pii/S0360544217300518>
- [4] Bay C, King J, Fleming P, Mudafort R and Martínez Tossas L 2019 *Wind Energy Science Discussions* 1–20
- [5] Gebraad P, Fleming P, Wright A, Dykes K and van Wingerden J W 2015 *Multidisciplinary Research on Wake Control in Wind Power Plants at NREL*
- [6] Bossanyi E 2018 *Journal of Physics: Conference Series* **1037** 032011
- [7] Jenkins N, Burton A, Sharpe D and Bossanyi E 2001 *Wind Energy Handbook* (John Wiley & Sons Ltd) ISBN 0-4714-8997-2

- [8] Lee J H and Chu V 2012 *Turbulent Jets and Plumes* (Springer US) ISBN 978-1-4020-7520-9
- [9] NREL 2020 Floris. version 2.2.0 URL <https://github.com/NREL/floris>
- [10] Katic I, Højstrup J and Jensen N 1987 *EWEC'86. Proceedings. Vol. 1* ed Palz W and Sesto E (A. Raguzzi) pp 407–410
- [11] Crespo A and Hernandez J 1996 *Journal of Wind Engineering and Industrial Aerodynamics* **61** 71 – 85 ISSN 0167-6105 URL <http://www.sciencedirect.com/science/article/pii/016761059500033X>
- [12] Niayifar A and Porté-Agel F 2015 *Journal of Physics: Conference Series* **625** 012039 URL <https://doi.org/10.1088%2F1742-6596%2F625%2F1%2F012039>
- [13] NREL 2020 Openfast URL <https://github.com/OpenFAST/openfast>
- [14] 2005 Eurocode 1: Actions on structures - part 1-4: General actions - wind actions Standard European Committee for Standardization Bruxelles, BE

Lifetime Fatigue Damage Estimation From Numerical Models and Validation With Experimental Data

F Pimenta^a, J Pacheco^a, M Bereznyak^a, and F Magalhães^a

^aCONSTRUCT-ViBest, Faculty of Engineering of the University of Porto

E-mail: ec09176@fe.up.pt

Keywords: Structural analysis, Numerical modelling, Lifetime fatigue damage

1 Introduction

The numerical model developed, presented and validated in [1] provided accurate predictions on the modelled VESTAS V100 wind turbine dynamic response. However, being able to correctly estimate fatigue damage and evaluate in real time the remaining fatigue lifetime is crucial to better operator any wind turbine.

To provide accurate fatigue damage estimations for the design lifetime of any wind turbine, 2 major aspects must be taken into consideration. On one hand, the fatigue damage for different operating conditions must be properly computed. On the other hand, the prevalence of every wind conditions over the design period must be estimated. In this work, only the first issue will addressed and the predictions of the numerical model are tested against real experimental data.

2 Method and Results

To evaluate the accuracy of the model's prediction, firstly a reference value must be obtained from the experimental bending moments data described in detail in [2]. Knowing the geometrical properties of the instrumented section, the stress history was obtained and the fatigue damage was computed from Eurocode S-N curves for a type 80 detail presented in Figure 1 for every recorded time series. The experimental data was then divided in bins according to the recorded mean wind speed and turbulence intensity and a representative damage computed for each from the average of all time series within the bin, as represented in Figure 1.

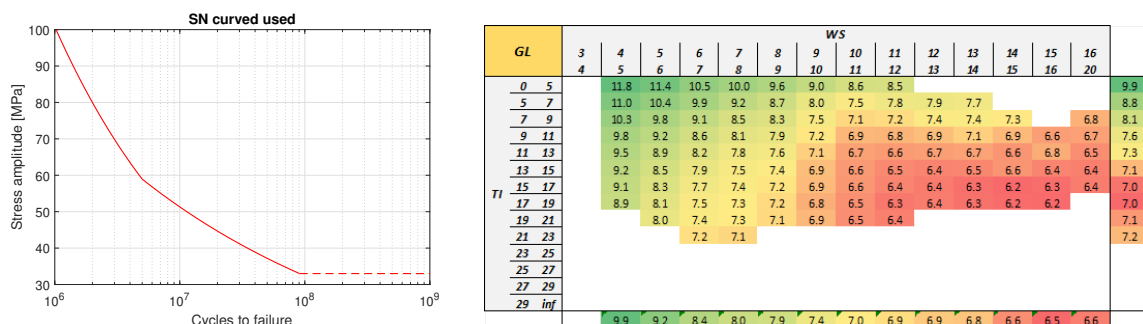


Figure 1: Eurocode 80 MPa detail fatigue curve used (on the left) and the symmetric value of the logarithm of the mean fatigue damage (on the right).

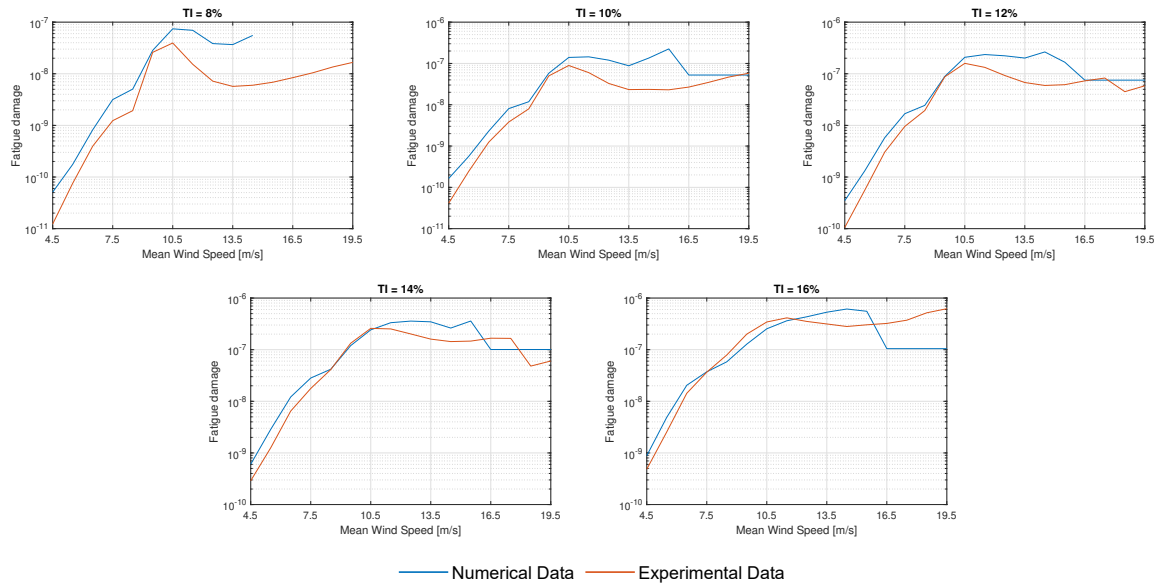


Figure 2: Comparison of simulated and experimental fatigue estimations for different mean wind speeds and turbulence intensities.

In parallel, 100 simulations for the corresponding mean wind speeds and turbulence intensities were computed with FAST model described in [1]. Having the numerical bending moments time series generated, the numerical fatigue damage estimations were computed in the same way as the experimental values.

The obtained fatigue evolution with the wind speed for all the tested turbulence intensities can be found in Figure 2, where the results for both experimental and numerical data are plotted together for each TI and good agreement is found for most mean wind speeds and turbulence intensities.

3 Conclusions

From the presented results, the model appears to be able to correctly estimate the fatigue damage for the modelled wind turbine. In future works, this model may be used to estimate the lifetime fatigue damage under design conditions.

Acknowledgements

The support of EDP Renewables and VESTAS is greatly acknowledged. This work was financially supported by: PhD Grant SFRH/BD/138980/2018, Base Funding UIDB/04708/2020 of the CONSTRUCT-Instituto de I&D em Estruturas e Construções and the project PTDC/ECI-EST/29558/2017, funded by national funds through the FCT/MCTES (PIDDAC).

References

- [1] Pimenta F, Pacheco J, Branco C M, Teixeira C M and Magalhães F 2020 *Journal of Physics: Conference Series* **1618** 022065 URL <https://doi.org/10.1088/1742-6596/1618/2/022065>
- [2] Magalhães F, Pacheco J, Moutinho C, Guimarães S, Noites L, Cunha A, Marques M and Carlos Matos J 2019 *8th IOMAC - International Operational Modal Analysis Conference, Proceedings* ed Sdr K E P A M R pp 737–747

Analysis of the validation of an EMT model of a WTG based on instantaneous electrical signals

A.J Pujante-López^{a,b}, F. Jiménez-Buendía^a, A. Honrubia-Escribano^b, E. Gómez-Lázaro^b,

^a Siemens Gamesa Renewable Energy (SGRE), S.A., 31621 Pamplona, Spain

^b Renewable Energy Research Institute, ETSII-AB UCLM, 02071 Albacete, Spain;

E-mail: Antonio.Pujante@siemensgamesa.com

Keywords: EMT simulation, Validation criteria, Voltage dip, WPP requirements, WT modelling

1 Introduction

Nowadays, most of the Transmission System Operators (TSOs), such as ONS (Brazil, [1]) and UTE (Uruguay, [2]), etc., request to the project owner of each Wind Power Plant (WPP) a simplified Wind Turbine Generator (WTG) model, known as RMS model. In addition, some TSOs also request a more detailed WTG model, known as EMT model. These RMS and EMT models are used to accomplish typical and specific electrical studies at the Point of Common Coupling (PCC) of the WPP. These studies, comprising the WTG steady and transient states, are needed to ensure the stability and reliability of the WPP into the electrical system [3]. The following studies are applied to EMT models:

- Analysis of balanced and unbalanced short circuits in the electrical system.
- Analysis of transformer or connection line energizations.
- Analysis of Transient Recovery Voltages (TRV) in switches.

Usually, such WT models must be validated against field data. The RMS models are validated according to well-known criteria from the IEC international Standards [4]-[6]. The EMT models could be validated as the RMS models, because there are no international Standards for validating the EMT models. Most of the TSOs admit the RMS and EMT models validated as RMS ones. However, some TSOs, such as UTE (Uruguay, [2]), only accept the EMT model validated according to other criteria (referred as visual approach in this paper) more focused on the proper fitting of instantaneous electrical responses.

This paper attempts to emphasize the extended complexity of such visual approach for the EMT model validation and the need to release at least one international Standard focused on EMT models similar to the Standards for validating the RMS models. Meanwhile, to obtain the EMT model acceptance from this visual approach, it is needed to improve the detail level of the WTG modelling and the electrical network.

In this paper, the WTG user model (see Fig. 1a) and the network (see Fig. 1b) implemented in ATP/ATPDraw for validation purposes, has been developed with the required detail level in order to fulfill the additional requirement of matching the instantaneous response of the WTG.

The test considered for this validation is a three-phase voltage dip at full load operation of the WTG. The graphical results from simulation and test are compared (see Fig. 2) for both RMS variables (voltage, active / reactive powers) and instantaneous signals (voltage and current). Then, it is included a summary of main comments for each variable of the test performed at MV side:

- Pre-fault: No comments for the RMS variables of powers, voltage and current (P & Q, V & I).
- Fault: Very similar trend with a small difference at the first transient zone (P & Q, V).
- Post-fault: Very similar trend with a very small difference after the recovery (P & Q).

Finally, the validation results are satisfactory as shown in the graphical responses (see Fig. 2) of the WTG during the considered test.

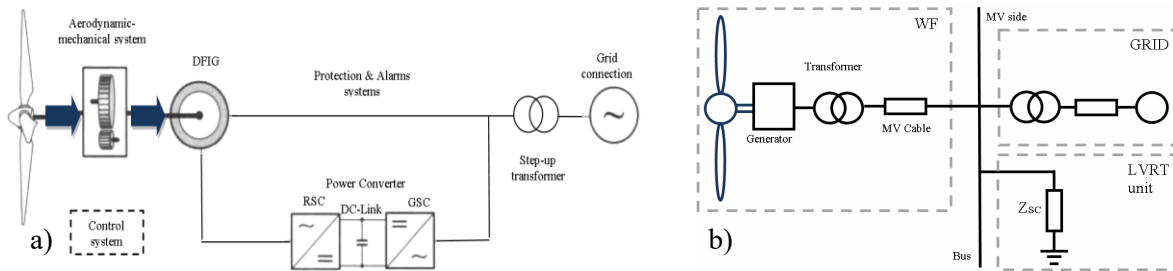


Figure 1 a) Configuration of a Type 3 WT generator; b) Simplified schematic of the electrical circuit.

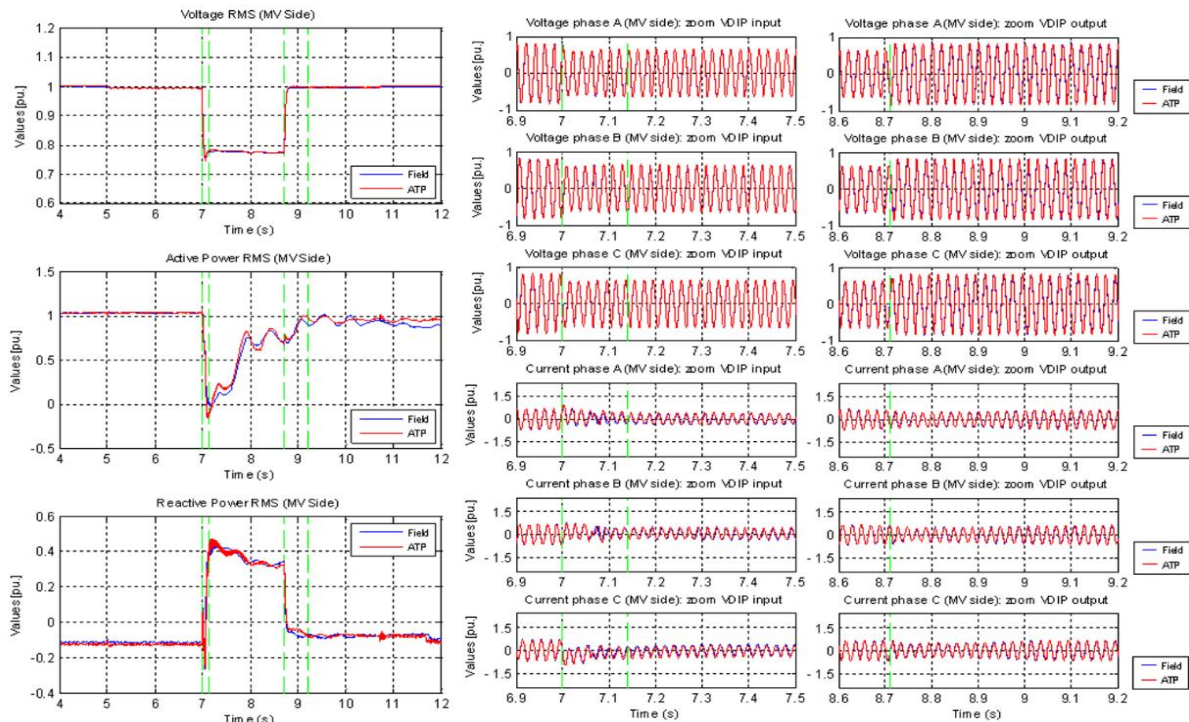


Figure 2 Results. RMS: Voltage, Active/Reactive powers; Instantaneous 3-phase voltage and current.

Acknowledgements

The authors would also like to express their gratitude to the WT manufacturer Siemens Gamesa Renewable Energy for the technical support received. This research was partially funded by the Council of Communities of Castilla-La Mancha and the E.U. FEDER (SBPLY/19/180501/000287).

Bibliography

- [1] ONS. “Requisitos básicos para modelagem e simulação de parques eólicos no programa ATP”. **2015**.
- [2] UTE. “Requerimientos asociados al modelo electromagnético de parques eólicos a ser conectados en la red de UTE”. **2017**.
- [3] Villena-Ruiz, R; Requirements for Validation of Dynamic Wind Turbine Models: An International Grid Code Review. *Electronics* **2020**, *9*, 1707.
- [4] IEC61400-27-1 Wind energy generation systems - Part 27-1. **2020**.
- [5] FGW TR4-9 Ed. **2019**.
- [6] IEC61400-27-2 Wind energy generation systems - Part 27-2. **2020**.

FOUNDATION & GEOTECHNICS

Probabilistic assessment of the critical buckling resistance for bucket foundations

M Böhm^a and P Schaumann^a

^aInstitute for Steel Construction, Leibniz University Hannover/ ForWind

E-mail: boehm@stahl.uni-hannover.de

Keywords: offshore wind, foundations, suction bucket, buckling, geometric imperfections

1 Introduction

Suction buckets are large cylindrical shell structures used as foundation for offshore wind turbines. Due to the low noise emission during installation as well as the possibility of removal from the seabed, they are considered as a promising environmentally friendly alternative to the common pile foundations of offshore wind turbines. They are embedded in the seabed using a pressure difference (suction) between the inside and the outside of the skirt. This pressure difference leads to a high risk of buckling during installation.

The aim of this work is to reduce uncertainties in the determination of the critical buckling load. A substantial part of the disagreement between theoretically and experimentally determined buckling resistance of cylindrical shells is due to geometric imperfections. In civil engineering, it is common to introduce imperfections based on the linear buckling modes. However, previous work on suction buckets revealed that it is not possible to identify the “worst” imperfection shape based on only one linear buckling mode [1, 2]. On the contrary, measured imperfections are dissimilar to linear buckling modes and it is likely that at least the superposition of several imperfection shapes and amplitudes has to be considered. Promising approaches include the representation of imperfections with homogeneous random fields [3] or as Fourier series where the Fourier coefficients of are treated as random variables [4].

2 Current Work

Due to the random nature of the imperfections, an extensive probabilistic study is planned within this project. Hence, a robust and reliable finite element (FE) model which can be automatized for sensitivity analysis and Monte Carlo simulation is designed. The bucket is modelled with geometric nonlinear quadrilateral shell elements and using the material properties of structural steel S355. Geometric imperfections are modelled as nodal deviation in the out-of-plane direction. The soil is modelled using brick elements, employing the material properties of dense sand with a Mohr-Coloumb model as shown in Figure 1. The nonlinear post-buckling problem is solved using an arc-length static analysis. Further, an abortion criterion for the FE-simulation needs to be formulated, which avoids branch switching if the solver encounters an equilibrium state in the post-buckling path. The numerical model will be validated with large-scale experimental tests. After successful validation, the complexity of the numerical model is gradually reduced to allow for efficient simulation while maintaining essential mechanical properties.

3 Outlook

The generation of the numerical model is automatized to assess a sensitivity analysis of geotechnical and structural parameters and conduct a probabilistic analysis of the critical buckling load considering stochastic imperfection patterns.

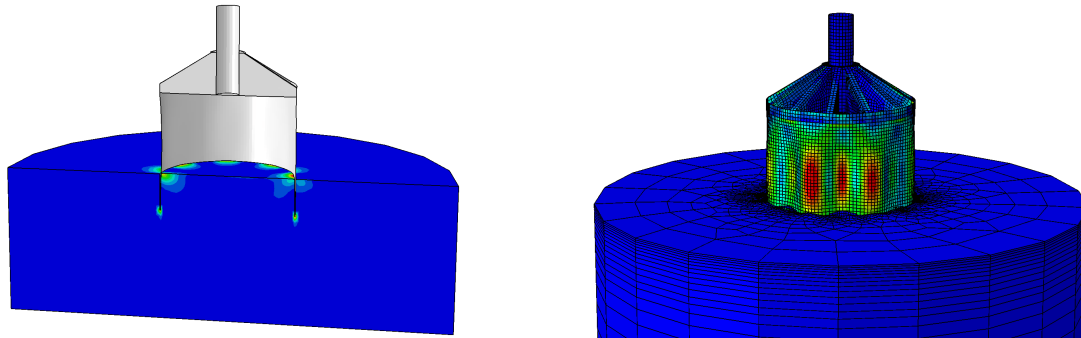


Figure 1: Numerical model, exhibiting plasticity in the soil (left panel) and structural stress in the perfect shell after reaching the critical buckling pressure (right panel).

The influence of the geotechnical and structural parameters on the critical buckling pressure are quantified by a sensitivity analysis. Material parameters like Young's modulus, angle of internal friction and cohesion are examined. For this purpose, a suitable sampling strategy (e.g. Latin Hypercube or importance sampling) has to be elaborated to obtain a sufficient significance level. Further, the sensitivity of these parameters on the critical embedment depth, at which buckling is most likely to occur, is evaluated. In the following studies, only the most important input variables are assumed as statistically distributed.

Due to the non-linearity of the problem, the probabilistic analysis will be carried out by applying Monte Carlo simulations (MC), and, if applicable, enhanced MC, multilevel MC and multi-index MC or an efficient sampling technique, e.g. hierarchical sequences. Further, the applicability of other stochastic methods such as response surfaces, perturbation methods and meta-models is also examined. Measured data from the physical experiments and data obtained by other researchers will be evaluated to find an adequate representation of the initial stochastic imperfection patterns of large steel shell structures and to infer the statistical properties needed for their description.

The probabilistic study will help understanding the main influences on the stability of suction buckets and minimize the uncertainties in the assessment of structural integrity regarding the installation procedure. This work will thus contribute to optimizing the design and minimizing the costs of bucket foundations. A further target of the project is to advance existing practice-oriented verification methods regarding the buckling of suction buckets and to provide recommendations for suitable imperfection patterns.

Acknowledgements

The work presented in this contribution was carried out within the joint project ProBucket. The authors kindly acknowledge the financial support provided by the German Federal Ministry of Economics and Technology (FKZ 03EE3033B). The technical support provided by the project partners is also gratefully acknowledged.

References

- [1] Madsen S, Andersen L and Ibsen L 2013 *Engineering Structures* **57** 443–452 ISSN 0141-0296
- [2] Gottschalk M 2017 *Zur Beultragfähigkeit von Suction Buckets* Doctoral thesis Leibniz University Hannover
- [3] Schenk C and Schuller G 2003 *International Journal of Non-Linear Mechanics* **38** 1119 – 1132 ISSN 0020-7462
- [4] Elishakoff I and Arbocz J 1982 *International Journal of Solids and Structures* **18** 563 – 585 ISSN 0020-7683

Building an Updatable Integrated Model of an Offshore Wind Turbine with a Reduced Soil-Model Using the Open-Source FEM Software OpenSees

Javad Fattahi^{a,b}, Bruno Stuyts^{a,b,c}, Carlos Sastre Jurado^{a,b}, Wout Weijtjens^{a,b},
and Christof Devriendt^{a,b}

^a Offshore Wind Infrastructure (OWI-Lab)

^b Vrije Universiteit Brussel (VUB)

^c Ghent University

E-mail: seyed.javad.fattahi@vub.be

Keywords: Offshore Wind Turbine, Monopile Foundation, Numerical Modeling, Model Updating, Dynamic Analysis

1 Introduction

The growing demand for renewable energy has led to a substantial increase in the construction of offshore wind turbines (OWT). It can be expected the rising trend continues because the European Union predicts to generate about 100 GW of electricity from OWTs by 2030 [1]. Conventional fixed foundations found for OWTs are monopiles, gravity-based, jackets and suction caissons of these the monopile is still most widely used [2].

On the other hand, the design of recent monopile foundations is driven by the interaction between structural dynamics and the loads (e.g., wave-loading); hence, fatigue plays a vital role in designing OWTs. Therefore, the inability to accurately predict real-world dynamics from soil investigations leads to an erroneous estimation of consumed fatigue life and, consequently, a sub-optimal design and higher cost of the monopile foundation [3].

In essence, any little improvement in the output of the current finite element model of OWTs provides a potential way to reduce offshore wind energy costs. Today we see an industry-wide mismatch between design expectations and the as-built dynamics of OWTs installed on monopile foundations, in particular an underestimation of the first resonance frequency. The likely cause is that monopiles for OWTs are relatively short and large diameter piles, length-to-diameter ratios (L/D) less than 12 and diameters between 3.5 and 7 m, subjected to strong cyclic lateral loading. The industry has ventured outside the geotechnical design codes for offshore Oil and Gas [4],[5]. Because traditionally, the p-y curve method, which is employed for analyzing pile deflections, was developed for small-diameter long (with generally $L/D > 12$). Also, in this method, the load rate's effect was not considered [6].

2 Objective

The OWI-Lab Soilwin project's objective is to improve the fatigue design of offshore monopiles through better modelling the soil-pile interaction. The project aims to update these models based on in-situ measurements over an entire fleet of OWTs on monopile foundations. Therefore, the

project aims to create an updatable ‘digital twin’ FE model for each OWT within the offshore windfarm. Consequently, a novel fleet-wide model updating strategy will be developed.

3 Methodology

The finite element model updating technique could facilitate the correction of invalid initial conditions/parameters, which are inevitably assumed during the creation of a numerical model due to parameterized soil-structure systems [7]. Additionally, the reduced soil-model will be compared with a commercial package, both calibrated and validated against a unique dataset of monitoring data, which includes both geotechnical and structural measurements.

A model in the loop monitoring scheme (Figure 1) is obtained, in which abstract monitoring data such as a resonance frequency is translated into actionable data, e.g., a scour depth or confirm the passing of a sand-dune, which is a local phenomenon that affects adjacent turbines.

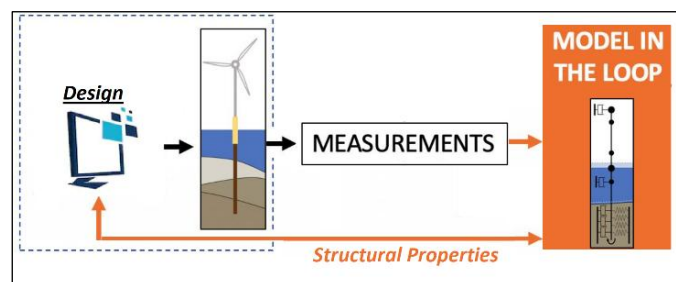


Figure 1 Schematic representation of the model in the loop

The results of this approach can also be served to quantify the stiffness of the soil. Through the obtained soil stiffness, a comparison can be made with design. Simultaneously the model will quantify the variation in soil conditions and assess the severity in the frame of system health monitoring.

Bibliography

- [1] E. P. P. Soares-Ramos, L. de Oliveira-Assis, R. Sarrias-Mena, and L. M. Fernández-Ramírez, “Current status and future trends of offshore wind power in Europe,” *Energy*, vol. 202, p. 117787, 2020, doi: 10.1016/j.energy.2020.117787.
- [2] Y. Xu *et al.*, “Support condition monitoring of offshore wind turbines using model updating techniques,” *Structural Health Monitoring*, vol. 19, no. 4, pp. 1017–1031, 2020, doi: 10.1177/1475921719875628.
- [3] D. Kallehave, C. L. Thilsted, and A. Troya, “Observed variations of monopile foundation stiffness,” in *Frontiers in Offshore Geotechnics III: Proceedings of the 3rd International Symposium on Frontiers in Offshore Geotechnics (ISFOG 2015)*, 2015, vol. 1, pp. 717–722.
- [4] L. C. Reese, W. R. Cox, and F. D. Koop, “Analysis of laterally loaded piles in sand,” *Offshore technology in civil engineering hall of fame papers from the early years*, pp. 95–105, 1974.
- [5] P. Doherty and K. Gavin, “Laterally loaded monopile design for offshore wind farms,” *Proceedings of the Institution of Civil Engineers-Energy*, vol. 165, no. 1, pp. 7–17, 2012.
- [6] M. Bayat, L. v. Andersen, and L. B. Ibsen, “P-Y-Y Curves for Dynamic Analysis of Offshore Wind Turbine Monopile Foundations,” *Soil Dynamics and Earthquake Engineering*, vol. 90, pp. 38–51, 2016, doi: 10.1016/j.soildyn.2016.08.015.
- [7] M. Bruns, B. Hofmeister, D. Pache, and R. Rolfes, “Finite Element Model Updating of a Wind Turbine Blade—A Comparative Study,” *EngOpt 2018 Proceedings of the 6th International Conference on Engineering Optimization*, pp. 569–580, 2019, doi: 10.1007/978-3-319-97773-7_51.

Monitoring and advanced numerical modeling to evaluate the behavior of onshore wind turbine foundations

Mário Sobrinho^a, Mário Pimentel^a, Filipe Magalhães^a

^a CONSTRUCT, Faculty of Engineering (FEUP), University of Porto, Portugal

mario.sobrinho@fe.up.pt

Keywords: Wind turbine, Foundation, Non-linear finite element analysis, Monitoring

1 Introduction

Onshore wind turbine foundations are generally in reinforced concrete and most of the designs rely on linear elastic analyses, neglecting the effect of material non-linear behavior. Non-linear finite element analysis can be a powerful tool to optimize the solutions, reducing costs and CO₂ emissions. An appropriate monitoring campaign can deliver critical information on the real behavior of the foundation and wind turbine, providing the data for calibration of accurate structural models.

At the same time, many wind farms are reaching the end of design lifetime. The life extension requires the risk assessment for major components of wind turbines. In the specific case of foundations, the most used solution to connect the tower to the foundation, proved to be problematic, being commonly observed relative movements of the tower against the foundation [1][2]. Those movements can be explained by the development of gaps in the connection. Those gaps induce a non-linear behavior in the rotational stiffness at the tower base that has impacts on other structural elements, that are still not fully understood. Currently, maintenance operations are costly and decided on a case-by-case basis, in a process where wind farm owners do not have the technical information to decide wisely.

2 Objectives

The present research is focused on the investigation of the behavior of onshore wind turbine foundations under operational load conditions and extreme load events. For that, a monitoring system was designed and implemented to evaluate the behavior of wind turbine and foundation during operation and advanced non-linear models are being developed to interpret the experimental data.

In parallel, it will be analyzed the behavior of an existing wind turbine with relative movements between the steel tower and the concrete foundation. The results from the monitoring system developed to capture this behavior will be compared with the outputs of advanced non-linear models developed for this purpose. The present PhD is a initial phase of development.

3 Numerical models under development

Two foundations were modeled considering two different types of connection between the steel tower and the concrete foundation: one resorts to an anchor-cage constituted by post-tensioned vertical bolts fixing the flange of the steel tower to the flange embedded in the concrete footing (Figure 1 (a)); in the other, the steel tower is directly embedded in the concrete footing (Figure 1 (b)). The “anchor-cage” solution is prestressed (active) and the bolts can be re-stressed at any time during their lifetime. The flow of forces is clear, and this type of foundation has shown good behavior. On the other hand, the solution with embedded tower relies on a more complex stress path inside the concrete mass and the stresses can only develop upon deformation of the steel and surrounding concrete (passive solution).

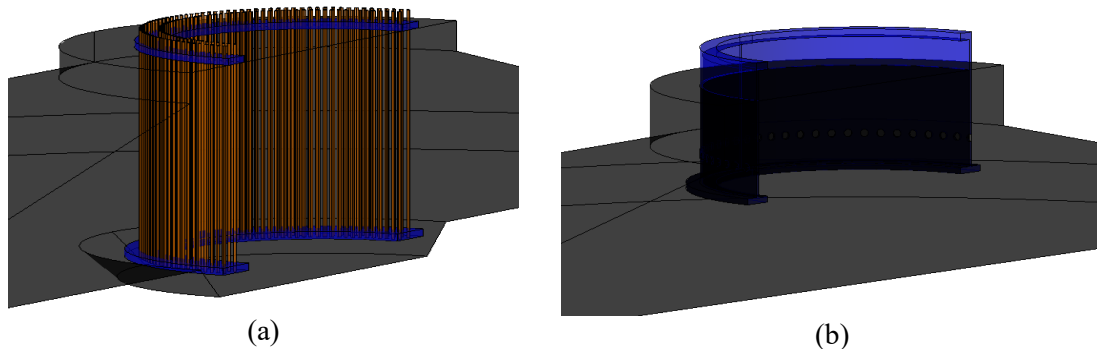


Figure 1 (a) foundation with the “anchor cage” solution; (b) foundation with the tower embedded in the concrete

Wind turbine foundations were modeled using non-linear three-dimensional numerical models that includes: (1) the effects of soil nonlinearity under cyclic loading [3]; (2) the effect of the nonlinearity of reinforced concrete using total strain crack models [4]; (3) the nonlinearity of the interface tower/slab foundation.

4 Monitoring system under installation

A monitoring system was designed and is being implemented to evaluate the behavior of the wind turbine and foundation, during operation. Six pressure cells were placed below the slab foundation, in contact with the rock mass, and four load cells were placed in the anchor bolts. Two cross-sections of the steel tower were equipped with four strain gauges each, allowing the calculation of the bending moment and shear force at the base of the tower. The system also includes four accelerometers for continuous monitoring of the natural frequencies and one clinometer at the top surface of foundation. All the monitoring devices are connected to a central acquisition unit and the system is expected to operate continuously during a minimum period of 1 year. The monitored data is to be compared with the results obtained with a detailed 3D non-linear finite element model of the foundation.



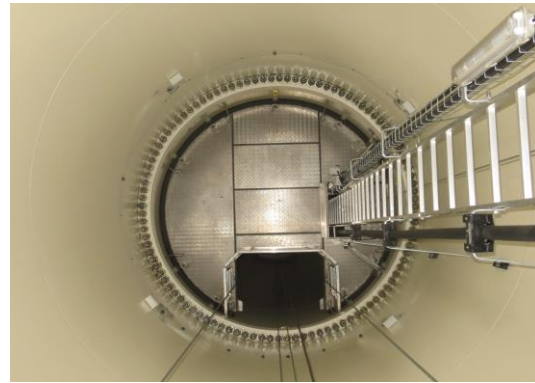
(a)



(b)



(c)



(d)

Figure 2 (a) Pressure cells installed in the foundation bottom surface. (b) Load cell installed in the anchor bolts. (c) Accelerometer installed in the steel tower. (d) Strain gauges installed in the steel tower

5 Future work

Numerical models will be validated using the monitoring results. These models will serve to: (1) quantify the stresses induced in the slab/foundation elements; (2) evaluate the soil properties beneath the foundation due to cyclic loading effects; (3) quantify the rotational stiffness of the foundation according to the bending moment applied, including effects resulting from the existence of gaps between the steel tower and concrete foundation; (4) evaluation of simplified strategies for modeling the structural behavior of the slab foundation and design methods systematization; (5) assessment of acceptable effort redistribution that may lead to optimized solutions.

Acknowledgments

This work was also financially supported by: PhD Grant 2020.06563.BD, UID/ECI/04708/2019-CONSTRUCT - Instituto de I&D em Estruturas e Construções and the project PTDC/ECIEST/29558/2017, all funded by national funds through the FCT/MCTES (PIDDAC)

The authors would also like to thank EDPR for the financial support for the monitoring campaign and, in particular Eng. Diogo Silva from EDPR that made the monitoring campaign possible.

Bibliography

- [1] He, M.; Bai, X.; Ma, R.; Huang, D.; Liu, H. (2018). “Field experimental study on the retrofit of cracked onshore wind turbine foundations using externally prestressed anchor bolts”, *Structural Concrete*, Vol. 19, pp.864-875.
- [2] Chen, J.; Xu, Y.; Li, J. (2020). “Numerical Investigation of the Strengthening Method by Circumferential Prestressing to Improve the Fatigue Life of Embedded-Ring Concrete Foundation for Onshore Wind Turbine Tower”, *Energies*, Vol. 13, No. 3, 533 doi: <https://doi.org/10.3390/en13030533>.
- [3] Schanz, T.; Vermeer, P.A.; Bonnier, P. G. (1999). “The hardening soil model: Formulation and verification”, *Beyond 2000 in Computational Geotechnics*, Rotterdam, Balkema, ISBN 90 5809 040 X.
- [4] De Borst, R.; Crisfield, M. A.; Remmers, J. J. C.; Verhoosel, C. V. (2012). *Non-linear Finite Element Analysis of Solids and Structures (2nd Edition)*, ISBN 978-0-470-66644-9, Wiley.

NEW CONCEPTS

Airborne Wind Energy: UPWIND Project

Manuel C.R.M. Fernandes^a, Luís Tiago Paiva^a, and Fernando A.C.C. Fontes^a

^aSystemec - ISR, Faculdade de Engenharia, Universidade do Porto

E-mail: mcrmf@fe.up.pt

Keywords: Airborne Wind Energy, Optimisation, Control

1 Introduction

Wind is one of the most promising Renewable Energy Sources being currently exploited, however, most of its productive potential lies at high altitudes where it is stronger and more consistent, not being affected by surface roughness. Conventional wind energy conversion systems are limited to a certain altitude due to physical, economical and logistical reasons, since to reach these altitudes there is the need for an increasing amount of resources and structure dimension, leaving unexplored these altitudes with high production potential.

In order to reach higher altitudes, several different concepts of Airborne Wind Energy Systems (AWES) are being developed. AWES are characterized by a light structure, being, therefore, resource-efficient and able to operate at large altitudes. Among the different AWES concepts (lighter-than-air systems, rotary kite systems, etc.), the ones that are demonstrating to be the most promising are Kite Power Systems. These are based on tethered kites, with flexible or rigid wings, that can be generally divided into Ground Generation Systems or On-board Generation Systems, depending on where the conversion from mechanical to electrical energy takes place, respectively on a generator placed on the ground or on board of the aircraft [1].

This area of research holds several open questions, some regarding challenging optimisation and control issues. In order to respond to these problems, the University of Porto has been working on the project UPWIND in the area of AWES which is focused on developing a rigid-wing ground-generation prototype and tackling problems regarding three main topics: Identification, Modelling and Estimation; Optimisation and Control; and Multiple Kite Systems.

This presentation starts from a general explanation of Airborne Wind Energy, the different concepts in development as well as the current state of the industry, and it will then part to a brief presentation of the UPWIND Project, its goals and developed work.

2 The Concept

The kite power system currently being explored by UPWIND is a Ground Generation system, usually known as Pumping Kite Generator (PKG). This concept relies in an airfoil or kite connected to a tether which is coiled around the shaft of a generator on the ground. Its operative process relies on the conclusions reached in [2] that state that the maximum mechanic power withdrawn from a tethered kite is achieved during a crosswind flight. Therefore, a PKG operation comprises two phases, a power productive reel-out phase and a power consuming reel-in phase.

During the first phase, the kite is controlled to move in a fast crosswind motion, maximising the tether tension force, reeling out the tether and forcing the generator to produce electricity.

When the tether reaches a maximum length, in the second phase, the kite is controlled to minimise the tether tension force and the generator, acting as a motor, reels the cable back in.

The overall energy balance is kept positive due to the power production maximisation during the reel-out phase and minimisation during the reel-in phase.

3 UPWIND [3]

A system such as this raises several questions that are yet to be answered.

Firstly, there is the need to provide a detailed modelling and identification of the system. We aim at using Moving Horizon Estimation techniques to estimate the system parameters and variables.

It is also required to define a path which maximises power production, thus Optimal Control can be a tool to find that path in order to later parametrise it and use it as a reference for a path-following controller.

In order to guarantee a stable and optimal operation for the kite, so it not only functions autonomously and reliably but it produces the most possible power, it is required advanced control and optimisation techniques, such as Model Predictive Control. These techniques will be applied and tested both in simulation and in physical prototypes in order to thoroughly assess their performances.

A large open research question is the use of several kite systems within a wind farm. This holds several challenges such as the layout of the units in a given land area, in order to reduce the terrain usage, while guaranteeing that there are no collisions among kites.

The different research objectives and challenges that are being pursued by the UPWIND project can be summarised by three main different topics:

- Identification, Modelling and Estimation of AWES
- Optimisation and Control of AWES
- Multiple Kite Systems

This presentation will attempt to introduce briefly the general area of AWES and the current challenges facing the development of this technology. It will then present the UPWIND project, both what has been done within this project and what we are planning to work on in the future.

References

- [1] Cherubini A 2017 *Advances in Airborne Wind Energy and Wind Drones* PhD Scuola Superiore Sant'Anna Pisa, Italy
- [2] Loyd M L 1980 *Journal of Energy* 4 106–111
- [3] UP Wind URL <http://www.upwind.pt/>

Validating a dynamic performance model for flexible kite pumping airborne wind energy systems

M Schelbergen^a and R Schmehl^a

^aFaculty of Aerospace Engineering, Delft University of Technology, Kluyverweg 1, 2629
HS Delft, The Netherlands

E-mail: m.schelbergen@tudelft.nl

Keywords: Airborne Wind Energy, Model Validation, and Optimal Control

Abstract

This paper presents the current status of an ongoing study about the development of a 4 degrees of freedom model for flexible kites that is well suited for validation purposes. Such simple model has the potential to fulfill the demand for a validated model for energy production assessments. By applying the model in an optimal control problem that fits the simulation to flight data, model deficiencies can be easily identified. The path found by the optimisation is in good agreement to flight data of Kitepower B.V. and shows that the dynamics of a flexible kite can be well described using the yawing motion as the only rotational degree of freedom.

Keywords: Airborne Wind Energy, Model Validation, and Optimal Control

1 Introduction

Motivated by the vivid development of technology demonstrators, there is a high demand for validated models to assess the power output of airborne wind energy (AWE) systems and their potential contribution to the energy mix. Numerous models have been developed with varying complexity that can be used for this purpose. Examples are quasi-steady approaches [1, 2, 3] or dynamic models [4, 5, 6] of varying level of detail, accuracy and computational effort. The degree to which these models are validated is generally limited to specific wind conditions. No commercial systems are in operation yet. Consequently, little operational data are available for validation purposes. Moreover, the data that are available includes only little information about the wind field, which poses major challenges for the validation of these models.

In earlier work [7], a preliminary validation was performed on the quasi-steady model using flight data of the company Kitepower B.V., which employs a flexible kite, pumping AWE system. The flight path is highly idealised in this type of model, which makes it problematic to directly compare the simulation results to the time series of the flight data. Dynamic simulations resolve the flight path and are better suited for comparing to flight data. Malz [8] uses the simple 6 degrees of freedom (DOF) dynamic model proposed by Gros [9] in an optimal control problem to fit a simulated flight path to flight measurements of the rigid wing AP2 prototype of Ampyx Power. The current state-of-the-art is lacking a dynamic flexible kite model that is as thoroughly validated as the latter rigid kite model. This work presents the formulation of the 4 DOF model for flexible kites, which enables the same validation approach.

2 Flexible kite model derivation

Rigid kites use a yawing and rolling motion to initiate a turn, whereas flexible kites predominantly use yawing. Therefore, we hypothesize that the dynamics of a flexible kite system can be well described using merely 4 DOF (3 translational + yaw), instead of 6, as is often used for rigid wing systems. The Cartesian formulation of the model proposed by Gros [9] reduces the nonlinearity of its equations compare to using

spherical coordinates and makes the model well suited for optimisation. The 3 Cartesian coordinates of the kite position together with the 3 x 3 direct cosine matrix (DCM) yield a total of 12 generalised coordinates. We assume that the vertical axis of the kite is aligned with the straight tether, thereby the pitch and roll angle are fully defined by the position of the kite. Due to this assumption, the DCM can be constructed using only the sine and cosine of the yaw angle and the kite position and leaves us with 5 generalised coordinates:

$$R = \begin{bmatrix} x \cdot z \cdot (l \cdot l')^{-1} & -y/l' & x/l \\ y \cdot z \cdot (l \cdot l')^{-1} & x/l' & y/l \\ -l'/l & 0 & z/l \end{bmatrix} \cdot \begin{bmatrix} \cos \psi & -\sin \psi & 0 \\ \sin \psi & \cos \psi & 0 \\ 0 & 0 & 1 \end{bmatrix}, \quad (1)$$

in which x , y , and z are the Cartesian coordinates of the kite position, l is the tether length, $l' = \sqrt{x^2 + y^2}$ is the tether length projected onto the ground plane, and ψ is the yaw angle of the kite. Note that the nonlinear sine and cosine operations can be left out of the model equations by including the sine and cosine of the yaw angle as separate generalised coordinates. The related states are kept consistent due to the formulation of the model equations. For more details on the model we refer to the derivation of Gros [9]. For simplicity the yaw dynamics of the kite are not resolved in this study, instead the yaw rate is directly imposed as a control variable in the state-space representation. The state and control vectors read as:

$$\mathbf{x} = [\mathbf{r} \quad \mathbf{v} \quad s\psi \quad c\psi]^T, \quad \mathbf{u} = [\dot{\psi} \quad \ddot{\psi} \quad \alpha_d]^T, \quad (2)$$

in which \mathbf{r} is the kite position, \mathbf{v} is the kite velocity, $s\psi$ and $c\psi$ are the sine and cosine of the yaw angle, and α_d is the depower angle. The latter control variable accounts for the actuated lowering of the angle of attack of the wing in the retraction phase [10, 7].

Since the yaw rate is imposed, we do not need to consider the aerodynamic moments acting on the kite in the model equations. Additional to the lift and drag forces, a side force is acting on the kite that accounts for most of its steering capabilities. The side force is a linear function of the side force coefficient, which scales linearly with the side slip angle:

$$C_S = -\beta, \quad (3)$$

in which β is the side slip angle experienced by the kite in radians.

The lift and drag coefficients are commonly modelled as functions of the angle of attack. At the current preliminary stage of this study, the lift and drag coefficients are assumed to be constant during the reel-out and reel-in phases and only change when switching flight phase.

3 Optimal control problem for validation

An optimal control problem is formulated to find the control input which yields the best fit of the simulation to flight data. Flight test data of a single pumping cycle (reference cycle in [7]) flown on 8 October 2019 of the company Kitepower B.V. is used. For this specific experiment the development system was equipped with the old 25 m² leading edge inflatable V3 kite. Representative lift and drag coefficient values of the kite are listed in Table 1 and follow from the preceding validation study [7]. Consult the latter study for more specifics about the flight test.

	Reel-out	Reel-in
C_L	0.71	0.39
C_D	0.18	0.12

Table 1: Representative lift and drag coefficients during the reel-out and reel-in phases of the old V3 kite of Kitepower B.V. [7].

The cost function of the optimisation is the sum of the weighted squared errors of the kite position, velocity, yaw angle, and tether force time series. The weights allocated to each of the properties are listed in Table 2. The control input during the ~2 minute pumping cycle is discretised in 125 intervals. Within each interval, the control input remains constant. Note that a discrete yaw rate signal is physically not

possible. However, by limiting the allowable step size, the optimisation still produces nearly realistic results. The optimisation searches the control input that minimises the cost function while satisfying the model equations. The problem is solved using the CasADi [11] library and its direct collocation method. The evolution of each state within each control interval is approximated by a Lagrange polynomial using a Radau scheme of degree 3.

For the model validation, Malz [8] introduces the horizontal wind speed components as states. Here, for this preliminary analysis, we assume the wind speed is constant at 10 m s^{-1} .

4 Results

Finding a good starting point for the optimisation is a challenging task. After a good starting point is obtained by trial and error: the optimisation converges rapidly with low computational effort. Table 2 dissects the different contributions to the cost function at the optimal solution and shows that the tether force error contribution is largest. Figure 1 reveals a good match between the control input from the flight data and the optimal solution. At the end of the reel-in phase, the optimal yaw rate shows excessive variations and thereby prevents the kite of overshooting the ground station. The resulting excessive steering is believed to be caused by underestimating the drag coefficients for this part of the pumping cycle. Although also the optimal reeling acceleration shows some excessive variations, the general trend is in fair agreement with the measurements.

Figures 2 and 3 show that the optimal solution improves the match between the simulation results and flight data substantially relative to the starting point and show no indications of major model structure deficiencies. From this observation, we can conclude that the dynamics of a flexible kite can be well described using merely 4 DOF for this pumping cycle.

Figure 4 shows that the mismatch between the measured and simulated tether force is a little more substantial. The mismatch can to a large extent be explained by the wind speed modelling. The tether force is scaling quadratically with the wind speeds and thus is very sensitive to the wind speed. The work of Malz [8] reports a wind speed range of 7 m s^{-1} within a pumping cycle. Therefore we can conclude that assuming a constant wind speed in the current modelling approach is too simplistic. During the reel-out phase, the angle of attack of the optimal solution is in good agreement with the measured angle of attack (fluctuating around 10 degrees [7]). During the reel-in phase, the angle of attack is substantially higher than the measured angle of attack (roughly 4 degrees [7]). This mismatch is believed to be caused by not accounting for tether sag in the model: in reality tether sag lowers the angle of attack. The side slip angles found are in good agreement with the experiment of Oehler [10] which reports that angles up to ten degrees are common.

Error	Weight	Squared weighted errors
Kite position	0.3	808
Kite velocity	1	977
Reeling speed	5.5	788
Yaw angle	1	13
Tether force	0.007	1392

Penalty	Value
Excessive reeling acceleration variations	132

Table 2: Cost function contributions at the optimal solution.

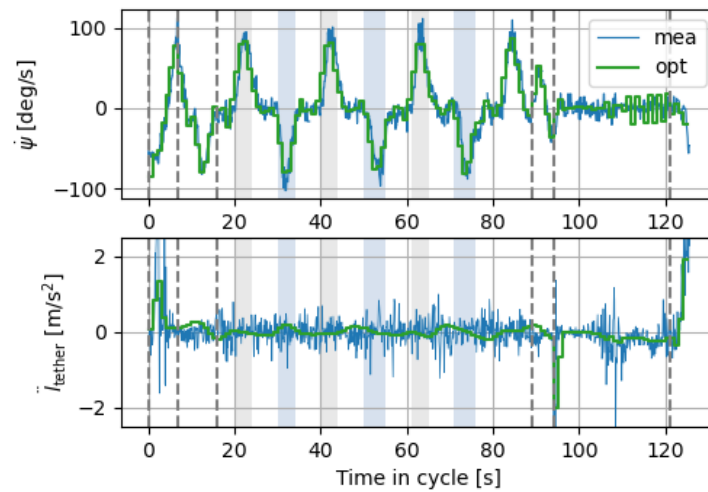


Figure 1: Control input (yaw rate and reeling acceleration) from the measurements and that of the final solution of the optimisation. The reel-out and reel-in phase take place between 15–89 s and 94–121 s, respectively. The grey and blue shade indicate right and left turns, respectively.

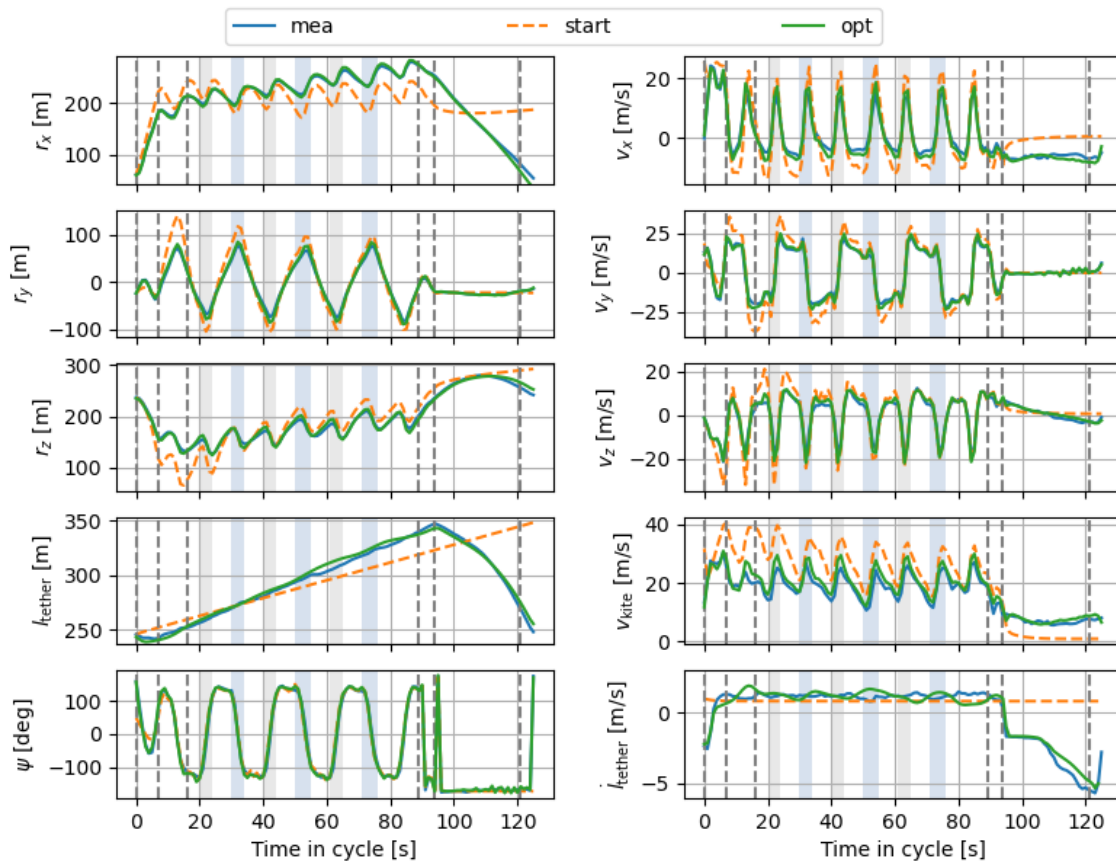


Figure 2: Time evolution of the states and related properties from the flight data and those of the starting point and final solution of the optimisation. The reel-out and reel-in phase take place between 15–89 s and 94–121 s, respectively. The grey and blue shade indicate right and left turns, respectively.

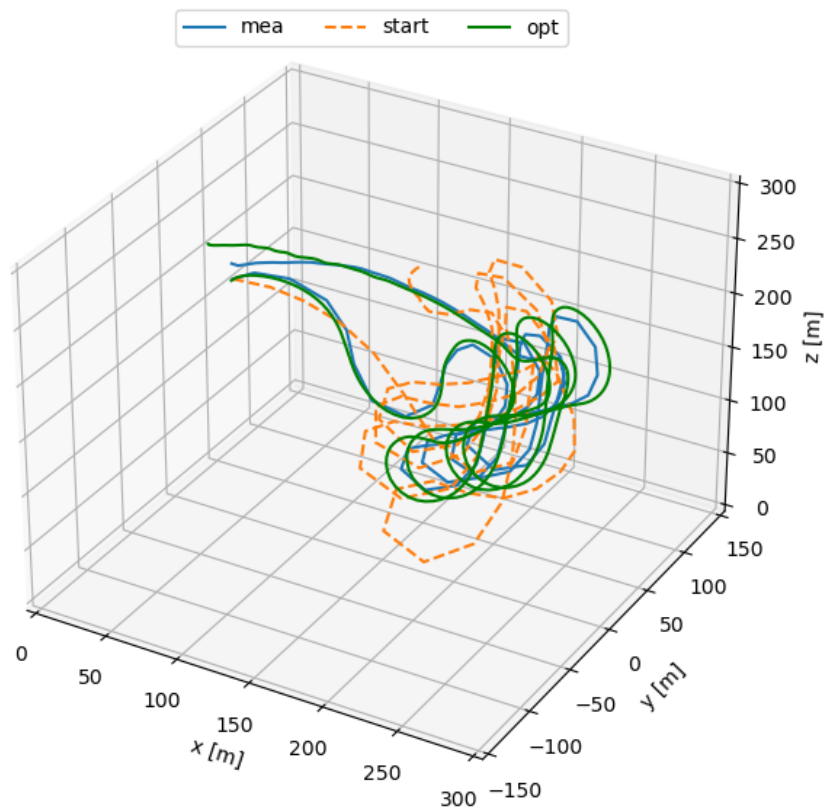


Figure 3: Flight path of the reference cycle from the flight data and that of the starting point and final solution of the optimisation.

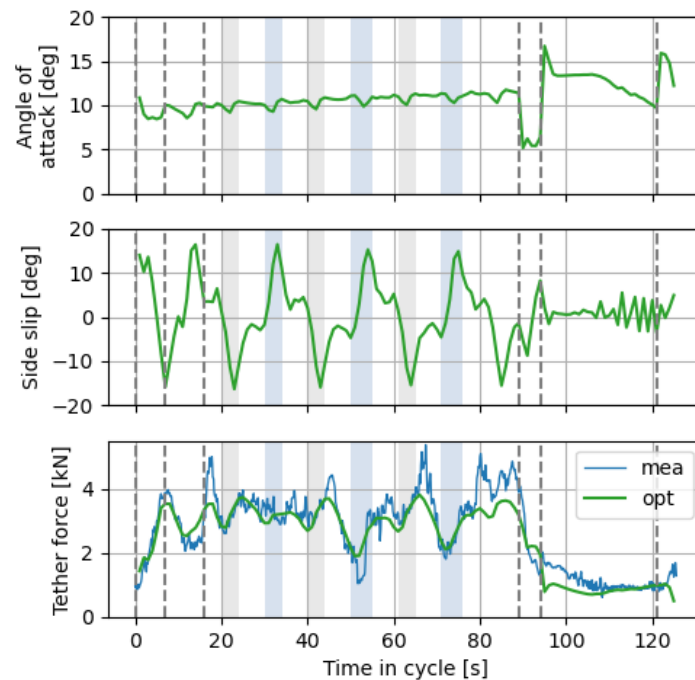


Figure 4: Time evolution of inflow angles at the kite of the optimal solution and the tether force from the flight data and optimisation solution. The reel-out and reel-in phase take place between 15–89s and 94–121s, respectively. The grey and blue shade indicate right and left turns, respectively.

5 Conclusions

We have presented the formulation of a simple 4 DOF model for flexible kites that is well suited for optimisation due to the reduced nonlinearity of its equations. The model is successfully used in an optimal control problem for identifying potential model deficiencies by fitting the simulation to flight data of Kitepower B.V. The optimal path found by the optimisation shows that the dynamics of a flexible kite can be well described using the yawing motion as the only rotational DOF. The mismatch between the measured and simulated tether force is believed to be caused by the steady wind assumption. In future work, enhancements to the wind speed modelling will be investigated. Furthermore lift and drag curves will be implemented, thereby making the aerodynamics dependent on the angle of attack. This requires that the effect of tether sag on the angle of attack is quantified and corrected for in the model.

Acknowledgements

The authors are grateful to Kitepower B.V. (<http://kitepower.nl>) for sharing their flight data and simulation expertise and in particular to Joep Breuer for giving helpful feedback in our meetings. Mark Schelbergen and Roland Schmehl have received financial support by the project REACH (H2020-FTIPilot-691173), funded by the European Union's Horizon 2020 research and innovation programme under grant agreement No. 691173.

References

- [1] Ranneberg M, Wölflé D, Bormann A, Rohde P, Breipohl F and Bastigkeit I 2018 *Airborne Wind Energy – Advances in Technology Development and Research* Green Energy and Technology ed Schmehl R (Singapore: Springer) chap 25, pp 623–641 ISBN 978-981-10-1947-0

- [2] Van der Vlugt R, Bley A, Schmehl R and Noom M 2019 *Renewable Energy* **131** 83–99
- [3] Schelbergen M, Kalverla P C, Schmehl R and Watson S J 2020 *Wind Energy Science* **5** 1097–1120
- [4] Ruiterkamp R and Sieberling S 2013 *Airborne Wind Energy* Green Energy and Technology ed Ahrens U, Diehl M and Schmehl R (Berlin Heidelberg: Springer) chap 26, pp 443–458 ISBN 978-3-642-39964-0
- [5] Fechner U, Van der Vlugt R, Schreuder E and Schmehl R 2015 *Renewable Energy* **83** 705–716
- [6] Eijkelhof D, Rapp S, Fasel U, Gaunaa M and Schmehl R 2020 *Journal of Physics: Conference Series* **1618** 032020
- [7] Schelbergen M and Schmehl R 2020 *Journal of Physics: Conference Series* **1618** ISSN 1742-6588 science of Making Torque from Wind 2020, TORQUE 2020 ; Conference date: 28-09-2020 Through 02-10-2020
- [8] Malz E, Koenemann J, Sieberling S and Gros S 2019 *Renew. Energ.* **140** 1004 – 1011 ISSN 0960-1481
- [9] Gros S and Diehl M 2013 *Airborne Wind Energy* ed Ahrens U, Diehl M and Schmehl R (Berlin Heidelberg: Springer) pp 181–203
- [10] Oehler J and Schmehl R 2019 *Wind Energy Science* **4** 1–21
- [11] Andersson J A E, Gillis J, Horn G, Rawlings J B and Diehl M In Press, 2018 *Mathematical Programming Computation*

Folding of wind turbine blades through flexible hinges for transportation purposes: optimised laminates

Aileen G. Bowen¹, Giovanni Zucco¹, and Paul M. Weaver¹

^aSchool of Engineering and Bernal Institute, University of Limerick

E-mail: aileen.bowenperez@ul.ie

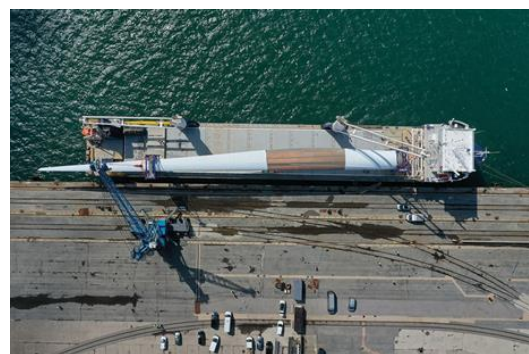
Keywords: Nonlinear bending of thin-walled tubes, flexible hinges, transportation of wind turbine blades

1 Introduction

As a response to the high demand of cost-effective renewable energy, the wind energy industry steadily increases the size of wind turbine generator (WTG) rotors. Larger rotors reduce the cost of wind energy thanks to the increase of blade swept-area. Among the challenges which accompany cost reduction stands the transportation of supersized WTG blades. Fig. 1 shows the transportation of two of the current largest WTG blades. Recently Berkeley [1], described and assessed proposed strategies for transporting supersized WTG blades. These strategies include on-site assembling of segmented blades, on-site manufacturing, constraining blade dimensions according to road/rail restrictions, alternative means of transport (e.g. airships) and controlled blade bending to reduce blade dimensions during transportation.



(a) LM88.4 P



(b) LM107.0 P

Figure 1: Transportation of large wind turbine blades.

Flexible hinges are morphing structures which embed localised compliance to thin-walled structures to achieve folding without the use of conventional folding mechanisms. The benefit of flexible hinges are currently exploited in aerospace deployable booms with circular cross-section [2]. Considering aerofoil cross-sections, Lachenal et al. [3] developed and tested a deployable wing concept whose folding process is shown in Fig. 2. These morphing structures have potential to enable the controlled bending of WTG blades as a practical solution to the transportation of supersized WTG blades. This solution eliminates the drawbacks of hinged mechanisms, i.e. additional weight, lubrication systems and increased system complexity. The key to the hingeless folding of flexible hinges is a structural instability characteristic of thin-walled structures under bending known in literature as the Brazier effect [4].

As such, considering the application of a large WTG blade made of composite material with an embedded flexible hinge, the minimisation of the folding load plays a key role in design. The minimisation reduces induced stress during the folding process and ensures minimum required actuation loads for



Figure 2: Folding process of Lachenal's et al. conceptual deployable wing [3].

folding. Recently, Bowen et al. [5] found an analytical solution to obtain the optimum layup that minimises the load necessary to fold composite laminated tubes with circular cross-sections. However, a knowledge gap exists for the case of aerofoil cross-sections. With the aim of obtaining engineering knowledge for preliminary design and considering the extensive available research for circular cross-sections, the objective of this work is to explore whether the optimum laminate for circular cross-section also applies for aerofoil cross-sections. Numerical results for aerofoils characteristic of WTG blades are obtained through geometrically nonlinear finite element analysis. Careful assessment of these results show that the folding load for flexible hinges with aerofoil cross-section can be optimised and predicted using identical stiffness properties, i.e. longitudinal stiffness and circumferential bending stiffness, as in the case of circular cross-sections. These findings are explored in detail including additional notes on local buckling which is also characteristic for these structures and interacts with Brazier instability.

Acknowledgements

The authors would like to thank Science Foundation Ireland for funding the Spatially and Temporally Variable Composite Structures grant no. (15/RP/2773) under its Research Professor program.

References

- [1] Berkeley L and Laboratory N 2019 URL www.dnvg1.com
- [2] Mallikarachchi H M Y C and Pellegrino S 2011 *Journal of Spacecraft and Rockets* **48** 187–198 (Preprint <https://doi.org/10.2514/1.47321>) URL <https://doi.org/10.2514/1.47321>
- [3] Lachenal X, Weaver P and Pirrera A 2014 *ASME 2014 Conference on Smart Materials, Adaptive Structures and Intelligent Systems, SMASIS 2014* vol 2
- [4] Brazier L G 1927 *Proceedings of the Royal Society of London Series A* **116** 104–114
- [5] Bowen P A G, Zucco G and Weaver P M 2020 *Thin-walled Structures - Accepted for publication*

Integrated design and LCOE minimization of horizontal and vertical axis floating wind turbines

Kutay Yilmazlar^a and Alessandro Croce^a

^aDipartimento di Scienze e Tecnologie Aerospaziali, Politecnico di Milano, Milano, Italy.

E-mail: kutay.yilmazlar@polimi.it

Keywords: Floating wind, design optimization

1 Introduction

In recent years, the increasing exploitation of land-based areas for the construction of wind farms has reduced the capacity to build very large wind plants, thus forcing the exploitation of new resources in the deep sea. Due to the excellent wind conditions in deep seas, floating wind turbines (FWT) promise to be a favorable alternative to fixed-bottom offshore wind turbines. As a matter of fact, it is already shown that floating wind energy represents a huge potential for Europe to achieve its renewable energy goals [1].

The support structures for floating applications are more expensive than the fixed-bottom ones within the commonly exploited water depths, as much as triple the cost of its counterpart [2]. However, the levelised cost of energy (LCOE) of FWTs is less sensitive to the increasing depth of installation [3], thus indicating that FWTs would be the optimal choice beyond a certain threshold of water depth. At the same time, the design driver of a FWT, as well as the land-based one, is the LCOE reduction. Given the fact that FWTs are highly complex systems, this requires an integrated multidisciplinary design optimization as exemplified in [4].

Although there have been significant developments of FWT concepts both in the research and industrial area in recent years, there are still number of issues to be investigated to make floating wind turbines competitive in the energy market. To that end, FLOWER (FLOating Wind Energy netwoRk [5]) is formed to tackle various tasks related to floating wind. As a part of FLOWER project, this work will focus on integrated design of FWTs with the aim of minimizing LCOE. Since the present research is at a very early stage, this abstract gives only a brief description of planned approach to be followed in the upcoming years, which can be found in the next chapter.

2 Methodology

The starting point of this research is based on the more than ten years experience of the research group in the development of technologies for the integrated design of wind turbines. Within this research topic, an in-house design optimization software Cp-Max (Code for Performance Maximization) has been developed. In Cp-Max, the wind turbine model is defined and simulated by the aero-servo-elastic multibody solver Cp-Lambda (Code for Performance, Loads, Aeroelasticity by Multi-Body Dynamic Analysis). Recent design studies performed with Cp-Max and hereby applied simulation procedures are documented in [6] and the references therein. Over the past years, Cp-Max has been continuously developed and validated in the context of many research projects. Nonetheless, the use of this software is limited to onshore applications and offshore monopile structures. Therefore, the primary task of this research work is to implement an offshore/floating subroutine into the existing code. At this point, different strategies arise to realize a physical model of a FWT. The first is to use the already developed and tested hydrodynamic codes such as HydroDyn module of OpenFAST by NREL and create an interface between HydroDyn and Cp-Lambda. The second, which is a more challenging approach, is to extend Cp-Lambda with

hydrodynamic models. In order to verify the accuracy of the methods used, ideally, both should be followed and verified against each other iteratively until a realistic simulation set-up is found. Simulation results from baseline turbine configurations will be also compared with the literature.

Unlike the fixed-bottom structures, for FWTs there is not a standard foundation design that is used almost exclusively. In consequence, the geometry of the floating bodies needs to be parametrized in such a way that all introduced floater designs (e.g. spar-buoy, tension leg, semi-submersible, barge) can be accounted for. Since high fidelity fluid dynamics simulations cannot be afforded in a design optimization loop, input geometry should be simplified as much as possible.

Cost models that are used within Cp-Max will be extended with the ability to assess floating platform cost contributions. Moreover, these cost models should take into account the rapid advances in the FWT technologies which are predicted to provide a notable reduction of LCOE in the next years [7].

Following the completion of FWT optimization routine, a set of design studies is going to be conducted. A comparative analysis between different turbine configurations will provide insights about the design space for each subsystem. For example, vertical axis wind turbines may have an advantage over horizontal axis configuration to reduce the platform costs, mainly due to their lower center of gravity [8]. These investigations will light the way for future design guidelines and a better understanding of the integrated system behaviour of FWTs.

Acknowledgements

This work is part of a project that has received funding from the European Union's Horizon 2020 research and innovation programme under the Marie Skłodowska-Curie grant agreement No 860879.

References

- [1] Arapogianni A, Genachte A B, Ochagavia R M, Vergara J P, Castell D, Tsouroukdissian A R, Korbijn J, Bolleman N, Huera-Huarte F J, Schuon F *et al.* 2013 *European Wind Energy Association (EWEA)*
- [2] Collu M, Kolios A, Chahardehi A and Brennan F 2010 *RINA, Royal Institution of Naval Architects-Marine Renewable and Offshore Wind Energy-Papers* 63
- [3] Myhr A, Bjerkseter C, Ågotnes A and Nygaard T A 2014 *Renewable energy* **66** 714–728
- [4] Hegseth J M, Bachynski E E and Martins J R 2020 *Marine Structures* **72** 102771
- [5] FLOWER Project home page URL: <https://www.floower-h2020.eu/>
- [6] Bortolotti P, Sartori L, Croce A and Bottasso C L 2019 *Wind Energy* **22** 65–79
- [7] Musial W D, Beiter P C and Nunemaker J 2020 Cost of floating offshore wind energy using new england aqua ventus concrete semisubmersible technology Tech. rep. National Renewable Energy Lab.(NREL), Golden, CO (United States)
- [8] Griffith D T, Barone M F, Paquette J, Owens B C, Bull D L, Simao-Ferreira C, Goupee A and Fowler M 2018 Design studies for deep-water floating offshore vertical axis wind turbines. Tech. rep. Sandia National Lab.(SNL-NM), Albuquerque, NM (United States)

O & M

Fatigue Assessment of the Tower of an onshore Wind Turbine from Monitoring Strains

J Pacheco^a, F Pimenta^a, F Magalhães^a, A Cunha^a

^a Construct-ViBest, Faculty of Engineering, University of Porto, Porto, Portugal

E-mail: ec11142@fe.up.pt

Keywords: Wind Turbine, Dynamic Monitoring, Strain Gauges, Fatigue Assessment

1 Introduction

Wind energy has experienced a truly remarkable evolution during the last two decades in terms of installed capacity and technological developments. In the EU, wind was the fastest growing energy source between 2005 and 2017, surpassing coal in 2016 as the second largest total installed power generation capacity [1]. Although at a different pace, the installed capacity is expected to continue to grow [2]. However, wind turbines were designed to operate 20 years, so it is estimated that about one half of the accumulated capacity currently installed in the EU will reach the end of design life in 2030 [2]. It is therefore essential to create a regulatory framework that defines the rules for the actions to be taken when the expected design life of the structures is exhausted.

Considering this background, the main goal of the WindFarmSHM research project is the development, validation and optimization of new methodologies to continuously assess the structural elements of wind turbines: tower, blades and foundation. This implies the development of algorithms for data processing in order to: i) Evaluate the remaining fatigue life of the main structural components based on the direct measurement of strains with strain gages and ii) Extrapolate the results obtained for instrumented wind turbines to non-instrumented wind turbines of the same wind farm, using SCADA data. As a first step, this work briefly describes the methodology for the experimental estimation of the bending moments applied in the tower. These results are the input for the fatigue assessment of the tower, being some preliminary results of this step also presented.

2 Tower strains and fatigue assessment

The monitoring system installed on the tower for forces characterization is composed by 6 2D rosette strain gages, 4 temperature sensors and 3 clinometers connected to a central acquisition system, then linked with a modem for remote access to the data. Having in mind the evaluation of the static bending moments diagrams along the tower, the six strain gages are distributed in two tower sections: one with four sensors at 6.6m from the tower base and another section with 2 sensors at 7.8m from the tower base.

Strain gauges are very sensitive sensors and many factors can easily preclude accurate measurements. So, the experimental determination of bending moments in the tower requires the acquired raw data to be pre-processed to obtain the real deformation. Thus, special attention is given to tuning of the strain signals processing, which includes temperature effects compensation and signal calibration according to IEC 61400-13 [3]. Figure 1 a) shows the 10 min average bending moment at the tower base for the fore-aft direction versus the 10 min average wind speed provided by the SCADA system during normal operation, considering different turbulence intensities.

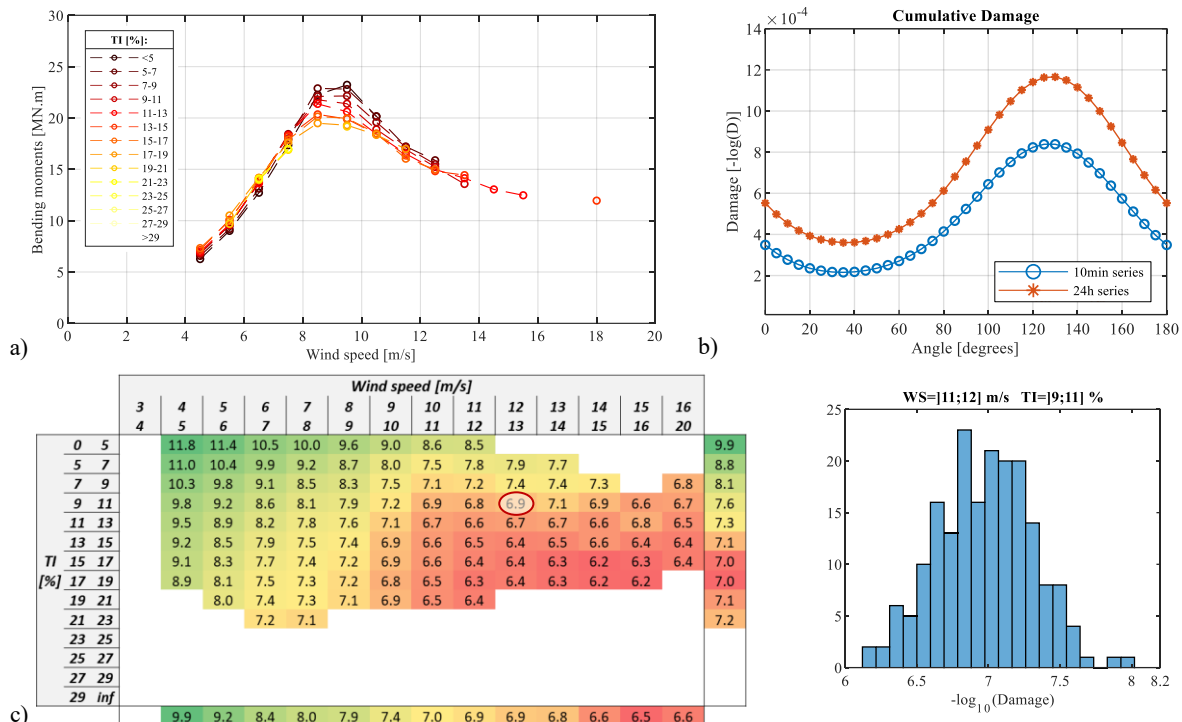


Figure 1 (a) 10min average bending moment at the tower base for fore-aft direction versus the 10min average wind speed during normal operation, considering different turbulence intensities; (b) Total fatigue damage accumulated for different sectors of the instrumented section; (c) Capture matrix ($-\log_{10} \text{Damage}$) and damage distribution for the selected cell of the matrix. (results obtained for the period from February 2019 to April 2020)

The fatigue assessment of the tower was performed by combining S-N curves and rainflow counting algorithm. The rainflow cycle-counting algorithm translates the hysteresis loops experienced by the material during the loading history into a stress histogram. The Palmgren-Miner linear accumulation damage rule is used to calculate the total damage and this analysis is performed around the section (every 5°) considering alternative windows length: for every day and for every 10 minutes period (Figure 1 b)). The fatigue resistance of the critical detail is given by the S-N curves provided in EC3 [4] (detail category is 80).

Figure 1 c) shows the capture matrix for normal operating conditions, giving average damage values for different combinations of wind speed and turbulence, showing that higher damage is correlated with higher wind speed and higher turbulence intensity.

Acknowledgements

The support of EDP Renewables and VESTAS is greatly acknowledged. This work was also financially supported by: PhD Grant SFRH/BD/129688/2017, UID/ECI/04708/2019- CONSTRUCT - Instituto de I&D em Estruturas e Construções and the project PTDC/ECIEST/ 29558/2017, all funded by national funds through the FCT/MCTES (PIDDAC).

Bibliography

- [1] EAWE 2018 *Wind in power 2017 - Annual combined onshore and offshore wind energy statistics*. Brussels, Belgium.
- [2] EAWE 2017 *Wind energy in Europe: Scenarios for 2030*. Brussels, Belgium.
- [3] International Electrotechnical Commission 2015 *IEC 61400 Wind turbines - Part 13: Measurement of mechanical loads*, Geneva, Switzerland
- [4] DIN 2010 *EN 1993-1-9:2010-12: Eurocode 3 – Design of steel structures – Part 1-9: Fatigue*.

Literature review on offshore substructure lifetime assessment and the potential of data-driven methodologies.

K Robbelein^a, N Noppe^a, W Weijtjens^a, C Devriendt^a

^a Vrije Universiteit Brussel (VUB) / Offshore Wind Infrastructure lab (OWI-lab)

E-mail: koen.robbelein@vub.be

Keywords: Lifetime assessment, substructure, industry practice, new concepts, fatigue, structural health monitoring.

1 Introduction

While the first offshore wind farms in Belgium are in the early phase of their design lifetime¹, the offshore wind industry is increasing its focus on the opportunities for lifetime extension.

The lifetime assessment of offshore wind farms based on supervisory control and data acquisition (SCADA) data has been subject of earlier research at OWI-lab. [1] The current research work is a continuation of this work within our recently approved Supersized 4.0 project.

The Supersized 4.0² project [2] will focus on monopile substructures for +7MW wind turbines and supplements the SCADA data with structural health monitoring (SHM) data, including the use of novel SHM technology such as IoT sensors and advanced data-analysis, supplemented with relevant project specific information from design, construction and operations and maintenance (O&M) phases. The present work, and one of the main deliverables of Supersized 4.0, has the objective to respond this increasing interest from the industry by developing a certifiable data-driven lifetime extension methodology and corresponding toolbox for the substructure.

While this research is based on a collaboration of the Belgian offshore wind industry and academic institutes, its relevance and application is industry wide.

A broad literature review has been initiated to explore current practices and ongoing research in the domain of lifetime assessment and monitoring of offshore foundations. The literature review allows to identify the opportunities for improvement to the current practices. These improvements can be taken into account as targets for the present research within Supersized 4.0.

2 Literature review

The nature of this research requires a thorough literature review. In the first 3 months of research, the literature review focused on the relevant offshore wind industry standards and guidelines, exploration of ongoing research projects and industry applications in view of lifetime.

¹ In Belgium the offshore wind has been operational since 2008, C-Power phase 1. The first wind farm with relevance for the current research has been commissioned in 2018.

² Supersized 4.0 research project concerning “Smart O&M for a fleet of supersized wind turbines in an industry 4.0 context”.

2.1 Literature in relation to the evaluation of lifetime for extension of lifetime.

First source of literature, when aiming for a certifiable method for the lifetime assessment of offshore structures, are the publications from regulatory institutes, also referred to as certification authorities, such as DNVGL, BV, UL, TÜV Süd [3-4,12, 13]. The referenced guidelines published by certification authorities provide in essence similar recommendations. The guidelines' approach for lifetime assessment is currently based on an analytical and practical part. The essence of the approach is to update the input – and design methods - of the analytical or numerical models in order to re-evaluate the (certified) design. The updated inputs are a result of in-depth design and as-built documentation reviews, updated environmental and operating conditions (EOC) and observations from periodic inspections. In relation to the subject of this research the guidelines lack a data-driven lifetime assessment approach, yet do not exclude the use of condition monitoring for the lifetime assessment. The legal obligations, market expectations and requirements for certification for extended lifetime are not conclusive.

The industry's focus concerning lifetime, has been mainly on the wind turbine generator and components (such as bearings, blades, generator components) to achieve optimization of power production and lifetime assessment of these turbine components. This includes the monitoring and assessment of performance and condition data (typically collected in the SCADA system). There is a potential spill-over between an industry-wide recognized data-driven lifetime assessment of turbine components and substructure and therefore this industry practice is – and will in the future be - consulted. A near future publication which could provide valuable insights in best-practices is the IEC61400-28 standard. [11-18-30]

In relation to the substructure, the existing model-driven engineering tools are being further exploited to find a response to the industry's requests in relation to lifetime. Examples of these tools are the use of detailed finite element analysis (FEA) and (true) digital twins of the structure. The supplementary use of structural health monitoring data in these model-driven approaches is getting increased attention. [6-7-8] While the data-driven approach as independent, yet complementary tool to model-driven approaches, remains an area for exploration and therefore the subject of this research.

In 2019 The Carbon Trust and its Offshore Wind Accelerator (OWA) partners ordered a desktop study which is collecting the state-of-the-art concerning structural health monitoring and lifetime assessment in view of lifetime extension of offshore wind substructures. The result is a comprehensive publication³, including the review of current - and future innovative - technologies, applicable standards, analysis methods and concludes with a holistic lifetime extension framework. The framework – as is the entire document – is written from the perspective of the wind farm owner. Purpose is that it can be consulted by OWA partners' asset engineers and managers to support them in the process of data-collection, re-assessing the remaining lifetime of the substructure and the commercial evaluation thereof. [5] Important to note is that the publication is not linked to regulations or standards and thereby a non-binding document.

In comparison to the current practices and lifetime extension framework explained in [5], the research within Supersized 4.0 aims at truly data-driven approach, centralizing the use of measured EOC and structural conditions, with a reduction of the retrospective in-depth documentation review. The publication [5] is a valuable source of information. Especially to benchmark our data-driven lifetime assessment methodology within Supersized 4.0 - with the current industry perception of the topic - such our research is recognizable for the industry.

In parallel with The Carbon Trust, several research and development projects on the topic of lifetime assessment and research domains related to lifetime consumption such as corrosion, fatigue, soil conditions are ongoing. (see Table 1) To the knowledge of the author at time of writing this extended abstract the following research projects are considered relevant to follow, yet not coincidental nor

³ The contents of this publication [5] may not be provided to any third parties. The author of this abstract could consult the publications since the Vrije Universiteit Brussel is one of the publishing contractors on behalf of The Carbon Trust.

conflicting, in relation to the subject of the research within Supersized 4.0. The below listed projects are in essence related to either optimizations in the operations and maintenance phase by a data-driven decision tool (short term), investigating the lifetime of wind turbine generator components or focusing on a supporting research domain related to lifetime consumption. Within Supersized the objective is to liaise with peer-research projects as listed below.

*Table 1: Overview relevant peer R&D projects.
A further description of the below research projects can be consulted in the references.*

Project name	Brief description	References
LifeWind	Focus of study is the wind turbine generator and components. Objective is to demonstrate procedures, relying on all available data incl. SHM, that can quantify the risk of failure, the remaining structural reliability and the maintenance costs upon extending the life of operational (in Denmark) wind turbines nearing their end of certified life. LifeWind has made recommendations for the IEC [11] technical specification on Lifetime extension which is expected in 2021. 2017-2020	[5] [18] [30]
IEA Task 42	The coordination of international research activities towards the assessment of remaining operational life of wind turbines near the end of the certified design life and identification of strategies for extending the useful life. No publications encountered. 2019-2022	[31]
H2020 AWESOME	Particular interest in workpackage 8 in relation to SHM for wind turbine extended life operation. Resulting in publication of the doctoral thesis by Ziegler. 2015-2018	[5] [14]
H2020 ROME0	Research objective is to develop reliable O&M decision tools and strategies. Including the use of novel SHM technology such as an IoT platform, data-driven analysis for failure diagnosis. To the knowledge of the author, the focus is on short term (O&M) assessments and not on lifetime extension of substructures. 2017-2022	[5] [20] [24]
O&O Nobelwind	Research and development project in collaboration with a Belgian wind farm operator. Topics of the project included the use of optical strain gauges, validation of virtual sensing, monitoring of bolted connections, fleet wide assessments using SCADA data. 2016-2019	[5] [32]
MAXWind	Research with focus on fatigue and corrosion modelling with the goal to have an improved estimation of the remaining life of in-service wind turbines. 2020-2024	[28]
SoilTwin	Development of a soil model which allows for a more accurate frequency analysis. 2020-2022	[29]
C-FLO	Corrosion fatigue life optimization by development and calibration of corrosion fatigue models. The aim is an optimization of design and maintenance of monopiles. 2019-2022	[26]

Monitor JIP	Development and validation of an effective SHM system and data-analysis methods. 2016 – 2018	[5] [27]
SLIC	Fatigue and crack propagation curves have been re-evaluated based on experiments. Samples, in both in-air and seawater conditions, have been subjected to loads which are comparable to the loads experienced by offshore wind turbines. 2015-2020	[5] [37]

Lifetime assessment of monopiles has been subject of recent academic research activities. In 2018 the Ziegler's thesis has been published. Ziegler's research was part of the H2020 AWESOME project. The research involved a.o. a novel fatigue load monitoring concept which has been validated with real-life measurements. The damage equivalent fatigue loads along the entire monopile have been predicted based on the extrapolation of strain measurements at one level. [14]. Similar work, so called virtual sensing strategies, has been performed by researchers within OWI-lab [40] [41] and Aarhus University [42]. The lifetime assessment of offshore wind farms based on supervisory control and data acquisition (SCADA) data has been subject of earlier research at OWI-lab by Noppe [1] and ongoing research by Santos [43].

The topic of lifetime assessment is relying on several research domains. A provisional list of research domains which are of interest is given below. The in-depth review of academic publications has been limited to this day. For completeness and future reference, the to-date encountered publications are referenced.

- Fatigue capacity of steel offshore structures
 - o Re-evaluation of the fatigue thickness effect for thick specimen [21]
 - o Re-evaluation of fatigue and crack propagation performance [36] [37]
 - o Measurement based fatigue damage extrapolation [38] [39]
- Corrosion
 - o Performance of corrosion protection systems in relation to lifetime extension [23]
 - o Corrosion fatigue behavior [19] [25] [26] [28]
- Soil – structure interaction [29]
 - o Fatigue influence of pile head rotations [33]
 - o Fatigue influence due to changes stiffness as a result of cyclic loading [33] [34]
- Scour protection influence to dynamics [35]
- Operational Modal Analysis techniques [22]
 - o Damage identification [20] [24]
 - o Virtual sensing [40]
- Structural reliability [44]
- Machine learning [24] and also subject of other work packages within Supersized 4.0.

2.2 Literature in relation to structural health monitoring technology

A focal point of reference for the structural health monitoring industry is the SAMCO Network (Structural Assessment, Monitoring and Control). A thematic network, funded by the European Commission, 2001-2005. Although the available SAMCO publications [15-17] date from 2006, these are still a reference for the industry. SAMCO publication [17] is referenced in the VDI 4551:2020 [10] and the methodologies are recognizable in the current regulations. The application of novel structural health monitoring technology in Supersized 4.0 is in accordance with the SAMCO vision towards and beyond 2020. [15]

The earlier referenced publications by The Carbon Trust [5] and the publicly available deliverables from ROMEO project provide a comprehensive overview of the current monitoring technology,

including innovative techniques which are already (widely) applied in the industry and innovations which are incubating and expected to be market mature within the next years.

- Typical structural health monitoring setup consists of: Accelerometers (in WTG tower and foundation), strain gauges (incl. temperature measurement) typically at the interface level, inclinometers, supplemented with corrosion monitoring (e.g. ER probes or reference cells) and environmental monitoring equipment if required.
- Recent innovations applied in the industry involve amongst others: The use of strain gauges made out of fibre glass (such as fibre bragg grating, FBG), big data handling in cloud-based solutions, digitalization of inspection records.
- Innovations for the near future are amongst others: The further development of FBG, introduction of IoT sensors in the monitoring setup and advanced data-analysis and operational modal analysis techniques leading to virtual sensing, fleet-wide extrapolations, machine learning also referred to as artificial intelligence.

In 2020 the Verein Deutscher Ingenieure (VDI) published the updated standard VDI4551. [10] From the current set of regulations (codes, standards, guidelines), [10] is the most relevant standard in relation to good practice for structural health monitoring of offshore wind substructures. It contains recommended practices for the hardware, data-analysis and the roles of responsibilities for asset owners and measurement equipment providers. Important to note in relation to certification is that the VDI is a non-binding document as it is not (yet) linked to any regulation such as DNVGL or BSH. It is expected that the VDI 4551 will be integrated in the next version of the DIN 18088-6 (periodic inspections), which is expected in 2022-2023.

3 Conclusions and way forward

3.1 Opportunities for improvement to the current practices

The literature study allowed to determine a couple of opportunities for improvement to the current practices. This exercise is of added value for the determination and future evaluation of the research objectives for a data-driven approach within Supersized 4.0.

Table 2: Determined opportunities for improvement and corresponding ambition how to respond to them by the present research.

OFI to the current practice	Improvement in Supersized 4.0
Holistic approach subject to interpretation and without clear acceptance criteria	Development of a roadmap based on data-analysis techniques for various lifetime consuming elements and alignment on design-driven and data-driven alarm levels
Reactive approach for decision support	Proactive approach by planning the lifetime assessment evaluations as from development / design phase
Risk of pitfalls and “blackboxes” when relying on project documentation packages	Recording the actual behaviour of the structure as basis for the assessment, supplemented with relevant design and operational information which is agreed during the planning of the works
Gap of data-driven approach in regulations	Implementing state-of-the-art fundamental R&D know-how - with consideration of its relevance in offshore wind structures lifetime consumption – in the data-analysis toolboxes.

<p>Improvements to the current definition and application of digital twin modelling.</p> <ul style="list-style-type: none"> - Indirect approach to get the stain histories which are important for a fatigue and thus lifetime assessment - Extensive work to clarify uncertainties in digital twin model calibrations - Digital twin modelling expected to be a man-hour consuming activity 	<p>Using the recorded data to develop an empirical digital twin of the structures for lifetime assessment exercises.</p> <ul style="list-style-type: none"> - SHM and data-analysis is a direct method to get to the required information for lifetime assessments - Bypass uncertainties by monitoring of the as-is configuration - Using mainly computer processors are used instead of human processors / man-hours - The structural model-driven assessment expected to be complementary with the empirical model.
---	--

3.2 Way forward

Based on the literature review, a framework and decision model for the data-driven lifetime analysis will be developed. The framework will be a gradual process going from specifying the needed information, ensuring the collection of this data, performing an initial assessment concerning the potential for lifetime extension, continuous follow-up, followed by a detailed assessment aiming for a quantification of the lifetime with certain probability.

The decision model will provide structure to investigate lifetime consuming elements and evaluate their impact towards a potential lifetime extension. Further advanced data-analysis work would be required to quantify this potential.

Continuation of the literature review in the domains on which the data-driven lifetime assessment framework is relying is necessary. Essential in this is to obtain mutual acquaintance – and collaboration - with researchers in these supporting domains.

Many of the technical solutions for the objective in this research are believed to be currently available or in research phase, one of the keys will be the collaboration to fit these into the process towards a data-driven lifetime extension methodology.

Acknowledgements

This research has been performed in the framework of the interdisciplinary cooperative research (Interdisciplinair Coöperatief Onderzoek, ICON) Supersized 4.0 project. This ICON project is a collaboration between partners of the strategic research enter The Blue Cluster and the Innovative Business Network Offshore Energy (IBN OE) (Innovatief BedrijfsNetwerk Offshore Energie).

The authors gratefully acknowledge the financial support by Flanders Innovation & Entrepreneurship (Agentschap Innoveren & Ondernemen, VLAIO).

Bibliography

- [1] Noppe N, 2019, *Performance monitoring and lifetime assessment of offshore wind farms based on SCADA data*, PhD Thesis
- [2] <https://owi-lab.be/supersized>
- [3] DNVGL-ST-0262, 2016, *Lifetime extension of wind turbines*
- [4] Bureau Veritas, 2017, *Guidelines for Wind Turbine Lifetime Extension, version 0*
- [5] London Offshore Consultants, 2019, *The Carbon Trust Offshore Wind Accelerator – Foundations Lifetime Extension Overview*, work packages 1 to 4. Confidential publication.
- [6] Augustyn D, Tygesen U, Ulriksen M and Sørensen J, 2019, *Data-Driven Design and Operation of Offshore Wind Structures*, conference paper Twenty-ninth (2019) International Ocean and Polar Engineering Conference Honolulu, Hawaii, USA, June 16-21, 2019
- [7] <https://ramboll.com/ingenuity/true-digital-twin>
- [8] <https://akselos.com/solutions/asset-life-extension/>
- [9] BSH (2015). Federal Maritime and Hydrographic Agency. *Minimum requirements concerning the constructive design of offshore structures within the Exclusive Economic Zone (EEZ)*
- [10] VDI 4551, 2020, *Structure monitoring and assessment of wind turbines and offshore stations*
- [11] IEC TS 61400-28 Wind energy generation systems - Part 28: *Through life management and life extension of wind power assets*, draft circulating within TC 88, expected 11-2021
- [12] UL-4143, 2016, *Outline of investigation for wind turbine generator life time extension (LTE)*
- [13] DNVGL-SE-0263, 2016, *Certification of lifetime extension of wind turbines*
- [14] Ziegler L, 2018, *Assessment of monopiles for lifetime extension of offshore wind turbines*, PhD Thesis
- [15] SAMCO Network publication, 2006, *Strategic Research Agenda*
- [16] Prof. Dr. W. Rücker, Dipl.-Ing. F. Hille, Dipl.-Ing. R. Rohrman, SAMCO Network publication, 2006, *F08a Guideline for Assessment of Existing Structures*
- [17] Prof. Dr. W. Rücker, Dipl.-Ing. F. Hille, Dipl.-Ing. R. Rohrman, SAMCO Network publication, 2006, *F08b Guideline for Structural Health Monitoring*
- [18] <https://www.lifewind.dk/about-lifewind>
- [19] Wangwen Z, Wei-Ting H, 2020, *re-evaluation of fatigue thickness effect based on fatigue test database*, Journal of Marine Science and Engineering
- [20] Richmond M, Smolka U and Kolios A, 2020, *Feasibility for Damage Identification in Offshore Wind Jacket Structures through Monitoring of Global Structural Dynamics*, ROMEO project article.
- [21] Pedersen M, 2019, *Thickness effect in fatigue of welded butt joints – a review of experimental works*, International Journal of Steel Structures, <https://doi.org/10.1007/s13296-019-00254-y>
- [22] Ghalishooyan M, Shooshtari Ac, 2015, *Operational modal analysis techniques and their theoretical and practical aspects: a comprehensive review and introduction*, 6th international operational modal analysis conference Gijón, Spain
- [23] Stutzman J, 2017, *Cathodic Corrosion Protection in the Context of Lifetime Extension of Monopile-based Offshore Wind Turbines*, Master's thesis in Master Programme Sustainable Energy Systems
- [24] Cevasco D, Tautz-Weinert J, Kolios A, Smolka U, 2020, *Applicability of machine learning approaches for structural damage detection of offshore wind jacket structures based on low resolution data*, ROMEO project article, Journal of Physics: Conference Series 1618(2020)
- [25] Gkatzogiannisa S, Weinertb J, Engelhardt I, Knoedela P, Ummenhofera T, 2019, *Correlation of laboratory and real marine corrosion for the investigation of corrosion fatigue behaviour of steel components*, International Journal of Fatigue 126 (2019) 90-102
- [26] <https://www.grow-offshorewind.nl/project/c-flo>
- [27] <https://www.offshorewind.biz/2016/06/16/monitor-jip-consortium-creating-structural-health-monitoring-system-for-offshore-wind-farms/>

- [28] <https://owi-lab.be/maxwind>
- [29] <https://www.blauwecluster.be/project/soil-twin>
- [30] Natarajan A, Dimitrov N. K., William Peter D. R, Bergami L, Madsen J, Olesen N, Krogh T, Nielsen J, Sørensen J. D, Pedersen M, Ohlsen G, Lauritsen J. L, Daub P, Steiniger M, Jørgensen E, Vives X, Skriver S, Simmons G, Ahmadikordkheili R, ... Bruun S, 2020, *Demonstration of Requirements for Life Extension of Wind Turbines Beyond Their Design Life*. DTU Wind Energy. DTU Wind Energy E, No. E-0196
- [31] <https://community.ieawind.org/task42/home>
- [32] Weijtjens W, Stang A, Devriendt C, Schaumann P., 2020, *Bolted ring flanges in offshore-wind support structures - in-situ validation of load-transfer behaviour*. Journal of Constructional Steel Research. 2021 Jan;176. 106361. <https://doi.org/10.1016/j.jcsr.2020.106361>
- [33] Schafhirt S, Page A, Eiksund G. R., and Muskulus M, 2016, *Influence of soil parameters on the fatigue lifetime of offshore wind turbines with monopile support structure*, Energy Procedia, vol. 94, pp. 347–356
- [34] Aasen S, Page A.M, Skau K.S, and Nygaard T.A, 2017, *Effect of foundation modelling on the fatigue lifetime of a monopile-based offshore wind turbine*, Wind Energy Science, vol. 2, no. 2, pp. 361–376.
- [35] Ens G, Tsiapoki S, 2020, *Probabilistic approach for detection of scour on monopile substructures using measured SHM data*, www.woelfel.de.
- [36] Sadeghia N, D'antuonoa P, Noppe N, Weijtjens W, Devriendt C, 2020, *Towards A Comprehensive Fatigue And Crack Propagation Toolbox For Offshore Wind Foundations*, EAWE PhD Seminar December 2020
- [37] Mehmanparast A, Brennan F, Tavares I, 2017, *Fatigue crack growth rates for offshore wind monopile weldments in air and seawater: SLIC inter-laboratory test results*, Materials and Design 114 (2017) 494–504
- [38] Clemens H, Weijtjens W, Gebhardt C, Rolfes R, Devriendt C, 2019, *Validation of Improved Sampling Concepts for Offshore Wind Turbine Fatigue Design* <http://www.mdpi.com/1996-1073/12/4/603>
- [39] Noppe N, Clemens H, Christof Devriendt C, Weijtjens W, 2020, *Validated extrapolation of measured damage within an offshore wind farm using instrumented fleet leaders*, TORQUE 2020
- [40] Iliopoulos A. N., Weijtjens W, Van Hemelrijck D, Devriendt C, 2016, *Remaining useful life assessment of offshore wind turbines: Validation of virtual sensing on long term measurements*. In: 8th European Workshop On Structural Health Monitoring (EWSHM 2016)
- [41] Henkel M, Häfele J, Weijtjens W, Devriendt C, Gebhardt C.G, Rolfes R, 2020, *Strain estimation for offshore turbines with jacket structures using dual-band modal expansion*, Marine Structures 71 (2020)
- [42] Tarpø M, 2020, *Stress Estimation of Offshore Structures*, PhD Thesis.
- [43] Santos F, Noppe N, Weijtjens W, Devriendt C, 2020, *SCADA-based neural network thrust load model for fatigue assessment: cross validation with in-situ measurements*, Journal of Physics 1618, doi:10.1088/1742-6596/1618/2/022020
- [44] Mai QA, Weijtjens W, Devriendt C, Morato PG, Rigo P, Sørensen JD, 2019, *Prediction of remaining fatigue life of welded joints in wind turbine support structures considering strain measurement and a joint distribution of oceanographic data*. Marine Structures. 2019 Jul;66:307-322. <https://doi.org/10.1016/j.marstruc.2019.05.002>

Finding meaningful representations of SCADA-log information for data-driven condition monitoring applications

Simon Letzgus^{a,b}

^aTechnische Universität Berlin, Machine Learning Group

E-mail: simon.letzgus@tu-berlin.de

Keywords: wind energy, SCADA log data, condition monitoring, NLP, machine learning

1 Introduction

Analysis of data from supervisory control and data acquisition (SCADA) systems to monitor wind turbine condition has attracted considerable research interest in recent years. Most approaches utilize time series data from sensors placed all over the turbine and apply methods from the machine learning (ML) domain for early failure detection (compare [1]). Besides, SCADA systems usually produce log-files which contain information about operation conditions or control events but also warning and alarm messages in case sensors measurements come close to or exceed pre-defined limits. In the condition monitoring context, this data is also of high value and has been used to filter and annotate sensor time series [2], identify message-patterns related to failures ([3], [4], [5]) and predict unplanned stoppages directly from the log-messages ([3]). However, most of these approaches use time-sequence or probability-based analysis rather than ML methods. One reason is that a ML model usually requires a numeric vector representation of fixed size as input. The challenge of finding such representations for symbol sequences of variable length is well known in the ML domain, especially in natural language processing (NLP). Within this study, we extend the Correlated Occurrence Analogue to Lexical Semantic (COALS) algorithm by incorporating temporal information (COALS-t) and apply it to SCADA log-data. We demonstrate that the method can find meaningful representations of SCADA log messages and message sequences. This enables the application of off-the-shelf ML methods. The approach will be illustrated using multiple years of operational SCADA data from several turbines. The remainder of the paper introduces the SCADA data set (section 2) and the methods being applied (section 3) before presenting and discussing the results (sections 4 and 5).

2 SCADA log data

Format and content of SCADA log files vary for different manufacturers and systems. What they have in common, however, is a tabular structure in which operational events are logged in temporal order. Each event is assigned a starting time which often is accompanied by additional temporal information, such as an event end time or the time of an event-related turbine restart. Apart from the mandatory temporal information, events are usually characterized by an event identifier, mostly a system-specific multi-digit event code, and a short event description which gives high-level information about the nature of the event and therefore helps operators, maintainers and analysts to partially decode the cryptic event-ids. Other columns of the log file might contain a classification of the event into different severity categories (information, warning, alarm, fault), assign the event to a certain turbine sub-assembly or provide information on the current operational status of the turbine. Due to the wide range of potential log configurations and formats this study will focus on representations derived from basic information which can be found across almost all SCADA log files, namely start-timestamp, message-ids and message description.

For the analysis, we use data SCADA data from a wind farm consisting of 5 geared 2 MW turbines with asynchronous generators. Over 2 years 313,590 log messages were generated by the wind farm's

Turbine	A	B	C	D	E	Farm
Total messages	76,485	54,068	61,014	60,983	61,040	313,590
10min avg	0.73	0.51	0.58	0.58	0.58	2.98
10min max	179	94	223	601	66	610
Unique messages	165	184	154	226	150	281

Table 1: Summary statistics of wind farm log count

Timestamp	ID	Description
2020-12-11 10:23:45	m_005	high temperature tX: X°C
2020-12-11 11:23:50	m_097	pause Xkw Xrpm
2020-12-11 11:23:50	m_157	extra info. err:309
2020-12-11 11:28:50	m_055	restart

Table 2: Exemplary excerpt from log files.

SCADA system which corresponds to an average of around 3 messages per 10min interval (compare Table 1). However, in some 10min intervals, up to 610 messages were triggered. These numbers are in line with earlier count-based analysis of WT SCADA logs (compare [4]). The log data format contains a single (start) timestamp and a description of each message from which a unique message-id can be derived (compare Table 2).

3 Methods

We first introduce the NLP tools used in this study, then discuss their application to the given data format. Therefore, we will generally talk about the representation of log-instances and afterwards emphasize the different implications for event ids or event descriptions. Finally, we introduce some metrics to evaluate the representations.

3.1 Methods to find log-message vector representations

A rather straight forward representation of a non-numeric data instance is a so-called one-hot-encoding. For a fixed set of unique instances $M = (m_1, m_2, \dots, m_N)$ each instance is represented by a binary N -dimensional vector R_{OH-m} with all but one entries being set to zero. The non-zero entry at position i uniquely identifies the instance m (compare (1)). This generally enables the application of ML-algorithms and it has been applied in the context of SCADA log processing (e.g. in [3] to detect pitch faults based on SCADA-logs and in [5] for alarm clustering). However, the method creates overly sparse high-dimensional representations which at the same time do not contain any information about relations between instances. This points towards a powerful concept in NLP which is to describe an instance with the help of its surrounding.

$$R_{OH-m} = [r_1, r_2, \dots, r_N] \quad \text{with} \quad r_i = \begin{cases} 1 & \text{if } m = m_i \\ 0, & \text{otherwise} \end{cases} \quad (1)$$

Within this study, we adjust and apply the Correlated Occurrence Analogue to Lexical Semantic (COALS) algorithm [6], a method from the Latent Semantic Analysis (LSA) family. It extracts vector representations by singular value decomposition (SVD) of a normalized instance co-occurrence matrix (compare 1). We propose to incorporate the temporal information contained by each log entry's timestamp into the co-occurrence matrix by adding up processed timestamp differences between neighbouring log messages instead of the commonly used counts (compare Figure 1). The inversion of the time-difference keeps the co-occurrence matrix intuitive with large entries representing high similarity (compare eq. (2)). Additionally, the parameter ϵ prevents numeric instability and acts as a bandwidth parameter which controls for how aggressive time differences are taken into account. Also, this allows for the window size to be selected rather large because the time-differences serve as a natural weighting factor (in NLP the window size is often a one-digit number since sentences usually don't stretch across thousands of words). The subsequent normalization and decomposition procedure remains as described in [6]. For the remainder of the paper, we refer to this procedure as COALS-t.

$$\Delta count_t = \frac{1}{\Delta t_{sec} + \epsilon} \quad (2)$$

Timestamp	Message
2020-12-14 10:07:03	m ₁
2020-12-14 11:01:15	m ₂
2020-12-14 11:23:50	m ₃
2020-12-14 11:23:55	m ₄
2020-12-14 20:31:17	m ₃
2020-12-14 20:31:22	m ₄

		Window count			
		m ₁	m ₂	m ₃	m ₄
Center	m ₁	0	1	0	1
	m ₂	1	0	1	0
	m ₃	0	1	0	3
	m ₄	1	0	3	0

		Window times *			
		m ₁	m ₂	m ₃	m ₄
Center	m ₁	0	2	0	0
	m ₂	2	0	4	0
	m ₃	0	4	0	20
	m ₄	0	0	20	0

* compare Δcount_t in equation (2) with $\epsilon = 1000$

Figure 1: Exemplary sequence of log messages (left) with construction of traditional count-based co-occurrence matrix (center) and the proposed time-based co-occurrence matrix (right).

3.2 Methods to find log-message sequence representations

In NLP series of words add up to sentences and then to documents which represent natural sequence structures to be analysed. In the log-analysis context, the question of how to properly define the length of a log-sequence is less trivial. When having in mind potential fusion of SCADA sensor and log data 10min intervals seem to be a reasonable choice allowing simple temporal synchronization between the two data formats. For other applications, event-based sequence selection might be more suitable (compare e.g. [5]). While the optimal choice of sequences will always be problem-specific, the methods to transform them into vector-representations are mostly independent from the actual sequence length.

A relatively simple but often sufficient representation of instance sequences is the so-called bag-of-words (BOW) or term-frequency approach. The sequence representation R_{BOW} is constructed by simply summing up all vector representations R_k of a sequence $S = (R_1, R_2, \dots, R_K)$ (compare (3 - left)). Despite ignoring the order of instances the method was often reported to be surprisingly effective, especially in text classification [7]. For our application both, the one-hot as well as COALS-t representations can be processed this way. An extension to the idea of a simple BOW sequence is to weight the individual instance representations R_i with their inverse sum of overall occurrences N_{R_k} (compare 3 - right). This incorporates the idea from information theory that rare instances contain more information and are therefore weighted higher. Such term-frequency inverse-document-frequency (TF-IDF) representations have been successfully used in the context of information retrieval and will be applied for log-sequences within this study.

$$R_{BOW} = \sum_{k=1}^K R_k \quad \text{and} \quad R_{TFIDF} = \sum_{k=1}^K \frac{R_k}{N_{R_k}} \quad (3)$$

3.3 Evaluation of log-representations

Before applying the individual NLP tools used in this study, lets quickly emphasize the goals we have in mind when applying them. The aim is to construct a dictionary which maps each log-instance or log-sequence to an M-dimensional real-valued vector. Additionally, we aim for the vector to implicitly contain information about the nature of the respective instance which facilitates solving a downstream task. This means one way to evaluate each set of representations is to evaluate their corresponding performance on the specific task. However, in this study, we discuss representations generically which makes such an extrinsic evaluation infeasible. Therefore, we focus on so-called intrinsic evaluation which tests the representations for coherence with our intuition. In our example, this would mean that syntactically or semantically similar events are grouped closer together in vector space than their unrelated counterparts. Put concretely, we evaluate log-message-representations for the intuitive principles shown in Table 3 and compare distances between those grouped examples against distances to other message representations. For the evaluation of the log-sequence representation we rely on the same intuition: we assume that message sequences that proceed the same error message look more similar than the sequences proceeding other error messages. We therefore evaluate and compare the similarity of sequences consisting of the messages triggered in a 10-minute window before the respective error message.

Similarity in vector space is measured utilizing different distance metrics which can be applied to both, log-embedding and log-sequence-embedding evaluation. For binary comparisons of representations,

Table 3: Examples for different categories of SCADA log-message similarity

	Syntactic twins	Syntactic / semantic siblings	Semantic cousins
Description	messages almost identical	message body with major similarity	syntactically different but shared root
Example	igbt pump off igbt pump on	feedback = 0, hydraulicmotor feedback = 0, gearoil cool feedback = 0, nacelle fan	event service state 0 keq switch remote control pause pressed on keyboard

we apply the popular cosine similarity (compare 4). Additionally, we project the high dimensional vector representations into a two dimensional plain which allows for visualization and interpretation of the respective distances between individual instances. It must be noted that during the dimensionality reduction some information will be lost but the most prominent characteristics are usually preserved. In this study we apply t-SNE, a non-linear dimensionality reduction technique designed to preserve similarity information from the high dimensional space [8].

$$similarity(R_a, R_b) = \frac{R_a * R_b}{||R_a|| * ||R_b||} = \frac{\sum_{i=1}^n R_{ai} * R_{bi}}{\sqrt{\sum_{i=1}^n R_{ai}^2} * \sqrt{\sum_{i=1}^n R_{bi}^2}} \quad (4)$$

4 Results

4.1 SCADA-log messages representations

In this section, we focus on the analysis and comparison of the log-message representations. Since one-hot representations do not capture any inter-message relations we focus on the representations yielded by the COALS-t method. We chose a 10-dimensional vector representation obtained with a window size of 100 to either side of the central log-message and a temporal bandwidth ϵ of 1000.

Firstly, we will look at the representations of messages from the syntactic twins category. It must be noted that the method was not given any syntactical information about the messages itself. Similar vector representations of syntactically close messages emerge from the fact that they are likely to appear in a similar context. We automatically group all messages which syntactically differ by not more than 2 characters. Then we calculate the binary cosine-similarities within each of the 26 sub-groups, which contain up to four highly similar messages (quadruplets, if you will). As a result, we obtain 48 intra-group distance values. For their better interpretation, we compare them to an equal amount of binary cosine-distances between random messages. The results are shown on the left side of Figure 1. Messages of the twin category are indeed grouped much closer to each other in vector space than their randomly selected counterparts.

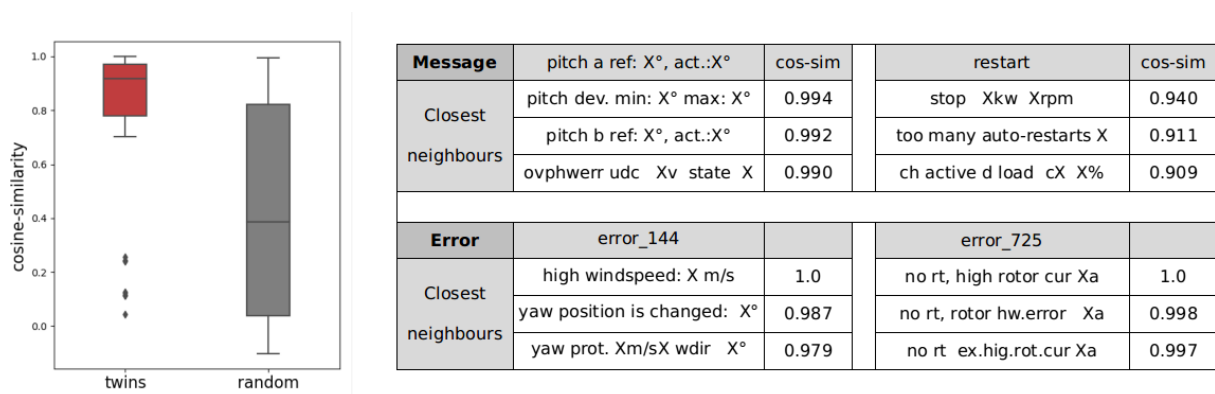


Figure 2: Left: comparison of similarity between twin and random messages. Right: examples of most similar messages to selected messages (top) and errors (bottom).

Secondly, we compare messages from the syntactic/semantic siblings and semantic cousins category by visualizing their two-dimensional t-SNE representations relative to all other messages (compare Figure 3). The top row presents three syntactic/semantic sibling examples where all message representations that contain the respective title words are highlighted. The bottom row presents semantic message clusters, such as the *Thermal* category which groups message names containing *high* and *temperature* or *ventilation* (or their respective abbreviations). The *Service* category contains messages connected to physical on-site visits (examples can be found in Table 3). The plots show that coherent message clusters connected to a particular frequent event (cable twist example), prevailing condition (thermal example) or general status (service example) are formed. Moreover, their relative position is partially intuitive as well. The cable-twist related messages for example can be found close to the clusters where most of the yaw-related messages are located indicating their causal relation. Finally, the *Error* example visualizes the relative location of error messages. Many can be interpreted by associating them with a nearby error message or the theme of their cluster (also compare Figure 2 -right/bottom). Note, that in the main region of service messages there is no related error messages indicating that service activities are not directly related to a specific error.

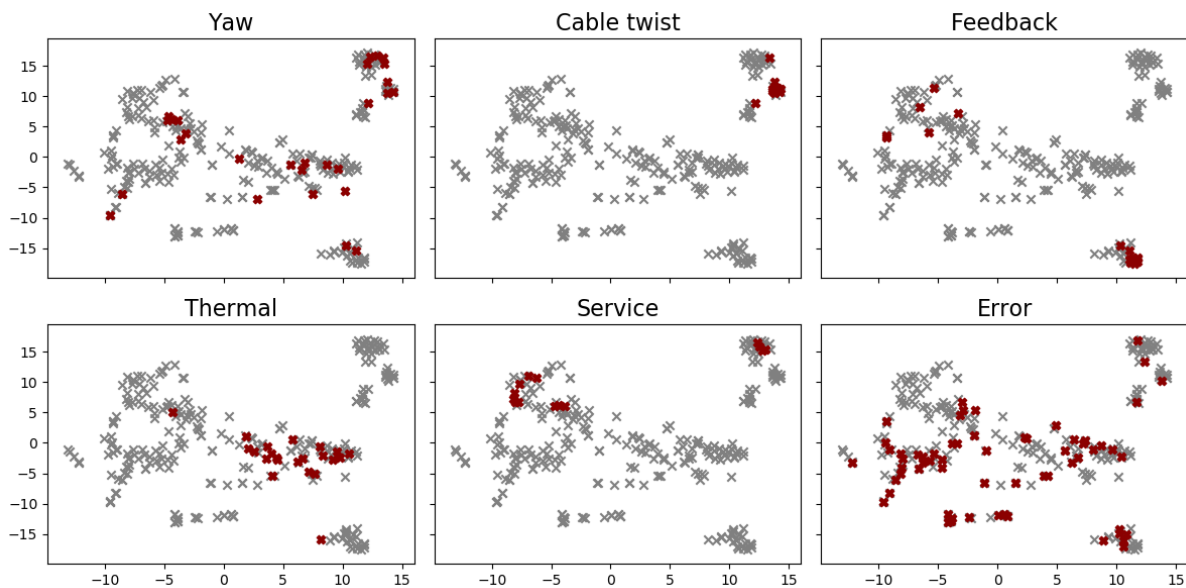


Figure 3: Visualization of t-SNE projections of message representations grouped by intuitive themes (red) in relation to all other messages (grey).

4.2 SCADA-log sequences representations

To construct the SCADA-log sequence representations we combine both presented methods of log-message encoding (one-hot and COALS-t) with either the BOW or the TF-IDF approach. This results in 4 different representations for each of 1341 sequences proceeding one of the 62 unique error messages. Since we want to run binary similarity comparisons we first had to exclude a few sequences connected to errors that occur only once during the recorded time. Then we compute the binary cosine-similarity within each error category. This means that if an error occurs five times in the data set we will compute 10 binary distances. This results in approximately 65,000 binary similarity measures for the same error-type analysis. To facilitate interpretation we calculate the same amount of distances in between sequences proceeded by different error types. The results in Figure 4 show that all configurations can group sequences proceeding the same error message closer together than their random counterparts. The one-hot configurations are characterized by a much stronger dissimilarity between randomly chosen sequences. COALS-t embeddings can minimize the distance between similar sequences, but the difference to randomly chosen sequences is not as pronounced. This might originate from the fact that the error messages themselves form clusters

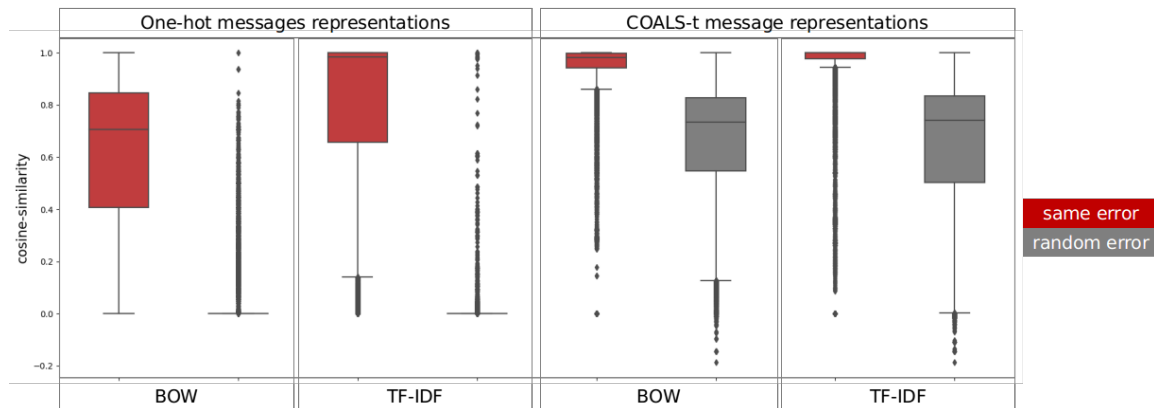


Figure 4: Cosine distances for sequences proceeding the same error messages (red) and random error messages (grey) for different combinations of log-message- and sequence-representations.

and a random choice does not ensure a large distance between them (compare Figure 3). When comparing the sequence representation methods itself superiority of TF-IDF weighting over the simple BOW becomes apparent in all configurations.

5 Summary & Discussion

The presented results show that methods from the NLP domain are powerful tools to find meaningful representations of SCADA log-messages and sequences. They allow to capture and encode syntactic and semantic similarities into the respective vector representations. This enables and facilitates the successful application of off-the-shelf ML algorithms for CM-related tasks. The proposed COALS-t method has shown to be particularly useful for analysis where relations between messages play an important role, such as log-message clustering or the investigation of causal relations between messages. The same holds for sequence embeddings based on COALS-t representations. On the other hand, sequences represented by a sequence of one-hot-encoded messages have shown to allow a sharper distinction between sequences related to different error messages. This could be a useful characteristic in an anomaly detection setting. Moreover, the results show that using a TF-IDF instead of a BOW approach amplifies the observations described above and is therefore preferable. However, this study represents only an initial step towards harvesting the full potential of SCADA-log information for data-driven CM applications. Further research has to prove the value of the proposed representations for respective CM-related tasks.

References

- [1] Tautz-Weinert J and Watson S J 2016 *IET Renewable Power Generation* **11** 382–394
- [2] Leahy K, Gallagher C V, Bruton K, O’Donovan P and O’Sullivan D T 2017 *Journal of Physics: Conference Series* (IOP Publishing) pp 1–14
- [3] Chen B, Qiu Y, Feng Y, Tavner P and Song W 2011
- [4] Qiu Y, Feng Y, Tavner P, Richardson P, Erdos G and Chen B 2012 *Wind Energy* **15** 951–966
- [5] Leahy K, Gallagher C, O’Donovan P and O’Sullivan D T 2018 *IET Renewable Power Generation* **12** 1146–1154
- [6] Rohde D L, Gonnerman L M and Plaut D C 2006 *Communications of the ACM* **8** 116
- [7] Liu Z, Lin Y and Sun M 2020 *Representation Learning for Natural Language Processing* (Springer Nature)
- [8] Maaten L v d and Hinton G 2008 *Journal of machine learning research* **9** 2579–2605

Offshore Wind Applications for Satellite-derived Met-Ocean Measurement

R Tait^a, D McMillan^a, C Clemente^{a,b}, and M Collu^a

^aUniversity of Strathclyde, Glasgow, UK

^bCentre for Signs and Image Processing, Department of Electronic and Electrical Engineering, University of Strathclyde, Glasgow, UK

E-mail: `rebekah.tait@strath.ac.uk`

Keywords: O&M

1 Introduction

The offshore wind industry currently makes little use of data obtained by satellites orbiting the Earth. For operational wind farms, this is generally limited to applications such as workboat tracking, communications, or weather modelling. This work looks to seek out further uses for satellite-derived data, specifically for met-ocean measurements, and investigate the feasibility of using such data within the life-cycle of an offshore wind farm.

There has been limited academic research thus far into the utilisation of satellite data within the industry. Broadly, existing research falls into two categories — wake modelling; and resource assessment [1][2]. This work seeks to expand upon this existing research, with a focus on extracting met-ocean characteristics from freely available SAR data, an area where there has been little to no research in the context of offshore wind.

2 Data

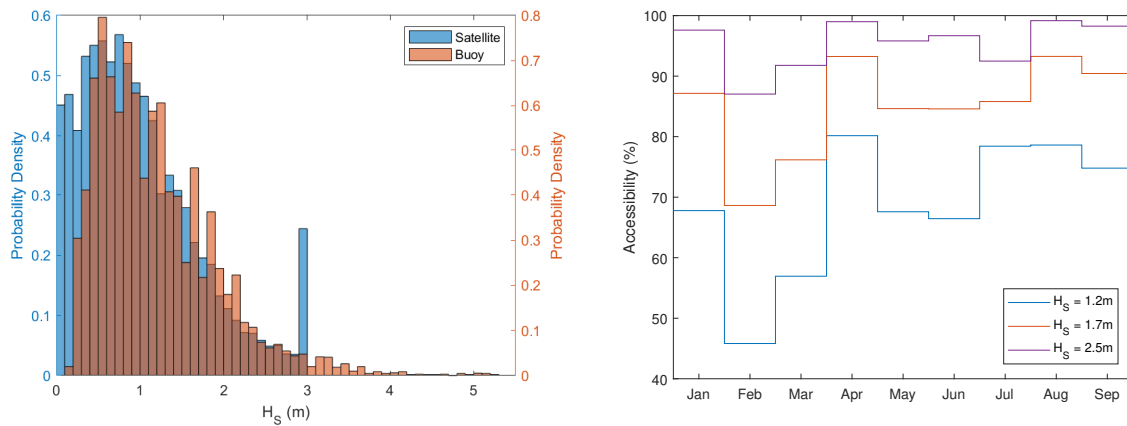
The data employed for this analysis was captured by the Sentinel-1 SAR satellites operated by the Copernicus programme, a joint EC and ESA initiative. Data captured by the Sentinel satellites is freely available to download via the *Copernicus Open Access Hub* [3]. The region of interest chosen for this project was the area of the North Sea which will soon be home to the world's largest offshore wind farm, Dogger Bank — specifically the zone covering the footprint of the first phase, Dogger Bank A. SAR data was downloaded from Copernicus encompassing the period from January 1st to September 30th 2020.

3 Method

The post-processing of the SAR data was performed using the *Sentinel Application Platform* (SNAP), to retrieve a wind field estimation from the wave features in the SAR images. An empirical relationship, derived from data in [4], was then utilised to transform the wind speed into an estimation of significant wave height (H_S) across the image.

4 Results

To validate the significant wave height derived in Section 3, H_S measurements from a nearby *Cefas* Wavenet buoy were utilised [5]. The probability density distribution of H_S determined by both methods



(a) Comparison of H_S derived from SAR data and Cefas buoy from January 1st – September 30th 2020 (b) Accessibility by month: January – September 2020 for three wave height limits

Figure 1: Significant wave height and accessibility data covering the 9 month period of interest

is shown in Figure 1a, which demonstrates reasonable agreement between the two measurements. Particularly, the roll-off in the shape of the curves after the peak is in good alignment. The spike at 3m in the satellite data is an artefact of the wind field estimation in SNAP, which took a maximum of 20ms^{-1} .

As mentioned, there is currently little research relating satellite-derived met-ocean measurements to the offshore wind industry. One area where a niche has been identified is that of access calculations for offshore O&M. For an offshore wind farm, operations and maintenance activities are limited by weather and access windows, with significant wave height typically taken as a limiting state.

For this analysis, three vessel types were considered, with varying wave height limits. Firstly, Crew Transfer Vessels (CTV) with a limit taken as 1.7m; Service Operation Vessels (SOV) with a 2.5m limit; and SOV daughter crafts with a limiting wave height of 1.2m.

Using the H_S values determined from the SAR images, the percentage of time that each vessel would have been able to operate was calculated on a month by month basis. For January to September 2020, the percentage of the time that the wind farm could be accessed by each of the three vessels is shown in Figure 1b.

5 Conclusion

By utilising Sentinel-1 SAR data, it has been shown that a measurement of significant wave height can be inferred to a reasonable accuracy. The feasibility of using this data in access calculations for an offshore wind farm has been demonstrated, and is a novel use for wave characteristics derived from satellites. The access considerations here could be applicable at the planning stage of an offshore wind farm, to replace or reinforce met-ocean data gathered by typical avenues such as point measurement or hindcast. Years worth of satellite data could be analysed to help form the access strategy for the wind farm. However, this type of data would not be feasible to use for access considerations within day-to-day operations due to the sparsity of the data available from the satellites.

References

- [1] James S F 2017 *Journal of Physics: Conference Series* **926** 012004
- [2] Hasager C B and et al 2005 *Wind Energy* **8** 403–419
- [3] Copernicus Open Access Hub 2020 ESA URL <https://scihub.copernicus.eu/dhus/#/home>
- [4] Dinwoodie I, Quail F and McMillan D 2012 *Proceedings of ASME Turbo Expo 2012* (Copenhagen)
- [5] Cefas 2020 URL <https://www.cefas.co.uk/data-and-publications/wavenet>

Intelligent Monitoring of Scada Data for Prediction of Failures in Wind Turbines

Jorge Maldonado-Correa^a, Sergio Martín-Martínez^a, Estefanía Artigao^a, Emilio Gómez^a

^a Renewable Energy Research Institute (IER) and DIEEAC-ETSII-AB, University of Castilla-La Mancha, 02071 Albacete, Spain

E-mail: jorgeluis.maldonado@alu.uclm.es

Keywords: Condition Monitoring, SCADA data, Fault prediction

Abstract

Condition monitoring and early detection of wind turbine failures are current research topics because of the benefits they offer in improving wind farm availability and reliability. In this regard, the use of data acquired by the SCADA system (Supervisory Control And Data Acquisition), is presented as a technically and economically viable solution for condition monitoring and early detection of failures in wind turbines, due to the availability of the data. With the help of artificial intelligence and automatic learning techniques, the set of data collected by the SCADA system can be converted into useful information for the early detection of wind turbine failures, thus facilitating wind turbine operation and maintenance tasks. Under this scenario, this research work proposes the development of a model to automatically predict failures in different wind turbine components sufficiently in advance, using data from the SCADA system and artificial intelligence techniques for this purpose. This model will contribute to the development of appropriate and efficient predictive maintenance, which will ultimately reduce the consequences of unexpected failures and the associated costs.

1 Introduction

The wind energy industry has experienced rapid growth worldwide in recent years, as stated by the World Wind Energy Council (GWEC) in its latest annual report, which shows that the wind power installed on the planet at the end of 2017 was of 546 GW, and by the end of 2019, it increased to approximately 650 GW [1].

The growth of wind power installed worldwide has been possible, among other aspects, thanks to the technological development of the different components and subsystems of wind turbines (WTs), and also thanks to the development of SCADA systems, which is responsible for guaranteeing the individual performance of the WT and the overall performance of the Wind Farm (WF).

Most modern WTs record more than 200 variables in intervals of 1 to 10 min using their SCADA systems, generating a rich historical data set of WTs and WF operational parameters. Several authors in the scientific literature explain the use of SCADA data to monitor WTs or to predict failures in a specific component of this. To name just one example, [2] is a recent work that presents a systematic review of the literature on the use of data from the SCADA system for the condition monitoring (CM) of WTs. In this literature review work, more than 90 scientific articles are analyzed, four research questions are posed, one of them has the objective of knowing which are the artificial intelligence techniques that are currently applied to the monitoring and prediction of WT failures, the results show that in 39% of the consulted studies artificial neural networks (ANN) are applied, and in 27% of the consulted works

Support Vector Machine (SVM) is used. This work presents a methodology for the development of a Machine Learning (ML) model for the prediction of failures in WT based on the operation data of the SCADA system.

2 Methodology

The present research work proposes the development of a model to automatically predict failures in different WT components sufficiently in advance, using data from the SCADA system and artificial intelligence techniques. The methodological process used in this research will be developed in two stages (Figure 1a), which are described below:

Stage I: Data collection and processing: the collection, systematization and labelling of SCADA data are carried out. Through the use of Big Data techniques, missing data and outliers are identified, and historical patterns of behaviour are established. Missing data in the dataset is filled in using the interpolation and regression methods. In addition, key performance indicators (KPIs) are established, based on the history of maintenance and replacement of WT components.

Stage II: Elaboration and validation of the model: In this phase, one of the cognitive services of Microsoft Azure will be used for the development of the WTs failure prediction model. The services requested initially include Azure ML, Anomaly Detector and Data Science Virtual Machines.

Figure 1b shows, through a flow chart, the main modules used in the failure prediction model. Once the algorithm has been trained, the model is validated using experimental testing techniques with information extracted from the SCADA that has not been part of any of the training stages, which allows verifying if the system does not overfit the data provided in the training.

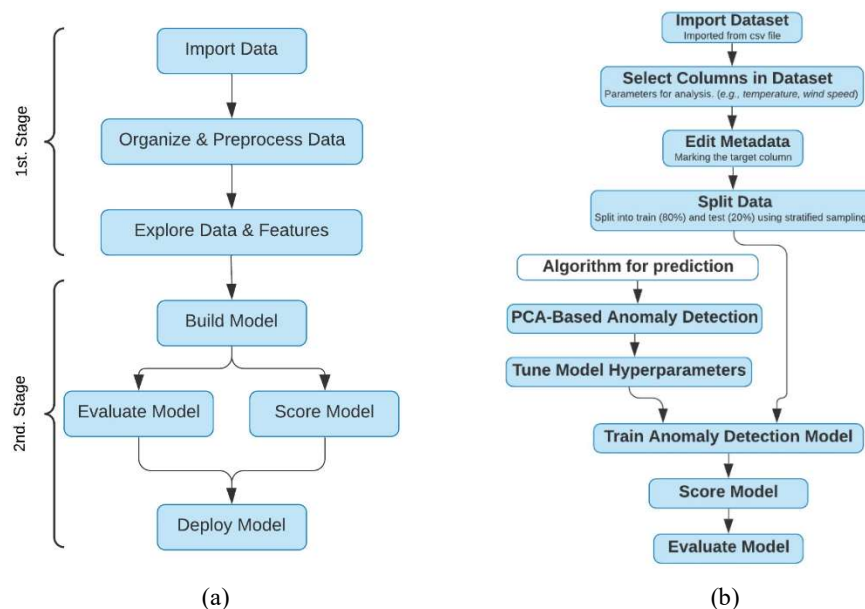


Figure 1 (a) Machine learning flowchart. (b) Flowchart with the use of library blocks of Azure ML.

Acknowledgements

This research was partially funded by the Junta de Comunidades de Castilla-La Mancha and the E.U. FEDER (SBPLY/19/180501/000287), and Microsoft AI for Earth Grant.

Bibliography

- [1] Global Wind Energy Council GWEC., “Global Wind Report 2019,” Brussels, 2020.
- [2] J. Maldonado-Correa, S. Martín-Martínez, E. Artigao, and E. Gómez-Lázaro, “Using SCADA Data for Wind Turbine Condition Monitoring: A Systematic Literature Review,” *Energies*, vol. 13, no. 12, p. 3132, Jun. 2020, doi: 10.3390/en13123132.

Early Failure Detection in Wind Turbines using Kramers-Moyal Coefficients

Ch Philipp^{a,b}, M Wächtera, J Peinke^a, and J Freund^b

^a ForWind Center for Wind Energy Research, Institute of Physics, University of Oldenburg, 26129 Oldenburg, Germany

^b Institute for Chemistry and Biology of the Marine Environment, University of Oldenburg, 26129 Oldenburg, Germany

E-mail: Chritian.Philipp@Uni-Oldenburg.de

Keywords: Wind Turbine, Operation and Maintenance, Early Failure Detection, Stochastic Differential Equation, Langevin Equation, Kramers-Moyal Coefficients

Abstract

We model wind turbine data with the Langevin equation. In this work we present a new kind of estimator for the Kramers-Moyal coefficients in order to estimate the drift and diffusion of components in wind turbines. We use highly resolved temporal wind turbine data in order to improve state observation and by that early failure detection. We use the first and second Kramers-Moyal coefficients to estimate the coupling between different components of a wind turbine. The first Kramers-Moyal coefficients, the drift, models the deterministic behavior of the system. The second Kramers-Moyal coefficient, the diffusion, reflects the stochastic behavior of the system. A component failure of a wind turbine will change the system's behavior, which in turn will be represented in the Kramers-Moyal coefficients.

We will show the accuracy of this method in comparison to the Nadaraya-Watson Estimator with a global bandwidth on simulated multi-dimensional time series. Furthermore, we give an outlook on how we want to use this method for this specific goal and we will show first results of this estimation method on real wind turbine data.

1 Introduction

Typically, the state of a wind turbine is observed via Condition Monitoring Systems (CMS) or 10-min averages of Supervisory Control and Data Acquisition (SCADA) operational data. In recent years, methods to analyze 10-min-SCADA-Data were studied but were found insufficient for early failure detection due to the poor time resolution. These data are usually stored but so far not widely used by the companies. High resolution data allow for the usage of more advanced analysis methods in comparison to working with the averaged data. Due to this, we have information about the fluctuations in the system and can use stochastic differential equations, namely the Langevin equation, to model and diagnose the system. In order to estimate the drift and diffusion of specific components of a wind turbine, a robust estimator for this task is needed. In this work, we present a new kind of estimator for the Kramers-Moyal Coefficients, which will be referred to as Linear Averaged Cluster Estimator (LACE). The LACE is used to estimate the drift for specific channels with temporal highly resolved ($\approx 1\text{Hz}$) SCADA operational data from wind turbines. Failures of components in wind turbines influence the dynamics of the system, and thereby the drift and/or the diffusion. Here, we show first results of the LACE on wind turbine data to approximate the drift of the active power considering the wind speed.

OFFSHORE WIND

Analysis of hub height cluster wake velocity deficits

Arjun Anantharaman^a and Martin Kühn^a

^aForWind, Institute of Physics, Carl von Ossietzky University Oldenburg, Küpkersweg
70, 26129 Oldenburg, Germany

E-mail: arjun.anantharaman@uni-oldenburg.de

Keywords: Offshore wind farms, cluster wakes, wind turbine wakes, scanning lidar

1 Introduction

In June 2020, Germany set a target for offshore wind energy of 20 GW by 2030 (65% share of renewable energy in gross electricity consumption) and further 40 GW by 2040 [1]. To facilitate such an expansion, more wind farms will be inevitably set up in proximity to each other. This results in the operation of wind farms in the (partial) wake region of their neighbours, characterised by lower wind speeds, higher turbulence and reduced power output. The first evidence of far-reaching wind farm wakes was observed via satellite images and aircraft measurements [2]. The length of these wakes was found to strongly depend on the atmospheric stability, reaching as far as 55 km downwind in stable atmospheric conditions [3]. It is thus imperative to study the effects of these wind farm wakes or "cluster wakes" and their effect on not only surrounding wind farms but also the atmospheric boundary layer.

Remote sensing has proven to be an effective tool in offshore wind farms to detect these cluster wakes, due to the ease of remote measurements and large areas/trajectories possible for scanning [3, 4]. However, cluster wakes have not been classified accurately in a quantitative way yet, as engineering models fail to predict the wake development downstream. The objective of the current work is to analyse the near cluster wake region of a large offshore wind farm and its development downstream using lidar measurements.

2 Lidar measurements

A long-range Doppler lidar (type Leosphere WLS 200S) placed on the transition piece (24 m a.s.l.) of a wind turbine enables wind velocity measurements at distances up to 8 km. The scans are averaged over a period of 90 minutes, where the wind direction remains nearly constant. Plan-Position-Indicator scans are used to observe the wakes downstream of the GlobalTech 1 wind farm, situated in the German North Sea. Each scan takes about 2 minutes and the elevation angle of the scanner is fixed at 0.8° , resulting in higher measurement locations at longer distances. Parameters such as the sea surface temperature, humidity, pressure and air temperature are obtained from sensors placed on the transition piece with the lidar. The instantaneous atmospheric stability is thus available for the entire measurement period. Using the stability corrected logarithmic law assumption, all the velocities are extrapolated to hub height to obtain the velocity field, as shown in Figure 1.

The definition of a cluster wake requires a "free-stream" velocity of the wind as a comparison to observe the reduction in velocities due to the presence of the wind farm. The free-stream velocity is quantified in the current scan scenario as the mean of the velocities in the region unaffected by the wind farm in the dominant wind direction (South-East sector of Figure 1 with higher velocities). Since the inflow velocity is not known, the deficit is thus defined as the difference in wind speed between the free-stream and the wake region as followed in other studies [2, 3]. The selection of the wake region and its boundary is performed manually on a scan-by-scan basis.

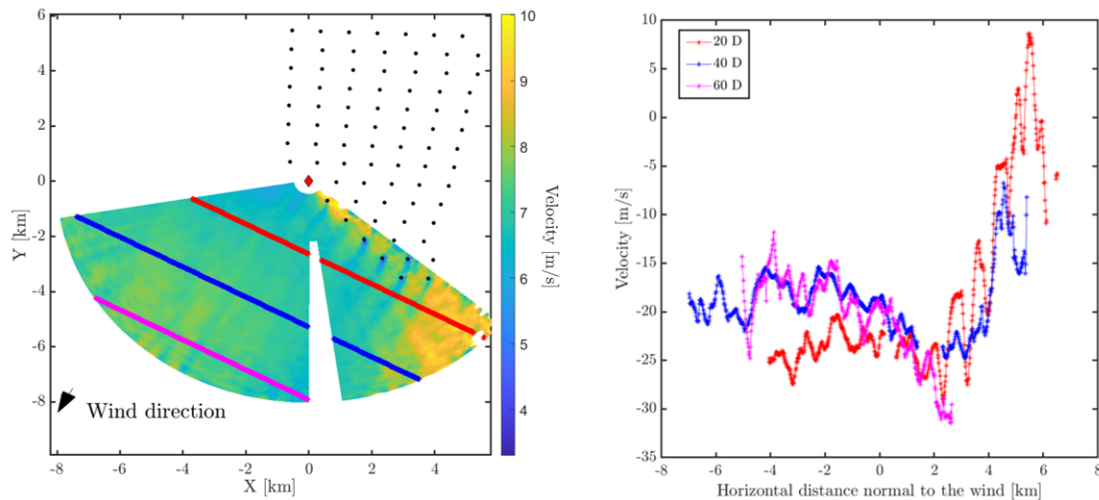


Figure 1: (a) Lidar (red diamond) scan with corrected velocities in an unstable atmospheric case averaged over 90 min. (b) Velocity profiles at $20D$, $40D$ and $60D$, colour coded accordingly.

3 Results and outlook

A sharp boundary is observed between the wind farm wake and the free-stream wind at hub height that is partially sustained downstream (~ 60 rotor diameters or $60D$) for weakly unstable and unstable atmospheric conditions. Differences in the wind speed within the wake region and the free-stream are then compared at successive downstream distances. The reduction in velocity is between 10-20% at roughly $20D$, but there are other cases where the reduction is as high as 25% at $50D$. For unstable conditions, the wake recovery is expected to be quicker due to enhanced vertical mixing. In the current scenario, the wake deficit maintained, though it is not possible to predict with the current dataset how this will develop further. It is nevertheless interesting to observe these phenomena 5 km downstream, when other studies in unstable atmospheres show wakes fully recovering at 15 km [2, 5].

Future work is aimed at the analysis of more cases and a deeper look into the velocity profiles to try and understand how the wake develops in a physical sense. Applications of this work could improve large scale wake models and aid in the efficient planning and operation of future offshore wind farms.

Acknowledgements

The project LIKE (Lidar Knowledge Europe) H2020-MSCA-ITN-2019, Grant number 858358 is funded by the European Union.

References

- [1] German Cabinet Approves 40 GW by 2040 Offshore Wind Target — Offshore Wind URL <https://www.offshorewind.biz>
- [2] Platis A, Siedersleben S K, Bange J, Lampert A, Bärfuss K, Hankers R, Cañadillas B, Foreman R, Schulz-Stellenfleth J, Djath B, Neumann T and Emeis S 2018 *Scientific Reports* **8**
- [3] Schneemann J, Rott A, Dörenkämper M, Steinfeld G and Kühn M 2020 *Wind Energy Science* **5** 29–49 ISSN 2366-7451
- [4] Nygaard N G and Christian Newcombe A 2018 *Journal of Physics: Conference Series*
- [5] Cañadillas B, Foreman R, Barth V, Siedersleben S, Lampert A, Platis A, Djath B, Schulz-Stellenfleth J, Bange J, Emeis S and Neumann T 2020 *Wind Energy* **23** 1249–1265 ISSN 10991824

Installation and decommissioning of large floating offshore windfarms

Rahul Chitteth Ramachandran, Jimmy Murphy^a, Cian Desmond^a

^a MaREI, University College Cork, Ireland

E-mail: rahulcr33shiptech@gmail.com

Keywords: Floating wind, Installation, Operation & Maintenance, Decommissioning, Innovations

1 Introduction

In recent years, the amount of energy generated by offshore wind farms has risen steadily. In the global scenario, there is still a lot of potential for growth in this sector. The focus is gradually shifting from shallow water to deeper water, where there is an untapped resource that is still not properly exploited. As the wind turbines move to deeper waters, they invite additional challenges in the design, installation, operation and decommissioning operations. The installation, O&M and decommissioning processes for fixed offshore wind energy represent up-to a third of the total cost of an offshore wind farm [1]. In the case of floating wind farms, this is expected to be even more complex and costly, as there is an additional challenge due to the motion of the vessel and wind turbine due to the prevailing meteocean conditions. This presentation study will provide an overview of the engineering and economic challenges associated with floating wind turbines and the innovations with the greatest potential to provide solutions. The work represents the initial stages of a PhD in which a detailed analysis will be conducted to systematically identify and assess innovations and technologies to reduce the LCOE (Levelized Cost of Energy), risk and environmental impact of the various marine activities associated with floating wind arrays. The PhD work would be carried-out at MaREI Centre, University College Cork, Ireland in active collaboration with MARIN, Wageningen, Netherlands. The PhD fellowship is part of the STEP4WIND project which is funded under the Marie Skłodowska-Curie H2020 ITN Research Program.

The additional challenges applicable to deep water marine installations are not unknown. Similar challenges were faced by the O&G industry when the drilling installations moved to deeper waters (eg: North Sea). Floating offshore wind is not just an extension of the offshore wind energy industry, but a new technology. Numerous technological, geological and political factors will be important in the development of these systems [2]. There are clear signs that offshore floating wind turbines will be the next breakthrough in renewables. In the recent years, many O&G majors like Equinor, BP, Shell etc. have shown interest investing in the offshore floating wind business. This shows a major shift in the energy focus of the world. As the world faces climate change and global warming challenges, the call for renewable energy is higher than ever. Floating wind has enormous potential to cater to the cleaner and greener energy demands of the future. Since 2007, single prototypes have been installed off the coasts of Norway, Italy, Portugal, Sweden, Japan and the United States. The first fully functional floating offshore wind farm, Hywind Scotland, was installed 25km off the coast of Aberdeen, UK. Experts foresee that this trend is going to spread to other regions of the world, such as the US, Asia and the Middle East.

The offshore floating wind turbines (FOWTs) are huge, making it time consuming and expensive for construction and installation. Apart from this, these massive structures require anchors and mooring chains that weigh several tons, to operate in harsh environments. Minimizing the motion of the floater is also a challenge. Access to the FOWTs is another challenge that needs to be addressed. The various stakeholders that would play important roles and their level of engagement are needed to be assessed also [3]. This PhD work will focus on the various innovations that would help bring down the costs by addressing these challenges. In the first phase of the PhD study, the engagement of the key stakeholders in the installation, O&M and decommissioning of FOWTs will be identified and analysed. The important engineering, logistic and economic factors will also be considered during these assessments. This will give a clear idea on the factors that contribute to the costs as well as environmental impact, which will be critical to the progress of the work. The next step in the analysis will be to identify the various innovations and technologies with the potential to reduce the costs and environmental impact of the marine

operations. The knowledge and expertise in the fields of aerodynamics, hydrodynamics, structural engineering and ship operations would be utilized during these assessments. The various numerical tools and methodologies to analyse and test these innovations would be also identified. Numerical and analytical calculations will be performed to develop a robust theoretical model of the various innovations applicable in this scenario.

Some of the potential innovations are:

1. Shared use of mooring systems
2. Dynamic positioning during lifting operations
3. Centralized control during towing
4. Rapid mooring (de)coupling systems
5. Sea-bed preparation techniques
6. Walk-to-work for floating systems
7. Recoverable anchors
8. Artificial reefs for scour protection

Above listed innovations and technologies will be studied and analysed to assess the impact, risk and possibility of cost reduction, using the various numerical methods. A comprehensive study will be presented and the most promising will be selected for the next phase of the PhD study.

In Phase II, the focus will be given to the already identified innovations. The innovations will be studied in detail, potential to reduce impact will be thoroughly assessed and a viability plan for each innovation will be produced. The engineering methods developed at MARIN will be used to analyse the impact of these innovations on the transport and installation of FOWTs, as well as the environmental footprint. Experimental facilities at MARIN will be utilized to test and verify the theoretical models developed.

In the Phase III, these innovations are studied in depth and the impact assessment for each innovation and viability plan will be presented. It is expected that these innovative methods would help in reducing the LCOE and environmental impact individually or combined. The impact of the use of these techniques on workability during other operational phases can be further investigated. It is expected that this PhD work would help in the better understanding of towing and installation operations of large FOWTs and factors, such as towing stability, tug handling, operational logistics and hydrodynamic response in waves. Also, it would help in identifying the role of simulations and experimental techniques for the assessment of the impact of installation innovations on cost, risk and environmental impact. Finally, the comprehensive guidelines on the assessment of innovations for the reduction of impact during installation and decommissioning phases of FOWT farms will be produced.

It is expected that this PhD work will be applied to commercial activities, and will support the realization of optimized, cost-effective wind farms with the least carbon-foot print and environmental impact. The presentation of the PhD work would serve as guidance and advice to the students and researchers, on the importance and need of the development of floating wind energy sector. It will also emphasize on the various challenges on the way and the innovations that would address and tackle them. Also, it will provide the analysis necessary to allow industry and policy makers to make investments and frame policies that will promote and lead to the growth of offshore floating wind sector in all parts of the world.

2 Bibliography

- [1] A. Kolios and F. Brennan, "Deliverable Report 8.1 : Review of existing cost and O&M models , and development of a high fidelity cost/revenue model for impact assessment," 2018.
- [2] N. Bento and M. Fontes, "Emergence of floating offshore wind energy: Technology and industry," *Renewable and Sustainable Energy Reviews*, pp. 66-82, 2019.
- [3] D. Ahsan and S. Pedersen, "The influence of stakeholder groups in operation and maintenance: Lesson from Denmark," *Renewable Energy*, vol. 125, pp. 819-828, 2018.

Advanced Physical Modelling Methods for Floating Wind Turbines

Navid Belvasi, Cian Desmond, Jimmy Murphy

Centre for Marine and Renewable Energy, Environmental Research Institute, University
College Cork, Ireland

E-mail: Belvasi.navid@gmail.com

Keywords: FOWT, Experimental Testing, Aero-Hydro Loading, LCOE Modelling, High-Quality
Validation Datasets

1 Introduction

Currently, offshore wind farms have a significant share of wind power generation due to their capacity to produce higher and more unimpeachable renewable power. Respecting offshore wind share in the green energy market, the technology of floating wind turbines is developing at a remarkable pace. Comprehending the 30 MW project in Scotland and the 24 MW Atlantic project in Portugal [1], Europe can be undoubtedly the world leader in offshore wind technology. At least seven countries on the continent have comprehensive plans to install and fully benefit offshore wind turbines in the next decades. New projects are underway in France, the UK, Norway, Portugal, Spain, Italy and Sweden, and Europe plans to increase the share of offshore winds in electricity generation by 25% until 2050. Evaluations show that by 2022, Europe has the potential to install floating wind turbines in the North Sea, Atlantic and Mediterranean with a nominal capacity of 330 MW. To achieve the European perspective, this capacity must be increased to 150 GW by 2050, which means that by this year, about a third of all offshore wind turbines will be floating.

For the technology to become fully commercial, costs must cut down. FOW is still more expensive than fixed offshore wind because this technology is in the early stages of development. However, under the right conditions, the FOW can potentially lower costs for Europe. Therefore the cost-cutting rhythm of this type of power generator platforms can be significantly reduced, even compared to fixed offshore wind market. As we have seen so far [2], the rate of these costs has dropped dramatically from 150 €/MWh in 2014 to 65 €/MWh in 2017. The FOW cost in Europe for current operational sites is in the order of 180 to 200 €/MWh for pre-commercial projects. While these were relatively small projects, large-scale projects can bring with them learning technology effects, and it also significantly reduces the central costs of each project.

In order to extract the maximum possible power from offshore wind turbines, it is crucial to examine and design its parts for responding to different operating conditions of the studied area. The development of advanced numerical modelling approaches will be vital in developing our understanding of these technologies, reducing risk and accelerating the development of cost-saving innovations. It is an indisputable fact that experimental testing is an integral part of validating numerical works, especially in the case of floating offshore wind turbines, where the uncertainty of applied force on the platform substructure and presents of ocean-wave by itself, increase the order of uncertainty to indicate farm's output power. Therefore, robust open access validation data sets are required to allow the development and benchmarking of these numerical codes.

The present research intends to create an open-source database for validation purposes and develop multi-disciplinary capabilities and methodologies for designers, engineers, and researchers of the

offshore wind field. For this idea, various aspects of the physical modelling of the problem will be examined. Through the development of the desired methodology, a tight relationship will be established with researchers and industrial designers in this field so that the developed methodology meets their design requirements. This research would prepare reference material for future numerical simulations and researches in this field. To complete the desired database, traditional experimental approach and most up-to-date methods are two available options. Traditional testing methods, such as classic wave basin testing are abundant in this field and always render relatively accurate results. However, these methods always have a specified level of accuracy and resolution. It is impossible to accurately understand the studied flow regime's insights and the phenomenon within it.

Stereo Particle Image Velocimetry (SPIV) technique can offer considerable enhancement to overcome the limitations of the mentioned methods. It is a more comprehensive and concrete approach, enabling the test taker to extract results to an accuracy of several thousand points [3]. Additionally, the dimension of the test environment is one of the slightest obstacles and are solely restricted to the type of lens used for the device. Moreover, granting the high frame-rate in this device's cameras, phenomena with a transient nature can be efficiently captured and monitored. Accordingly, this research will utilise underwater stereoscopic PIV to provide high fidelity data which describe the full 3D flow around a series of fixed and floating structures. In general, the experimental set up of the Stereo-PIV device includes two or more digital cameras, a light source, light-sheet op-tics, and a synchronisation unit [4]. In this manner, the fluid is pervaded with traceable particles that can be reached and examined by the device, and digital cameras record the overall path of the fluid particles. All Stereoscopic systems, regardless of widespread use in different industries, can record two or more scenes simultaneously but from different angles of view. Then the captured views are merged by one of the sorting algorithms to create a three-dimensional image of the phenomenon.

Given the challenges and uncertainties in developing a comprehensive method, a multi-step approach has been considered to increase the process accuracy, initially starting with a simple working model. Gradually, in the intermediate steps, hydrodynamic loads, aero-hydro reloads, the effects of considering survival waves and subsequent slamming, and other essential and decision-making parameters will be added to the model. Therefore, these parameters will be examined in the form of several steps to drive the method and advance the edge of knowledge in different marine experimental testing areas. Then a comprehensive database will be created in the final steps by considering the critical fundamental and detailed parameters in the experimental test, in a dimensionless way. So that researchers and designers would have access to comprehensive validation data for different scenarios, utilising either new or old approaches for their works. Finally, this method will not suffice in this state and economically locate the optimal methodology. Besides, the LCoE models developed in UCC during the FP7 LEANWIND project will address the economic challenges in each offshore wind project and also be included and validated in the methodology. Therefore this comprehensive methodology will provide a broader understanding of the challenges facing the floating wind energy industry. With this model's aid, the impact of innovation across the lifecycle of the wind farm will also be considered. To make a long story short, this comprehensive model, as a reliable contemporary dataset, will contain almost all of the essential engineering and economically parameters that guide the decision-makers through the planning and engineering calculations up to construction phases.

Bibliography

- [1] Floating offshore wind is gearing up for take-off, Windeurope, <https://windeurope.org/newsroom/news/floating-offshore-wind-is-gearing-up-for-take-off/>.
- [2] Floating offshore wind energy- a policy blueprint for Europe, Windeurope, 1 October 2018
- [3] Pan, Z., Zhang, *et al.*, Unscented Kalman filter (UKF)-based nonlinear parameter estimation for a turbulent boundary layer: A data assimilation framework, 2020 *Measurement Science and Technology*, 31 (9), art. no. 094011
- [4] ITTC, Guideline on Best Practices for the Applications of PIV/SPIV in Towing Tanks and Cavitation Tunnels, 7.5-02 -01-04.

A methodology for the design optimization of modular support structures for offshore wind turbines with focus on reliability.

S Drexler^a and M Muskulus^a

^aDepartment of Civil and Environmental Engineering, Norwegian University of Science and Technology (NTNU), Trondheim, Norway

2020-11-27

E-mail: sebastian.drexler@ntnu.no

Keywords: offshore wind turbines, support structures, reliability-based design optimization

Abstract

Within the design of wind turbine support structures, it has always been a major goal to ensure a resource saving design. This classical optimization problem is typically solved by the application of deterministic design methods. The underlying structural calculations are based on characteristic values, where possible uncertainties are observed by predefined safety margins. However, the design practice changes towards the application of probabilistic methods since they promise higher and more economic utilization of the structural resources by detailed consideration of the actual uncertainties. Finding an appropriate design becomes now a reliability-based design optimization problem. Since these methods are computationally expensive their solution can be quite challenging. Particularly, when more complex support structures are considered like jackets. For this, existing solution strategies are exemplary presented and discussed. Further, possibilities for future research within this field is outlined.

1 Introduction

The main objective in future wind turbine designs is to produce energy in the most economical way. Besides striving for high efficiencies during the actual turbine operation, the reduction of costs and utilized resources to a minimum within the structural design are of prime importance, leading to a typical optimization problem. Focusing on tower and sub-structure designs of offshore wind turbines, already various investigations exist on finding optimized solutions. Thereby mainly classical deterministic design approaches are implemented where predefined safety margins and characteristic design values are used. In contrast to this, the consideration of uncertainties during the optimization process and by that, converting this deterministic optimization into a reliability-based design optimization (RBDO), is more of a novel idea. Taking uncertainties into account during a structural analysis provide the possibility to adjust the applied safety concept more precise towards the actual real-world design conditions. Compared to the rigid and universally valid safety concept within deterministic design, this gives possible room for higher utilizations and therefore more economical designs. Since this approach is computationally costly, it was shown so far that RBDO for offshore wind turbines is generally feasible, but more reasonable for rather simple support structures such as monopile designs [1]. Therefore, it is at first striven for to demonstrate the application of RBDO on more complex support structures, e.g. jacket structures. Later on, it can be aimed for an extension of the RBDO problem towards another promising idea, namely to design support structures in a modular way. This approach could give the benefits that the manufacturing process can be easily industrialized going along with possible cost reductions, and that the structural modules can be simply adapted to different site conditions. The problem to solve is then to find a suitable methodology to determine optimal module shapes for given site conditions under consideration of uncertainties. In this paper the aim is therefore to give an overview of the challenges within RBDO of conventional jacket

support structures, and to present and discuss possible ideas on how to overcome them. The document is structured thereby as follows: Section 2 introduces the general concepts of reliability-based structural design, RBDO and the main challenges arising when offshore wind turbine structures are considered. Sections 3 and 4 present examples of existing solution approaches and show possible ideas and research topics which seem promising to explore.

2 Background

Reliability-based structural design

As mentioned in the introduction, reliability-based structural engineering is the discipline of structural design with consideration of uncertainties. Traditionally, when it is spoken of deterministic design the structural analysis is conducted based on characteristic loads, resistances and fixed design properties together with a general-purpose safety margin compensating for possible uncertainties. In contrast to this, within reliability analysis possible uncertainties are explicitly broken-down and quantified in order to evaluate the performance of the structure for its purpose. In the context of wind turbine support structures this purpose mainly corresponds to the non-occurrence of structural failure during the intended design life. The measurement of the performance is thereby often expressed through the failure probability p_f . However, since it is common within structural design to rather describe the safe state than the possibility of failure, the performance measure is often also expressed through the probability that no structural failure will occur which is denoted as reliability R . Failure probability and reliability are complement events, meaning $R = 1 - p_f$. To obtain these performance measures random variables \mathbf{X} are introduced which bring the actual uncertainties into the design process as they portray the statistical behaviour of the loads, the material properties and all other quantities with major impact on the design, e.g. variations in the soil stiffness. Typically, random variables are expressed through analytical probability distribution functions or at least their second moment representations. Together, they define a probability space which contains all possible combinations of realizations of these random variables. The underlying probability density is described by the joint probability density function (PDF) $f_X(\mathbf{X})$. The probability space possesses a safe domain where specific realizations of these random variables do not lead to failure, and a failure domain where this is actually the case. The border between safe and failure domain is described by the limit state function (LSF) $G(\mathbf{X})$ which is dependent on the studied failure mechanism. The simplest form of a LSF is described by the basic reliability problem $G = R - S$ comparing a resistance R with a load effect S where failure occurs when $G(R, S) \leq 0$. Even this LSF can be complex, non-linear and dependent on a variety of different random variables. Failure for an arbitrary shaped LSF is therefore simply described through the generalized form $G(\mathbf{X}) \leq 0$. The related failure probability p_f of the structure corresponds then to the integral over the PDF within the failure domain's limits which are defined by the LSF:

$$p_f = P[G(\mathbf{X}) \leq 0] = \int \cdots \int_{G(\mathbf{x}) \leq 0} f_X(\mathbf{x}) d\mathbf{x}$$

The iterated integral has a dimension equal to the number of considered random variables. Its direct evaluation is only possible for simple problems. The majority of engineering applications require the utilization of numerical integration, sampling approaches or second-moment and transformation methods. Most prevalent in practice are the First Order Reliability Method (FORM) and the Monte Carlo Simulation (MCS) technique. Within FORM the failure probability is estimated by transformation of the problem into the standard normal space and by linearization of the LSF through a first order Taylor series expansion. Thereby the linearization point resulting in the highest failure probability, which is often denoted as most probable point (MPP), is found through special search algorithms [2]. FORM is exact for linear LSF and considered as an adequate approximation for non-linear cases, although the implementation can be elaborate. In contrast to FORM the application of MCS is the most straightforward approach to estimate the failure probability. This is done by randomly sampling the values of the random variables and evaluating the LSF for each sample set \hat{x} . The amount of LSF evaluations leading to failure $\#(G(\hat{x}) \leq 0)$ in relation to the total number of samples N is an estimate for the failure probability

$$p_f = \frac{\#(G(\hat{x}) \leq 0)}{N}$$

The estimate possesses an error which in general decreases with $\frac{1}{\sqrt{N}}$. To achieve a sufficient accuracy the sample size should be chosen adequately high so that the additional model uncertainty has insignificant influence on the obtained results. Since failure probabilities within structural design are supposed to be very small, sample sizes of 100,000 and even more are not unusual. When each LSF evaluation of a sample set requires a sophisticated analysis, which is commonly the case in the context of structural analyses and especially within offshore wind turbine structures, the method becomes computationally expensive and the advantage of an easy implementation is balanced out. Further details on structural reliability and corresponding evaluation methods with focus on FORM and MCS can be found in Melchers [3] and Ditlevsen [4].

Reliability-based design optimization

The reliability-based design optimization (RBDO) can be considered as special case of structural optimization (SO). Within SO one tries to obtain an optimum design for a defined objective under the observance of specific constraints. RBDO extends the task by considering uncertainties as well. Generally, to draft SO problems special functions and variables need to be introduced. To define the property towards which the design is tried to be improved an objective function f is required. It describes the key measure that quantifies the performance of the design during the optimization process. This can be the total mass, overall costs or other characteristics important to the application of the structure. Also several objective functions can be implemented, in such cases it is spoken of multicriteria optimization [5]. In order to influence the objective function, the design must be modified. Hence, design variables \mathbf{d} are selected. These define specific design properties which are then exposed to possible changes. Their extent is significantly influenced by the selected type of optimization. Within the context of wind turbine support structures, the sizing optimization type is dominant. This means that the design variables typically correspond to properties of certain elements within a bigger system. During optimization the performance of the system changes but the general specifics of the system are retained. This becomes explicit when a jacket structure is considered. The design variables may correspond to certain thicknesses, diameters, distances or material parameters such as the yield strength. During the optimization process the values of these variables change, but the overall predefined jacket shape is maintained. Other optimization types like shape optimization and topology optimization which alter the overall design shape are not considered here. Beside design variables additional state variables \mathbf{s} are introduced which constitute the structural response and need to be observed during the SO, e.g. strains, stresses or deflections. The general SO problem can then be defined according to Christensen [6] as follows:

$$\begin{aligned} & \text{minimize } f(\mathbf{d}, \mathbf{s}) \text{ with respect to } \mathbf{d} \text{ and } \mathbf{s}(\mathbf{d}) \\ & \text{subject to } \left\{ \begin{array}{l} \text{design constraints on } \mathbf{d} \\ \text{behavioral constraints on } \mathbf{s}(\mathbf{d}) \\ \text{state problem} \end{array} \right. \end{aligned}$$

Thereby the design constraints set limits for the changeable design variables. These can be lower and upper values for geometric properties or certain ratios which must be observed, e.g. a thickness to diameter ratio for tubular cross-sections. Behavioral constraints are similar, but only applied to the state variables. They are usually used to implement required code checks, e.g. that no excessive yielding or buckling occurs. Both design and behavioral constraints can be summarized in some cases by a nested formulation. The remaining state problem defines the underlying structural task which must be analyzed, typically by a numerical simulation, to enable a verification whether the described constraints are satisfied. Traditionally, classical SO is based on a deterministic design approach, meaning certain safety margins are implemented to account for uncertainties. This type of SO is therefore referred to as deterministic design optimization (DDO). To formulate a RBDO, the SO problem is simply extended by an additional reliability constraint, e.g. that a maximum allowable failure probability must be observed. In doing so, the state problem becomes a reliability state problem which, as described earlier, require special solution approaches like FORM or MCS in order to be evaluated. The solution of the SO problem is generally an iterative process for which a variety of different algorithms exist. From gradient-based techniques, over gradient-free and heuristic methods, towards surrogate modeling algorithms, all approaches have in common that they require multiple computations of the state problem [7][8]. This can be already computationally demanding for DDO but rises dramatically in case RBDO is considered. It must therefore be clarified whether this considerable additional effort is appropriate. A justification

is given by Tsompanakis [9] considering the accompanying effects which occur by utilization of generally calibrated safety margins within DDO. Between the expected performance of a deterministic designed structure, where influences of uncertainties are assumed to remain steady as manifested through the applied safety margins, and the obtained performance with its real specific sensitivity towards uncertainties, a gap exists. This gap usually becomes larger when the structure is optimized which can be matched to the attempt of utilizing the available resources at a maximum. The design obtained by DDO is commonly located closely to the admissible domain boundaries, leading to a changed sensitivity towards uncertainties compared to a non-optimized design. Two cases can be derived from these mismatching reliability levels. Either the optimum obtained with DDO is less sensitive towards uncertainties and the expected performance is surpassed, or a higher sensitivity is in place and the reliability is thereby overestimated. It is comprehensible that both cases are far from an optimal design since resources remain unexploited, or even worse, the safety level cannot be trusted. The central issue, however, is that by application of DDO the information which case might emerge for the optimum design is not provided. Since RBDO can overcome this lack of knowledge by providing a design optimization approach which makes the influence of uncertainties manageable, its additional effort is justified.

RBDO in the context of offshore wind turbine support structures

The application of RBDO on offshore wind turbine support structures (OWTSS) involves certain specifics compared to other types of structures and it might therefore be helpful to get more insights on the underlying state problems. In general, to prove the structural integrity of an offshore wind turbine (OWT) several different limit states must be considered. The governing design standards of the International Electrotechnical Commission require the verification of the structure's ultimate strength, the fatigue strength, its stability or buckling strength and to conduct a critical deflection analysis in order to avoid rotor-tower-collisions [10]. At first glance, there is no difference compared to other structures, but the difficulties mainly lie within the OWT's non-linear dynamical behavior and the complex loading situations. For one, OWT are commonly prone to vibrations since they possess several slender and long members. Excitations can thereby emerge from wind gusts, wind shear and possible tower shadow effects, also a dynamic impact from other turbine components is prevailing [11]. For another, the overall loading of a wind turbine is always an interaction of cyclic, transient and stochastic effects and their possible combinations are diverse. This becomes more understandable when the major dynamic load sources of wind, wave and gravity are considered. Modern variable-speed wind turbines operate in a wide range of different rotor speeds, possible excitation frequencies due to the rotor's inertia loading hence change. Likewise, over the turbine's lifetime several distinct sea states with various wave periods occur, leading to a big bandwidth of different excitation possibilities. This is aggravated by the special aerodynamic damping property of OWT. In non-operational conditions the structural damping is mainly reduced to the material damping. During operation when the rotor blades are rotating, an aerodynamic damping effect appears which rises with increased rotor speed and which is substantial for the damping of the overall response [12]. However, the dampening effect is only present in the direction normal to the rotor plane which is referred to as fore-aft direction. Loads accessing the OWT from its side are experiencing much less damping. This is particularly important if wind and wave loading are not aligned and multi-directional. To consider all these different effects and their interactions among themselves, the application of multi-physics simulation software is required. The current state of the art primarily combines aerodynamics, hydrodynamics, structural dynamics and control dynamics, so that overall dynamic responses of wind turbine systems can be obtained through sophisticated analyses in the time domain. Several different open-source and commercial codes exist, an overview with comparison is given by Vorpahl et al. [13]. To obtain accurate results for verifying the governing limit states, a very high number of simulation runs are required. Already during the check for the ultimate strength several load case evaluations are needed, since so many excitation possibilities exist, and it is not known which of the extreme load cases will actually result in the maximum structural response. The fatigue evaluation is even more demanding. To perform a full fatigue analysis all possible combinations of different wind speeds, wave heights and wave periods must be considered in conjunction with the anisotropy of wind and wave. For a typical offshore site, e.g. the K13 site of the Upwind project [14], scatter diagrams can possess over 40,000 unique load cases. The design standards stipulate at least 10 minutes of simulation time during the determination of the structural response. Hence, it is evident that the large number of load cases and the high simulation effort makes a single structural verification of a wind turbine already to a very demanding task. If this is seen again

in the context of RBDO it is obvious that the required effort is increased by several magnitudes. No matter if methods like FORM or MCS are utilized, the limit states must be evaluated multiple times to complete a single reliability analysis loop, and again, many of such loops are necessary to perform the actual optimization process. The computational expense is simply too much, and a solution can only be of an approximating nature. The central issue to address is therefore to spot the existing possibilities to make the RBDO problem solvable at reasonable computational costs with sufficient accuracy.

3 Solving the RBDO problem

The key task to make RBDO possible is to overcome the high effort commonly involved during each optimization loop by solving the underlying reliability problem. Subsequently different existing approaches within the offshore wind setting are presented.

Simplification of the structural analysis

A common approach often used within structural engineering is the simplification of the model used for the determination of the structural response. Instead of conducting a complete multi-physics simulation, the problem is divided into separate parts. Chew et al. [15] for example are reducing the complexity of the transient analysis by implementing a linear de-coupled approach. The aero-servo loads acting on the rotor-nacelle assembly (RNA) are thereby still obtained within a multi-physics simulation environment for each wind speed. The time series of the resultant loads on the RNA are then used together with additional wave loads within a linear hydro-elastic model of the OWT system. To account for the aerodynamic damping effects the global system damping matrix is adjusted based on information gained from wind specific virtual decay tests. By this approach the elaborate aero-servo calculations need to be realized only once per wind speed. The actual load case evaluations are accordingly faster, and the obtained results have good agreements with a fully coupled aero-hydro-servo-elastic simulations since critical excitations and global eigenfrequencies are identified. Another decoupling approach worth mentioning is conducted by Schafhirt et al. [16]. Again, the RNA's aero-servo loads are computed within the time-domain and applied to a linear model. However, in this case the structural responses are not computed through further transient analyses, but rather by a technique called impulse based sub-structuring. The method is founded on the principle that for a linear system the total dynamic response can be calculated through superposition of several impulse responses. The load time series can be understood as a concatenation of several impulse loads. Each impulse load generates an individual response starting at a distinct point in time. The total response to the load time series is then simply the sum of all staggered responses. The integral expression for the response is often referred to as Duhamel integral [17]. Since the system is linear, only the computation of the response for a single unit impulse load is required. Within the referred investigation this is done in the time-domain with a unit load on the tower top node which is the same location on which the RNA's aero-servo loads would attack. This unit response is then simply scaled and shifted for each time step of the load time series. Since the remaining superposition process is just a summation, the method is extremely fast. Comparisons of the authors with multi-physics simulations show a good alignment. Solely the fact, that no wave loading is considered so far can be remarked as drawback. In order to add loading due to waves and current, the method requires the knowledge of unit impulse responses from every contributing degree of freedom (DOF), meaning the unit responses for each load direction of every submerged beam must be obtained. Adding these requires some preparatory work and a clever implementation which can be still rewarding in view of the possible gain in performance.

Surrogate modeling

Another widely used approach to accelerate the determination of the structural response within the reliability analysis loop is the utilization of so-called surrogate models (SM). These are also referred to as metamodels or response surfaces [18]. Within this approach the structural analysis is fully replaced by an approximation model which allows for a much faster determination of the structural response. In order to make such a prediction, the SM needs to be trained. This requires a basis set of structural response samples which are assigned to predefined input variables. Within the reliability context these input variables correspond to the involved uncertainties, so they usually match with the designated random variables required to establish the limit state function. The sampling process still relies on the original

structural analysis and simply computes responses for different manifestations of the input variables. The selection of appropriate manifestations or sample sets can be challenging since they determine the accuracy of the response. Different strategies exist like Latin Hypercube Sampling which tries to equally occupy the space of the input variables with a minimum number of required samples. In contrast, there are methods like importance sampling or stratified sampling which more focus on specific regions of the variable space [19] [20]. Their benefit become apparent when it is considered that the SM is detached from the actual physical background, meaning it can also be used to directly render the LSF. If for such cases, e.g. a FORM analysis is intended, the more focused sampling methods can achieve a higher accuracy if applied to the failure region. To implement such a SM based on obtained training samples, different approaches are available. The simplest form is the application of a polynomial interpolation function. Kim and Lee [21] are utilizing this method together with a FORM approach to perform a reliability analysis of a jacket structure under extreme load conditions. A further prevalent method used to generate the SM is the Gaussian Process Regression (GPR), or Kriging. GPR is a Bayesian non-parametric regression method utilizing a Gaussian process. Thereby, the spatial relationship between the obtained samples is described through a special covariance kernel function, and then used to make predictions for unknown locations [22]. In addition to the response approximation, the GPR methods returns information about the variance obtained during the prediction. This can be used as a helpful resource to measure the relative accuracy of the GPR, e.g. to evaluate whether a certain approximation is obtained from a region with sufficient sampling density or not. Although GPR is already used as SM for RBDO, the applications within offshore wind for purposes directly assigned to structural verifications are marginal. Yang et al. utilized the method to conduct a RBDO of a tripod structure [23]. Slot et al. implemented GRP as SM for the reliability analysis of rotor blades [24]. The heretofore mentioned practices have in common that they depend on a single set of design variables. If these are subjected to changes which can occur several times during a single optimization loop, the generation of a new SM must be performed. Dependent on the complexity of the structure, the number of load cases to consider and the amount of random or input variables, the effort for the SM generation can be still elaborate. A possibility to considerable reduce the computation cost is provided by Stieng and Muskulus [1]. Within their RBDO of a monopile support structure a compound SM is used. Therein the overall stochastic response is expressed as a combination of a design dependent mean response and a relative stochastic response. Based on earlier investigations of the authors this relative stochastic response can be assumed to be invariant as long as the design does not change considerable. This means in reverse that by knowledge of the relative stochastic response, the determination of the overall stochastic response only requires the calculation of the design depended mean response. This single SM fit approach decreases the computational effort drastically.

Simplification of the load approach

As mentioned in the introduction of the RBDO problem within the context of OWT, a high number of load cases must be evaluated, especially to determine the fatigue strength. Therefore, it is comprehensible that a reduction of these load cases has a direct impact on the computation time. A well utilized approach is introduced by Kühn [25] for load cases provided in the form of wave-wind-scatter diagrams. Based on simplified fatigue analyses the damage of each fatigue load case or elementary load cases is calculated. Then a lumping strategy is implemented which leads to a small number of load cases whose total damage is similar to the total damage obtained by the elementary load cases. Clear lumping instructions do not exist, but the author suggests strategies targeting for approximately similar damages per lumped load case or trying to consolidate all sea states associated with a certain wind speed class. The number of load cases can even be more reduced. Zwick and Muskulus [26] propose a simplified fatigue load assessment by implementing a regression based on a multivariate linear statistical model. By this the amount of load cases as proposed by Kühn can be reduced from 21 to 3 with a fatigue damage error of only 6%. With this low number of load cases RBDO can be accelerated significantly. However, it should be mentioned that these methods do not come without drawbacks. Dependent on the selected lumping strategy the consideration of dynamic effects can be inaccurate. The structural response is highly influenced by the prevailing wave period, but some lumping strategies simply disregard this dependence which makes overestimations or even an underpredictions of the total fatigue damage possible [27]. Another influence on the fatigue results is originating from the selected lumping location on the OWT structure. The accuracy is highest at that particular location but can decrease if other locations are evaluated.

4 Possible topics for further research

Single SM approach with extension

A fast-forward strategy to provide a performant RBDO approach for jacket structures would be to verify whether the presented simplification methods would be applicable as well. To start with, it would be very interesting to find out whether an adaption of the single SM fit approach described by Stieglitz and Muskulus would be possible. The approach has the major advantage that the modelling effort is comparatively low since existing multi-physics simulation software can be used as basic framework. This makes it easy to apply and attractive for an application in practice. Provided the constant character of the relative stochastic response can be confirmed for jacket structures, the method could be even extended by another SM which would render the deterministic response. If a state problem evaluation is required, the overall structural response is obtained by the two SM. This could be beneficial towards the optimization performance.

Adjusted frequency domain analysis

The requirement for sophisticated transient analyses is still a drawback since they require a lot of computational time. Unfortunately, this is still the case even when SM are utilized because of the required training samples. The application of linear models and the possibility to work within the frequency domain would accelerate the limit state evaluations dramatically, but as they do not account for non-linear effects, they might be inaccurate in cases where nonlinearities are prevailing. Interesting to investigate would be how these two approaches differ, e.g. for the fatigue limit state, and how this difference could be quantified. The research goal should be to provide a model, maybe realized through an artificial neural network, which adjusts the frequency domain analysis to follow the result of the full transient analysis. If it could be shown that this is feasible and that a possible dependency on changed design variables can be considered, then a significant reduction of the computational effort would be possible.

S-N curve and Miner sum as random variables

Up to this point, this topic is not addressed within the paper at hand, yet, but during implementation of a SM for a reliability-based fatigue verification, the selection of the random variables for the material resistance can be challenging. To elaborate this the Palmgren-Miner linear damage hypothesis is reviewed. Therein, failure of a structure or component is assumed to occur in case the total accumulated fatigue damage D , also denoted as Miner sum, reaches a critical value D_{cr} :

$$D_{cr} \leq D = \sum_{i=1}^k \frac{n_i}{N_i}$$

Therein k describes the number of considered stress ranges, n_i the number of stress cycles experiences at a certain stress range $\Delta\sigma_i$ and N_i the number of stress cycles leading to failure at that same stress range. Within this formulation two different material properties are combined. The material's resistance to cyclic loading with constant amplitude is described through the stress cycles to failure N_i which in turn are defined by the underlying S-N curve. Whereas the material's resistance to cyclic loading under varying amplitude is in a way processed by the critical damage value. Under deterministic measures this is normally not considered, but within a reliability analysis this distinction must be observed as suggested by the Joint Committee on Structural Safety (JCSS) [28]. Incorporating these two random variables within the fatigue resistance is challenging due to the non-linear character of the S-N curve which is why in several investigations only the critical fatigue value is chosen to be a random variable, whereas the S-N curve remains deterministic which is more conservative. It would be interesting to investigate how the random character of the S-N curve could be observed without an increase of the computational effort. Thereby it should be elaborated if it's enough to simply add the S-N curve parameter as an input variable for the SM, or whether a more sophisticated approach is required which could adjust the Miner sum afterwards without enlarging the SM.

Introduction of modularity

So far, there are several simplification methods available. They all share that they are merely applied to optimize a single facility for a particular location. As mentioned in the introduction, within this PhD project it is strived for to include a modular concept into the jacket structure design in order to utilize possible cost reductions through economy of scale. This could mean that as an outcome it is strived for to provide a range of different jacket or jacket module designs which are all optimized based on RBDO and suited for different environmental conditions. If then new wind parks are projected, instead of designing individual jackets, the appropriate design could be simply chosen from the available design catalog. This modular concept reveals several issues to approach. At first glance, a major research goal to investigate would be to find a suitable classification of the general boundary and environmental conditions. If the final portfolio should possess designs covering for possible constraints of a certain maritime area, e.g. the complete North Sea, then a methodology is required to gather all the environmental conditions of this region and to condense or classify them adequately for different environmental severities. These environmental classes would then serve as design bases for the catalogue jackets. In reverse, this methodology should also make it possible to select a design of the portfolio which would suit the best for a given location or use case. Another fundamental research goal would be to formulate the actual design optimization problem and to address the challenge of the design load characteristics. Otherwise to a single location, now a range or continuum of environmental conditions must be considered. It would be interesting to investigate how this can be implemented or how it changes the overall effort. A simple approach could be to deduct several discrete manifestations from the complete domain of this environmental condition range and to utilize these as multiple state problems. The optimum would then be a compromise between all these discrete manifestations, but with the drawback of very high computational costs. It should therefore be investigated whether a smoother approach exists which does not require the implementation of additional state problems.

5 Conclusion

After an introduction to the general RBDO problem, the specifics and challenges towards its application on offshore wind support structures are outlined. The central issue therein is exposed as the elaborate computational effort for which existing solution approaches are shown and discussed. Thereby, simplifications within the structural analyses are introduced which mainly utilize a de-coupling between the aero-servo calculations and the actual structural analyses of the support structure, or alternatively which make use of an impulse based sub-structuring approach which allows for a very fast calculation of the total response. Next, different surrogate model approaches are discussed which replace the sophisticated structural analyses by a more simple and faster approximation model. It is concluded with the presentation of load case lumping in order to reduce the amount of computational time during fatigue evaluation through radical reduction of the considered number of load cases. Following this, an outlook is given to address possible future research topics which could be interesting to investigate. It is outlined how a single fit SM approach could be adapted towards jacket structures and how it could be extended. It is addressed how frequency domain analyses could be used to accelerate the structural computation and how the consideration of uncertainty in the fatigue resistances could be simplified. Finally, the modularity within the design of jacket structures was discussed. It can be concluded, that a RBDO of jacket structures is generally feasible and economically possible if simplifications are introduced. Most promising are structural model simplifications and the implementation of SM.

References

- [1] Stieng L E S and Muskulus M 2020 *Wind Energy Science* **5** 171–198 ISSN 2366-7451 URL <https://doi.org/10.5194/wes-5-171-2020>
- [2] Rackwitz R and Fiessler B 1978 *Computers & Structures* **9** 489–494 ISSN 0045-7949 URL [https://doi.org/10.1016/0045-7949\(78\)90046-9](https://doi.org/10.1016/0045-7949(78)90046-9)
- [3] Melchers R E and Beck A T 2018 *Structural Reliability Analysis and Prediction* (John Wiley & Sons) ISBN 978-1-119-26599-3 google-Books-ID: tKMnjwEACAAJ

- [4] Ditlevsen O and Madsen H O 1996 *Structural reliability methods* (Chichester ; New York: Wiley) ISBN 978-0-471-96086-7
- [5] Haftka R T and Gürdal Z 1992 *Elements of Structural Optimization* 3rd ed Solid Mechanics and Its Applications (Springer Netherlands) ISBN 978-0-7923-1504-9 URL <https://doi.org/10.1007/978-94-011-2550-5>
- [6] Christensen P W and Klarbring A 2009 *An introduction to structural optimization (Solid mechanics and its applications no 153)* (Dordrecht: Springer) ISBN 978-1-4020-8665-6 978-1-4020-8666-3 oCLC: 254620396
- [7] Koziel S, Yang X S and Kacprzyk J (eds) 2011 *Computational Optimization, Methods and Algorithms (Studies in Computational Intelligence vol 356)* (Berlin, Heidelberg: Springer Berlin Heidelberg) ISBN 978-3-642-20858-4 978-3-642-20859-1 URL <https://doi.org/10.1007/978-3-642-20859-1>
- [8] Kochenderfer M J and Wheeler T A 2019 *Algorithms for optimization* (Cambridge, Massachusetts: The MIT Press) ISBN 978-0-262-03942-0
- [9] Tsompanakis Y, Lagaros N and Manolis P 2008 *Structural design optimization considering uncertainties* journal Abbreviation: Structural Design Optimization Considering Uncertainties Pages: 635 Publication Title: Structural Design Optimization Considering Uncertainties
- [10] Commission I E 2019 IEC 61400-1 Wind energy generation systems – Part 1: Design requirements
- [11] Manwell J F, McGowan J G and Rogers A L 2010 *Wind Energy Explained: Theory, Design and Application* (John Wiley & Sons) ISBN 978-0-470-68628-7 google-Books-ID: roaTx_Of0vAC
- [12] Anderson C 2020 *Wind Turbines: Theory and Practice* 1st ed (Cambridge University Press) ISBN 978-1-108-77746-9 978-1-108-47832-8
- [13] Vorpahl F, Strobel M, Jonkman J M, Larsen T J, Passon P and Nichols J 2014 *Wind Energy* **17** 519–547 ISSN 1099-1824 eprint: <https://onlinelibrary.wiley.com/doi/pdf/10.1002/we.1588> URL <https://doi.org/10.1002/we.1588>
- [14] Fischer T, de Vries W and Schmidt B 2010 139
- [15] Chew K H, Tai K, Ng E Y K and Muskulus M 2016 *Marine Structures* **47** 23–41 ISSN 0951-8339 URL <https://doi.org/10.1016/j.marstruc.2016.03.002>
- [16] Schafhirt S, Verkaik N, Salman Y and Muskulus M 2015 (International Society of Offshore and Polar Engineers) ISBN 978-1-880653-89-0 URL <https://www.onepetro.org/conference-paper/ISOPE-I-15-747>
- [17] Naess A and Moan T 2013 *Stochastic Dynamics of Marine Structures* (Cambridge University Press) ISBN 978-0-521-88155-5 google-Books-ID: 8B32BYME4XUC
- [18] Jiang P, Zhou Q and Shao X 2020 *Surrogate Model-Based Engineering Design and Optimization* Springer Tracts in Mechanical Engineering (Singapore: Springer Singapore) ISBN 9789811507304 9789811507311 URL <https://doi.org/10.1007/978-981-15-0731-1>
- [19] McKay M D, Beckman R J and Conover W J 1979 *Technometrics* **21** 239–245 ISSN 0040-1706 publisher: [Taylor & Francis, Ltd., American Statistical Association, American Society for Quality] URL <https://doi.org/10.2307/1268522>
- [20] Schuëller G, Bucher C, Bourgund U and Ouypornprasert W 1989 *Probabilistic Engineering Mechanics* **4** 10–18 URL [https://doi.org/10.1016/0266-8920\(89\)90003-9](https://doi.org/10.1016/0266-8920(89)90003-9)
- [21] Kim D H and Lee S G 2015 *Renewable Energy* **79** 161–166 ISSN 0960-1481 URL <https://doi.org/10.1016/j.renene.2014.11.052>
- [22] Roberts S, Osborne M, Ebdon M, Reece S, Gibson N and Aigrain S 2012 27

- [23] Yang H, Zhang X and Xiao F 2018 (International Society of Offshore and Polar Engineers) ISBN 978-1-880653-86-9 URL <https://onepetro.org/conference-paper/ISOPE-P-18-141>
- [24] Slot R M M, Sørensen J D, Sudret B, Sørensen L and Thøgersen M L 2020 *Renewable Energy* **151** 1150–1162 ISSN 0960-1481 URL <https://doi.org/10.1016/j.renene.2019.11.101>
- [25] Kühn M J 2001 *Dynamics and design optimisation of offshore wind energy conversion systems* Ph.D. thesis DUWIND, Delft University Wind Energy Research Institute Netherlands ISBN: 9789076468075 OCLC: 47225991
- [26] Zwick D and Muskulus M 2016 *Wind Energy* **19** 265–278 ISSN 1099-1824 _eprint: <https://onlinelibrary.wiley.com/doi/pdf/10.1002/we.1831> URL <https://doi.org/10.1002/we.1831>
- [27] Passon P and Branner K 2014 *Ships and Offshore Structures* **9** 433–449 ISSN 1744-5302 publisher: Taylor & Francis _eprint: <https://doi.org/10.1080/17445302.2013.820108> URL <https://doi.org/10.1080/17445302.2013.820108>
- [28] JCSS PROBABILISTIC MODEL CODE URL jcss-lc.org/jcss-probabilistic-model-code/

A methodology to evaluate advanced floating offshore wind turbine mooring system design

E M Schmitt^a and M Muskulus^a

^aDepartment of Civil and Environmental Engineering, Norwegian University of Science and Technology NTNU, Trondheim, Norway

E-mail: eva.m.schmitt@ntnu.no

Keywords: Floating Offshore Wind Turbine, Mooring, System Design

1 Introduction

Floating Offshore Wind Turbines (FOWTs) have been a strongly growing point of interest for academia and industry in the recent years; with development and testing of different prototypes ^{1 2 3 4 5} and the employment of the first full-scale FOWTs ^{6 7 8 9} taking place since around 2009, whereas the first FOWT wind park Hywind Scotland was constructed in 2017 ¹⁰.

The growing interest in FOWTs is founded on the advantages that FOWTs offer as opposed to the currently more widely employed bottom-fixed offshore wind turbines, being amongst others the potential of employment in deeper water depths [1] and prospective cheaper mass production.

However, as a still developing technology, FOWTs face certain challenges; for FOWT moorings in particular that is the lack of specific design guidelines for new design developments, such as e.g. multi-floaters, the question of which factors influence system reliability to which extend and how system reliability should be assessed. Also, as of now, there is no clearly defined procedure to achieve an optimal system design, and simulations using currently available modeling software are often very time-consuming and limited in their functionality.

The ongoing work will approach the above mentioned issues by developing a methodology to evaluate FOWT mooring system reliability, considering complex system configurations and new technological developments, such as multi-floaters and synthetic fibre rope.

Though, the limitations and high computation times of presently available software hinder the optimal workflow on methodology development. To illustrate; popular commercial mooring software, such

¹SeaTwirl – the future of offshore wind URL <https://seatwirl.com>, accessed 28.09.2020

²Das GICONR@-SOF schwimmendes offshorefundament URL <http://www.gicon-sof.de/en/sof1.html>, accessed 28.09.2020

³EOLINK cost effective floating wind parks URL <https://www.eolink.fr/en>, accessed 28.09.2020

⁴Final report summary - DEEPWIND (future deep sea wind turbine technologies)—report summary — DEEPWIND — FP7 — CORDIS — european commission URL <https://cordis.europa.eu/project/id/256769/reporting/>, accessed 28.09.2020

⁵VoltturnUS - advanced structures composites center - university of maine URL <https://composites.umaine.edu/research/voltturnus>, accessed 28.09.2020

⁶Hywind demo - equinor.com URL <https://www.equinor.com/en/what-we-do/floating-wind/hywind-demo.html>, accessed 28.09.2020

⁷Principle power, inc. - WindFloat URL <https://www.principlepowerinc.com/en/windfl>, accessed 28.09.2020

⁸Fukushima floating offshore wind farm - power technology—energy news and market analysis URL <https://www.power-technology.com/projects/fukushima-floating-offshore-wind-farm>, accessed 28.09.2020

⁹ideol floating platform—offshore wind power URL <https://www.ideol-offshore.com/en/floatgen-demonstrator>, accessed 28.09.2020

¹⁰Hywind scotland - equinor.com URL <https://www.equinor.com/en/what-we-do/floating-wind/hywind-scotland>, accessed 28.09.2020

as ORCAFLEX¹¹ or SIMA¹², are well validated and provide reliable results at the expense of a time-intensive computation, which is inter alia caused by using Finite Element Modeling (FEM) and a high degree of software complexity. As for commercial software, the source code is not accessible or editable by users, limiting the exploration of new, not yet embedded, concepts. To circumvent the inaccessibility of commercial code, open source software can be used. At the moment the most advanced open-source software is MoorDyn¹³, and while freely available and editable, its suitability is not ensured. A first analysis of the code has shown lack of ability to simulate multi-segment lines, multi-floaters, diverse number of mooring lines, amongst others.

Due to the aforementioned hindrances that current software presents, the methodology development will be implemented in a software which is created coupled with the methodology exploration. During its development, the software will be validated against the well established and experimentally validated SIMA. The software will allow for more adaptable and time efficient analysis of complex mooring systems, ultimately accompanying and enabling efficient research in methodologies for reliability assessment and optimization. By exploring the latter points, new insights into mooring reliability and design optimization will be gained, which may amongst others be implemented in future FOWT mooring guidelines as well as in determining the optimal mooring design for future FOWT projects.

The presentation in the 16th EAWE PhD Seminar on Wind Energy will focus on the planned improvements beyond the capabilities of the open source mooring software MoorDyn and touch on an early stage approach to methodology development for mooring reliability assessment and optimization.

References

- [1] Milborrow D *The Age of Wind Energy: Progress and Future Directions from a Global Perspective* ed Sayigh A and Milborrow D (Springer International Publishing) pp 3–22 ISBN 978-3-030-26446-8 URL https://doi.org/10.1007/978-3-030-26446-8_2

¹¹OrcaFlex-dynamic analysis software for offshore marine systems URL <https://www.orcina.com/orcaflex>, accessed 28.09.2020

¹²Marine operations and mooring analysis software — sima - digital solutions - DNV GL URL <https://www.dnvgl.com/services/marine-operations-and-mooring-analysis-software-sima-2324>, accessed 28.09.2020

¹³MoorDyn by Matt Hall URL <http://www.matt-hall.ca/moordyn.html>, accessed 20.09.20, website is currently not accessible

Condition Monitoring of Drivetrains in Large Offshore Wind Turbines

D W van Binsbergen^{a,b}, A R Nejad^a, and J Helsen^b

^aDepartment of Marine Technology, Norwegian University of Science and Technology (NTNU), Otto Nielsens veg 10, 7052 Trondheim, Norway

^bDepartment of Mechanical Engineering, Vrije Universiteit Brussel, Pleinlaan 2, Elsene 1050, Belgium

E-mail: dirk.w.van.binsbergen@ntnu.no

Keywords: Condition Monitoring, Fault Detection, Prognosis, Physical Model

1 Introduction

Wind turbines are moving further offshore and are increasing in size. Optimizing maintenance strategies for these large offshore wind farms can help reduce the cost of maintenance. Condition monitoring with the use of turbine supervisory control and data acquisition (SCADA) and vibration measurements can be used for early fault detection of wind turbine components. Based on the fault detection method and the fault diagnosed maintenance can be planned or a method for life extension can be applied. Conventional condition monitoring is generally based on data-driven methods that do not require a significant amount of system knowledge. Methods to diagnose faults are already developed and proven to work [1, 2, 3]. However, fault prognosis using data-driven methods is still a large challenge due to limited knowledge regarding the behaviour of the system. Further more, limited knowledge regarding slow rotating machinery and its behaviour and failure characteristics is known to this day.

Physical-based condition monitoring requires more system knowledge than for data-driven condition monitoring. Accurately predicting failure is difficult [4, 5] and more than often the properties needed to develop a physical-based model are not known by the wind turbine operator, leaving this as a not feasible method to determine the wind turbine condition and its remaining useful life (RUL).

2 Objectives

The objective of the PhD is to develop an advanced condition and health monitoring system by using a hybrid (physical and data driven) model which can detect early faults of rotating machinery, with emphasis on bearings and gears, in offshore wind turbines. This model is then further extended to determine the RUL of these components and will be verified using field experiments. The aim of the PhD is also to get a better understanding of large slow rotating machinery in non stationary and non linear load conditions and to reduce the overall model uncertainty through field experiments.

3 Methodology

First, a method is proposed to determine the system properties of a wind turbine drivetrain using SCADA data and vibration measurements. Using the acquired data a physical model using the software SIMPACK [6] will be developed, which is tuned on the system properties found by the inverse system identification and operational modal analysis. This model should be able to capture drivetrain dynamic behaviour in a way it can be used for RUL calculation.

The above methodology will first be applied on a commercial 1.5 MW drivetrain, instrumented with a SCADA system and proximity sensors on the main bearing and will later be applied on larger Multi MW wind turbines. Further details on the 1.5 MW turbine can be found in NREL/TP-5000-70639 [7] and NREL/TP-5000-71529 [8].

Gear properties will be determined using KISSsoft [9], bearing properties will be determined using finite element/contact mechanics modelling [10] and the shaft properties will be tuned on system properties found from stop, start or ringing occurrences found in the measurement data. SIMPACK [6] will be used to model the full drivetrain, which has been done previously by Nejad et al. (2016) [11] and Wang et al. (2020) [12].

4 Expected Results

The model will be used for damage estimation, fault detection and remaining useful life estimation.

References

- [1] Tautz-Weinert J and Watson S J 2017 *IET Renewable Power Generation* **11** 382–394
- [2] Schlechtingen M, Santos I F and Achiche S 2013 *Applied Soft Computing* **13** 259 – 270
- [3] Schlechtingen M and Santos I F 2014 *Applied Soft Computing* **14** 447 – 460
- [4] Gray C S and Watson S J 2010 *Wind Energy* **13** 395–405
- [5] Breteler D, Kaidis C, Tinga T and Loendersloot R 2015
- [6] Simpack. multi body system software . URL : <http://www.simpack.com>
- [7] Keller J and Lambert S 2019 Tech. rep. National Renewable Energy Laboratory. NREL/TP-5000-70639
- [8] Keller J, Guo Y and Sethuraman L 2019 Tech. rep. National Renewable Energy Laboratory. NREL/TP-5000-71529
- [9] Kisssoft ag . URL : <https://www.kisssoft.com>
- [10] Guo Y and Parker R G 2012 *Mechanism and Machine Theory* **51** 32 – 45
- [11] Nejad A R, Guo Y, Gao Z and Moan T 2016 *Wind Energy* **19** 1089–1106
- [12] Wang S, Nejad A R and Moan T 2020 *Wind Energy* **23** 1099–1117

An Optimal Control Strategy to Maximize Power in an Offshore Wind Farm by Reducing Wake Interaction

Nezmin Kayedpour^{a,b}, Arash E. Samani^{a,b}, Narender Singh^{a,b}, Jeroen D. M. De Kooning^{a,c}, Lieven Vandeveldel^{a,b}, and Guillaume Crevecoeur^{a,b}

^aDepartment of Electromechanical, Systems and Metal Engineering, Ghent University, Tech Lane Ghent Science Park-Campus Ardoyen, Technologiepark Zwijnaarde 131, B-9052 Ghent, Belgium

^bFlandersMake@UGent.be - Corelab EEDT-DC, B-9052 Ghent, Belgium

^cFlandersMake@UGent.be - Corelab EEDT-MP, B-9052 Ghent, Belgium

E-mail: nezmin.kayedpour@ugent.be

Abstract

Large-scale offshore wind farms are growing considerably fast in Europe. Optimal operational strategies are needed to improve the economic and reliability conditions of these sources. Maximising the total energy production, minimising the operating costs, and providing grid balancing services to transmission system operators are potential objectives of the optimal problem. This paper deals with an optimal operation strategy, which intends to optimise the operation of the whole wind farm by operating some wind turbines at sub-optimum points instead of optimising the power extraction of each wind turbine individually without considering the wake effect inside the wind farm. The wake formation can be minimised by reducing the wind turbine thrust force. Therefore, the axial induction based wake control can be achieved by adjusting the pitch angle and rotor speed, which results in an optimal tip speed ratio. In this work, we use the FLORIS model, which predicts the time-averaged three-dimensional flow field and turbine power capture of a wind farm as a function of the turbine control settings and the incoming wind field. The proposed approach is performed to analyse the axial induction control results in increased energy production. The analysis of the simulations of the C-Power phase one offshore wind farms in the North Sea indicates that the wake controlled strategy using axial induction control results in increased energy production.

Keywords: Wind farm, Wake control, Power maximisation

1 Introduction

The global energy consumption has been growing since the industrial revolution. In Europe, crude oil and petroleum products with their inevitable consequences on the environment are still quantifying the most significant energy sources. Fortunately, the European Union's (EU) goal is to make Europe climate neutral by 2050. The EU has been creating an inclusive and sustainable growth of renewable energy technologies over the past decade and has become a global leader in tracking the record of decarbonising power systems [1]. Wind energy offers the most extensive contribution to the EU renewable energy and is expected to be responsible for supplying up to 759 TWh by 2030, which will be 23% of electricity demand [2]. Deployment of offshore wind, in particular, and finance in its underlying technologies are fully supported by the European parliament and its established policies. There are now 110 offshore wind farms in 12 European countries with a total capacity of 22,072 MW [3]. The Belgian government is targeting to extend the installed capacity of wind farms in the North Sea up to 5.4 GW by the end of 2028.

For moving towards a truly green vision, two key elements need to be considered, i.e., the efficient integration of wind energy into the power grid by involving wind farms in the electricity market, which increases the grid resilience, and to enhance the energy production capability of wind farms by using optimal operation strategies. The stochastic nature of wind flow is the primary cause of the uncertainties, which have been introduced to the grid. A solution to this problem is that offshore wind farms actively contribute to grid balancing [4], which is quite challenging. Nevertheless, enhanced knowledge of fluid dynamics and improved forecasting algorithms, along with optimal control strategies, enable the offshore wind farms to maximise their total power generation by reducing the wake interaction among wind turbines, and might also enhance the capability of wind farms in positive contributions to grid balancing [5, 6, 7].

The conventional wind farm control approach relies on greedy control, in which the operation of wind turbines is optimised individually in order to maximise its power extraction and to minimise structural loading. However, advanced control strategy aims to optimise the wind farm total production by operating some turbines at suboptimal points to reduce wake interactions [8, 9, 10]. In particular, the Belgian offshore is recognised as a high-density production zone, the proposed approach might lead to a low variability of the wind farm power, especially in case of a severe turbulent condition [11]. Moreover, to enable offshore wind farms to comply with the grid codes requested by transmission system operators, the power reserve dispatching should be conducted such that the aerodynamic coupling is less affected by the wake [12, 13].

In literature, among wind farm operation and active wake control strategies, two major control approaches can be characterised, i.e., Axial Induction Control (AIC) and Wake Redirection Control (WRC) through yawing or tilting wind turbines [14]. Steering the wakes away from downstream wind turbines by operating the wind turbines with a yaw misalignment is widely discussed in the literature [15, 16, 17].

The concept of axial induction control, which is the focus of this paper, is to reduce upstream wind turbines' thrust force and weaken wake formations by adjusting their axial induction factor through the pitch angle or tip speed ratio. This enables downstream wind turbines to extract more power and experience fewer wake turbulences [14]. A control design is proposed in [8] based on a coordinated control between a wind farm centralised and wind turbine local controllers. The central controller optimises the operation of each wind turbine to maximise the farm total power production, and the local controllers are responsible for regulating wind turbine speed at a predetermined setpoint. Furthermore, advanced control approaches with the target of lowering the Levelised Cost Of Energy (LCOF), including the reduction of fatigue load and enhancement of grid support measures, gained much attention in recent years [18, 19, 20].

This paper investigates the optimal operational strategy of the C-Power phase one offshore wind farm in the North Sea, which consists of six 5MW turbines in a single row, based on axial induction control. Section 2 discusses the axial induction control method and its fundamentals. Section 3 introduces the control Strategy and Wind Farm Modeling. Results of the wind farm simulation are given in section 4. The paper concludes with a summary in section 5.

2 Axial induction nontrol

To achieve axial induction based control, which aims to reduce the wake deficit downstream by reducing the axial induction factor of upstream wind turbines, the free-streamed wind turbines need to be operated outside their aerodynamic maximum by increasing the blade pitch angle or reducing the tip-speed ratio (operating at a suboptimal) [21]. This reduces the mechanical power P_m and the magnitude of the rotor's thrust force F_T given by (1) and (2).

$$P_m = \frac{1}{2} \rho A C_P(\beta, \lambda) v^3 \quad (1)$$

$$F_T = \frac{1}{2} \rho A C_T(\beta, \lambda) v^2 \quad (2)$$

where ρ is the air density, A is the rotor radius, C_p is the power coefficient, which is a function of the pitch angle β and tip speed ratio λ , and v is the wind speed. The tip speed ratio is defined as the ratio

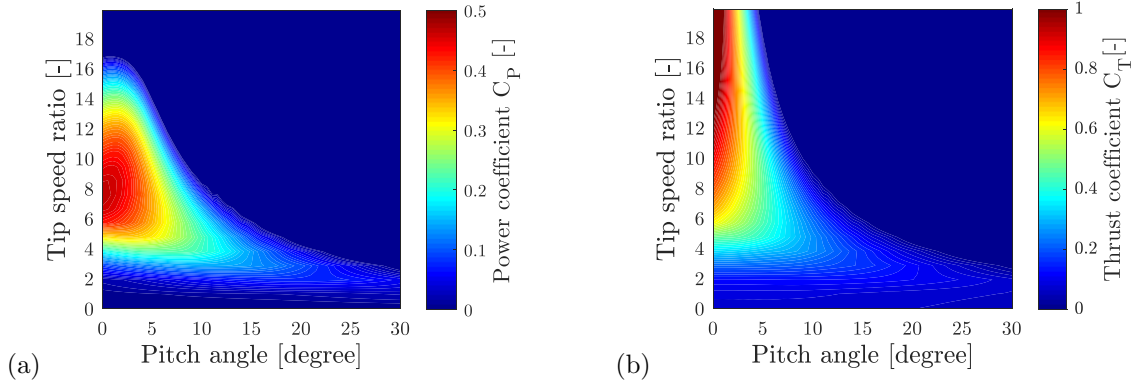


Figure 1: (a) Power coefficient and (b) Thrust coefficient in terms of the pitch angle and tip speed ratio distribution in the downstream direction.

of the blade tip speed over the speed of the incoming wind is given by (3).

$$\lambda = \frac{\omega R}{v} \quad (3)$$

The power coefficient and thrust coefficient of the 5 MW offshore turbine in terms of the pitch angle and tip speed ratio is shown in Figure 1. The power coefficient is 0.46 obtained at the pitch angle of 0° and the tip speed ratio of 7.56, whereas the maximum thrust coefficient of the wind turbine can be obtained at the pitch angle of 0° and the tip speed ratio of 18.6. Classically, the average wind velocity at the turbine can be given by the axial induction factor a . As shown in Figure 2, the extraction of energy by the turbine blades causes a reduction in the wind velocity at the turbine disk, and also in the wake of the turbine. Based on the continuity equation in the steady-state, the flow area will increase at the turbine, and even more at the wake, which results in flow reduction [22].

In this paper, the wake model available in FLORIS is employed, which incorporates Jensen's model incorporated with the wind farm model and its control tools [7, 23, 24]. It is necessary to have a sufficient understanding of the coupling between C_P and C_T to achieve the controllability of the wind farm. To provide a realistic description of turbine interactions in a wind farm, the 5 MW turbine model is simulated in FAST, which consists of a C_P/C_T table based on wind speed and blade pitch angle [7]. Moreover, C_P and C_T , correspond to the local conditions that each turbine is operating at, and can be defined as a function of the axial induction factor (a) as follows

$$C_P = 4a(1 - a)^2 \quad (4)$$

$$C_T = 4a(1 - a) \quad (5)$$

The wake model is also able to compute the turbulence that is generated by turbine operation and ambient turbulence conditions based on the number of turbines affecting the downstream turbines, the ambient turbulence intensity, and the added turbulence due to each turbine operation, which can be calculated in terms of C_T as a function of the axial induction factor.

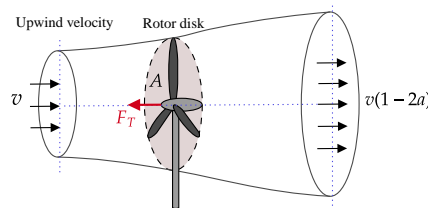


Figure 2: Stream-tube of a wind turbine.

3 Wind farm modeling and proposed control strategy

The simulation of the axial induction control strategy is implemented to the C-Power first phase offshore wind farm, which is the first operational wind farm located in the Belgian North Sea. The wind farm is neighbored by the second and third phases of the C-Power project consisting of 48 of 6M Senvion turbines with a total capacity of 295.5 MW. The first phase has been positioned in one row consisting of 6 5MW turbines with 500-meter distances between the turbines, which assumed are not influenced by the wakes of the C-Power second and third phases. The simulated wind farm layout and the flow estimation, by using FLORIS, is illustrated in Figure 3.

The purpose of axial induction control is to adjust the power production of upwind turbines away from their optimal settings to control the axial induction so that downwind turbines can produce more. This strategy is beneficial if the reduced power generation of the upwind turbine can be compensated by the downwind turbines and/or when the upstream turbine significantly affects the performance of the downstream turbines by its wake. In this work, the wind direction is aligned with a row of 6 turbines. For a given wind direction, maximum wake conflicts, less wake recovery, and fairly wake-rotor overlap can occur subsequently.

The wind farm total power generation is given by [25] can be maximized by solving the following optimization problem

$$\text{Max} \sum_{i=1}^6 \frac{1}{2} \rho A C_P(a_i) v_i^3 \quad (6)$$

Varying an axial induction factor a_i not only influences the power production of the turbine i but also changes the speed of the wind traveling downstream of the turbine i due to the wake interaction. The control parameters a_i can be iteratively updated to search for an optimized solution. The optimisation process for the below-rated wind conditions with 10% turbulent intensity performs a reference calculation using the modified C_P/C_T map based on the pitch setting. The wake parameters are computed at each turbine location to adjust the axial-induction factor of the individual turbine. It is worth mentioning that the power coefficient C_P is less sensitive to the control settings at the maximum operating point, whereas the thrust coefficient C_T is more sensitive to the pitch action. Therefore, only the pitch of the most upstream turbines is optimised in this process. Earlier studies have indicated that increasing the pitch angle of downstream turbines does not improve the energy yield [21].

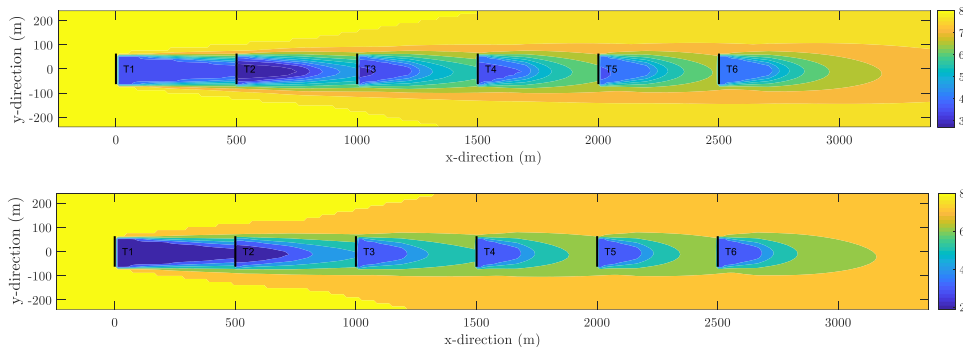


Figure 3: The layout of the simulated wind farm and flow estimation using FLORIS. Top: wake controlled. Bottom: nominal operation.

4 Simulation results

The results of the simulation at different wind speeds below the rated shows that using the axial induction control method can be beneficial in energy production since the overall power production is increased. The reduced turbulence intensity and the wake deflection of the upstream turbine can be observed in Figure 3. Due to the semi-uniform reduction in the axial induction factor, the wake shape remains similar for downstream turbines, and a small part of the kinetic energy of the wake can be diffused into the downstream turbine rotor diameter.

As shown in Figure 4, the power of the upstream turbine decreases when the wake controlled approach is activated through axial induction control. This is due to the pitch angle offset, which reduces the aerodynamic effectiveness of the blades. For most of the remaining turbines of the row, an increase in power can be observed, resulting in an overall power gain. The numerical results are given in Table 1.

Table 1: Numerical results

Wind speed m/s	5	6	7	8	9	10	11	12
Total power (MW) Nominal operation	1.39	3.31	4.00	6.03	8.50	14.44	18.35	22.09
Total power (MW) Wake controlled	1.43	3.43	4.17	6.31	8.90	14.76	18.83	22.44
Power gain %	2.59	3.68	4.25	4.60	4.70	2.21	2.60	1.58

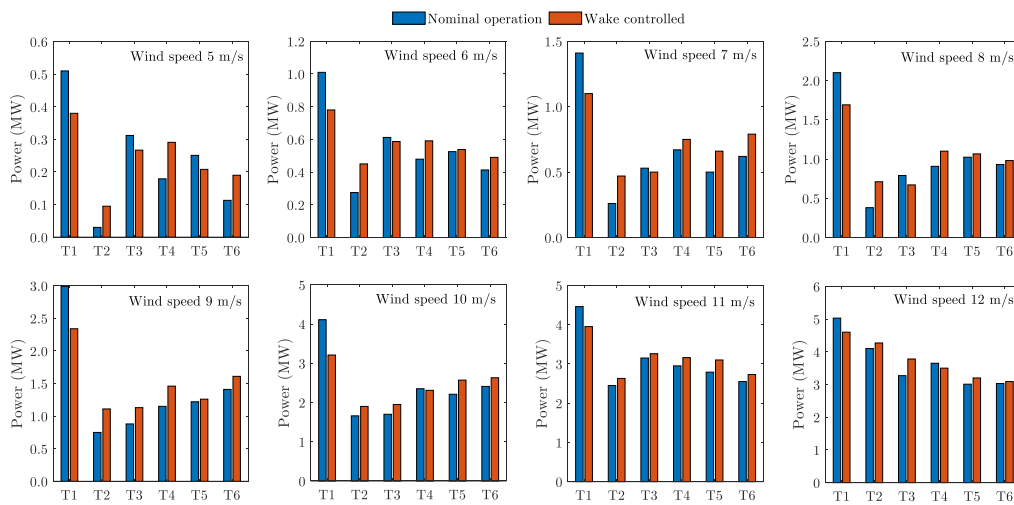


Figure 4: Power of turbines in row T1-T6 for wind speed of 5 m/s to 12 m/s in case of nominal operation and wake controlled.

5 Conclusion

In this paper, the performance of the wake controlled strategy using the axial induction control method is compared with the wind farm nominal operation. The first phase of the C-Power offshore wind farm layout is simulated using FLORIS. The axial induction control approach tries to optimise the total power production of a wind farm by minimising the overall wake deficit through adjusting control inputs. The results show that there is an advantage in using the proposed control method, particularly when the wind direction is aligned with the row of wind turbines. It has been conducted that this strategy can significantly improve the efficiency of the wind farm.

Further investigation can be made to analyse the impact of the wind turbines' structural load in case of applying this strategy. In this paper, it has been assumed that the wind turbines in the first phase are not affected by the wakes of the C-Power second and third phases. However, future studies can explore additional effects to see if the optimal wake adjustment can be reasonably used for the entire C-Power farm.

Acknowledgements

This work was performed in the framework of the Energy Transition Fund project BEOWind of the Belgian federal government, and the FWO research project G.0D93.16N, funded by the Research Foundation Flanders.

References

- [1] Haar L 2020 *Energy Policy* **143** 111483
- [2] Pineda I 2015 *A position paper by the European Wind Energy Association*
- [3] Ramírez L, Fraile D and Brindley G 2020 *Windeurope Annual Offshore Statistics*
- [4] Gea-Bermúdez J, Pade L L, Koivisto M J and Ravn H 2020 *Energy* **191** 116512
- [5] Howland M F, Lele S K and Dabiri J O 2019 *Proceedings of the National Academy of Sciences* **116** 14495–14500
- [6] Boersma S, Doekemeijer B, Vali M, Meyers J and van Wingerden J W 2018 *Wind Energy Science* **3** 75–95
- [7] Annoni J, Fleming P, Scholbrock A K, Roadman J M, Dana S, Adcock C, Porte-Agel F, Raach S, Haizmann F and Schlipf D 2018 *Wind Energy Science (Online)* **3**
- [8] De-Prada-Gil M, Alías C G, Gomis-Bellmunt O and Sumper A 2015 *Energy conversion and management* **101** 73–84
- [9] Zhang B, Soltani M, Hu W, Hou P, Huang Q and Chen Z 2017 *IEEE Transactions on Sustainable Energy* **9** 862–871
- [10] Kazda J and Cutululis N A 2019 *IEEE Transactions on Control Systems Technology*
- [11] Murcia Leon J P, Koivisto M J, Sørensen P and Magnant P 2020 *Wind Energy Science Discussions* 1–23
- [12] Ahmadyar A S and Verbič G 2016 *IEEE Transactions on Sustainable Energy* **8** 230–238
- [13] Liu T, Pan W, Quan R and Liu M 2019 *IEEE Access* **7** 68636–68645
- [14] Boersma S, Doekemeijer B M, Gebraad P M, Fleming P A, Annoni J, Scholbrock A K, Frederik J A and van Wingerden J W 2017 A tutorial on control-oriented modeling and control of wind farms *2017 American control conference (ACC) (IEEE)* pp 1–18
- [15] Doekemeijer B M, van der Hoek D and van Wingerden J W 2020 *Renewable Energy*
- [16] Bastankhah M and Porté-Agel F 2019 *Journal of Renewable and Sustainable Energy* **11** 023301
- [17] Dou B, Qu T, Lei L and Zeng P 2020 *Energy* **209** 118415
- [18] Zhao R, Dong D, Li C, Liu S, Zhang H, Li M and Shen W 2020 *Energies* **13** 1549
- [19] Siniscalchi-Minna S, Bianchi F D, De-Prada-Gil M and Ocampo-Martinez C 2019 *Renewable energy* **131** 37–44
- [20] Yin X, Zhang W, Jiang Z and Pan L 2020 *Renewable Energy*
- [21] van der Hoek D, Kanev S, Allin J, Bieniek D and Mittelmeier N 2019 *Renewable Energy* **140** 994–1003
- [22] Neill S P and Hashemi M R 2018 *Fundamentals of ocean renewable energy: generating electricity from the sea* (Academic Press)
- [23] NREL 2020 FLORIS. Version 2.2.0 URL <https://github.com/NREL/floris>
- [24] Jensen N O 1983 *Citeseer*
- [25] Gebraad P M O 2014 *Data-driven wind plant control* Ph.D. thesis Delft University of Technology

RELIABILITY

Comprehensive investigation of meta models for fatigue load approximation of offshore wind turbines

F Müller^a, C Hübler^a, and R Rolfes^a

^aLeibniz University Hannover, Institute of Structural Analysis, ForWind, Appelstr. 9a,
D-30167 Hannover

E-mail: f.mueller@isd.uni-hannover.de

Keywords: wind energy, meta model, surrogate model, Kriging

1 Introduction

The simulation of offshore wind turbines in the time domain is very time-consuming due to many load cases to be calculated and stochastic simulation models. A possible alternative to simulations in the time domain can be the use of meta models. A meta model is a mathematical model that approximates the relationship of input to output data in a significantly reduced time. Meta models are already used in the wind energy sector. So far, there are only a few studies that have comprehensively investigated the use of a meta model for a simulation model of a wind turbine as well as sampling methods used to generate the training data for the meta model. Training data are the data used to create the meta model. In addition to the mentioned points, there are only a limited number of studies that compare various meta models with each other.

A meta model that is already used in wind energy is the Kriging meta model. There are already some more detailed studies on Kriging, but there is still a general need for research, e.g. with regard to different sampling methods, the number of seeds, input variables and with regard to a comprehensive comparison with other meta models.

In this study, the Kriging meta model is analysed with respect to two different sampling methods to generate the training data. The two sampling methods investigated are Monte Carlo Sampling and a deterministic grid. The investigation is similar to the procedure described in Wilkie [1]. However, a more advanced sampling technique, an adapted fractional factorial design, is investigated. This design does not consider combinations that do not occur in reality (e.g. very small wind speed and high wave height).

2 Methodology

2.1 Simulation model

To generate the training data the NREL 5MW reference turbine [2] with the OC3 Monopile and soil [3] is used. The environmental conditions measured at the research platform FINO 3 [4] are used. Five parameters are considered as scattering parameters: wind speed v_s , turbulence intensity TI , significant wave height H_s , wave peak period T_p and wind wave misalignment θ_{mis} . The operating condition of power production is considered and the loads are evaluated at mudline and at the rotor blade root.

2.2 Monte Carlo Sampling

When creating the first training set, N random numbers in the interval $[0,1]$ are first generated for each parameter. N is the number of samples. Then, the random numbers are used to determine the values via the inverse of the cumulative distribution of the parameter. Dependencies of the parameter distributions

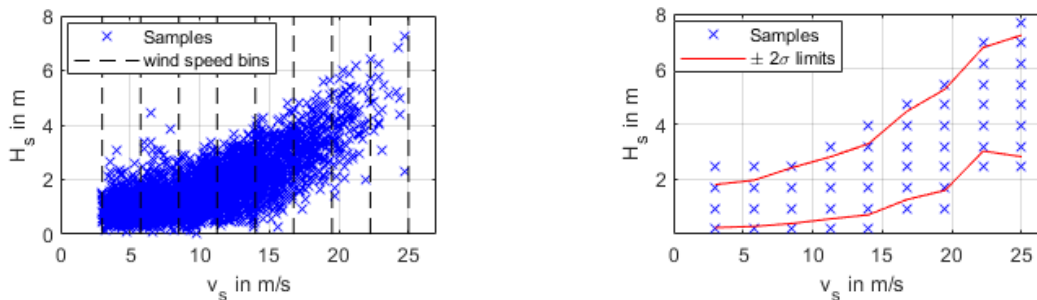


Figure 1: correlation between wind speed and wave height (a) Monte Carlo sampling (b) deterministic grid

on wind speed and wave height are taken into account as shown in Figure 1(a). More information can be found in Hübler et al. [4].

2.3 Deterministic grid

A deterministic grid is created for this approach. Here, combinations that are unlikely to occur should be excluded. This is considered as follows: First, the range of wind speed is divided into equally spaced intervals as shown in Figure 1(a). The distributions of the other parameters depend on the wind speed. Therefore, the lower and upper limits of each parameter are determined for each chosen wind speed. The interval $\pm 2\sigma$ is used as limits. Since the parameter range should be divided into intervals of equal size (for all selected wind speeds), the determined lower limits are rounded down and the upper limits are rounded up to the next grid point. This, as well as the correlation between wind speed and wave height is shown in Figure 1(b).

3 First Results and Outlook

First results with Monte Carlo Sampling show that the Kriging meta model leads to good results. A disadvantage is that load cases, which occur rather rarely, cannot be represented well by the meta model, because there are only few training samples that represent these load cases. This can significantly increase the error of the meta model. For the Kriging model, which is based on the training data generated with the grid sampling, it is to be expected that the mean error of the meta model will be higher than for Monte Carlo Sampling. However it is assumed that all load cases can be represented due to the evenly distributed samples. If this is confirmed, a further interesting step would be to combine the two sampling procedures.

Acknowledgements

We gratefully acknowledge the financial support of the Leibniz University Hannover for the research project MetaWind within the program Leibniz Young Investigator Grants.

References

- [1] Wilkie D 2020 *Advancing probabilistic risk assessment of offshore wind turbines on monopiles* Dissertation University College London London
- [2] Jonkman J, Butterfield S, Musial W and Scott G 2009 *Technical Report NREL/TP-500-38060*
- [3] Jonkman J and Musial W 2010 *Technical Report NREL/TP-5000-48191*
- [4] Hübler C, Gebhardt C G and Rolfes R 2017 *Wind Energy Science* **2** 491–505

Input parameter selection for full load damage neural network model on offshore wind structures

F d N Santos^{a,b}, N Noppe^{a,b}, W Weijtjens^{a,b}, and C Devriendt^{a,b}

^aOffshore Wind Infrastructure-lab (OWI-Lab)

^bVrije Universiteit Brussel, Pleinlaan 2, 1050 Elsene, Belgium

E-mail: `francisco.de.nolasco.santos@vub.be`

Keywords: Artificial Intelligence, Neural Networks, Feature Selection

Abstract

In this contribution several feature selection techniques are tested in order to better understand the relevance of different input parameters in the estimation of a wind turbine's tower damage and their relative validity. Firstly, a number of input parameters stemming from supervisory control and data acquisition (SCADA) and accelerometer sensors of an instrumented wind turbine are processed into 10-minute metrics. This instrumentation setting is enabled through the framework of the On- and Offshore Wind Infrastructure Application Lab's (OWI-Lab) projects Safelife and Supersized 4.0. In this stage, an artificial neural network (ANN) model, based on previous research, is also used to estimate the thrust load impacting the tower through the use of high frequency SCADA data (1Hz). After the data has been processed, a random set of representative data points are selected. This dataset is then the basis for the feature selection algorithms. These can be divided into filter-based, wrapper and intrinsic techniques. The specific techniques tested are Pearson (also with K-Best), Kendall and Spearman's Correlation, Dominance Analysis, Random Forest and Recursive Feature Elimination (with both random forest and decision tree classifier). The results attained for each technique are then compared and global trends extrapolated.

Keywords: Artificial Intelligence, Neural Networks, Feature Selection

1 Introduction

Wind turbine fatigue, the remaining useful lifetime and possible lifetime extensions are increasingly relevant topics as older wind farms are reaching the end of their design lifetime, being a key industrial concern. An informed decision to extend the lifetime of a wind turbine ought to take into account the fatigue assessment of said turbine, which can be based on measurements of the load history taken in the turbine [1, 2]. In order to properly assist wind farm operators on such decisions, an accurate fatigue assessment is required for each and every wind turbine of the farm. Due to the prohibitive costs of strain gauge installation, an alluring alternative appears through the combination of supervisory control and data acquisition (SCADA) and accelerometer data, the latter of which enables the incorporation of structural dynamics, thus ensuring a fuller picture of the corresponding fatigue behaviour. Within the framework of OWI-lab's projects Safelife and Supersized 4.0, data coming from the SCADA system and additionally installed accelerometers are used to get a better insight in the consumed lifetime of, respectively, jacket foundations and monopile foundations.

Additionally, based on an earlier work [3], the estimated thrust load from 1Hz SCADA is also included as a feature of interest. With the advent of widespread use of artificial intelligence (AI), in particular deep neural networks, this technique appears to be especially suitable for this application. As previous research has demonstrated, neural networks are particularly sensitive to the input data and the proper selection of input variables is paramount [4]. In the present contribution, a methodology for the proper selection

of the input features is developed. These features consist on 10 minute metrics of each acceleration-, SCADA - and thrust signal, namely, mean, median, standard deviation, rms, maximum, minimum, range, kurtosis, skewness and spectral moments (1st-4th). Additionally, the accelerations and thrust are also cycle counted. Several feature selection techniques are tested, such as Pearson (also including K-Best), Kendall and Spearman Correlation, Dominance Analysis, Random Forest and Recursive Feature Elimination (with random forest and decision tree classifier algorithms) in order to assess which features are of relevance, the importance of individual sensors and the level of feature reduction attainable.

2 Data Structure and Processing

The instrumented turbine has two different types of high frequency sensors that allow the attainment of data: SCADA-related sensors placed in the nacelle (1Hz sampling frequency) and accelerometers (12.5Hz sampling frequency) placed on three different heights of the turbines' tower (the bottom, middle and upper levels is abbreviated as BL, ML and UL, respectively). Additionally, multiple strain gauge sensors are placed in the tower at the same height but different headings, which allows the calculation of the damage equivalent moment (DEM) of the fore-aft bending moment, the intended target of this research. The SCADA data includes wind speed, wind direction, rpm, yaw angle, ambient temperature, pitch, power and two small accelerometers (one fore-aft, FA, and another side-to-side, SS). The accelerometers present at 3 distinct levels (BL, ML and ML), produce signals in the X and Y directions, along with FA and SS. These signals also undergo an additional transformation into displacements, in meters.

The high-frequent SCADA data is also used to estimate the thrust load on a 1s basis. This parameter, apart from its intrinsic relevance, is of significant interest because it synthesises into a single value a vast amount of information from the SCADA data. In addition, the thrust load is one of the major contributors to the structure's damage, thus its estimation and inclusion appear even more important.

All of these variables (SCADA, accelerometer, thrust) are processed into 10-minute metrics. These include widely-known metrics as mean, minimum, maximum, median, mode (most common repeated value), standard deviation, range and root mean square, but also spectral moments, skewness and kurtosis. Their implementation was enabled by the package `scipy.stats`.

- Spectral Moments

Moments of functions are, in general, ways of quantitatively obtain measures related to the shape of the function's graph. These form a set of values by which the properties of a function can be usefully characterized. Spectral moments are, as the name implies, moments of a spectrum. They are of practical relevance as in, for example, the analysis of the velocity distributions of turbulent phenomena [5]. In this particular application the central spectral moments are calculated. The central moments are the moments of a probability distribution of a random variable about the random variable's mean; this is useful as, unlike ordinary moments which are dependant on location, central moments are solely related to the spread and shape of the distribution. Thus, for a continuous univariate probability distribution with a probability density function, $f(x)$, the i th moment about the mean μ is [6]:

$$\int_{-\infty}^{+\infty} (x - \mu)^i f(x) dx \quad (1)$$

We can translate equation (1) to its discrete form:

$$m_i = 1/n \sum_{k=1}^n (x_i - \bar{x})^i \quad (2)$$

With n , number of samples and \bar{x} the mean of the sample.

We can then intuitively understand the first spectral moment as being 0, the second as representing the variance (σ^2 , with σ the standard deviation) and the third and fourth moments enable the attainment of skewness and kurtosis, respectively.

- Skewness

The skewness of a function is the measure of the asymmetry of the probability distribution; that is, how much extent to which a function "leans" to one side of its mean. For normally distributed data, the skewness should be about zero. For unimodal continuous distributions, a skewness value greater than zero means that there is more weight in the right tail of the distribution. As previously mentioned, the 3rd central moment is related to the skewness. This relationship can be translated as m_3/σ^3 (3rd central moment divided by the cube of the standard deviation), and is known as a standardized moment, wherein the moment scale is rendered invariant. We can then calculate the sample's skewness as the Fisher-Pearson coefficient of skewness:

$$g_1 = (m_3)/(m_2^{3/2}) \quad (3)$$

where m_i is the biased sample's i th central moment. Equation (3) can be corrected for bias and the value computed will be the adjusted Fisher-Pearson standardized moment coefficient:

$$G_1 = \frac{\sqrt{n(n-1)}}{(n-2)} \frac{(m_3)}{(m_2^{3/2})} \quad (4)$$

- Kurtosis

The kurtosis describes the shape of a probability distribution by measuring its 'tailedness', or how 'fat' the tail is. It corresponds to the 4th standardized moment, or m_4/σ^4 (4th central moment divided by the standard deviation, or the square root of the 2nd central moment, to the power of 4). Usually 3 is subtracted (Fisher's definition), in order to have a result of 0 for the normal distribution, as in equation (5).

$$g_2 = \frac{m_4}{\sigma^4} - 3 = \frac{m_4}{m_2^2} - 3 \quad (5)$$

Apart from these metrics, the damage equivalent moment (DEM) of the thrust load and the damage equivalent acceleration (DEA; it has no physical significance, the nomenclature is just an adopted convention) were calculated. The damage calculation is similar to the one performed to obtain the DEM of the fore-aft bending moment (the intended target of this research). It depends on the number of cycles and the stress range (or amplitude) of those cycles. These values are obtained through cycle counting, using a rainflow algorithm. The principle is explained in [7]. This procedure to obtain the damage of the bending moment is visualized in Figure 1.

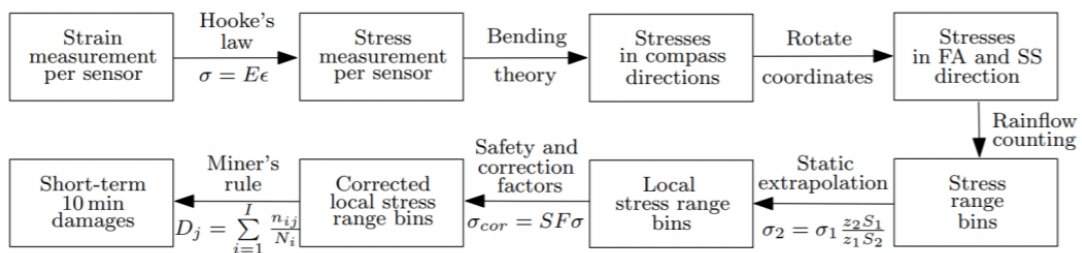


Figure 1: Diagram with overview of the procedure required to attain a fatigue damage estimate. Extracted from [8].

Finally, after processing all of the data into 10-minute metrics, a randomised set of points is selected from the original dataset. Preliminary investigation found that the minimal amount of points that ensures a representative random sample is 2500. However, in this contribution the amount of random points selected was of about 4000. We can inspect the histograms of both the original and the reduced (random) datasets for different parameters (*vd.* Figure 2). As we can observe, there is a good accordance between the original values and the ones from the randomised selection, thus ensuring a representative dataset.

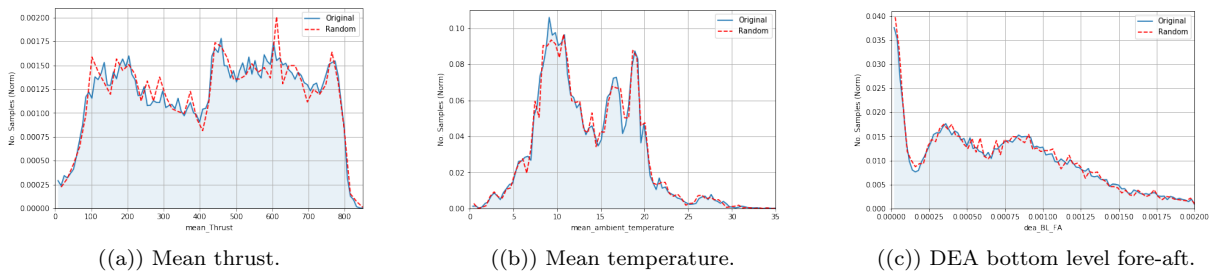


Figure 2: Comparison between original processed data (blue line) and randomly selected dataset (red dashed line).

3 Feature Selection

Feature selection is an umbrella-term for a number of methods focused on the reduction of input variables of predictive models into the variables believed to be the most useful to the models. Input variable reduction is highly desirable as, through the removing of redundant variables, not only are the computational, memory and time costs reduced, but it may also improve the overall performance of the model, as non-informative variables can add uncertainty to the predictions and reduce the overall effectiveness of the model [9].

As mentioned, there are numerous feature selection methods, but all aim at a dimensionality reduction. This constellation of methods can, however, be classified and grouped. The first distinction one can make is between supervised and unsupervised methods: if the outcome isn't ignored (*i.e.* we have a target variable), then the technique is supervised. As this is our case, in the form of the DEM of the FA bending moment, the present contribution will solely focus on these methods. They can be further sub-divided into filter, wrapper and intrinsic methods and will be discussed more deeply in sections 3.1, 3.2 and 3.3, respectively. We can observe all these distinctions in Figure 3. Finally, one must briefly mention the popular principal component analysis (PCA) dimensionality reduction method and its nonlinear counterpart, Kernel PCA [10]. Their non-inclusion resides with the fact that they generate new variables, which clashes with one of the objectives of this contribution, to determine the importance of individual sensors.

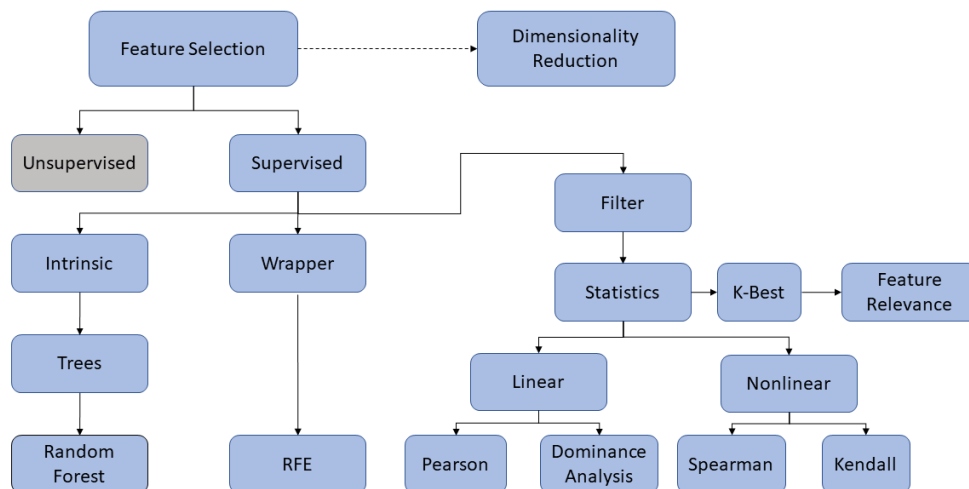


Figure 3: Diagram of different feature selection techniques.

3.1 Filter-based Feature Selection

Filter-based feature selection methods employ statistical techniques to evaluate the relationship between each input variable and the target variable, assigning a score for the relevance of the input variable. The scores obtained for the relationship between the variable and the target are then used to choose (filter) the inputs that will be used in the model.

- Pearson's Correlation

Pearson's correlation coefficient, or Pearson's r , is a statistical value that measures linear correlation and defined as the ratio between the covariance of two variables, X and Y , divided by the product of their standard deviations (σ). This is expressed by equation (6), which expands this definition to a sample.

$$r = \frac{\text{cov}(X, Y)}{\sigma_X \sigma_Y} = \frac{\sum_{i=1}^n (x_i - \bar{x})(y_i - \bar{y})}{\sqrt{\sum_{i=1}^n (x_i - \bar{x})^2} \sqrt{\sum_{i=1}^n (y_i - \bar{y})^2}} \quad (6)$$

Pearson's r assumes values between -1 and 1, where $0 > r > 1$ represents a positive linear correlation, $-1 < r < 0$ a negative linear correlation, and values close to 0 a weak correlation. As mentioned, Pearson's correlation is a linear method.

A threshold of $|r| > 0.7$ was defined in this contribution.

- Spearman's Correlation

Spearman's correlation is nonparametric measure of rank or ordinal correlation which defines if two variables are monotonically related. Unlike Pearson's correlation, Spearman's correlation isn't linear, as it is nonparametric, just depending on the ranking of the variables. It is, per definition, the Pearson's correlation coefficient between the rank variables, and represented as ρ ($-1 < \rho < 1$).

Thus, if Y tends to increase when X increases, ρ is positive (monotonically increasing function). If Y tends to decrease when X increases, ρ is negative (monotonically decreasing function). A Spearman correlation of zero indicates that there is no tendency for Y to either increase or decrease when X increases (non-monotonic function). This strong dependence on monotonic functions might represent a hindrance when dealing with different datasets.

A threshold of $|\rho| > 0.8$ was defined in this contribution.

- Kendall's Correlation

Kendall's correlation coefficient, τ , like Spearman's correlation, is a nonparametric rank correlation measure. It is expressed by equation

$$\tau = \frac{n^+ - n^-}{\binom{n}{2}} \quad (7)$$

Where n^+ is the number of concordant pairs, n^- , the number of discordant pairs and $\binom{n}{2} = \frac{n(n-1)}{2}$ the binomial coefficient for the number of ways to choose two items from n items. A pair $(x_i, y_i), (x_j, y_j)$ with $i < j$ is concordant if $x_i > x_j$ and $y_i > y_j$ or $x_i < x_j$ and $y_i < y_j$. Thus, Kendall's τ measures how similarly the orderings of the data are when ranked by each of the quantities.

A threshold of $|\tau| > 0.6$ was defined in this contribution.

- K-Best Selector

Once the statistics have been determined, we can apply a filtering method (besides thresholds or percentiles), as the K-Best Selector. In this specific contribution, this filter was applied using a univariate linear regression test, f-regressor. This a linear model (scoring function) for testing the individual effect of each of many regressors. It starts by computing the correlation between each regressor and the target, which then converts to an F-score and to a p-value.

A threshold of score > 7000 was defined in this contribution.

- Dominance Analysis

Dominance Analysis measures relative importance pairwise, where two predictors are compared in the context of all 2^{p-2} models that contain some subset of the other predictors (p). Thus, we build $2^p - 1$ models (all possible subset models) and compute the incremental R^2 contribution of each predictor to the subset model of all other predictors. The increase in R^2 resulting from the addition of a predictor to the regression model measures then the contribution of that predictor. It is, nonetheless, linear, but with the ability of calculating the interactional dominance of each variable. It uses F-regression to select the top K-features.

In this contribution a maximum of 50 variables was defined.

3.2 Wrapper Feature Selection

Wrapper feature selection methods generate several models evaluating different subsets of input variables, wherein the selected variables (features) are the ones that present the model that performs better, according to a performance metric. These methods' models use processes that add/remove predictors until an optimal combination that maximizes model performance is found. Unlike filter approaches, wrapper methods are able to detect the possible interactions between variables. There are, however, disadvantages, such as an increasing overfitting risk (for small samples) and a very significant computation time if the number of variables is large.

- Recursive Feature Elimination (cross-validation)

Recursive Feature Elimination (RFE), being a wrapper-type feature selection method, has a different algorithm present at its core wrapped around the RFE proper. This method's process begins with all features in a training dataset and then removes features by searching for a subset of features that are in accordance with a certain parameter (e.g. maximum number of features). In linear terms, the machine learning algorithm present in the core of the model is fitted, the features ranked by importance, the least relevant features iteratively discarded and the model is re-fitted, with the processes being repeated until the required number of features is achieved. The feature ranking is used either by a machine learning model or a statistical method. If a cross-validation of different numbers of features is performed, then the number of features required is automatically calculated.

In this contribution the feature ranking algorithms (estimators) used were a decision tree classifier and random forest.

3.3 Intrinsic

Intrinsic feature selection models entail built-in feature selection. This means that the model only includes features that maximise the accuracy, thus performing automatically a feature selection during training. These include penalized regression models and decision trees.

- Random Forest

Random forest algorithms are an intrinsic ensemble of decision trees algorithms. These act by generating several decision trees during training and outputting the mean/average prediction of the individual trees. Random decision forests are preferred to classical decision trees because they prevent latter's habit of overfitting in the training set [11].

In this contribution a threshold of score > 0.001 was defined.

4 Comparative Analysis

All of the aforementioned feature selection techniques are applied to a dataset of 4249 points, wherein the permutations of 35 parameters (between accelerations, SCADA data and thrust) with the corresponding metrics generate 430 separate input variables. The selected features are represented in Table 2. Table 1 is the companion table to Table 2, where the numerous abbreviations and symbols can be deciphered.

There are some noticeable global trends. Some metrics pop-up far more often than others. For example, the cycle counted accelerations (DEA), RMS, range (and max and min) and the standard

deviation seem to be very well represented for the features related to the tower accelerometers. These acceleration signals also present an interesting characteristic: for all levels, FA and X-direction signals seem to be selected more frequently than SS. This isn't nonsensical as our target is the fore-aft tower bending moment DEM, and that for the wind farm in which the training wind turbine is located, historic data shows that the fore-aft loading is the main source of fore-aft bending moment damage in the structure (we can see this in Figure 4, where the FA parameters present a behaviour more linear than the SS). A notable exception is the bottom level side-to-side acceleration signal, which a great number of methods detected for many metrics. Keeping with the acceleration sensors (white part of the table), the RFE methods (both for random forest and decision tree classifiers) also present some metrics which aren't selected for filter-based or intrinsic methods. These metrics include the kurtosis, mean, median, skewness and both the 2nd and 3rd spectral moments. These methods (RFE) should be closely followed, as they purport to be able to better capture nonlinearities that might escape filter-based or even intrinsic methods.

If we now look into the grey area of the table (features related with SCADA data), we can observe that RFE and Intrinsic methods are much more represented than filter-based (apart from the DEM of thrust, and some nacelle accelerations metrics). The detection of the thrust by filter methods might be due to its initially linear relationship to the tower fore-aft bending moment DEM (*vd.* Figure 5). SCADA parameters as temperature, pitch and wind direction are just picked-up by the wrapper methods. These, along with the intrinsic method, also signal more the spectral moments. Again, this is to be expected, as filter-based methods (even 'nonlinear' ones such Spearman and Kendall) can't pick-up the more complex interactions between the SCADA data and the target variable. Although some of these filter methods might be considered nonlinear, because they depend, as with Spearman's ρ , on monotonic functions, not all nonlinearities will be captured.

The overall conclusions can be read in section 5.

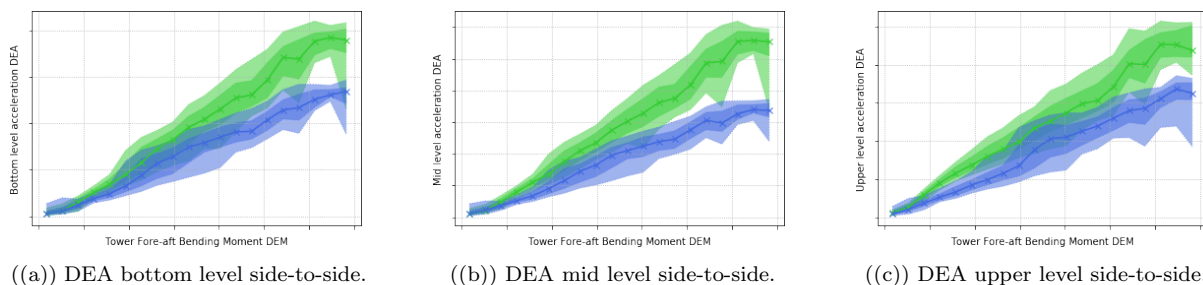


Figure 4: Comparison between fore-aft (green) and side-to-side (blue) DEA in bottom, mid and upper levels. Plotted *vs.* tower fore-aft bending moment DEM (target).

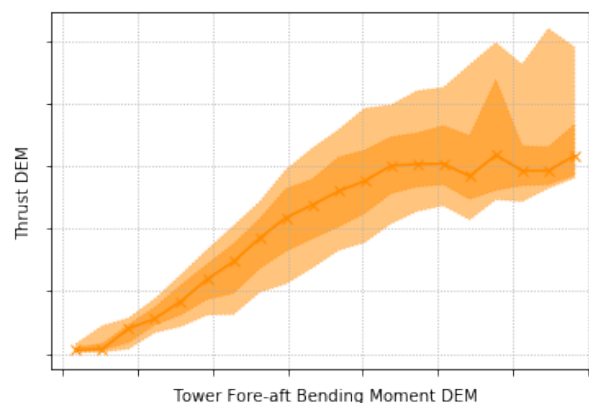


Figure 5: Thrust DEM *vs.* tower fore-aft bending moment DEM.

Abbreviation/Symbol	Meaning
ACC	Acceleration Sensor
BL	Bottom Level
ML	Mid Level
UL	Upper Level
FA	Fore-Aft
SS	Side-to-Side
X	X-Direction
Y	Y-Direction
disp	Displacement
dea	Damage Equivalent Acceleration
dem	Damage Equivalent Moment (for Thrust)
g_2	Kurtosis
g_1	Skewness
m_i	i -th spectral moment
std	Standard Deviation
Temp	Temperature
o	Pearson's correlation coefficient, r
Δ	Spearman's correlation coefficient, ρ
\square	Kendall's correlation coefficient, τ
\diamond	Dominance Analysis
\dagger	K-Best Selector (F-regression)
\star	Recursive Feature Elimination (cross-validation) using a Random Forest Estimator
*	Recursive Feature Elimination (cross-validation) using a Decision Tree Classifier
\times	Random Forest Estimator

Table 1: Variable abbreviation explanation.

	dea	dem	g_2	max	mean	median	min	mode	range	rms	g_1	m_2	m_3	m_4	std
ACC BL X	\dagger , Δ ,o, \diamond , \square			\dagger , Δ ,o, \square			\dagger , Δ ,o, \square		\dagger , Δ ,o, \square	\dagger , Δ ,o, \diamond , \square					\dagger , Δ ,o, \diamond , \square
ACC BL Y	\dagger , Δ ,o, \square			\dagger , Δ ,o, \square			\dagger , Δ ,o, \square		\dagger , Δ ,o, \square	\dagger , Δ ,o, \square					\dagger , Δ ,o, \square
ACC BL FA	\star , \star , \dagger , Δ ,o, \diamond , \square			\dagger , Δ ,o, \square			\dagger , Δ ,o, \square		\star , \dagger , Δ ,o, \diamond , \square	\dagger , Δ ,o, \diamond , \square					\dagger , Δ ,o, \diamond , \square

ACC BL SS	*, †, Δ, o, ♦, □					†, Δ, o, □		†, Δ, o, □	†, Δ, o, ♦, □				†, Δ, o, □
ACC BL X disp	†, Δ, o, □			†, Δ, o, □		†, Δ, o, □		†, Δ, o, □	†, Δ, o, □		Δ, □		†, Δ, o, □
ACC BL Y disp	†, Δ, o, ♦, □			†, Δ, o, □		†, Δ, o, □		†, Δ, o, □	†, Δ, o, □		Δ, □		†, Δ, o, □
ACC BL FA disp	*, ×, *, †, Δ, o, ♦, □			×, †, Δ, o, ♦, □		×, †, Δ, o, ♦, □		*, ×, *, †, Δ, o, ♦, □	*, †, Δ, o, ♦, □		×, †, Δ, o, □		*, ×, *, †, Δ, o, ♦, □
ACC BL SS disp	†, Δ, □			†, Δ, o, □		†, Δ, o, □		†, Δ, o, □	Δ, □		Δ, □		Δ, □
ACC ML X	†, Δ, o, ♦, □			†, Δ, o, □		*	*, †, Δ, o, □	*, †, Δ, o, □	†, Δ, o, ♦, □				†, Δ, o, ♦, □
ACC ML Y	†, Δ, o, □			†, Δ, o, □			†, Δ, o, □	†, Δ, o, □	†, Δ, o, ♦, □				†, Δ, o, ♦, □
ACC ML FA	†, Δ, o, ♦, □			*, †, Δ, o, □			†, Δ, o, ♦, □	*, †, Δ, o, ♦, □	†, Δ, o, ♦, □		*		†, Δ, o, ♦, □
ACC ML SS	†, Δ, o, ♦, □			†, Δ, o, □			†, Δ, o, □	†, Δ, o, □	†, Δ, o, ♦, □				†, Δ, o, ♦, □
ACC ML X disp	†, Δ, o, □			†, Δ, o, □			†, Δ, o, □	†, Δ, o, □	†, Δ, o, □		Δ, □		†, Δ, o, □
ACC ML Y disp	†, Δ, o, □			†, Δ, o, □			†, Δ, o, □	†, Δ, o, □	†, Δ, o, □		Δ, □		†, Δ, o, □
ACC ML FA disp	*, ×, *, †, Δ, o, ♦, □			×, †, Δ, o, ♦, □			†, Δ, o, ♦, □	†, Δ, o, ♦, □	†, Δ, o, ♦, □		†, Δ, o, □		*, ×, *, †, Δ, o, ♦, □
ACC ML SS disp	Δ, □			Δ, □			†, Δ, □	†, Δ, □	Δ, □		Δ, □		Δ, □
ACC UL X	†, Δ, o, ♦, □		*	†, Δ, o, □		*	†, Δ, o, □	†, Δ, o, ♦, □	†, Δ, o, □				†, Δ, o, □
ACC UL Y	†, Δ, o, ♦, □			†, Δ, o, □			†, Δ, □	†, Δ, o, □	†, Δ, o, ♦, □				†, Δ, o, ♦, □
ACC UL FA	†, Δ, o, ♦, □			†, Δ, o, □			†, Δ, o, □	†, Δ, o, ♦, □	*, †, Δ, o, ♦, □				†, Δ, o, ♦, □
ACC UL SS	†, Δ, o, □			Δ, □			Δ, □	†, Δ, o, □	†, Δ, o, □				†, Δ, o, □
ACC UL X disp	†, Δ, o, □			†, Δ, o, □			†, Δ, o, □	†, Δ, o, □	†, Δ, o, □		Δ, □		†, Δ, o, □

ACC UL Y disp	†, Δ, o, □			†, Δ, o, □			†, Δ, o, □		†, Δ, o, □	†, Δ, o, □		Δ, □		Δ, □	†, Δ, o, □
ACC UL FA disp	*, ×, *, †, Δ, o, ♦, □			†, Δ, o, ♦, □			*, ×, *, †, Δ, o, ♦, □		×, †, Δ, o, ♦, □	†, Δ, o, ♦, □		†, Δ, o, □		×, *, Δ, □	†, Δ, o, ♦, □
ACC UL SS disp	Δ, □			†, Δ, □			†, Δ, □		†, Δ, □	Δ, □		Δ, □		Δ, □	Δ, □
ACC FA				†, Δ, □	†, Δ, o, □	†, Δ, o, □			†, Δ, □	†, Δ, o, □		Δ, □	Δ, □	Δ, □	†, Δ, o, □
ACC SS				Δ, □	Δ, □	Δ, □	*		Δ, □	Δ, □		Δ, □	Δ, □	Δ, □	Δ, □
Temp			*									*			
Pitch			*												
Power				Δ, □		*									
Rpm				Δ, □						*					*
Wind direction							*								
Wind speed				†, Δ, o, □	†				†, Δ, □	□		□		Δ, □	□
Thrust		*, ×, *, †, Δ, o, □		×, *	*				*, *			*, ×, *		*, ×, *	×, *

Table 2: Comparative table for different feature selection methods, wherein the differences between the selected parameters/metrics are illustrated. The rows in grey are SCADA-dependant parameters. *N.b.* the features ACC FA and ACC SS are the fore-aft and side-to-side accelerations captured by the nacelle's accelerometer.

5 Conclusions

In this contribution several feature selection techniques where the target was the wind turbine's fore-aft tower bending moment damage were applied successfully. These included Pearson (also with K-Best), Kendall and Spearman's Correlation, Dominance Analysis, Random Forest and Recursive Feature Elimination (with both random forest and decision tree classifier). Their theoretical background, classification and division along with the necessary assumptions (thresholds), were explained. The data processing was thoroughly elucidated and the representativeness of the data confirmed.

Some key take-aways of this contribution are:

1. Filter-based methods capture the more linear relationship between the acceleration sensors' signals and the fore-aft tower bending moment damage, but doesn't perform the same for SCADA-related parameters;
2. Fore-aft accelerations are generally better predictors than side-to-side;
3. Recursive Feature Elimination and Random Forest algorithms are able to correctly pick-up more nonlinear behaviour entailed in the SCADA-related features, as well as different metrics, as spectral moments, kurtosis and skewness;
4. Wrapper-type feature selection and intrinsic models seem to be more trustworthy than filter methods for this application;
5. The importance of the inclusion of specific accelerometers, as the features from their signals are universally picked;
6. The relevance of cycle counting, both for accelerations and for thrust, along with the calculation of different metrics, such as spectral moments, kurtosis and skewness.

References

- [1] Iliopoulos A, Weijtjens W, Van Hemelrijck D and Devriendt C 2017 *Wind Energy* **20** 1463–1479
- [2] Ziegler L, Smolka U, Cosack N and Muskulus M 2017 *Wind Energy Science* **2** 469
- [3] d N Santos F, Noppe N, Weijtjens W and Devriendt C 2020 *Journal of Physics: Conference Series* vol 1618 (IOP Publishing) p 022020
- [4] Vera-Tudela L and Kühn M 2014 *Procedia Technology* **15** 726–736
- [5] Miller K and Rochwarger M 1970 *Biometrika* **57** 513–517
- [6] Grimmett G S *et al.* 2020 *Probability and random processes* (Oxford university press)
- [7] Dirlik T 1985 *Application of computers in fatigue analysis* Ph.D. thesis University of Warwick
- [8] Hübler C, Weijtjens W, Rolfes R and Devriendt C 2018 *J. Phys. Conf. Ser* vol 1037 p 032035
- [9] Kuhn M, Johnson K *et al.* 2013 *Applied predictive modeling* vol 26 (Springer)
- [10] Jolliffe I T and Cadima J 2016 *Philosophical Transactions of the Royal Society A: Mathematical, Physical and Engineering Sciences* **374** 20150202
- [11] Ho T K 1995 *Proceedings of 3rd international conference on document analysis and recognition* vol 1 (IEEE) pp 278–282

Mathematical Model for lifetime estimation of the structural components of wind turbines

Shadan Mozafari*, Anand Natarajan

DTU Wind Energy, Technical University of Denmark, Roskilde, Denmark.

E-mail*shmoz@dtu.dk

Keywords: life estimation, reliability, wind turbine components, fatigue, limit state

Introduction

A part of overall costs of implementing offshore windfarms includes failures and maintenance planning. Blades are one of the important structural parts of the turbines and are exposed to repeated load cycles, which makes them vulnerable to fatigue failures [1]. Within the wind farms, it has been shown that higher ambient turbulence together with turbulence caused by the wake effects of the neighboring turbines causes higher loads/stresses variations and makes the fatigue lifetime of shorter [2]. Reduction in the blade life due to excessive fatigue loads increases maintenance costs and causes financial loss [3]. These costs can decrease by providing improved site-specific estimates of the damages occurring during operational lifetime of a wind turbine. Thus, having a proper tool for estimation of the fatigue lifetime of the wind turbine blades in the windfarm is of high value. In the present work, a mathematical model for fatigue lifetime estimation of the wind turbine blades is provided. Effects of considering turbulence distribution in each mean wind speed and using of longer time durations is studied.

Long time aero-elastic load simulations of 200 minutes duration are performed in HAWC2 according to the IEC standard DLC1.2 [4]. The duration is chosen according to investigations of turbulence level in different turbulence realizations in HAWC2 and convergence of these values over time durations. A balance between the effects of the wind being nonstationary though long time simulations and the effects of convergence of turbulence through time due to the inclusion of wider bandwidth is considered in selection of time durations. These two effects are shown in figures 1 and 2.

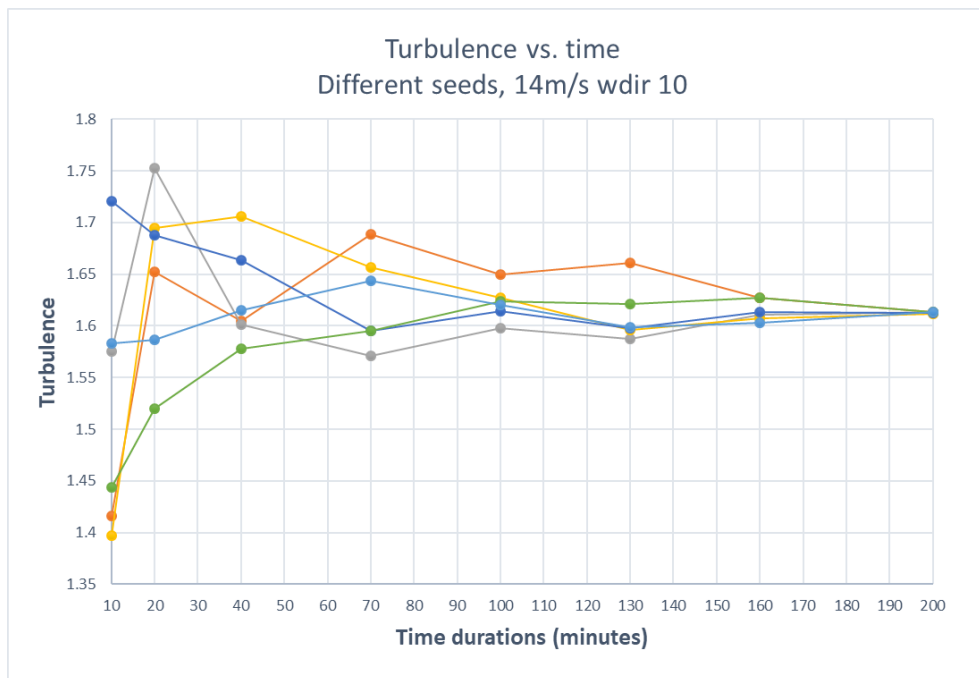


Figure 1. Actual turbulence magnitudes in different realizations (seeds) of each turbulence level in fixed wind condition (mean wind speed of 14m/s and wind direction of 10)

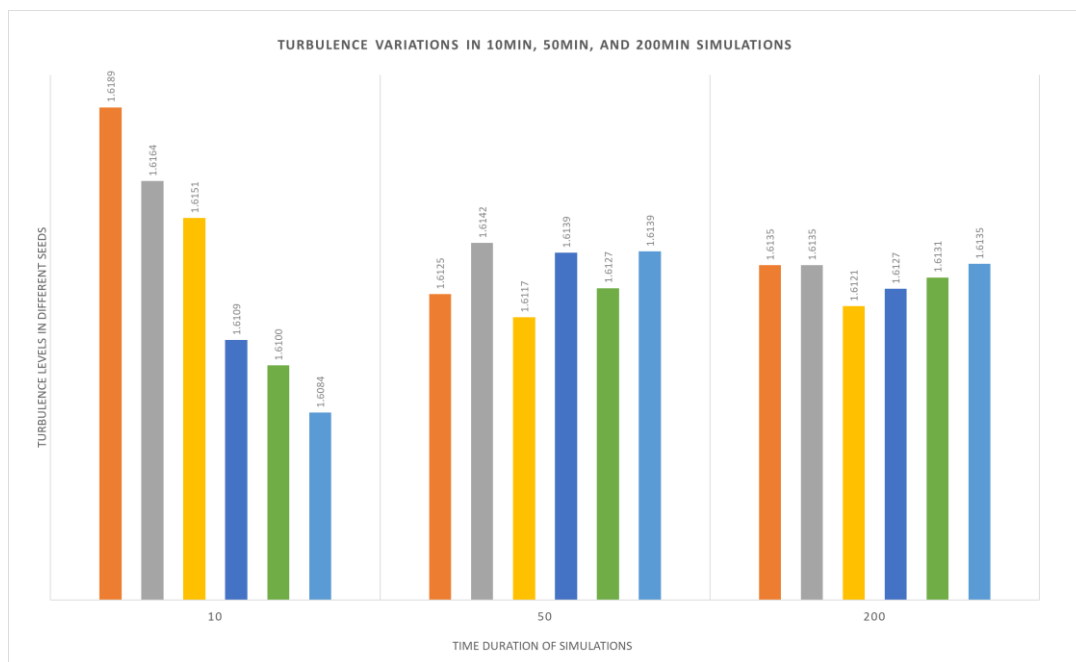


Figure 2. variations of turbulence levels in different time durations of simulations

In spite of the common assumption of constant turbulence, in the present work, a lognormal distribution is considered for turbulence level in each wind speed bin. Considering the turbulence as one of the stochastic parameters in the model would track wind conditions more accurately. Effects of this consideration in changing the lifetime distribution is investigated. .

Using the data obtained from truncated time series from one long time duration of 200minute, and using the rain flow and Miner's rule, the trend of the change of damage equivalent load (DEL) through time is investigated. Truncating data from one long time duration for each condition has created a better chance to track the load cycles in single turbulence seeds over time and have more realistic load changes though time. Estimation of the cumulative distribution function (CDF) of DELs in one time point is derived using median rank method. Using the estimated CDF, different distributions including two parameter and three parameter Weibull, Gamma, Normal, Lognormal, and exponential are fitted with investigations of the goodness of fit for inclusion of the most effective damaging part of the load histories for each fit. The fit is extrapolated considering the most effective fatigue boxes (including mean and altitude) and by considering the annual reliability level, the reliability of the blade is investigated. The model is applied to DTU10MW with 90% turbulence (as in IEC standard) and to Siemens 2.3MW in Lillgrund windfarm with log normally distributed turbulence levels using SCADA data accessible for one wind turbine in the wind farm. The wake effects are included using both wake modelling in simulations and increased turbulence intensity approach. The comparisons between the two approaches for considering wake effects in the model are done. The composite material specifications are not considered in the present model thus it is applicable to any structural part of the wind turbine.

The proposed model provides a more accurate stochastic lifetime model including turbulence distributions and allows having a controlling scheme based on the model predictions, in order to control the windfarm to maintain a specific target lifetime. All in all, by having a more accurate model for predicting the lifetime, the probability of failures and the frequency of repairs can be reduced and costs of design and inspection are reduced.

Bibliography

- [1] J. P.-C. D. C. L. I. M. Brian Loza, "Comparative fatigue life assessment of wind turbine blades operating with different regulation schemes," *Applied sciences*, vol. 21, no. 9, 2019.
- [2] S.T. Frandsen, "Turbulence and Turbulence-generated Structural Loading in wind turbine clusters," Risø National Laboratory, PhD Thesis, 2007.
- [3] W. Yang, Z. Peng, K. Wei and W. Tian, "Structural health monitoring of composite wind turbine blades," *IET Renew. Power Gener.*, vol. 11, pp. 411-416, 2017.
- [4] "IEC. International Standard IEC61400-1: Wind Turbines - Part 1: Design Guidelines," Third edition, August 2005.

Digital Twin Development for Wind Turbine Drivetrains based on Multibody Systems

O Kamel^{a,b}, S Hauptmann^a, and C L Bottasso^b

^aMesH Engineering GmbH, Wankelstr. 3, 70563 Stuttgart, Germany

^bChair of Wind Energy, Technical University of Munich, Boltzmannstraße 15, 85748 Garching, Germany

E-mail: omar.kamel@mesh-engineering.de

Keywords: System Identification, Digital Twin, Drivetrain, Multibody Systems

1 Introduction

Traditional high-fidelity multibody system (MBS) simulation models of wind turbines drivetrains provide vast and detailed information about the underlying physics. On the other hand, these models are often computationally expensive. The aim of the developed data driven model is the deployment of a digital twin for live monitoring of the drivetrain behavior under external loads during operation. Live monitoring implies that the quality of estimation and the speed of execution should be the key features of the proposed methodology.

2 Methodology

High Fidelity Simulation Model

The drivetrain under investigation is developed for the IEA 3.4MW onshore wind turbine (Fig. 1) [3]. Its high fidelity simulation model was developed in Simpack software and is incorporated in a virtual test bench used to generate the artificial input/output data used to train the reduced models. The model has

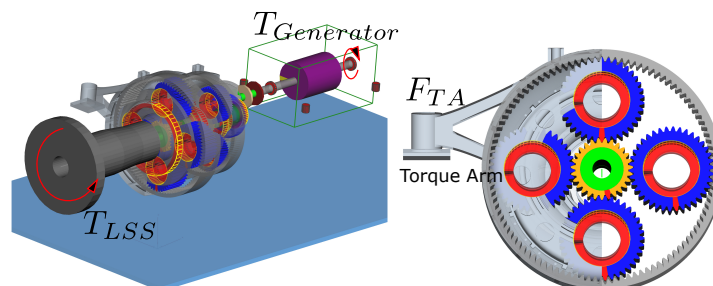


Figure 1: Left: MBS model with input signals: T_{LSS} and $T_{Generator}$, Right: Detailed view of the first stage of the planetary gearbox

two inputs, T_{LSS} and $T_{Generator}$. The objective is to infer the internal dynamics of the drivetrain model, namely 16 states that can neither be practically nor absolutely measured. The approach is only tested on the state variables in the first stage of the investigated planetary gearbox. The inferred states are circumferential and radial forces in the 4 planets and sun gear pairs, difference in angles between planets and sun in the 4 gear pairs, and vertical displacement and axial rotation of the left and right torque arms.

Estimation Models

Low frequency Gaussian white noise ($<1\text{Hz}$) was applied to the system as the excitation input signal. The MBS was then simulated for 1000 seconds and the output measurements (estimated features) were then collected. The data is pre-processed. This includes normalization of the features, then filtering using a moving average filter of width of 2 seconds in order to smooth the data specially with the noisy features as force states. The 16 features of the data were reduced using principal component analysis (PCA) with a linear kernel into 2 principal components [1]. Only two components were considered as they were able to capture 99% of the variance of the system response. Finally, the data was split into training and testing sets.

Two nonlinear approaches were considered because of the presence of nonlinearities in the system such as meshing between gear teeth and nonlinear force elements in the bearings inside the gearbox. Firstly a nonlinear autoregression model with exogenous inputs (NARX) that was realized using deep neural networks with sigmoid and hyperbolic tangent activation functions, considering 10 lagged timesteps [2]. The second approach is Hammerstein-Wiener (HW) model. This approach was investigated using two structures, firstly piecewise linear inputs with saturated outputs. The second structure is sigmoid network inputs and saturated outputs [4]. During fitting, the objective function was formulated as the error between measured and simulated outputs during training.

3 Results and Conclusion

The 3 models were validated and tested in the reduced space of the principle components (2-D), reaching 94.8%, 97.8% and 99.4% correlation for the first principle component for NARX, HW1, HW2 models respectively. The predictions were then transformed back to the original space to determine the original states (Fig 2).

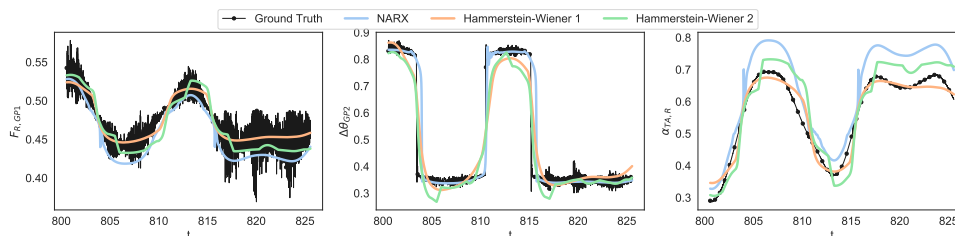


Figure 2: Predictions of state variables in original full space of $F_{R,GP1}$, $\Delta\theta_{GP2}$ and $\alpha_{TA,R}$

Pearson's correlation coefficients between the 3 models and unfiltered ground truth lie between 85% and 99% for all states. Some states were predicted more accurately using one approach than the other. This implies that a posteriori study of the suitability of the identification approaches is crucial during the deployment of the digital twin to decrease the uncertainty of the inferred states.

The developed approaches shall be validated in realistic load cases of operation such as emergency shut-down due to electric system failures or grid faults in order to assess their performance for further deployment in a digital twin framework.

References

- [1] Steven Lee Brunton and Jose Nathan Kutz. *Data-driven science and engineering machine learning, dynamical systems, and control*. 2019. ISBN: 978-1-108-42209-3.
- [2] Oliver Nelles. *Nonlinear System Identification*. Berlin, Heidelberg: Springer Berlin Heidelberg, 2001. ISBN: 978-3-642-08674-8. DOI: 10.1007/978-3-662-04323-3.
- [3] Pietro Bortolotti et al. *IEA Wind Task 37 on Systems Engineering in Wind Energy WP2.1 Reference Wind Turbines*. 2019. DOI: 10.2172/1529216.
- [4] Johan Schoukens and Lennart Ljung. "Nonlinear System Identification: A User-Oriented Roadmap". In: *arXiv:1902.00683 [cs]* (2019). DOI: 10.1109/MCS.2019.2938121. (Visited on 04/21/2020).

**SOCIAL ACCEPTANCE
&
TECHNO-ECONOMICS**

Experimental quantification of low-frequency sound of Wind Turbines

E. Blumendeller^a and P.W. Cheng^a

^aStuttgart Wind Energy @ Institute of Aircraft Design - University Stuttgart,
Allmandring 5b, 70569 Stuttgart

E-mail: blumendeller@ifb.uni-stuttgart.de

Keywords: Low-frequency sound, Meteorology, Long-term measurements

1 Motivation

The expansion of renewable energy usage is one of the major social and economic goals in Europe and therefore requires acceptance and support from the population. Especially due to the expansion on land, a growing number of people lives closer to wind turbines, which leads to reported annoyance due to expected visual or acoustic disturbances caused by the planned wind turbines (WT) [1]. In many cases, it is argued that low frequency (20 Hz to 200 Hz) and infrasonic (1 Hz to 20 Hz) sound emission lead to the perceptibility of WT even at large distances. Research shows a correlation between WT noise propagation and meteorological and site conditions [2] [3]. For example, season, time of day and geographic site condition, which can be either flat, hilly or complex terrain, influence the sound propagation and perception of the sound by residents. A specific phenomenon occurs at WT sites in low mountain ranges, which probably contributes significantly to current acceptance problems and complaints. In valley locations wind background noises may be absent for geographical reasons - but the sounds of the WT can still be heard. Furthermore sound refraction can occur due to meteorological effects like wind or temperature gradients. Under certain conditions, refracted sound rays are bended towards residential buildings in valley locations and lead to higher sound level [4][5].

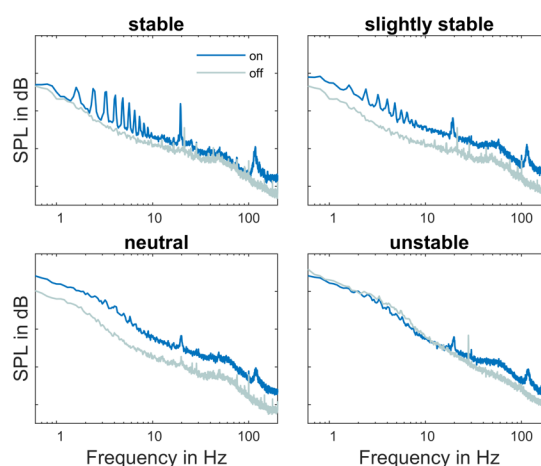


Figure 1: Comparison between on/off (rotating/non-rotating WT) unweighted sound pressure level measured in 240 m distance from a WT for different atmospheric conditions [3]

From previous research on low-frequency sound from WT, a relation between atmospheric stability and measured acoustic sound from the wind turbine was found in [3]. In aforementioned research atmospheric stability was defined due to [6] with the logarithmic shear exponent. Values above 0.4 are associated with moderately to very stable atmospheric condition, whereas a shear exponent with values below 0.1 is related to higher changes of wind speed and direction over time and space, and therefore unstable condition. In Fig. 1 unweighted frequency spectra at the point of emission and for similar wind speed, rotational speed and varying shear exponent show tones related to the blade passing frequency and its harmonics below 10 Hz. It is shown, that the tones are most dominant for stable atmospheric conditions. Therefore, simultaneous investigation of the low-frequency sound emission close to the WT and additionally in the point of immission at residential buildings is necessary to get a better understanding of WT noise, low-frequency sound propagation and its relation to meteorological and local conditions as well as annoyance of residents.

2 Research Scope

Considering these aspects, the aim of this research is to evaluate the influence of the above-mentioned conditions on low-frequency sound propagation in complex terrain of the Swabian Alps in southern Germany. Therefore simultaneous measurements are carried out on a wind farm and at residential buildings (Fig. 2). The relation of measured sound data with time periods where severe disturbance is documented by residents can help to identify, if low-frequency noise is a contributing factor to annoyance. The aim of the research is to derive recommendations for the sound propagation prognosis of wind farms in regions with pronounced orography and to provide a basis for the development of a noise-reduced operational management of WT.

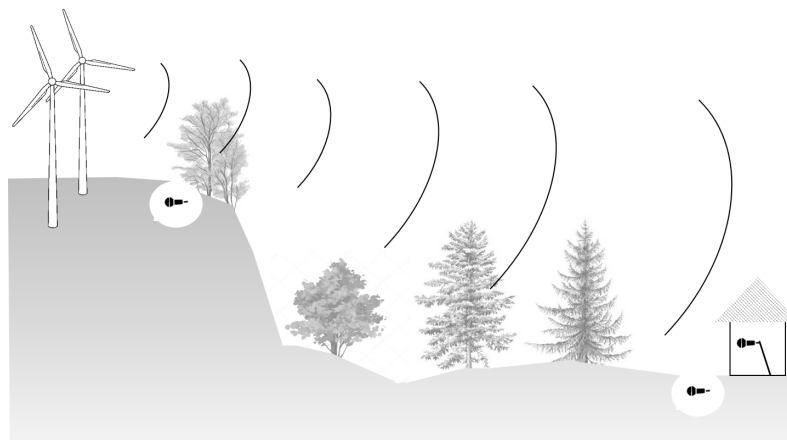


Figure 2: Acoustic measurements in the vicinity of a wind farm in complex terrain.

References

- [1] Doolan C 2013 *Wind Engineering* **37** 97–104 ISSN 0309524X
- [2] Zajamšek B, Hansen K L, Doolan C J and Hansen C H 2016 *Journal of Sound and Vibration* **370** 176–190 ISSN 10958568
- [3] Blumendeller E, Kimmig I, Huber G, Rettler P and Cheng P W 2020 343–365
- [4] Larsson C and Israelsson S 1991 *Applied Acoustics* **33** 109–121
- [5] Conrady K 2019 *Wind Turbine Sound in Cold Climates* URL <http://www.diva-portal.org/smash/get/diva2:1296842/FULLTEXT01.pdf>
- [6] Van Den Berg G P 2004 *Journal of Sound and Vibration* **277** 955–970 ISSN 0022460X

A new physics-based model for guiding bat carcass surveys at wind turbines

S Prakash^{a,b}, C D Markfort^{a,b}

^a IIHR-Hydroscience and Engineering, The University of Iowa, Iowa City, IA 52242, USA.

^b Civil and Environmental Engineering, The University of Iowa, Iowa City, IA 52242, USA.

E-mail: shivendra-prakash@uiowa.edu

Keywords: ballistics model, bat carcass, wind turbine, monte-carlo

We propose a new model for computing bat fate at wind turbines to guide carcass surveys and improve bat mortality estimates for surveys with limited coverage. Current approaches for guiding carcass search radius estimation are based on statistical analysis of prior survey data, which can result in an inappropriate search area. Additionally, studies relying only on empirical data are limited to the specific wind turbine models, bat species, and ambient conditions included in the dataset. Using a physics-based approach, the new model can provide insights about the effect of the governing parameters on the likely carcass fall zone distributions. A robust and economically efficient model is needed to guide surveys for wind farm operators to determine the extent that wind turbines adversely impact Threatened and Endangered Species and to evaluate the environmental effects of wind power generation facilities.

The new model is based on the hypothesis that the distribution of where bat carcasses fall after collision with wind turbines is sensitive to the variation in biophysical and aerodynamic properties of bats, wind turbine size and operational characteristics, and wind speed. The resulting ballistics model is introduced for simulating bat carcass trajectories after impact with wind turbine blades. The model can also be used to infer the behavior of bats near wind turbines to better predict the risk of collision between bats and turbine blades.

This research consists of three phases: In the first phase, we for the first time measured the aerodynamic properties of bat carcasses, including terminal velocity and drag coefficient, for three bat species using high-speed imaging of carcass drop experiments [1]. In the second phase, a 3-D ballistics model was developed by including bat properties, wind velocity and turbine blade rotation speed to determine the extent of the fall zone and the likely strike locations on the rotor plane, using SCADA and carcass survey data [2]. In the third phase, we demonstrate use of Monte-Carlo simulations of the new ballistics model and introduce a methodology for estimating bat fall zone distribution for the autumn migration season. The Monte-Carlo based ballistics model framework is demonstrated for guiding carcass surveys for individual visits as well as for full migration seasons involving various bat species, meteorological and turbine operational conditions. This framework can also be used for correcting carcass survey data for limited or unsearched areas.

Acknowledgements

The study was conducted with financial support from MidAmerican Energy Company (MEC), and with input from scientists at the U.S. Fish & Wildlife Service (USFWS) in support of development of a Habitat Conservation Plan for Wind Energy Facilities in Iowa.

Bibliography

- [1] Prakash S and Markfort C 2020 Experimental investigation of aerodynamic characteristics of bat carcasses after collision with a wind turbine. *Wind Energ. Sci.*, **5**, 745–758.
- [2] Prakash S and Markfort C Development and testing of a 3-D ballistics model for bat impact on wind turbines. Under revision in *Wind Energy*

Economic control of wind based hybrid energy system

Abhinav Anand^a, Carlo L. Bottasso^a, and Stefan Loew^a

^aTechnical University of Munich, Wind Energy Institute, Boltzmannstrasse 15,
85748 Garching bei Muenchen, Germany

15th November, 2020

E-mail: abhinav.anand@tum.de

Keywords: Hybrid system, Economic Control, MPC, Digital Twins, Battery energy storage

1 Introduction

The standard economic control formulations for wind based hybrid energy systems do not perform dynamic economic optimization [1]. A two-level approach is utilized which includes tracking pre-computed economically optimal steady state set-points via a standard model predictive controller (MPC) [2]. Additionally, explicit and accurate consideration of wind turbine and battery damage in the optimization objective is seldom witnessed [3]. This is possibly because the standard cyclic fatigue evaluation approaches, such as Rainflow algorithm, do not have an analytical formulation and contain algorithmic branches and loops. This does not allow calculation of sensitivities required for standard gradient-based optimization techniques. Consequently, cyclic damage minimization objective is approximated or even not considered [3, 4].

2 Methodology

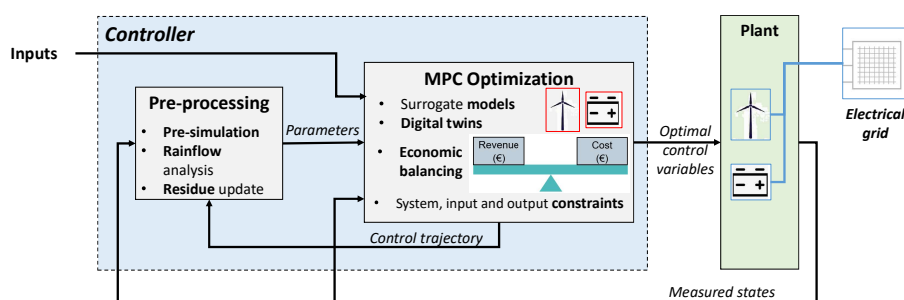


Figure 1: Process-flow using applied methodology

The proposed methodology, as shown in an implemented process flow in Fig. 1, focuses on formulating and solving a purely economic optimization problem for a grid-connected hybrid generation unit. This can be implemented inside an optimal controller operating in closed loop with the hybrid generation unit in receding horizon fashion. Such a controller can internally utilize a digital twin of the hybrid generation unit to calculate economically optimal control variables for the real plant by optimizing a chosen realistic and operationally meaningful economic objective (maximizing profit by balancing between cost and revenue). A novel parameter-based online rainflow counting (PORFC) approach, proposed first in our previous work [5] and illustrated in detail in [6], can be conveniently used for handling cyclic damage minimization within the MPC controller. The PORFC-based approach allows accurate sensitivity calculations based upon generated parameters via pre-simulation.

The formulated economic optimal control problem

$$\min_{\beta^{WT}, T_g^{WT}, P^B} -J_{generation}^{WT} + J_{tower\ fatigue}^{WT} + J_{cyclic\ loss}^B \quad (1)$$

is solved in an online MPC fashion for a grid connected wind turbine and battery based hybrid energy system. The optimization variables are turbine pitch angle β^{WT} , turbine generator torque T_g^{WT} , and applied battery power P^B . The optimization objective includes maximizing aerodynamic power capture $J_{generation}^{WT}$, minimizing tower fatigue from cyclic stress at its root $J_{tower\ fatigue}^{WT}$, and minimizing battery cyclic capacity loss $J_{cyclic\ loss}^B$. In addition to the system and input constraints, the optimization problem is also subject to $P_{elec}^{WT} + P^B = P_{demand}^{grid}$ denoting the balance between total generation and demand.

The optimal control problem, formulated in (1), is applied to a reduced order NREL 5 MW wind turbine model with a 1MW/1MWh Li-ion battery energy storage. The output is compared to a base case scenario

$$\min_{\beta^{WT}, T_g^{WT}, P^B} -J_{generation}^{WT} \quad (2)$$

with the only objective of maximizing the wind power capture subject to same constraints as in (1). The net profit is calculated as the difference of revenue from wind power generation and costs due to tower fatigue cost and battery capacity loss.

3 Initial results

Fig. 2 shows the simulation comparison results of the formulated economic MPC controller (green curve), as described in (1), which performs economically better than a base-case scenario (blue curve), as described in (2). This is because the controller manages to find an optimal-spot for turbine operation which balances the tower fatigue and power capture, at the same time also demanding lesser power from the battery. Although, the equality constraint of power balancing is numerically violated for both controllers, the absolute mismatch is in orders of magnitudes smaller than the reference power.

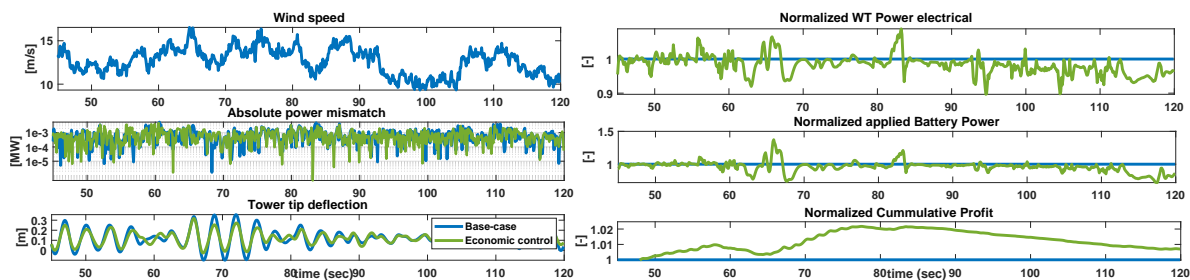


Figure 2: Simulation output for a realistic power reference ramped up/down periodically around turbine rated power

The initial results for the formulated purely economic control problem shows profit gain against a realistic base-case scenario with acceptable dynamic performance. This motivates extending the approach towards more complex dynamical systems such as wind farm and solar plants based hybrid systems participating in modern grid ancillary services for obtaining profit optimal operating-points.

References

- [1] Borhan H, Rotea M A and Viassolo D 2012 *Wind Energy* **24** n/a–n/a ISSN 10954244
- [2] Tran T, Linga K V and Maciejowski J M 2014 *Proceedings of the 31st International Symposium on Automation and Robotics in Construction and Mining (ISARC)*
- [3] Wang C, Du Z, Ni Y, Li C and Zhang G 2018 *IET Generation, Transmission & Distribution* **12** 2406–2414 ISSN 1751-8687

- [4] Shi Y, Xu B, Tan Y, Kirschen D and Zhang B 2019 *IEEE Transactions on Automatic Control* **64** 2324–2339 ISSN 0018-9286
- [5] Loew S, Obradovic D, Anand A and Szabo A 2020 *Accepted to European Control Conference 2020*
- [6] Loew S, Obradovic D and Bottasso C L 2020 *Accepted to TORQUE2020*

Development and optimisation of hydrogen storage coupled with FOWT farms

O. Ibrahim^{a,b} and C. Desmond^{a,b}

^aMaREI Centre, Environmental Research Institute, University College Cork, Ireland

^bSchool of Engineering, University College Cork, Ireland

30.09.2020

E-mail: o_ibrahim@outlook.de

Keywords: Floating offshore wind, Power-to-Gas, Hydrogen, Energy storage, Techno-economic assessment

1 Abstract

For effective climate change mitigation, the share of renewable energy is significantly increasing. Various developments in the wind technologies are actively taking place nowadays. On top of them, is the Floating offshore wind turbines (FOWTs). They offer promising potential over the ordinary mature offshore wind turbines technology in several aspects as: (i) the ease of commissioning and installation onshore, and then getting transported offshore, (ii) the attractive edge of fixations costs as they eliminate the need of building the base steel structure in the sea-bed, and just simply having their base floating and anchored to the sea-bed, (iii) the ability to get placed far away from the shore in great sea depths, so as to benefit from the higher wind speed ranges there; generating higher electricity yield.

The intermittent nature of renewable energy creates undesired curtailment need to accommodate them on grid for periods with production exceeding the demand. The FOWTs' theory of operation suggests they have sharper intermittent nature than other wind technologies or other renewables in general that consequently, pushes the call for research for solutions to adapt them well on grid.

Instead of being directly curtailed, excess energy can be store to balance the power supply and demand. Uprising electro-chemical storage methodologies has hydrogen as an energy carrier through electrolysis, a clearly promising path. This PhD work tackles this specific storage solution. Coupling hydrogen production from a green source contributes effectively to carbon abatement; by having it as clean fuel, as well as a buffering medium, and increasing utilisation of the generated wind power.

This work focus starts with the hydrogen production, i.e. with the electrolysis suitable technologies, and its important operational parameters; including efficiencies, system response, cold restart time, production rate, carbon emissions, capital, and operational costs. Followed by the hydrogen storage variables as; energy density, hydrogen content, pressure, costs, and safety requirements. Passing by hydrogen storage and transportation techniques; including liquid organic, metal organic, gaseous and even liquid hydrogen. The produced hydrogen is intended to get sold raw to the market, or used by the fuel cell vehicles in the hydrogen fuelling stations. This work also considers hydrogen storage as a buffer; so as it is to be used to operate fuel cells in the main cycle, generating electricity to be fed to the grid at other intervals when needed. For this, the project's fuel cell variables have fuel cell technologies, sizes, weight, storage time, and costs.

Integrating the above elements coupled with FOWTs and its floating substation, in a complete conceptual system represents the following steps in this work. Furthermore, both stand-alone (off-grid) and grid-connected systems will be considered, with more focus given to the off-grid scenario with intermittent electricity production. Techno-economic assessments will be performed, and the levelised cost of storage will be calculated for the various scenarios and the most promising ones will be considered for the following step in the project.

The wrapping phase of the project would have a deeper investigation of the most promising hydrogen system implementation methodology. All costs, capacities, and optimal operating parameters in this phase will be real-life ones from the relevant stakeholders. The proposed optimised design would be physically tested with the project's industrial partner to determine its impacts on cost and performance.

STRUCTURAL ANALYSIS

Numerical study on the use of strains for detection of damage in wind turbine blades

M.A. Fremmelev^{a,b}, P. Ladpli^a, L.O. Bernhammer^a, M. McGugan^b, and K. Branner^b

^aSiemens Gamesa Renewable Energy, Assensvej 11, 9220 Aalborg East, Denmark

^bTechnical University of Denmark, Department of Wind Energy, Frederiksborgvej 399, 4000 Roskilde, Denmark

15 November 2020

E-mail: mads.fremmelev@siemensgamesa.com

Keywords: Wind Turbine Blades, Finite Elements, Structural Health Monitoring, Strain

Abstract

The present work studies the use of variations in the strain distribution in wind turbine blades as an indicator of blade damage. Numerical studies of damaged and healthy blades are conducted for this purpose by modeling the strain field variation in an existing blade finite element model, discretized by shell elements. Damages introduced in the blade model consist of cracks transverse to the blade span. Changes in the spanwise normal strains resulting from the presence of a damage are studied. From these studies the distance at which a damage may be detectable is derived, and strategies for sensor placement with the purpose of damage detection are discussed.

Keywords: Wind Turbine Blades, Finite Elements, Structural Health Monitoring, Strain

1 Introduction

Issues with wind turbine blades are a major contributor to turbine downtime. Dao et al. [1] found that between 18% and 22% of the downtime for onshore and offshore wind turbines, respectively, is caused by issues with blades. The required maintenance contributes to a higher levelized cost of energy. To reduce the need for blade related maintenance, it is necessary to detect damage in blades while the damage can easily be repaired. Preferably, this is to be done automatically using structural health monitoring (SHM) systems exploiting sensors to monitor blades during operation. McGugan et al. [2] discuss possibilities for SHM of offshore wind turbines, with the mentioning of e.g. strain gauges for damage detection. Strain gauges are commonly used for load monitoring during blade testing and prototype turbine load validation. As such, it would be advantageous, if an already developed system could be used to extract additional information, e.g. the presence and development of damage during testing.

One way to reduce maintenance costs is to reduce or eliminate the need for scheduled maintenance through remote SHM, effectively introducing a condition based maintenance approach. Using a sensor system, data is collected during operation of a wind turbine, and a signal analysis algorithm is used to analyze the physical condition of the turbine's blades. The physical condition of the monitored blades is determined by comparison of a baseline signal, taken at a point in time where the turbine blades are undamaged, and the most recent signal. One example of such a system can be found in [3]. Different types of sensors can be used for SHM systems, with the literature presenting investigations of different SHM systems tested on wind turbine blades in laboratory environments and on operating wind turbines. There is also a need to accurately detect and monitor damage during blade testing, since validation of new designs and effect of damages are investigated in this manner. The present work focuses on strain analysis in the turbine blade as a method for damage detection in wind turbine blades.

Common damage types in wind turbine blades were presented by Sørensen et al. [4], based on damages observed from a quasi-static wind turbine blade test. Observed damage types include face/core debonding

in sandwich panels, cracks and delaminations in laminates, and cracks in adhesive joints. Sørensen et al. [5] also tested different SHM systems for detection of artificial damages in a wind turbine blade during testing. In the performed tests, strain gauges could be used to detect different types damage within a limited range. Fatigue testing of two 9-meter wind turbine blades was conducted by Paquette et al. [6, 7], using strain gauges for load and health monitoring of the blades. Using strain gauge data, the blade stiffness was shown to degrade over the course of the test campaign, indicating degradation, e.g. fatigue aging, in the blade. Comparing the values from different strain gauges over the course of the test, the presence and development of a damage could be detected. Taylor et al. [8, 9] performed multiple blade fatigue tests, where a pristine blade and a blade with artificial damage were subjected to cyclic loading. Strain gauges, accelerometers, acoustic emission and guided waves monitored a laminate crack developing in the root section. Further analysis of the test data was conducted by Taylor et al. [10, 11] and by Dervilis et al. [12, 13, 14], focusing on guided waves measurements. Guided waves captured relatively localized damages, at a distance of 0.5 m, while constituting a relatively high cost of the sensing system compared to a strain gauge system. A 34-meter blade was subjected to quasi-static testing by Haselbach et al. [15], with fiber Bragg gratings placed at the trailing edge, which were used to measure normal strains in the spanwise and edgewise directions. The strain measurements were used to monitor local buckling at the trailing edge, which may lead to debonding in the trailing edge adhesive joint and a subsequent blade failure. A 34-meter wind turbine blade, subjected to quasi-static loading, was tested to failure by Overgaard et al. [16]. Strain gauges were used to record the spanwise normal strains. These tests showed much larger strain magnitudes at the location of failure, where a delamination initiated and ultimately resulted in failure of the blade. Sierra-Pérez et al. [17] compared the performance of conventional foil strain gauges, fiber Bragg gratings and a distributed optical strain sensors for damage detection in a wind turbine blade during testing. Strain gauges and fiber Bragg gratings exhibited similar performance with respect to measurement accuracy and ability to detect damages. However, advantages of fiber Bragg gratings, such as embedding during manufacture, longer lifetime and electromagnetic immunity, were pointed out. Advantages of the distributed optical sensors included the variable sensing density, where it was found that a reduced distance between sensing points did not necessarily yield better resolution for damage detection, being due to reduced resolution in the sensor signal.

Ulriksen et al. [18, 19] investigated damage detection in wind turbine blades using operational modal analysis on a blade mounted on a test stand. Damage detection in an operating wind turbine was also studied by the authors [18], using an active vibration input and accelerometer data. Regarding the use of strain for damage detection in wind turbines, Benedetti et al. [20] conducted research on the topic, focusing on numerical studies of wind turbine towers. The difference in strain between adjacent sensors was found to be the most promising measure for damage detection. Studies were limited to steel towers, while the numerical studies on using strains for damage detection in fiber reinforced polymer sandwich structures, such as wind turbine blades, still needs to be explored. Arsenault et al. [21] proposed a distributed system of fiber Bragg gratings, using operational modal analysis to detect damage in blades. The literature thus covers the use of different sensing systems for damage detection during blade testing and in the field, one sensing system being strain measurements. While numerical studies on damage detection in wind turbine towers have been investigated, numerical studies on damage in wind turbine blades remains still an area of investigation.

The current work considers the following problem statement: How is the strain distribution in a wind turbine blade affected by a damage, and what is the potential for detecting changes in strain, caused by such a damage, through use of strain sensors?

The present work is concerned with numerical feasibility studies on the use of strain measurements for damage detection in wind turbine blades. Changes in the strain field, caused by the presence of damage, are desired to be used for detection of damage during blade testing. The damage types investigated are cracks in sandwich panels of a wind turbine blade. The paper is structured as follows: The utilized wind turbine blade model is presented in Section 2, including a presentation of the utilized approach for damage modeling. The results from the numerical analyses are presented in Section 3, and conclusions on the applicability of a strain based monitoring solution are drawn in Section 4.

2 Modeling Approach of Structural Damages

2.1 Blade Model

Strains near a damage in a wind turbine blade are simulated, using a model in the commercial finite element (FE) software ANSYS. The blade in question has a length of 52 meters. This work is concerned with the blade shell, which has been manufactured as a sandwich construction with glass fiber reinforced epoxy laminates as face sheets and a balsa core. The blade is fixed at the root, and loading is applied from the pressure side towards the suction side through a number of distributed nodal forces, resulting in a moment distribution which resembles operating conditions. A mesh convergence study is conducted for the blade model. Convergence of the tip deflection is obtained with an element length of approximately 0.1 meters. With this element size, in-plane strains have converged near the location at which a damage is to be modeled. This element size is relatively large, compared to the size of damages in wind turbine blades. To ensure a good resolution in the strain distribution around the crack, the element size is decreased to 0.01 meters. To reduce computational time, the strain distribution near the crack is modeled using a submodel of the blade geometry near the crack. First the full blade model is solved with an element size of 0.1 meters. Subsequently, a submodel is created, using the geometry near the crack. Using an element size of 0.01 meters and displacements from the full model as boundary conditions, the submodel is solved. Both the full model and the submodel are solved as quasi-static linear analyses, using linear shell elements (SHELL181 in ANSYS), with linear elastic material properties.

2.2 Blade Damage

The considered damage case is based on damages observed in literature on blade tests. For this work, a crack transverse to the span of the blade, located in the blade shell, is studied. The damage is placed near the maximum chord, as observed during testing by Rumsey et al. [7], on the pressure side of the blade. The damage location is shown on the blade surface and on the cross section, see Figure 1 and Figure 2, respectively. $2a$ designates the crack length, d is the distance between the crack faces and strain measurements, and d_{web} is the distance between the crack center and the shear web, measured along the circumference of the blade cross section. The crack center is placed at a distance d_{web} equal to 0.25 times the chord at the associated cross section. It is assumed that the crack will grow symmetrically around the initial crack center. Different crack lengths, centered around the same position, are considered. In the model, strains are recorded along a path of distance of twice the maximum crack length investigated. The measurement path is denoted along the cross-section of the blade with local coordinate x , ranging from 0 to 1 in normalized coordinates. The position of the utilized measurement paths relative to the crack are sketched on the submodel of the blade, see Figure 3.

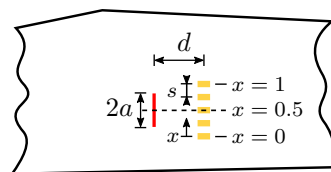


Figure 1: Part of blade, viewed from pressure side, showing crack location as well as strain measurement path.

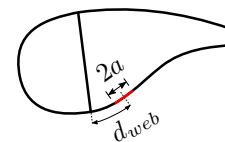


Figure 2: Blade cross section, showing crack location.

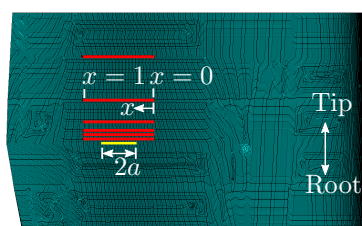


Figure 3: FE submodel mesh, showing crack of length $2a = 0.5$ m (yellow) and measurement paths (red).

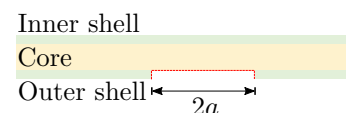


Figure 4: Location of crack in blade sandwich panel.

The crack is modeled as a face sheet crack, going through the entire outer shell laminate. In the FE model, the crack is implemented by nodal separation. The sandwich panel is modeled by single shell elements in the through-thickness direction. To include a crack through part of the sandwich layup, the shell elements around the crack location are duplicated. Part of the shell sections from the original shell elements are divided across the duplicate shell elements. A crack is included by disassociating nodes in the new shell elements. This results in a face sheet crack in the outer shell laminate, see Figure 4.

3 Results of Parameter Study of Crack

Using the blade model presented in Section 2, the strain distribution near the damage shown in Figure 1 and Figure 2 is simulated. Figure 5 shows the difference in spanwise normal strain $\Delta\varepsilon_{11}$ near the crack, normalized with respect to the maximum value of the undamaged blade $\varepsilon_{11,\text{healthy,max}}$, see Equation (1). Strains in the spanwise normal direction are used, since they are of largest magnitude, and changes affect the largest area around the crack. The spanwise direction is the main load carrying direction. Difference in spanwise-chordwise shear strain $\Delta\varepsilon_{12}$, see Equation (2), is shown in Figure 6.

$$\Delta\varepsilon_{11} = \frac{\varepsilon_{11,\text{damaged}} - \varepsilon_{11,\text{healthy}}}{\varepsilon_{11,\text{healthy,max}}} \quad (1)$$

$$\Delta\varepsilon_{12} = \frac{\varepsilon_{12,\text{damaged}} - \varepsilon_{12,\text{healthy}}}{\varepsilon_{12,\text{healthy,max}}} \quad (2)$$

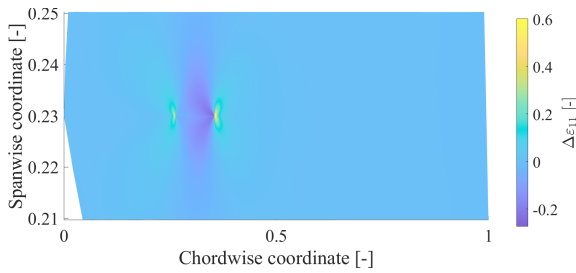


Figure 5: Difference in spanwise normal strains between healthy and damaged blade with a crack length $2a = 0.5$ m.

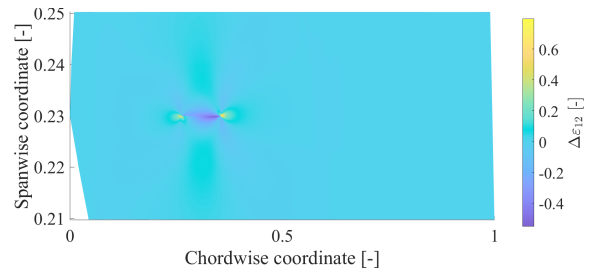


Figure 6: Difference in in-plane (spanwise-chordwise) shear strains between healthy and damaged blade with a crack length $2a = 0.5$ m.

The nodal normal strains in the spanwise direction are plotted along the circumference of the blade, sampled at different distances d from the crack with varying crack lengths $2a$.

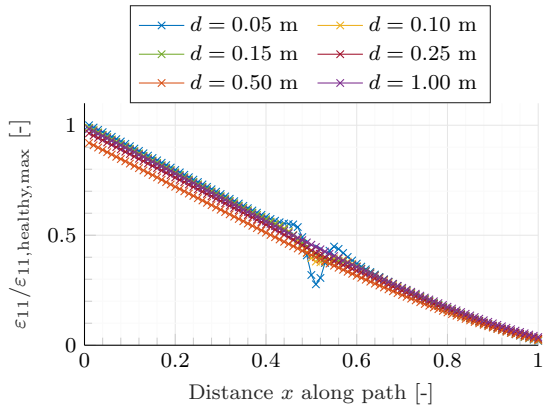


Figure 7: Spanwise normal strain at different distances d to the crack with length $2a = 0.05$ m.

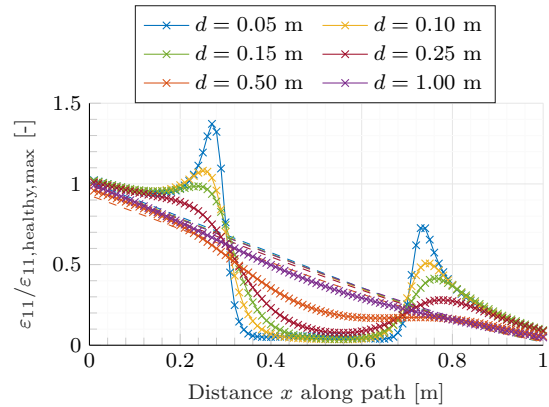


Figure 8: Spanwise normal strain at different distances d to the crack with length $2a = 0.5$ m.

Figure 7 and Figure 8 show the spanwise normal strains at different distances d from a crack with length $2a = 0.05$ m and $2a = 0.50$ m, respectively. Dashed lines show the nominal spanwise normal

strains of the undamaged blade, sampled at the same distance as the solid line with the same color. All strain values are normalized with respect to the largest nominal spanwise normal strain value, which is done consistently for all strain values presented in the present work. The strains are sampled at nodes along the circumference of the blade, as illustrated in Figure 1. With a crack of length $2a = 0.05$ m, significant changes in the strain distribution are only notable at a relatively small distance from the crack compared to the chord of the blade. Including a crack with length $2a = 0.50$ m, changes in the strain distribution are notable at a larger distance from the crack, as well as along a longer distance over the measurement path. Figures 9 and 10 show the spanwise normal strains at distances $d = 0.05$ m, and $d = 1.0$ m, respectively, from a crack with varying length $2a$. The plots show increasing values in the spanwise normal strain ε_{11} with increasing crack length $2a$ and decreasing distance d from the crack.

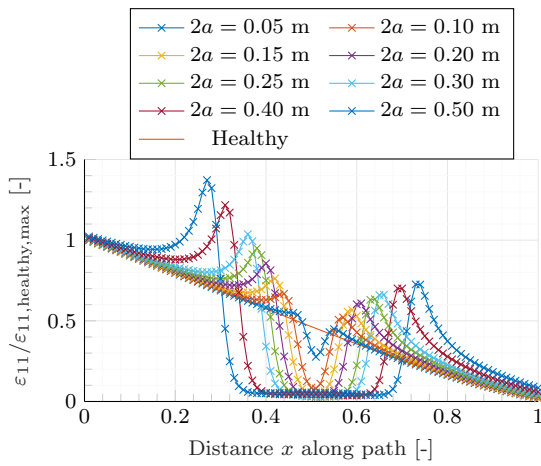


Figure 9: Spanwise normal strain at $d = 0.05$ m from the crack, with different crack length $2a$. The peaks above the healthy baseline approximately align with the tips of the crack with varying length $2a$.

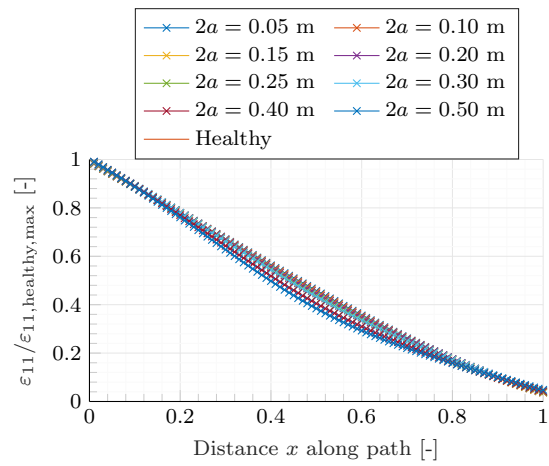


Figure 10: Spanwise normal strain at $d = 1.0$ m from the crack, with different crack lengths $2a$.

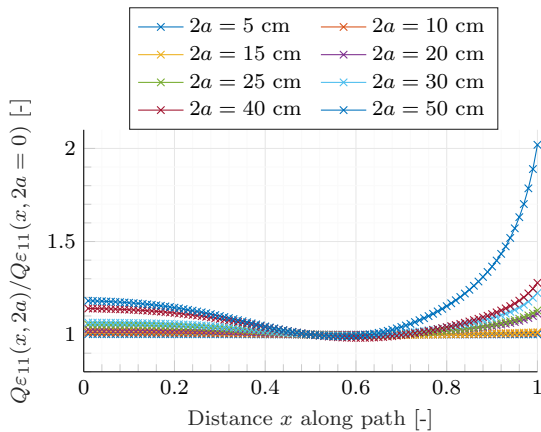


Figure 11: Quotient-ratio of spanwise normal strain $Q\varepsilon_{11}(x, 2a)/Q\varepsilon_{11}(x, 2a = 0)$ between sensors along the measurement path and the central sensor, at distance $d = 1.0$ m from a crack of different length $2a$, with sensor spacing $s = 0.01$ m.

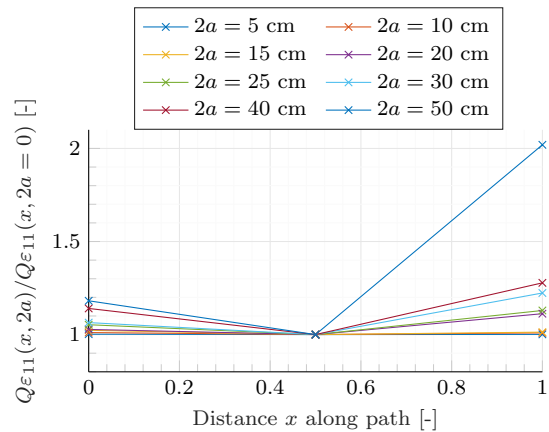


Figure 12: Quotient-ratio of spanwise normal strain $Q\varepsilon_{11}(x, 2a)/Q\varepsilon_{11}(x, 2a = 0)$ between sensors along the measurement path and the central sensor, at distance $d = 1.0$ m from a crack of different length $2a$, with sensor spacing $s = 0.5$ m.

To quantify changes in strain near the crack, the quotient-ratio of the strain measurements along the

measurement path to the strain centrally along the measurement path (see Figure 1) is calculated:

$$Q_{\varepsilon_{11}}(x, 2a) = \frac{\varepsilon_{11}(x, 2a)}{\varepsilon_{11}(x = 0.5, 2a)} \quad (3)$$

All values for $Q_{\varepsilon_{11}}(x, 2a)$ are normalized with respect to the quotient-ratio at the undamaged state $Q_{\varepsilon_{11}}(x, 2a = 0)$. Results are plotted in Figure 11 for strains sampled at a distance $d = 1.0$ m from a crack of different length $2a$, with sensor spacing $s = 0.01$ m (see Figure 1). Increasing the sensor spacing s will result in a coarser discretization of the graphs in Figure 11. In Figure 12, an increasing non-linear trend in the change in $Q_{\varepsilon_{11}}$ with increasing crack length $2a$ is shown. A non-linear trend in the quotient-ratio $Q_{\varepsilon_{11}}$ may thus be an indicator for the presence of a damage in the blade. Using the change in strain $Q_{\varepsilon_{11}}$, results show a relatively large change under the presence of a damage, which can be observed at a distance of 1 meter from the crack. Figures 12 and 13 show that using e.g. three sensors, changes in the quotient-ratio of the centrally placed sensor and those placed far-field may be used for detection of damage in the blade. It should be noted that the plotted values of the quotient-ratio $Q_{\varepsilon_{11}}$, which are normalized with respect to the respective values from the healthy blade, do not take into account the magnitude of the numerical strain values. Thus, the method relies on the changes in strain to be measured at locations where the nominal strains are of relatively large magnitude. For example, in Figure 11 the change in strain $Q_{\varepsilon_{11}}$ is higher at $x = 1$ than at $x = 0$, but the strain magnitude at $x = 0$ is higher than at $x = 1$, see Figure 10.

The strain gradient between adjacent sensors with spacing s are also considered as damage indicator, expressed for the damaged blade with a crack of length $2a$ as $\delta\varepsilon_{11}(x, 2a)$ through a forward difference approximation:

$$\delta\varepsilon_{11}(x, 2a) = \frac{\partial\varepsilon_{11}(x, 2a)}{\partial x} \quad (4)$$

$$\delta\varepsilon_{11}(x, 2a) \approx \frac{\varepsilon_{11}(x + s, 2a) - \varepsilon_{11}(x, 2a)}{s} \quad (5)$$

To visualize the changes between healthy and damaged states, the gradients in spanwise normal strain between adjacent sensors for the healthy blade $\delta\varepsilon_{11}(x, 2a = 0)$ are subtracted from the respective values for the damaged blade $\delta\varepsilon_{11}(x, 2a)$. The gradients in spanwise normal strains between adjacent sensors $\delta\varepsilon_{11}(x, 2a)$ with sensor spacing $s = 0.01$ m are shown in Figure 14. The strain gradients are based on the strain values plotted in Figure 10.

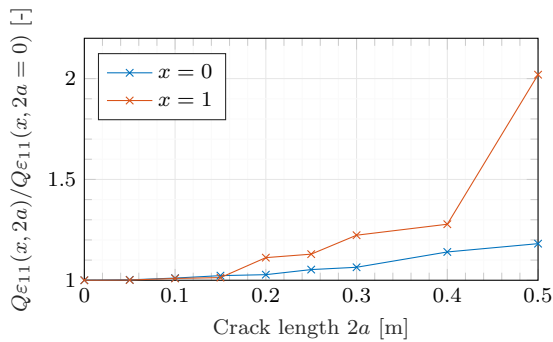


Figure 13: Quotient-ratio of spanwise normal strain $Q_{\varepsilon_{11}}(x, 2a)$ between sensors along the measurement path and the central sensor, at distance $d = 1.0$ m as a function of the crack length $2a$, with sensor spacing $s = 0.5$ m. The values at $x = 0.5$, which equate to unity, are not plotted.

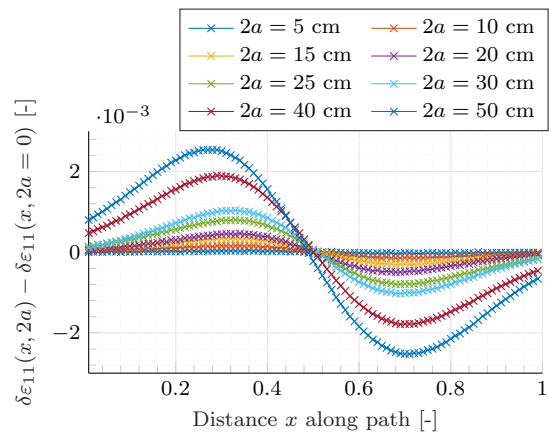


Figure 14: Changes in strain gradient from the healthy state $\delta\varepsilon_{11}(x, 2a = 0)$ to the damaged state $\delta\varepsilon_{11}(x, 2a)$ between adjacent sensors with spacing $s = 0.01$ m, at distance $d = 1.0$ m from cracks of different length $2a$.

By increasing the sensor spacing s , the changes in strain gradient $\delta\varepsilon_{11}$ from the healthy to the damaged state follows the curves in Figure 14 with coarser discretization. Based on the graphs in Figure

14, increasing changes in strain gradient from the healthy to the damaged state between adjacent sensors indicates an increase in crack length. At $x = 0.5$ along the measurement path, the change in strain gradient from the healthy to the damaged state equals 0. This may cause a crack to not be detected, if two sensors are used, and the strain values change equally for the two sensors. Using at least three sensors, this issue should be rectified for the considered distance $d = 1.0$ m from the crack.

4 Discussions

Using a FE model of a wind turbine blade, changes in the strain distribution near cracks have been studied. The used FE model is discretized using shell elements. Considering that in-plane normal strains are studied here, the approach presented is deemed reasonable, since the model is used for a feasibility study, investigating the expected extent of changes in the strain distribution caused by damage. Additionally, the used shell model offers good computational performance, which is advantageous for parametric studies. For accurate out-of-plane strains or progressive damage simulations, a solid model may however be preferable. Regarding the modeled damage, the crack is perfectly sharp, meaning strains at the crack tip tend towards infinity in the model. This study on the effect of cracks on the strain distribution in wind turbine blades has assumed prior knowledge of the location of the studied cracks. The results from this study indicate the range around cracks within which changes in the strain distribution may be detectable. With the largest crack length investigated, $2a = 0.5$ m, the strain distribution was affected at a spanwise distance d approximately equal to twice the crack length. At a distance d equal to the crack length $2a$, the change in the strain distribution is more significant, see e.g. Figure 8.

Considering monitoring of damage progression, an increase in the strain magnitudes over time, followed by a decrease in strain magnitudes, considering the same load level, may indicate crack growth, see Figure 9. For example, given a sensor placed at $x = 0.4$ for the considered crack position, which corresponds to the sensor being placed at a spanwise and chordwise offset relative to the crack center. At this position, the strain magnitude would increase until the crack reaches a length of approximately $2a = 0.2$ m. With further increase in crack length, the strain magnitude decreases at this position.

For experimental or operational application, the presented method would require a large number of strain sensors for monitoring of an entire blade, which may not be ideal. Local monitoring of critical locations, e.g. repairs and geometry transitions, is however deemed feasible for the presented method. Based on the mentioned distances relative to the investigated crack lengths, a large part of the chord, at a given spanwise position, could be covered by a single sensor, depending on the size of the blade. For example, if it were a viable option with respect to cost, an optical fiber, placed at the pressure and suction sides, could cover a large part of the spanwise and chordwise positions.

The presented method assumes knowledge of the load applied to the blades. For use on turbines during operation, it is thus necessary to measure the load, as shown by Hedges et al. [22] for an existing solution using strain gauges. Additionally, the utilized measures for change in strain are based on normalized values, which are used due to commercial interests. For the method to be validated, simulation results should be compared to measurements during testing with similar damages.

Acknowledgements

This work received partial funding from the Innovation Fund Denmark. This work is partly supported by the Danish Energy Agency through the Energy Technology Development and Demonstration Program (EUDP), grant no. 64018-0068. The supported project is RELIABLAD: Improving Blade Reliability through Application of Digital Twins over Entire Life Cycle.

References

- [1] Dao C, Kazemtabrizi B and Crabtree C 2019 *Wind Energy* **22** 1848–1871 ISSN 10991824
- [2] McGugan M, Pereira G, Sorensen B F, Toftegaard H and Branner K 2015 *Philos. Trans. R. Soc. A Math. Phys. Eng. Sci.* **373** ISSN 1364503X

- [3] Birkemose B and Egdal P 2017 Monitoring of blade frequencies of a wind turbine URL <https://patentimages.storage.googleapis.com/e6/ae/7f/dd9c7f89c183e5/EP2158402B1.pdf>
- [4] Sørensen B F, Jørgensen E, C P Debel, Jensen F M, Jensen H M, Jacobsen T K and Halling K M 2004 Improved design of large wind turbine blade of fibre composites based on studies of scale effects (phase 1) - summary report Tech. rep.
- [5] Sørensen B F, Lading L, Sendrup P, Mcgugan M, Debel C P, Kristensen O J D, Larsen G, Hansen A, Rheinländer J, Rusborg J and Vestergaard J D 2002 Fundamentals for Remote Structural Health Monitoring of Wind Turbine Blades - a Preproject Tech. rep. Risø National Laboratory
- [6] Paquette J, Van Dam J, Hughes S and Johnson J 2008 *46th AIAA Aerosp. Sci. Meet. Exhib.*
- [7] Rumsey M A, Paquette J, White J, Werlink R J, Beattie A G, Pitchford C and van Dam J 2008 Experimental Results of Structural Health Monitoring of Wind Turbine Blades Tech. rep.
- [8] Taylor S G, Jeong H, Jang J K, Park G, Farinholt K M, Todd M D and Ammerman C M 2012 *Ind. Commer. Appl. Smart Struct. Technol. 2012* **8343** 83430Q
- [9] Taylor S G, Jeong H, Jang J K, Park G, Farinholt K M, Todd M D and Ammerman C M 2012 *Ind. Commer. Appl. Smart Struct. Technol. 2012* **8343** 83430Q
- [10] Taylor S G, Park G, Farinholt K M and Todd M D 2013 *Struct. Heal. Monit.* **12** 252–262 ISSN 14759217
- [11] Taylor S G, Farinholt K, Choi M, Jeong H, Jang J, Park G, Lee J R and Todd M D 2014 *J. Intell. Mater. Syst. Struct.* **25** 613–620 ISSN 1045389X
- [12] Dervilis N, Choi M, Antoniadou I, Farinholt K M, Taylor S G, Barthorpe R J, Park G, Worden K and Farrar C R 2012 *J. Phys. Conf. Ser.* **382** ISSN 17426596
- [13] Dervilis N, Choi M, Taylor S G, Barthorpe R J, Park G, Farrar C R and Worden K 2014 *J. Sound Vib.* **333** 1833–1850 ISSN 0022460X
- [14] Dervilis N, Choi M, Antoniadou I, Farinholt K M, Taylor S G, Barthorpe R J, Park G, Farrar C R and Worden K 2014 *Key Eng. Mater.* **588** 166–174 ISSN 10139826
- [15] Haselbach P U, Eder M A and Belloni F 2016 *Wind Energy* **19** 1871–1888
- [16] Overgaard L C, Lund E and Thomsen O T 2010 *Compos. Part A Appl. Sci. Manuf.* **41** 257–270
- [17] Sierra-Pérez J, Torres-Arredondo M A and Güemes A 2016 *Compos. Struct.* **135** 156–166 ISSN 02638223
- [18] Ulriksen M D, Tcherniak D and Damkilde L 2015 *2015 IEEE Work. Environ. Energy, Struct. Monit. Syst. EESMS 2015 - Proc.* (Institute of Electrical and Electronics Engineers Inc.) pp 50–55 ISBN 9781479982141
- [19] Ulriksen M D, Tcherniak D, Kirkegaard P H and Damkilde L 2016 *Struct. Heal. Monit.* **15** 381–388 ISSN 17413168
- [20] Benedetti M, Fontanari V and Zonta D 2011 *Smart Mater. Struct.* **20** ISSN 09641726
- [21] Arsenault T J, Achuthan A, Marzocca P, Grappasonni C and Coppotelli G 2013 *Smart Mater. Struct.* **22** ISSN 09641726
- [22] Hedges A and Vronsky T 2010 Wind turbine blade load sensor URL <https://patentimages.storage.googleapis.com/e9/1b/97/c7f173aa249a1c/W02010049736A1.pdf>

Towards A Comprehensive Fatigue And Crack Propagation Toolbox For Offshore Wind Foundations

N Sadeghi^a, P D'antuono^a, N Noppe^a, W Weijtjens^a, C Devriendt^a

^a Offshore Wind Infrastructure-lab / Vrije Universiteit Brussel

E-mail: Negin.Sadeghi@vub.be

Keywords: Offshore Wind Foundations ; Fatigue Toolbox ; Crack Propagation ; Corrosion and Fatigue Interaction ; Deterministic and Nondeterministic Fatigue Life Prediction

1. Introduction

Currently, foundations design for offshore wind turbines (OWTs) – especially monopiles – is fatigue-driven. Therefore, increasing the understanding of fatigue and updating the current methodologies could lead to lifetime extensions of the currently existing foundations and design optimization for future OWTs. Wind and sea waves are the principal sources of variable amplitude fatigue loading for OWTs. Additionally, corrosion might play a role in reducing the fatigue tolerance capabilities of the structure at its critical locations. Currently, OWI-lab implements a deterministic stress-life approach based on the Palmgren-Miner rule (PM) combined with stress-life (SN) curves provided by industrial standards. Due to its simplicity, the current approach suffers from multiple shortcomings, and it is not able to catch the interactive effects of corrosion and fatigue on crack initiation and propagation at welded joints. Therefore, the development at OWI-lab of a reliable fatigue analysis tool to update the expected life at critical locations will address and try to overcome such points. MAXWind focus will be on monopile foundations, as these are the most used in the Belgian sea, and OWI-lab has a large amount of data for turbines installed on monopiles. As part of the MAXWind Project, improvement and extension of the existing fatigue toolbox are necessary. This contribution will give an introductory overview of the possibilities to achieve this goal using two different approaches of deterministic and non-deterministic, highlighting the benefits and the drawbacks of methods available for the specific application in the OWTs.

2. Current approach to OWT fatigue assessment

The fatigue toolbox currently implemented at OWI-lab suffers from multiple major limitations, in fact it does not account for the sequence of loading cycles. Moreover, based on PM, quantifying crack growth is not possible should any cracks be identified during a visual inspection. Therefore, PM only considers the crack initiation phase and does not assume any defect or crack in the material, and this means that, even though different SN curves are used for welds where corrosion might occur, a more exact fracture mechanics-based approach for corrosion and defects assessment is needed. Finally, PM neglects the statistical aspects of fatigue that are only partially included in the SN curve definition.

3. Improvements

3.1 Deterministic approaches

3.1.1 Mean stress effect correction models

Since the end of the 19th century, scientists and engineers understood that not only stress range, but also mean stress, plays a key role in fatigue life. Several researchers have proposed models to consider the mean stress effect in case of high cycle fatigue of steel components. The concept of these models is that the fatigue damage is the weighted sum of the damage caused by alternating stress and mean stress and they assume the alternating stress as a function of mean stress and stress amplitude [1](Figure 1) However, guidelines [2] only suggest accounting for the positive effect of compressive mean stress, though it might lead to non-conservative predictions. Nevertheless, a mean stress effect correction model is necessary as SN curves are obtained at a fixed mean stress level (usually zero), while OWTs are under variable amplitude loading with non-zero mean stress. In the last century, tens of mean stress-effect corrections have been proposed, mostly based on empirical observations on the constant life (Haigh) diagram. [1] In addition, as both Dowling [3] and D'Antuono and Ciavarella [4] highlight, a proper mean stress correction shall show a high level of generality and simplicity of application, similarly to PM for damage accumulation. For this purpose, the general linear, Goodman, Söderberg, Gerber, SWT, and Walker (cfr. Figure 1) models are going to be included in the OWI-lab fatigue toolbox. Next studies will focus on understanding which of these models is the most suitable for offshore wind foundations depending on the materials, treatments, and the environment.

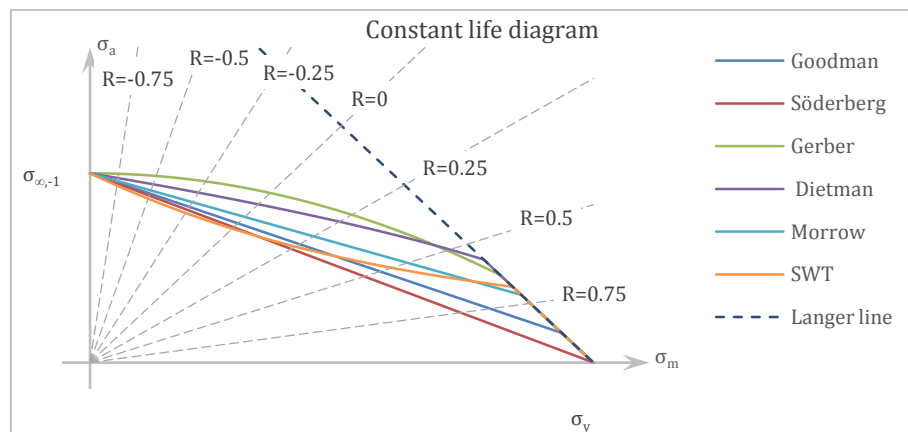


Figure 1 – Mean stress correction models in the constant life diagram. Each line defines infinite life at the fatigue limit $\sigma_{\infty(R=1)}$. If the applied stress falls below the constant life line, then the structure will have infinite life, otherwise SN curves are necessary.

3.1.2 Damage accumulation

3.1.2.1 Damage accumulation in crack initiation and non-propagation of existing defects

The first and most used fatigue damage accumulation rule is PM, although it suffers from the drawbacks already stated in § 2. Despite its limitations, PM is also suggested by the guidelines, as conservatism can easily be included in the formula, for example by reducing the critical damage. Furthermore, PM can be also used for non-propagation prediction of existing cracks/defects/pits, when combined with the threshold information available from fracture mechanics. For this purpose, an existing defect can be assumed, and as long as the stress at the defect root/crack tip lies below the

propagation threshold diagrams, SN curves can be shifted accordingly such that the initial defect is treated as if it has to reinitiate.

3.1.2.2 Damage accumulation in crack propagation

Fatigue crack growth can be subdivided in three phases called stages: Stage I (*initiation* phase, and short crack propagation), Stage II (*stable propagation* of a long crack), and Stage III (*unstable propagation* and sudden fracture). These stages can be observed in Figure 2.

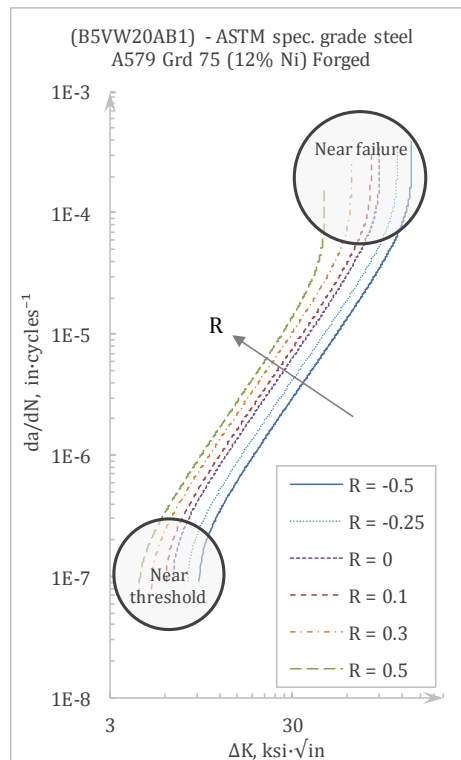


Figure 2 Typical fatigue crack growth curve for an ASTM steel. The effect of mean stress and the three stages are visible: I near threshold (initiation), II stable propagation (Paris'), III near failure (unstable propagation)[5].

PM rule is valid when there are no cracks/pits/defects in the structure. In the case of a non-perfect structure, the first step to validate the PM calculation is defining a factor that covers the non-propagation of cracks up to a certain size (The process is shown in Figure 3). If these factors cannot be calculated, the crack can propagate, while the crack propagation is modelled via Paris'/Walker's/NASGRO™ laws. Conventional SN curves only account for initiation, therefore, the fatigue crack growth rate curves are presented to consider the crack growth, plotting crack growth rate versus stress intensity factor (Figure 2). Paris' law, Walker' law, and the NASGRO equation are the most common crack growth models. The Paris' law describes the crack propagation zone reasonably, but it overestimates the crack initiation zone. The Paris' law does not consider crack initiation time and it is valid in certain conditions, i.e. constant amplitude mode-I loading, uniaxial loading, long cracks, and LEFM. Besides, it does not account for mean stress effects and load sequence effects [6]. Walker presented an equation which is a generalization of the Paris equation introducing mean stress effect through the Walker mean stress correction itself but still, no load sequence effect is accounted for. [7]. The NASGRO equation is the most general of the crack growth equations. Load sequence effect and Stage I and Stage III of growth are accounted for in this equation [8].

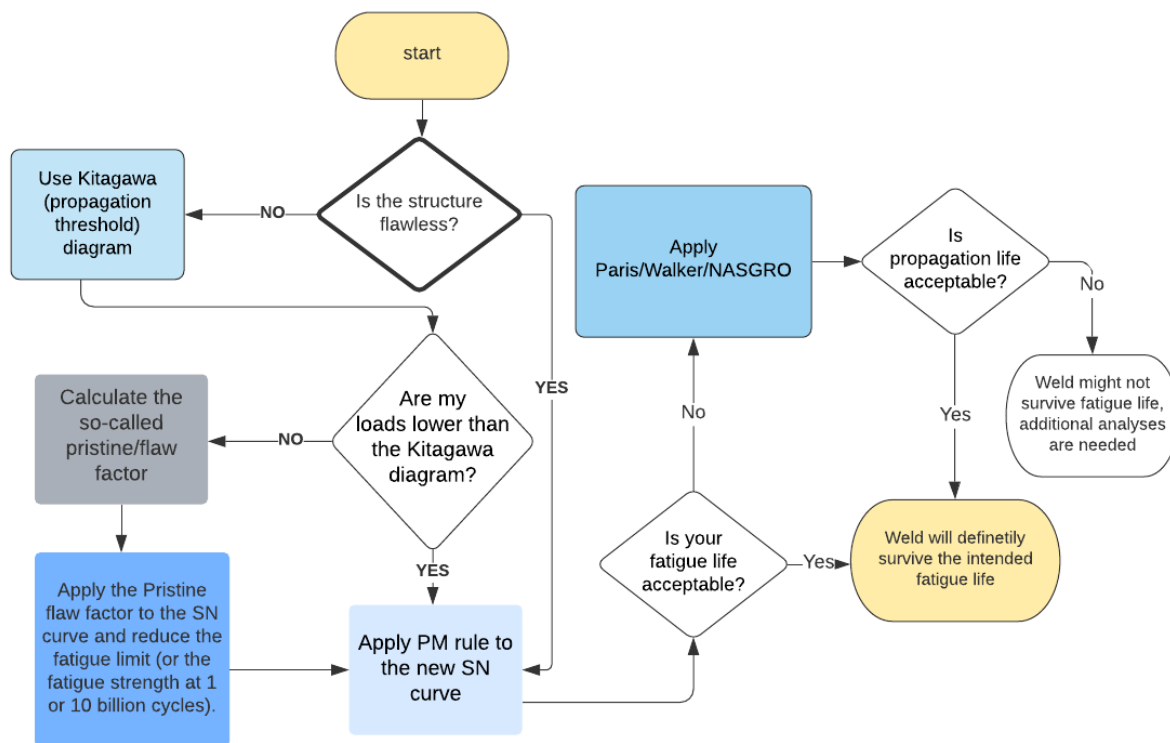


Figure 3 – Fatigue assessment flowchart including crack propagation.

3.1.3 Corrosion Assessment

The major difference between corrosion fatigue and ordinary fatigue is in the crack initiation and crack propagation stages. During the classical fatigue testing, initiation takes up to 90% of the specimen's lifetime, followed by fairly rapid crack propagation, while in the case of corrosion fatigue, usually only around 10% of the specimen life is spent in the crack initiation phase. As a result, fracture mechanics concepts are helpful in case of corrosion fatigue. Several equations try to model the propagation threshold, such as Kitagawa-Takahashi (KT) or Murakami (Figure 4). To account for corrosion, DNVGL guideline proposes dedicated SN curves (Figure 5). However, it is not transparent how these corrosion SN curves are obtained. Therefore, in the OWI-Lab toolbox, the D'Antuono-Ciavarella amplification factor for constant thickness reduction due to corrosion and KT diagram are going to be implemented (following the UK directive BS7910 [9], to include a factor in the existing SN curves for the case of corrosion. The KT diagram is used to predict the allowable stress range below which cracks of given length and stress range stay in non-propagation and therefore have an infinite life. It blends the long crack threshold and fatigue endurance limit lines to define the non-propagating cracks zone [10].

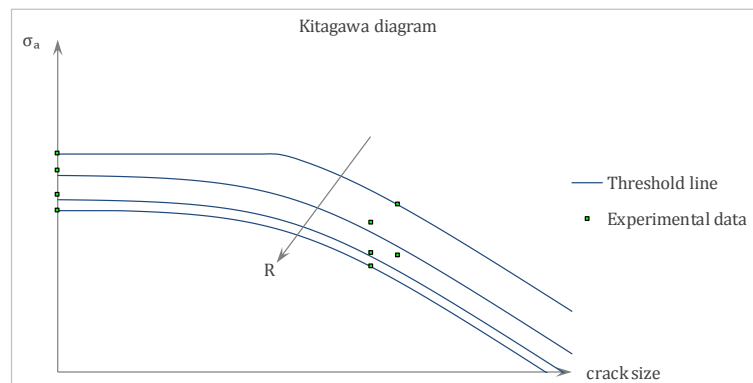


Figure 4 – Kitagawa-Takahashi diagram and its dependence on the load ratio

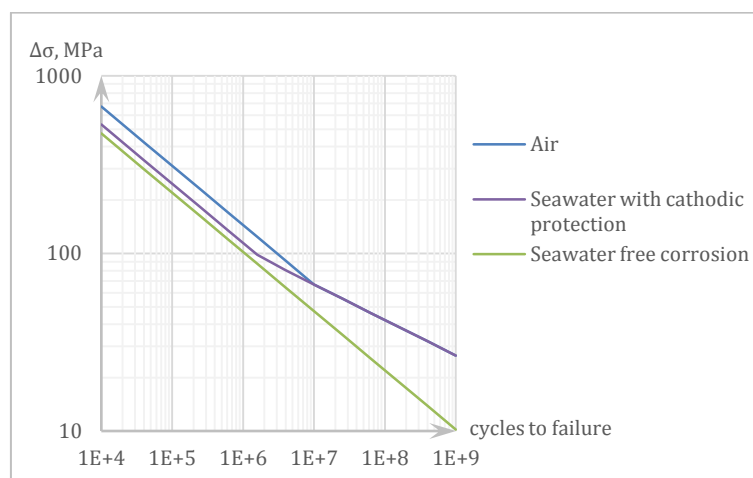


Figure 5 – SN curves for tubular joints in air and in seawater, with or without cathodic protection [2]

3.2 Non-deterministic approaches

All deterministic approaches discussed in previous section will result into one final datum, either for damage or crack length. However, offshore structures suffer damage from external loads such as wind, waves, and sea currents, which have a statistical nature. Given the irregularity of the loads, an estimation of the uncertainty on the final damage is actually needed. Therefore it is necessary to understand the irregularity of the loads and to apply a damage model depending on the type of random variable. Several articles studied different load probability distribution functions and showed the applicability of each distribution under different conditions, which motivates further research, regarding that the loading data is available in OWI-Lab. Some probabilistic and statistical fatigue damage models are proposed which take into account the load dependency such as loading cycle distribution. The main models used for wide-band Gaussian processes are the Dirlik, Ortiz and Chen, The Wirsching and Ligh, and the Lalanne-Rice. For further studies, the inclusion of these models in the offshore wind industry and their validity will be investigated.

4 Conclusion

In this contribution, the current approach used in OWT fatigue assessment was critically studied. Shortcomings were identified such as lack of mean stress effect, corrosion fatigue assessment or the inclusion of non-propagating defects and crack propagation. Some possible improvements to overcome these shortcomings have been suggested, such as the implementation of the mean stress correction models, corrosion factors based either on constant corrosion along the circumference, or on

non-propagation zone models such as Kitagawa-Takahashi, or applying Paris/Walker/NASGRO models to predict the crack propagation. Furthermore, non-deterministic damage accumulation models have been proposed for further investigations.

Bibliography

- [1] J. F. Barbosa, J. A. F. O. Correia, R. C. S. F. Júnior, and A. M. P. D. Jesus, ‘Fatigue life prediction of metallic materials considering mean stress effects by means of an artificial neural network’, *Int. J. Fatigue*, vol. 135, p. 105527, Jun. 2020, doi: 10.1016/j.ijfatigue.2020.105527.
- [2] ‘DNV-RP-C203: Fatigue Design of Offshore Steel Structures’, p. 176, 2011.
- [3] N. E. Dowling, ‘Mean stress effects in strain–life fatigue’, *Fatigue Fract. Eng. Mater. Struct.*, vol. 32, no. 12, pp. 1004–1019, 2009, doi: 10.1111/j.1460-2695.2009.01404.x.
- [4] P. D’Antuono and M. Ciavarella, ‘Mean stress effect on Gaßner curves interpreted as shifted Wöhler curves and application to smooth and notched geometries’, *Fatigue Fract. Eng. Mater. Struct.*, vol. 43, no. 4, pp. 818–830, 2020, doi: 10.1111/ffe.13197.
- [5] ‘NASA Technical Reports Server (NTRS)’. <https://ntrs.nasa.gov/citations/19990028759> (accessed Oct. 19, 2020).
- [6] S. Suresh and R. O. Ritchie, ‘Propagation of short fatigue cracks’, p. 31.
- [7] S. Beden, S. Abdullah, and A. K. Ariffin, ‘Review of Fatigue Crack Propagation Models for Metallic Components’, *Eur. J. Sci. Res.*, vol. 28, Jan. 2009.
- [8] ‘NASA Technical Reports Server (NTRS)’. <https://ntrs.nasa.gov/citations/19990028759> (accessed Oct. 19, 2020).
- [9] ‘Guide to methods for assessing the acceptability of flaws in metallic structures’, Dec. 2013.
- [10] J. Maierhofer, H.-P. Gänser, and R. Pippan, ‘Modified Kitagawa–Takahashi diagram accounting for finite notch depths’, *Int. J. Fatigue*, vol. 70, pp. 503–509, Jan. 2015, doi: 10.1016/j.ijfatigue.2014.07.007.

Fleet-Wide Operational Analysis During Different Construction Phases of an Offshore Wind Farm

A F de Oliveira Junior^a, W Weijtjens^a, C Devriendt^a

^a Vrije Universiteit Brussel (VUB) / Offshore Wind Infrastructure-lab (OWI-lab)

E-mail: Adelmo.Fernandes@vub.be

Keywords: Geotechnics and Structural Integrity, New Concepts

1 Introduction

Inside the scope of the Soiltwin project the Offshore Wind Infrastructure-lab (OWI-lab) is conducting an extensive measurement campaign of the resonance frequencies and damping ratios of offshore wind structures. For this purpose, a mobile measurement unit (MMU), the black box in the Figure 1 (a), is used to collect data through all different phases of construction of an offshore wind farm. In other words, when there is just the Transition Piece (TP) the MMU is installed on it and starts to measure and sent data to the cloud. After that, the installation process begins and tower, nacelle and blades are installed. Then, the MMU is installed on the next TP and process continue until the last turbine is installed. After the data is collected it is processed using operational modal analysis (OMA)[1],[2] to determine resonance frequencies (and damping ratios). With this approach will be possible to have unique information on the structural dynamics of the entire offshore wind turbine farm during different phases of its construction.

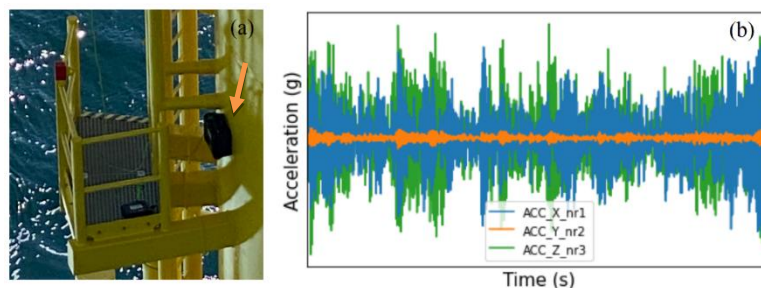


Figure 1 (a) MMU installed on the TP. (b) Typical acceleration time series.

2 Methodology

The MMU is capable to measure accelerations from three orthogonal axis and after processing the signal it is plotted the acceleration time series showed in the Figure 1 (b). After applying Welch's method the Power Spectral Densities (PSD) are obtained in different phases of construction, Figures 2 (a), (b) and (c). From the Figure 2 (a), the first peak is the frequency that the waves hit on TP and the second is the resonance frequency of the 1st vibration mode. From the Figure 2 (b), the first peak is the 1st vibration mode and the second is the 2nd vibration mode. From the Figure 2 (c), the first peak is the 1st vibration mode, the second peak is the 1st rotor mode. Still in the Figure 2 (c), the set of three peaks together is due to misalignment between the rotor axis and the measurement axes of the MMU.

After yaw transformation, it is possible to obtain the 2nd forward vibration mode for X direction (FA2) and the 2nd side-side vibration mode (SS2) and the 3rd side-side vibration mode (SS3) for Z direction. All data is processed using 2 different OMA techniques, lscf and SSICOV. The modal parameters are extracted in an automated matter and manually checked to link the results with physical modes.

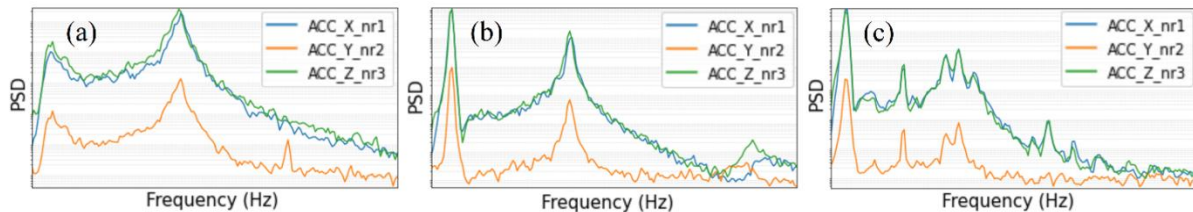


Figure 2 (a) Typical frequency spectrum with TP only. (b) Typical frequency spectrum without nacelle. (c) Typical frequency spectrum fully assembled.

3 Conclusion

After processing and analyzing 42 fully assembled WTGs, the results of the 1st side-side (SS1) resonance frequencies were condensed in the histogram of Figure 3 and compared to the design frequency values. Already from these results we can see more spread in the measurement than as suggested by design. Deeper research is needed in the field of offshore monopile foundations [3].



Figure 3 Distribution of the 1st side-side resonance frequencies of the 42 sites. (Red: as designed, Blue as measured)

Acknowledgements

current research is conducted in the frame of the “*cSBO SOIL-TWIN: data driven design optimization and smart monitoring of monopile*”

Bibliography

- [1] Devriendt C, et al. 2014 "Monitoring resonant frequencies and damping values of an offshore wind turbine in parked conditions." *IET Renewable Power Generation* **8.4**: 433-441
- [2] Magalhães F, Alvaro C. "Explaining operational modal analysis with data from an arch bridge." *Mechanical systems and signal processing* **25.5** (2011): 1431-1450
- [3] Kallehave D., Byrne B W, LeBlanc Thilsted C, Mikkelsen K K 2015 “Optimization of monopiles for offshore wind turbines.” *Philosophical Transactions of the Royal Society A: Mathematical, Physical and Engineering Sciences* **373** (2035), 20140100

A modelling approach to damage initiation and propagation from manufacturing defects in wind turbine blades

Íñigo Urcelay Oca and Lars Oliver Bernhammer

Siemens Gamesa Renewable Energy, Assensvej 11, 9220 Aalborg, Denmark

E-mail: inigo.oca@siemensgamesa.com

Keywords: Structural Analysis, Wind Turbine Blades, Damage Modelling, Composite Materials

The robust design of composite wind turbine blades aims at preventing damage, from initiating and propagating, thereby affecting the integrity of the blade or even causing its catastrophic failure. Damage modelling can be used in the blade design process to reduce safety factors generally employed to account for damage [1, 2]. Damage modelling can also be used to assess deviations originating in manufacturing or service. Numerical modelling can be used to decide if a wind turbine blade should be repaired or not during production, or whether it should be stopped immediately or monitored more frequently when already installed [3].

The production of wind turbine blades usually consists of the infusion of dry fibre-reinforced material with a matrix resin. Generally, the manufacturing process uses fabric composites for their drapability and ease of handling[4]. Unfortunately, the use of these fabric composites can also lead to defects such as wrinkles in the sheets placed in the mould or missing overlaps between different layers. These manufacturing defects can lead to a reduction in the blade structural strength and reduce the fatigue life by acting as stress concentrations. Often, these stress raisers act as damage initiators triggering further damage growth [2] until finally leading to the failure of the blade or a need to replace it. Despite advanced non-destructive test methodologies, some manufacturing non-conformances are not captured in the quality assurance process. Therefore, it is vital to improve understanding on how damage initiates and propagates from them.

The modelling of damage in composite structures is an area of great scientific interest, especially due to the complexity of interacting failure modes due to the heterogeneity of composite materials. Stitched fabric composites are even more heterogeneous as the infusion of the stitched dry plies with the resin leads to a characteristic distribution of the constituents in each ply. The fibres accumulate in bundles which are visible to the naked eye, surrounded by resin pools. The resulting distribution of fibres along the whole structure is not as homogeneous as typically assumed for non-textile composite materials. The latter have been the main focus of damage modelling in composites. As damage in composite structures can take place simultaneously at different scales, researchers have argued for the use of multi-scale models in order to study the damage initiation and propagation in microscopic and macroscopic levels [5]. That is, both at a level where the fibres, or fibre bundles, and the matrix are defined separately, or at a level where a ply of a composite laminate is considered as a homogeneous material.

In this paper, a new approach is presented to analyse the initiation and evolution of composite damage in wind turbine blades, in particular of damages which originate from manufacturing defects. A finite element model with explicitly modelled fibre bundles and resin is the core of the analysis. The key advantage of this approach is that the model scale is increased by several orders of magnitude compared to a micro-mechanical analysis, while maintaining the ability to analyse the key characteristics of typical damage cases in wind turbine structures. Based on material characterisation on fibre bundle and resin level, the model will be applied to and validated by experimental testing. Finally, this model will be integrated in a macro-scale model of the blade.

In order to build a model where the matrix and the fibre bundles are represented explicitly, both of these constituents must be characterised. While the matrix and the composite material as a whole are

commonly characterised experimentally, characterisation of fibre bundles is less common. Exceptions are the work performed by Olsson et al. [6], who tested impregnated fibre bundles, or the work by Marklund et al. in [7], who used unidirectional tape-based coupons of a representative fibre volume fraction. Other researchers have opted to assume the fibre bundles as equivalent to unidirectional laminates with a high fibre volume fraction [8, 9, 10] using micro-mechanical models or analytical expressions to obtain the fibre bundle properties from those of the matrix and the fibres. In the material characterisation, computing the stiffness properties of composite materials using the properties of its constituents can be achieved with an appropriate degree of accuracy, but the estimation of the strength properties presents a greater challenge. For this paper, the properties of the fibre bundles were computed analytically based on available properties of typical fibres and matrix. In a first step, the fibre volume fraction of the fibre bundles was determined. Micrographs of cross sections of specimens with a unidirectional lay-up (UD) whose fibre volume fraction was known were employed to obtain the fibre volume fractions within the fibre bundle. It was assumed that the area ratio in these cross sections was equivalent to the volume ratio in the whole composite specimen. Based on the fibre bundle volume ratio, the fibre bundles properties could be estimated by approximating the bundles as UD composites. For the longitudinal Young's modulus E_{11} and in-plane Poisson ratio ν_{12} the rule of mixtures was used, Halpin-Tsai relations [11] for the transverse Young's modulus E_{22} and in-plane shear modulus G_{12} and the self-consistent model for the out-of-plane shear modulus G_{23} and Poisson's ratio ν_{23} . The rest of the stiffness components were obtained based on the symmetry of the fibre bundle, where directions 2 and 3 were considered equivalent. The equations derived by Huang in [12] were used to calculate the strengths under tension, compression and shear loading based on the composite material strengths.

Next, as part of the validation of these stiffness properties and of the modelling approach, a Representative Volume Element (RVE) of the larger unidirectional model was created. In this RVE, one sole fibre bundle was modelled surrounded by the matrix. The shape of the fibre bundle was estimated from the aforementioned micrographs as being a rectangular prism with rounded corners. The amount of resin surrounding the bundle was chosen such that the overall fibre volume fraction coincided with that known for a composite laminate. The RVE was modelled in ANSYS using solid elements. And while the matrix was modelled as isotropic, the fibre bundle was assumed as transversely orthotropic, using the estimated properties obtained analytically. Following the work of Sun and Vaidya [13], four different analyses were run to obtain the stiffness components, loading the RVE longitudinally and transversely under normal and shear loads. For reasons of simplicity, the same mesh was employed in the four analyses, rather than taking advantage of the symmetry present in each of these cases. All properties showed values similar to those obtained experimentally. It was also studied how different shapes of the fibre bundles influence the results, simulating rectangles without rounded corners and elliptical bundles. The ellipse extends further in direction 2 and 3 compared to the rectangle, which explain why it overestimates E_{22} and ν_{23} , while underestimating properties related to direction 1. The approach was extended to an RVE of a larger specimen with multiple fibre bundles regularly distributed, while mimicking the distribution of fibre bundles found in the aforementioned micrographs. Each bundle is located right on top of the bundle from the ply below it, as seen in figure 1. The load cases mentioned above were applied to this model for validation.

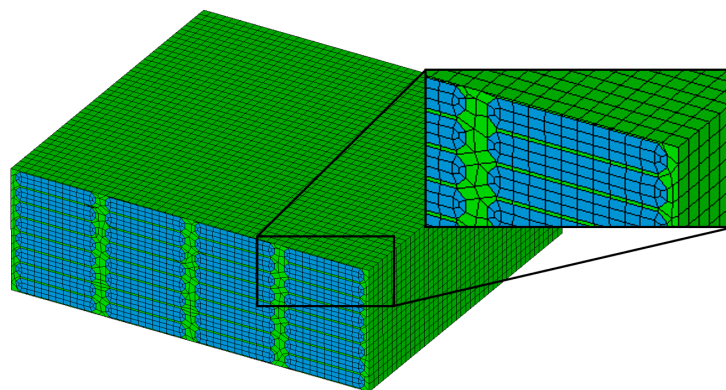


Figure 1: Multiple fibre bundles finite element model. Fibre bundles (blue), resin (green)

In a next step, damage modelling is included into the model. Due to the large number of elements and the need for an industry-efficient model, a smeared-crack approach where damage is modelled through material degradation was chosen. In this approach, upon exceeding a certain damage initiation criterion, the failed element sees its properties degraded based on the predicted failure mode [14]. The degradation of the properties can be instantaneous or gradual. The latter resembles reality much closer and by using the crack-band approach can eliminate the element size dependency observed in instantaneous degradation [15]. For these reasons, a gradual approach was chosen and has been included to ANSYS by a user-defined material subroutine using Hashin's failure criterion.

Acknowledgements

This project has received funding from the European Union's Horizon 2020 Research and Innovation Programme (DyVirt – Dynamic Virtualization: modelling performance of engineering structures) under the Marie Skłodowska-Curie grant agreement No 764547.

References

- [1] Verma A S, Vedvik N P, Haselbach P U, Gao Z and Jiang Z 2019 *Composite Structures* **209** 856–878
- [2] Toft H S, Berring P, Branner K and Sørensen J D 2009 *European Wind Energy Conference and Exhibition (EWECC) 2009* vol 1 (Marseille, France) pp 344–371
- [3] Montesano J and Singh C V 2015 *Mechanics of Materials* **83** 72–89
- [4] Zhang C, Binienda W K, Goldberg R K and Kohlman L W 2014 *Composites Part A: Applied Science and Manufacturing* **58** 36–46
- [5] Ye J, Chu C, Cai H, Hou X, Shi B, Tian S, Chen X and Ye J 2019 *Composite Structures* **212** 220–229
- [6] Olsson R, Marklund E and Jansson N 2012 *Proceedings of the 15th European Conference on Composite Materials* June (Venice, Italy) pp 24–28
- [7] Marklund E, Asp L E and Olsson R 2014 *Composites Part B: Engineering* **65** 47–56
- [8] Huang Y, Xu L and Kyu Ha S 2012 *Journal of Composite Materials* **46** 2431–2442
- [9] Ferreira L M, Graciani E and París F 2019 *Composite Structures* **225** 111115
- [10] Blacketter D M, Walrath D E and Hansen A C 1993 *Journal of Composites Technology and Research* **15** 136–142
- [11] Affdl J C H and Kardos J L 1976 *Polymer Engineering & Science* **16** 344–352
- [12] Huang Z 2001 *International Journal of Solids and Structures* **38** 4147–4172
- [13] Sun C T and Vaidya R S 1996 *Composites Science and Technology* **56** 171–179
- [14] Zhi J, Chen B Y and Tay T E 2019 *Computational Mechanics* **63** 201–217
- [15] van Dongen B, van Oostrum A and Zarouchas D 2018 *Composite Structures* **184** 512–522

Comparison of different load simulation methods on an offshore wind jacket foundation

Chao Ren^a, Younes Aoues^a, Didier Lemosse^a, and Souza De Cursi Eduardo^a

^aLaboratory of Mechanics of Normandy, INSA Rouen Normandie, France

E-mail: chao.ren@insa-rouen.fr

Keywords: Jacket substructure, offshore load simulation approaches, Superelement

1 Abstract

In this paper, three load simulation approaches based on an offshore wind turbine jacket are studied. One is uncoupled method, the second is sequential coupled approach and the final one is fully integrated (coupled) approach. For the offshore wind turbine (OWT) simulation, the two common load simulation methods are the sequential coupled approach and fully integrated approach. The sequential method is widely used in industrial field, due to the intellectual properties and confidential issues between the foundation designer and the turbine manufacturer. The overview of this approach can be found in [1] and [2]. The fully integrated method can be found in many wind turbine simulation tools including OpenFAST, Bladed, Flex5, and HAWC2. As for the uncoupled simulation method, it is not commonly used, which can have different cases. The multiphysics couplings (eg. aero-elastic or hydro-elastic coupling) are usually neglected in this approach and the load simulation may be not accurate. But compared to sequential and fully integrated methods, the uncoupled simulation is easily carried out and also can be noticed in some researches and applications. In this study, the fully integrated method with strong coupling is considered as the reference. The comparison with other two approaches is conducted. In addition, the wind turbine tool used in this study is OpenFAST and the finite element analysis tool is ANSYS. The wind turbine tool OpenFAST allows to carry out the sequential coupled [3] and fully integrated simulation. The jacket model used is referenced in [4] designed for the 5-MW wind turbine [5]. The load case set is composed of the design load case (DLC) 1.2 of the IEC standard [6] and the wind and wave conditions are based on the K13 Deep Water Site of the UpWind project [7]. The wind speed is divided into 11 wind bins, between the cut-in and cut-out wind speed, with each size 2 *m/s*.

The responses of dynamic analysis in the top of jacket are compared. The comparison between the fore-aft force (F_x), fore-aft moment (M_y) which mainly cause the fatigue damage and platform surge (U_x) are studied. Here, only the results of the fore-aft force (F_x) in 10 minutes with mean wind velocity 12m/s are displayed in Fig.1. Also, the mean, absolute maximum and standard deviation values of F_x in each load cases are depicted in Fig.2. In the two figures, "Uncoupled", "Fully" and "Sequential" are, respectively, the simulation results of uncoupled, fully integrated and sequential coupled approaches. The results show that the simulation results in sequential coupled are mostly in good agreement with that in fully coupled approach. The uncoupled approach leads to big differences in the extreme responses in dynamic analysis. The differences between uncoupled approach and fully coupled approach are mainly because hydro damping and hydro elastic are not included in the uncoupled simulation. Hence, in order to better calculate the loads in the OWT simulation, the fully and sequential coupled approaches are recommended.

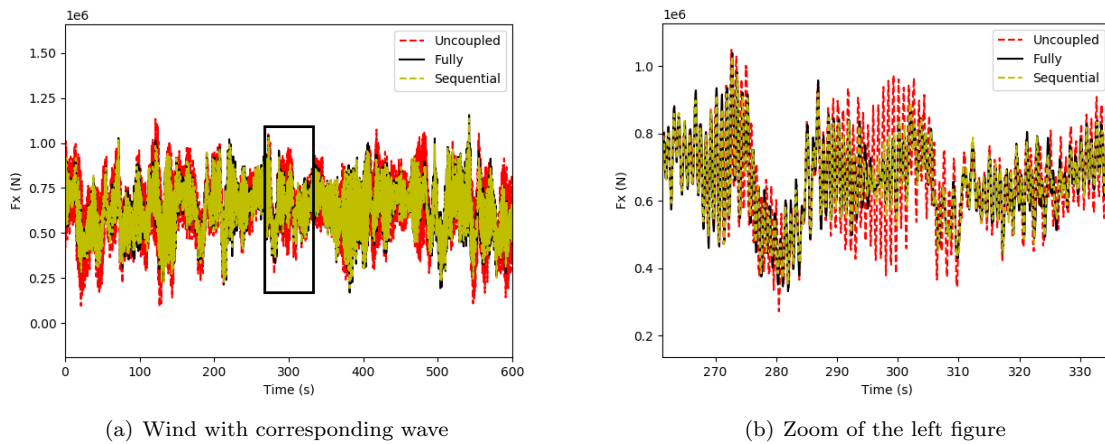


Figure 1: Fore-aft force F_x with mean wind velocity 12m/s

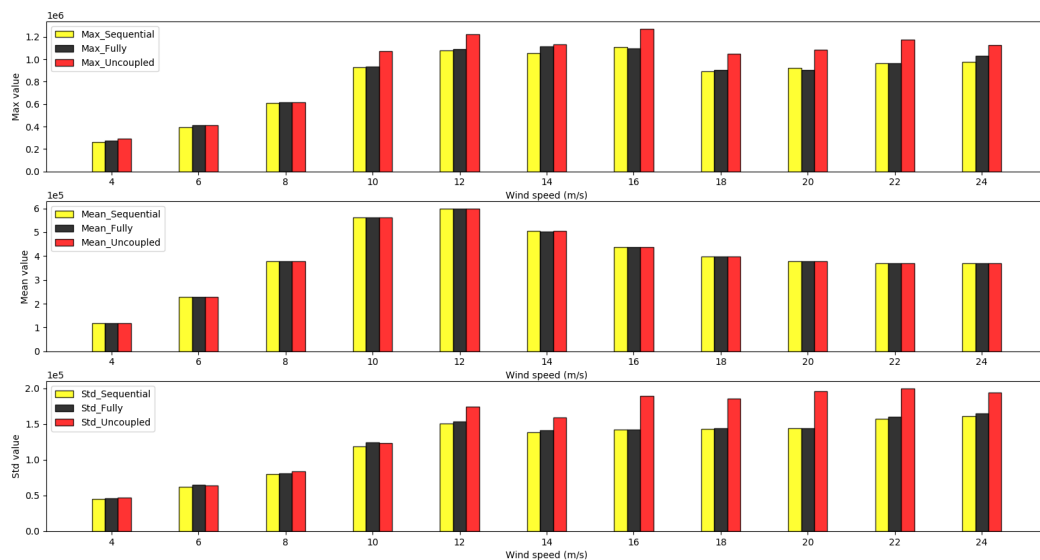


Figure 2: Mean, absolute maximum and standard deviation values of F_x (N) in each load cases

Acknowledgements

The research work is financially supported by China Scholarship Council (CSC).

References

- [1] Voormeeren S, van der Valk P, Nortier B, Molenaar D P and Rixen D 2014 *Wind Energy* **17** 1035–1054
- [2] van der Valk P L, Voormeeren S N, de Valk P C and Rixen D J 2015 *Journal of Computational and Nonlinear Dynamics* **10**
- [3] Branlard E, Shields M, Anderson B, Damiani R, Wendt F, Jonkman J, Musial W and Foley B 2020 *Journal of Physics: Conference Series* vol 1452 p 012033
- [4] Vorpahl F, Popko W and Kaufer D 2011 Description of a basic model of the "upwind reference jacket" for code comparison in the oc4 project under IEA Wind Annex XXX techreport Fraunhofer IWES
- [5] Jonkman J, Butterfield S, Musial W and Scott G 2009 Definition of a 5-mw reference wind turbine for offshore system development Tech. rep. National Renewable Energy Lab.(NREL), Golden, CO (United States)
- [6] IEC I 2009 *International Electrotechnical Commission, Geneva*
- [7] Fischer T, De Vries W and Schmidt B 2010 *Upwind deliverable (WP4: Offshore foundations and support structures)*, Endowed Chair of Wind Energy (SWE) at the Institute of Aircraft Design University at Stuttgart

Effect of Supporting Structure Flexibility on the Load Distribution of a Wind Turbine Pitch Bearing

E. Hurtado^a, H. Long^a, J. Carrell^a, R.S. Dwyer-Joyce^a, and W. Song^b

^aDepartment of Mechanical Engineering, The University of Sheffield, United Kingdom

^bOffshore Renewable Energy Catapult, United Kingdom

E-mail: eehurtadomolina1@sheffield.ac.uk (E. Hurtado)

Keywords: Pitch bearing, Load Distribution, FEA

Abstract

Pitch bearings in wind turbines are critical components. The main function of these bearings is to connect the blades to the hub allowing blades to rotate. Different damage modes have been observed in these bearings: edge loading, core crushing, rotational wear, false Brinelling and fretting corrosion. Load distribution among the bearing rolling elements is one of the relevant factors related to these damage modes.

Poor load distribution is a usual characteristic of pitch bearings due to the low stiffness provided by the supporting structures: hub and blades, as lightweight-design is an essential requirement for large-scale wind turbines. Although the effect of the stiffness of pitch bearing supporting structures on the load distribution has been largely studied, little evidence exists regarding how modifying the stiffness of these structures impacts on the load distribution of the bearing rolling elements.

In this work, the load distribution in a 2-metre diameter double row four-point contact ball pitch bearing is analysed considering different stiffness for the supporting structures. The analysis is carried out through finite element analysis, the flexibility of the hub and blades is modified by defining different thickness of the stiffener plates, and the different assembly stiffness configurations are compared by defining indexes to quantify the uniformity of the load distribution. Adding stiffener plates in the hub produces the best results to effectively improve the load distribution among the rolling elements, resulting in the maximum contact load reduced by 20% for the bearing analysed. Adding stiffener plates to the hub mainly increases its radial stiffness; therefore, it is possible to conclude that the radial flexibility of the hub has a major influence on the pitch bearing load distribution.

1 Introduction

Wind energy faces unique challenges to improve the reliability of wind turbine components. These challenges are not only associated with a large number of turbines and their remote location but also with modern large-scale wind turbines rapidly increasing their size with demanding lightweight design requirements to be fulfilled. The larger size of wind turbine mechanical components has resulted in higher replacement or repair cost of parts like gears and bearings. The increased cost associated with operation and maintenance affects the cost of wind energy and its competitiveness in the energy marketplace [1].

A mechanical system which has attracted more research interest from wind turbine manufacturers and wind farm operators recently is the blade pitch system. This system usually consists of a large slewing bearing (pitch bearing) built with gear teeth to be rotated either by an electric or hydraulic mechanism. The pitch bearing connects the blades to the hub allowing the blades to oscillate to change the angle of attack, which control power and loads in wind turbines.

Pitch bearings can be affected by different damage modes: fatigue, core crushing, ring fractures, edge loading, fretting corrosion and false Brinelling [2]. Stammler and Reuter [2] explain the damage modes in wind turbine pitch bearings; fatigue in through-hardened bearings initiates at the position of the maximum equivalent stress under Hertzian conditions, below the raceway surface. In pitch bearings,

which are commonly surface-hardened, fatigue may start at the same location or where the hardness is lower than the surface. In this case, the damage mode is known as core crushing. Bearing rings may also experience fatigue resulting in ring fractures due to high dynamic bending moments. Deformation of the rings because of flexibility of the surrounding parts causes translation of the contact area towards the raceway edge. When the contact path crosses the raceway edge, the contact area becomes smaller, and the remaining area withstands higher stresses. If the contact stresses exceed the allowable levels, the raceway will be damaged by edge loading. False Brinelling and fretting corrosion occur between loaded contacting surfaces under cyclic relative motion of small amplitude. False Brinelling is mild adhesive wear that occurs under lubricated contact conditions and fretting corrosion occurs under dry conditions [3].

The occurrence of the damage modes in wind turbine pitch bearings depends on several different factors, but certainly, one common parameter to all of them is the contact force between the bearing rolling elements and the bearing raceways. Pitch bearings are mounted on highly flexible structures: hub and blades. This results in bearing rings being subjected to large deformations and poor load distribution (load transmission from the blade to the bearing rolling elements). Due to the important role played by the hub and blades stiffness, pitch bearing testing and analysis should be done as a whole assembly [2].

The analysis of load distribution in pitch bearings is usually done through finite element analysis (FEA). The role of the surrounding structure has been studied by Chen et al. [4], Schwack et al. [5], and Stammeler et al. [6]. They have all demonstrated how the stiffness of blades and rotor hub affect the load distribution compared to analysing the bearing mounted on a rigid support. However, no evidence exists about how the load distribution is affected by modifying the stiffness of these components.

In this paper, the load distribution in a 2-metre diameter double row four-point contact ball pitch bearing is analysed considering different stiffness for the supporting structures.

2 Methods

The analysis of the load distribution was carried out developing a Finite Element (FE) model using the module ABAQUS/STANDARD 2017 considering a General Static Analysis. This type of analysis allows obtaining the contact forces acting on each bearing ball due to the equivalent static loads acting on the blades, neglecting any variation due to dynamic effects. This is a reasonable assumption, bearing in mind that this model aims to compare the load distribution under different configurations, and the magnitude of the contact forces between the balls and the raceway is given mainly by the static loads.

2.1 Description of the FE model of the pitch bearing assembly

Three 2-metre diameter double-rowed eight-point contact ball pitch bearings, three 40-metre blades and a 75mm-thickness hub were included in the FE model. The blade was modelled with arbitrary and simplified geometry, whose main dimensions were scaled from a 80-metre blade [7]. The assembly of these parts is presented in Figure 1(a). The model was meshed with a combination of solid and shell elements. The meshed geometry is presented in Figure 1(b). The main dimensions and material properties considered for modelling the pitch bearing are presented in table 1.

Table 1: Main dimensions and properties of the pitch bearing.

Parameter	Value
Ball diameter [mm]	45
Number of rows	2
Number of balls per row	120
Conformity	0.52
Contact angle [°]	45
Material	42CrMo4 EN10083-3 Steel
Young Modulus [MPa]	210000
Poisson's ratio	0.3

Bolted connections between the outer ring and the hub, and between the inner ring and the blade were simulated in detail. The balls were not modelled as solid bodies. Instead, they were modelled using traction-only springs and rigid elements as proposed by Daidie et al. [8]. The ball stiffness was calculated

using an analytical method described by Guay et al. [9]. Figure 2 shows a scheme with the balls contact modelling. This modelling strategy is highly efficient as it allows obtaining the contact forces without modelling hundreds of individual contacts.

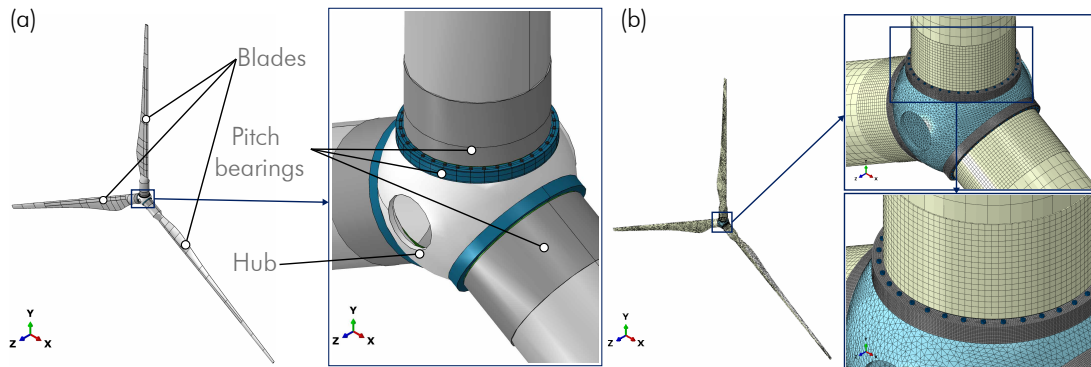


Figure 1: (a)Blades, pitch bearings and hub assembly. (b) FE model mesh.

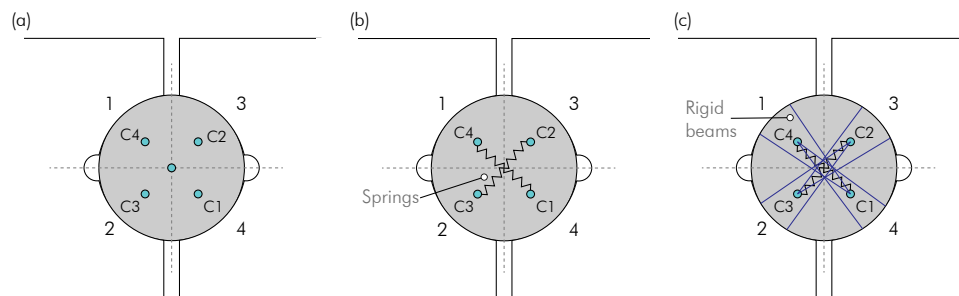


Figure 2: Balls contact modelling: (a) Contact arc centres definition. (b) Springs definition. (c) Rigid beams definition.

The rear flange that connects the hub to the main shaft of the drivetrain was fixed in all degree of freedom. Concentrated loads were applied on each blade along their local coordinate system. The loads were applied at a point such that the resulting forces and moments at the blade root are those listed in table 2. Load application points were linked to blade nodes by mean of couple interactions.

Load component	Value
Resultant axial force at blade root F_a [kN]	220
Resulting radial force at blade root F_r [kN]	72
Resulting moment at blade root M [kNm]	1600

2.2 Stiffness modification

This paper aims to understand the effect of modifying the stiffness of pitch bearing supporting structures. To achieve this aim, stiffer plates with different thickness were included in hub and blades. Six different assemblies are analysed, which are summarised in table 3. The locations of the stiffener plates are shown in Figure 3.

2.3 Analysis procedure

The results post-processed and analysed from the model are bearing ring displacements and contact forces acting on the bearing balls. The rings displacements are used to calculate the flexibility of the bearing

along the radial and axial axes. The contacts forces are analysed for the six assembly configurations compared by mean of the load distribution indexes.

3 Results and Analysis

Figure 4 presents the bearing rows numbering, contact pair definition, balls numbering, and angular position. These definitions are used in all the results presented in this section.

3.1 Bearing displacements

The displacements of the bearing rings were post-processed using a local cylindrical coordinate system, located at the centre of the bearing. Results for the base configuration are presented in detail, followed by summary plots for all the six assembly configurations.

Radial and axial displacements of the bearings are presented in Figure 5 and Figure 6, respectively. The radial displacement results show an oval shape of the ring, where two opposing points at 45° and 225° are deformed inwards and the opposite points at 135° and 315° are deformed outwards. The axial displacements results show that the higher difference between the inner and outer race happens at 225°, where the inner ring is more downwards deformed than the outer ring.

The maximum and minimum radial and axial displacements for the six assembly configurations are summarised in Figure 7(a) and Figure 7(b), respectively. Additionally, radial and axial flexibilities, defined according to the Equations 1 and 2, were included in these plots.

$$\delta_{radial} = \frac{d_{radial,max}}{P_{ea}} \quad (1)$$

$$\delta_{axial} = \frac{d_{axial,max}}{P_{ea}} \quad (2)$$

where, $d_{radial,max}$ and $d_{axial,max}$ are the maximum radial and axial displacement of the bearing, respectively, and P_{ea} is the bearing equivalent load defined in Equation 3 [10].

$$P_{ea} = 0.75F_r + F_a + \frac{2M}{d_m} \quad (3)$$

Table 3: Plate thickness in the six assembly configurations.

Configuration	Blade stiffener plate thickness [mm]	Hub stiffener plate thickness [mm]
Base	-	-
Blade stiffener plate 25mm	25	-
Blade stiffener plate 50mm	50	-
Hub stiffener plate 25mm	-	25
Hub stiffener plate 50mm	-	50
Blade and hub stiffener plate 50mm	50	50

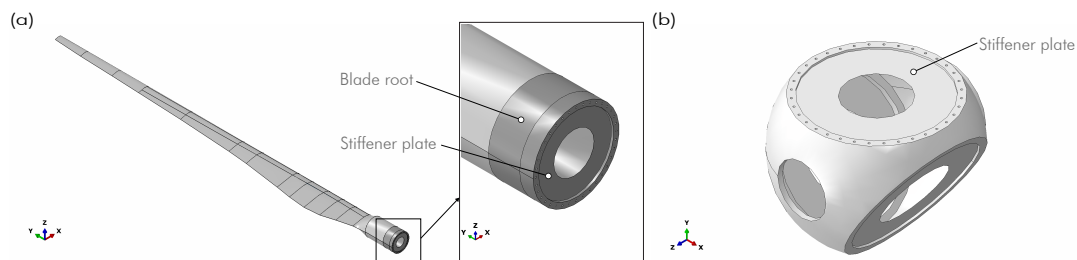


Figure 3: Locations of stiffener plates: (a) Blade. (b) Hub.

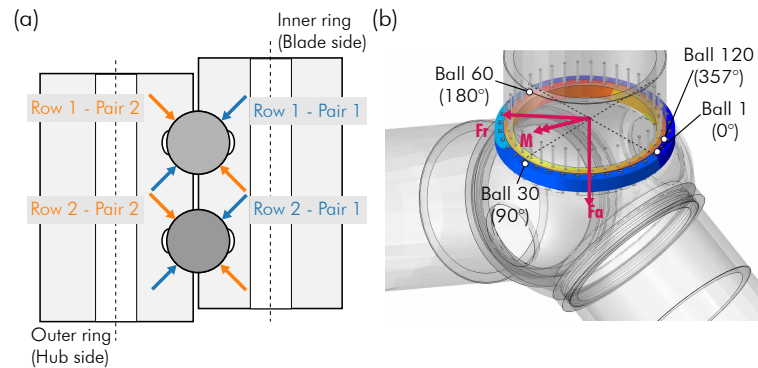


Figure 4: (a) Bearing rows numbering and contact pair definitions. (b) Ball numbering and angular position.

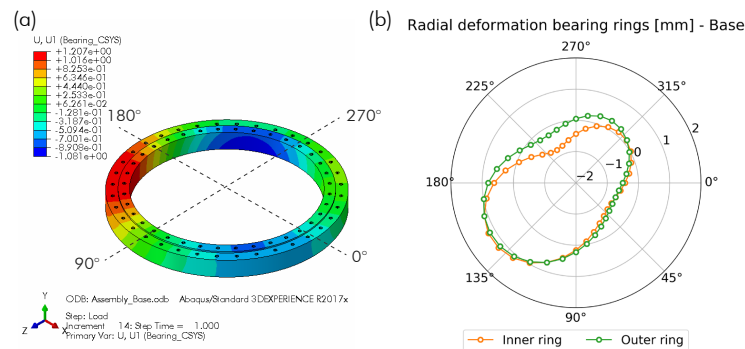


Figure 5: Bearing radial displacements a) View from FE model. b) Plotted in a polar graph.

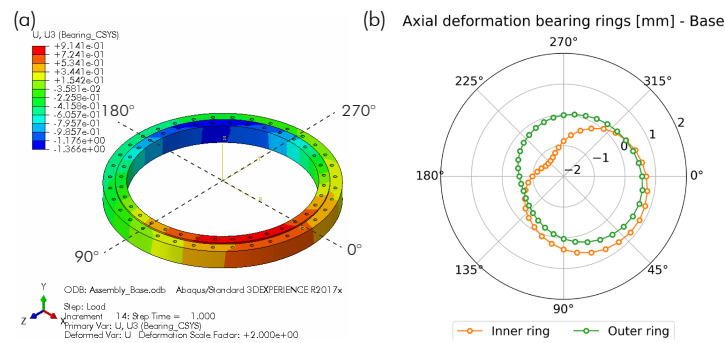


Figure 6: Bearing axial displacements a) View from FE model. b) Plotted in a polar graph.

where, F_r is the bearing radial force, F_a the bearing axial force, M the bearing bending moment, and d_m the bearing pitch diameter.

By comparing the results of all the assembly configurations, it can be observed that adding plates in the hub has a greater impact on reducing the radial displacements of the bearing. On the contrary, adding plates in the blades has a greater impact on reducing the axial displacement. The same can be observed in terms of the flexibility.

3.2 Load distribution

The load distribution is the contact force on every ball due to the loads applied to the blade. Similarly to the bearing displacement results, load distribution results are presented in detail for the base configuration

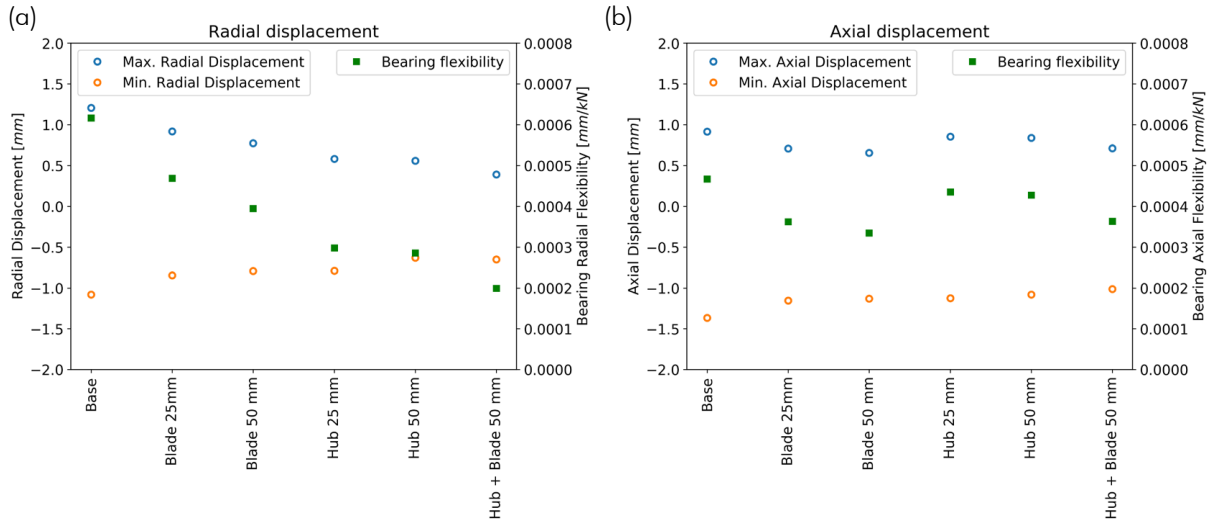


Figure 7: Summary of displacements for all configurations. (a) Radial. (b) Axial.

and summarised for all the six assembly configurations.

The load distribution for the base configuration (without any stiffener plates) in row 1 and 2 are shown in Figure 8(a) and 8(b). The maximum load is 26.2 kN in row 1, which is the row next to the blade. This value is 8.3% higher than the maximum contact load obtained using the analytical expression provided by Harris et al. [10] given by Equation 4.

$$Q_{max} = 0.55 \left(\frac{2Fr}{Z \cos \alpha} + \frac{F_a}{Z \sin \alpha} + \frac{4M}{d_m Z \sin \alpha} \right) \quad (4)$$

where, Z is the number of balls per row, and α the initial contact angle.

The maximum load in row 2, next to the hub, is 18.7 kN. The maximum load in row 1 is 55% higher than the maximum load in row 2. This difference is because row 1 is closer to the load application point in the blade. Maximum loads are located at the same angular position where the maximum and minimum displacements occur. The results also show that most balls are loaded at only two points.

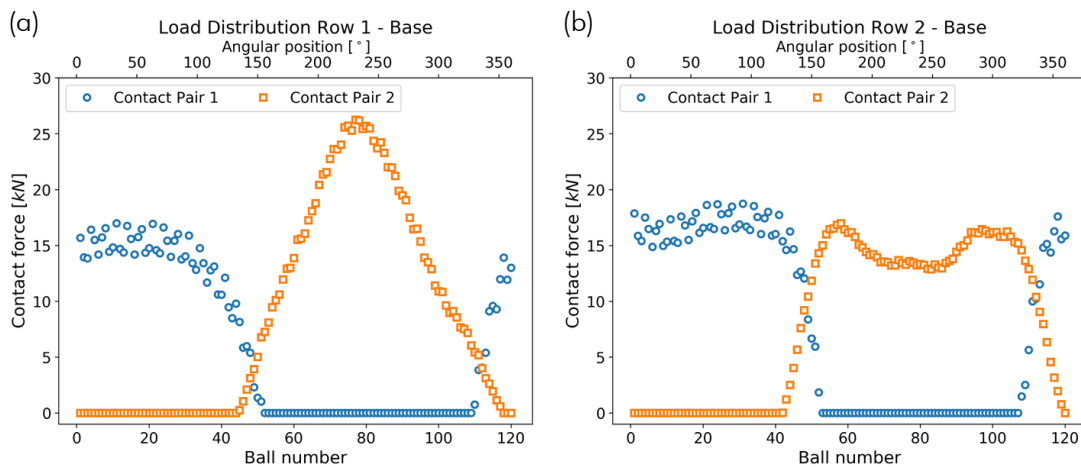


Figure 8: Load distribution base configuration. (a) Row 1. (b) Row 2

Defining a parameter to quantify the uniformity of the load distribution is essential to compare the different assembly configurations. Two indexes are defined for this purpose. The first index compares the

maximum load of contact pair 1 and 2 in a given row (LD_{row}). This index compares the load distribution within a row. The second index compares the maximum load of row 1 and 2, at the contact pair where the maximum value occurs ($LD_{bearing}$). This index compares the load distribution within the whole bearing. The expressions for these indexes are given in Equations 5 and 6. The closer the indexes are to 1, the better the load distribution will be. The load distribution indexes are presented in Figure 9.

$$LD_{row,i} = \frac{Max\ Contact\ Force(Row\ i - Pair\ 1)}{Max\ Contact\ Force(Row\ i - Pair\ 2)} \quad (5)$$

$$LD_{bearing} = \frac{Max\ Contact\ Force(Row\ 1)}{Max\ Contact\ Force(Row\ 2)} \quad (6)$$

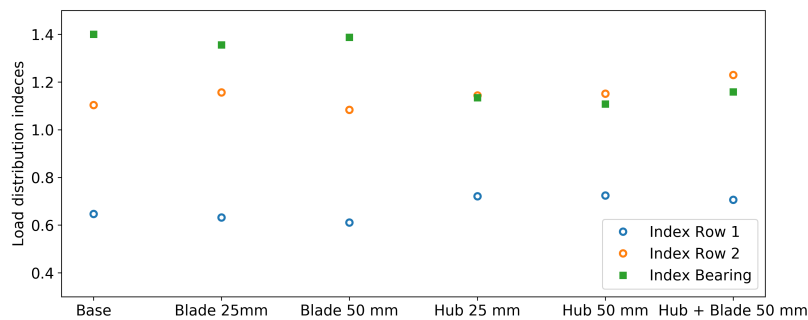


Figure 9: Load distribution indexes for all configurations.

The indexes comparison shows that adding a stiffener plate in the hub produces a more even load distribution as the indexes are the closest to 1.

Figure 10 presents a comparison of the load distribution for the base configuration and the configuration with the stiffener 50mm thickness plates in the hub. These plots illustrate the results of the

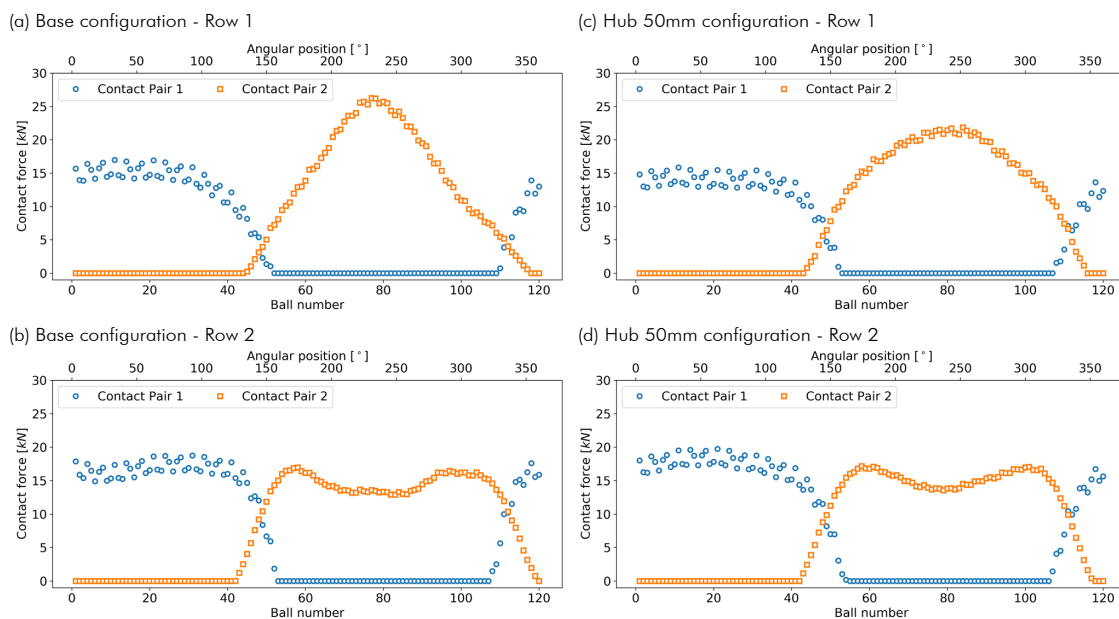


Figure 10: Comparison of load distribution between the base configuration and the configuration with the 50mm thickness plate in the hub.

improvement in the load distribution, which consists basically of a decrease of the maximum load of row 1, resulting in a more evenly distributed load around the location where the maximum load occurs.

4 Conclusions

An assembly FE model of the pitch bearing with its supporting structures was developed, post-processed and analysed. This model allows studying the load distribution among the bearing rolling elements. The analysis of the results shows the row next to the blade carries 55% more load than the row next to the hub because the row next to the blade is closer to the point of load application. The maximum load obtained from the model is 8% higher than the maximum analytical load obtained using the equation provided by Harris et al. [10]. This can be explained because that analytical expression does not take into account the flexibility of the adjacent structures. This specific difference is only valid for geometry considered in the model and will change for other pitch bearing designs. It is expected that the larger and more flexible the bearings are, the larger this difference will be.

Six different assembly configurations were assessed with this model. These configurations consist of modifying the stiffness of the supporting structures by adding stiffener plates. Adding plates in the hub results in the best load distribution, decreasing the load by 20%. In terms of the bearing displacements analysis, adding plates to the hub decreases the radial displacements and the bearing support flexibility. Therefore it is possible to conclude that the radial flexibility has a significant impact on the load distribution.

Having a more evenly distributed load is essential to reduce the occurrence of different damage mechanisms existing in pitch bearings and therefore improve their reliability. This is particularly important as modern large-scale wind turbines are rapidly increasing their size, resulting in more flexible bearings and supporting structures.

Acknowledgements

The first author is supported by the Chilean National Agency for Research and Development (ANID)/Scholarship Program / Doctorado Becas Chile/2018 - 72190145.

References

- [1] Kotzalas M N and Doll G L 2010 *Philosophical Transactions of the Royal Society A: Mathematical, Physical and Engineering Sciences* **368** 4829–4850 ISSN 1364503X
- [2] Stammler M and Reuter A 2015 *2nd Conference for Wind Power Drives, WD 2015*
- [3] Godfrey D 2003 *Tribology Lubrication Technology* **59** 28–30
- [4] Chen G and Wen J 2012 *Journal of Tribology* **134** 041105 ISSN 07424787
- [5] Schwack F, Stammler M, Poll G and Reuter A 2016 *Journal of Physics: Conference Series* **753** ISSN 17426596
- [6] Stammler M, Baust S, Reuter A and Poll G 2018 *Journal of Physics: Conference Series* **1037** ISSN 17426596
- [7] Sevinc A, Rosemeier M, Bätge M, Braun R, Meng F, Shan M, Horte D, Balzani C and Reuter A 2014 62
- [8] Daidie A, Chaib Z and Ghosn A 2008 *ASME J. Mech. Des.* **130** 0823011–0826018
- [9] Guay P and Frikha A 2015 *16th European Space Mechanisms and Tribology Symposium*
- [10] Harris T, Rumbarger J H and Butterfield C P 2009 *Nrel* 63

**WIND RESOURCE,
TURBULENCE AND
WAKE**

A new wake superposition method for wind-farm power prediction in presence of meso-scale background gradients

L Lanzilao and J Meyers

Department of Mechanical Engineering, KU Leuven, Celestijnenlaan 300A, 3001 Leuven

E-mail: luca.lanzilao@kuleuven.be

Keywords: Analytical wake model, wake-merging method, wind-farm power prediction, wakes, coastal gradient

1 Introduction

The flow obstructions caused by orographic obstacles and the different surface roughness and temperature found over land and sea make wind farms operating in velocity fields which are rarely uniform. However, existing wake-merging methods in engineering wind-farm wake models only rely on a single value of wind speed and turbulence intensity measured several hundreds of meters upstream of the farm [1, 2]. In the current work, we aim to fill this gap by developing a new wake-merging method for wind-farm power prediction in presence of heterogeneous velocity fields.

2 Methodology

Consider an arbitrary farm layout with N_t turbines immersed in a heterogeneous background velocity field $\mathbf{U}_b(\mathbf{x}) = (U_b(\mathbf{x}), V_b(\mathbf{x}))$ which changes magnitude and direction over the wind-farm area. To compute the waked flow through the farm, we use a recursive formula. To this end, we first order the turbines from most upstream to most downstream, so that for any $l > k$, the wake of turbine l does not interfere with turbine k . At the first iteration, the velocity field is given by the background wind speed $\mathbf{U}_0(\mathbf{x}) = \mathbf{U}_b(\mathbf{x})$. Next, at a generic iteration k , the velocity field downwind turbine k is computed as

$$\mathbf{U}_k(\mathbf{x}) = (\mathbf{U}_{k-1}(\mathbf{x}) \cdot \mathbf{e}_{\perp,k})(1 - W_k(\mathbf{x}))\mathbf{e}_{\perp,k} + (\mathbf{U}_{k-1}(\mathbf{x}) \cdot \mathbf{e}_{\parallel,k})\mathbf{e}_{\parallel,k}, \quad \text{for } k = 1, \dots, N_t \quad (1)$$

where $\mathbf{e}_{\perp,k} = (\cos \theta_k, \sin \theta_k)$ and $\mathbf{e}_{\parallel,k} = (-\sin \theta_k, \cos \theta_k)$ denote the unit vectors perpendicular and parallel to the rotor plane of turbine k with θ_k the orientation angle of the turbine. Note that we assume no yaw misalignment, hence

$$\theta_k \triangleq \arctan(V(\mathbf{x}_k)/U(\mathbf{x}_k)) = \arctan(V_{k-1}(\mathbf{x}_k)/U_{k-1}(\mathbf{x}_k)) \quad (2)$$

where $\mathbf{x}_k = (x_k, y_k, z_{h,k})$ denotes the turbine position. The total farm flow field corresponds to $\mathbf{U}(\mathbf{x}) = \mathbf{U}_{N_t}(\mathbf{x})$. Eq. 1 is derived using self-similarity in the wake of turbine k and simply expresses that the wake deficit is oriented in the axial direction of turbine k , while no velocity change occurs in the parallel direction. This axial velocity deficit is then transported along the streamlines of the background flow. Hence, the wake deficit function $W_k(\mathbf{x}) = \widehat{W}(\boldsymbol{\xi}_k(\mathbf{x}))$ where $\boldsymbol{\xi}_k(\mathbf{x})$ is a curvilinear reference frame which follows the background flow streamlines and with origin the position of turbine k (i.e., $\boldsymbol{\xi}_k(\mathbf{x}_k) = \mathbf{0}$). For more information, we refer to Lanzilao & Meyers [3].

3 Results and discussion

We consider a farm with 25 turbines with diameter $D = 154$ m and turbine hub height $z_h = 100$ m. The dimensionless streamwise and spanwise spacings are $s_x = s_y = 7$. The wake deficit function is the

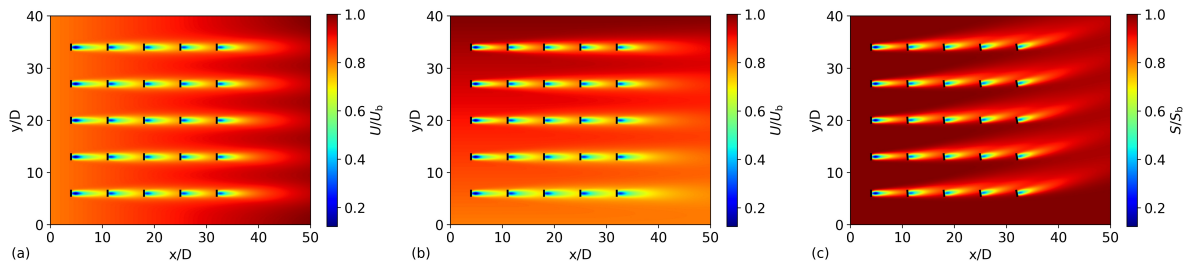


Figure 1: Normalized velocity field at a horizontal plane at hub height computed with the new wake-merging method coupled with the Gaussian wake model. (a,b) Abrupt change of background velocity magnitude along the streamwise and spanwise directions, respectively. (c) Abrupt change of background velocity direction over the wind farm. The black lines denote the wind-turbine rotor locations.

one proposed by Bastankhan & Porté-Agel [4] with $C_T = 0.85$. The ambient turbulence intensity is $TI_b = 12\%$ and the added turbulence is evaluated adopting the model proposed by Niayifar & Porté-Agel [2]. Fig. 1(a,b) illustrates the turbines' wake behaviour in presence of an abrupt change in background velocity magnitude along the streamwise and spanwise direction, respectively (i.e., the background wind speed increases linearly along the streamwise (spanwise) direction with a difference of 2 m/s between $x/D = 0$ ($y/D = 0$) and $x/D = 50$ ($y/D = 40$)). Note that the flow is uni-directional in these cases. Thereafter, Fig. 1(c) shows the flow through a farm which is subject to an abrupt change in wind direction. In this specific case, we assume $S_b = \|\mathbf{U}_b(\mathbf{x})\|_2 = 10$ m/s and we vary the wind direction with $\theta_b(x) = 0.35x/D$, so that there is a 10° change in background wind direction between the first and the last column of turbines.

The new wake-merging method is validated using LES data, Dual-Doppler radar measurements and SCADA data from the Horns Rev, London Array and Westermost Rough farm. The turbines power output is computed using different wake deficit function expressions taken from literature [4, 5, 6, 7]. Results show that the new method performs similarly to linear superposition of velocity deficits in homogeneous conditions but it shows better performance when a spatially varying background velocity is used. We refer to Lanzilao & Meyers [3] for more details.

4 Future work

Future research will focus on a more extensive validation of the new wake-merging method in presence of heterogeneous background velocity fields. The Anholt wind farm is a suitable candidate for this type of study due to the strong coastal gradient present in its location. Also, the new wake-merging model could account for velocity gradients generated by self-induced gravity waves. Hence, we plan to couple the new wind-farm model with the recently developed mid-fidelity three-layer model (see Allart & Meyers [8]) in the future.

References

- [1] Katic I, Højstrup J and Jensen N 1986 *EWEC'86. Proceedings* **1** Rome, Italy 407–410
- [2] Niayifar A and Porté-Agel F 2016 *Energies* **9** 741
- [3] Lanzilao L and Meyers J URL <https://arxiv.org/abs/2010.03873>
- [4] Bastankhan M and Porté-Agel F 2014 *Renew. Energy* **70** 116–123
- [5] Schreiber J, Balbaa A and Bottasso C L 2020 *Wind Energy Science* **5** 237–244
- [6] Blondel F and Cathelain M 2020 *Wind Energy Science* **5** 1225–1236
- [7] Ishihara T and Qian G W 2018 *J. Wind Eng. Ind. Aerod.* **177** 275–292
- [8] Allaerts D and Meyers J 2019 *J. Fluid Mech.* **862** 990–1028